CONSTRUCTING TENSEGRITY-INSPIRED MICROSTRUCTURES IN A POLYMER NANOCOMPOSITE WITH CELLULOSIC NANOMATERIALS

A Dissertation
Presented to
The Academic Faculty

by

Matthew Orr

In Partial Fulfillment
of the Requirements for the Degree
Doctorate of Philosophy in Materials Science and Engineering in the
School of Materials Science and Engineering

Georgia Institute of Technology
May 2019

CONSTRUCTING TENSEGRITY-INSPIRED MICROSTRUCTURES IN A POLYMER NANOCOMPOSITE WITH CELLULOSIC NANOMATERIALS

Approved by:

Dr. Meisha Shofner, Advisor
School of Materials Science and Engineering
Georgia Institute of Technology

Dr. Carson Meredith
School of Chemical and Biomolecular Engineering
Georgia Institute of Technology

Dr. Karl Jacob
School of Materials Science and Engineering
Georgia Institute of Technology

Dr. Donggang Yao
School of Materials Science and Engineering
Georgia Institute of Technology

Dr. Christopher Luettgen
School of Chemical and Biomolecular Engineering
Georgia Institute of Technology

Date Approved: November 05, 2018

To my wife Sarah and my family for pushing me to be my best self.

ACKNOWLEDGEMENTS

These past years as a Ph.D. candidate have been without a doubt the most trying times in my life both personally and academically. I would like to thank my parents for their unconditional love and support that I so desperately cherish. I would also like to thank my best friend and better half, Sarah for her ability to motivate me to be a better person than I ever thought possible each and every day.

I would like to acknowledge my advisor, Meisha Shofner for her guidance and advice as she helped me develop a deeper understanding and appreciation of polymer and polymer nanocomposite research. I would also like to thank my committee members, Karl Jacob, Christopher Luettgen, Carson Meredith, and Donggang Yao for their suggestions on my research and for providing time and equipment to further my dissertation work. I would like to thank Anselm Griffin for his time and input when I had questions about polarized optical images of my nanocomposite samples that eventually led to my first publication.

I would like to thank members of the Shofner Lab both past and present including Caitlin Meree, Prateek Verma, Natalie Girouard, Emily Fitzharris, and Cameron Irvin for their mentorship as I first started in the lab, friendship as we shared in common struggles as graduate students, and for training me on lab equipment that was needed for my work. I would like to acknowledge undergraduate research assistants Amidat Sonekan and Alex Munoz whom I mentored for their help with thermal characterization and making samples for hours on end. I would also like to thank Chinmay Satam for his help with oxygen permeability testing of my films.

I would like to thank Vinod Babu in the Koros group for his help training me on the FT-IR to use for my samples. I would like to thank Robert Moon and the CN@GT group for their invaluable discussion and insight on CN processing and characterization. I would like to thank James Collins and the Mechanical Properties Characterization Facility for allowing me to use grips for stretching my films on the universal testing frame. I would like to acknowledge the Georgia Tech Institute for Electronics and Nanotechnology, as this work was performed in part at their facilities. The Georgia Tech Institute for Electronics and Nanotechnology is a member of the National Nanotechnology Coordinated Infrastructure (NNCI), which is supported by the National Science Foundation (ECCS-1542174). I would like to thank Kuraray for providing one of the EVOH polymers in my work. Finally, I would like to express my gratitude towards the Renewable Bioproducts Institute for funding my research through a Paper Science and Engineering Fellowship and the purchase of some lab supplies and materials.

TABLE OF CONTENTS

LIST OF TABLES

LIST OF FIGURES

LIST OF SYMBOLS AND ABBREVIATIONS

$\dot{\gamma}$	Shear strain rate
44EVOH	Polyethylene-*co*-vinyl alcohol with 44 mol.% ethylene comonomer content
48EVOH	Polyethylene-*co*-vinyl alcohol with 48 mol.% ethylene comonomer content
ADMET	Acyclic diene metathesis polymerization
AFM	Atomic force microscopy
ASTM	American Society for Testing and Materials
ATR	Attenuated total reflectance mode
b	Percolation constant
CD	Cross direction, or direction of second stretching step
-CH	Methylidyne chemical group
$-CH_2$	Methylene chemical group
CN	Cellulose nanomaterial
CNC	Cellulose nanocrystal
CNF	Nanofibrillated cellulose, or cellulose nanofiber
CO	Carbonyl chemical group
d	Calculated thickness of polymer layer surrounding individual nanoparticle
DMA	Dynamic mechanical analysis
DNA	Deoxyribonucleic acid
DSC	Differential scanning calorimetry
E'	Storage modulus
E''	Loss modulus
E_{11}	Axial modulus of composite

E_c	Modulus of the composite
E_f	Modulus of the individual cellulose nanocrystal
E_f^{agg}	Modulus of the aggregated particle phase
E_m	Modulus of the matrix
$E'_{n,composite}$	Storage modulus of the composite for a specific stretching step, n
$E'_{n,polymer}$	Storage modulus of the neat polymer for a specific stretching step, n
E'_r	Relative contribution to storage modulus
EVAc	Polyethylene-vinyl acetate
FSC	Fast scanning chip calorimetry
FT-IR	Fourier transformed infrared spectroscopy
G'	Shear storage modulus
G_{12}	Shear modulus of composite
G_f	Shear modulus of CNC
G_m	Shear modulus of polymer matrix
h	Height
HAp	Hydroxyapatite
I_c	Intensity of the crystalline peak
IPA	Isopropyl alcohol
iPS	Isotactic polystyrene
I_{total}	Intensity of both the amorphous and crystalline peaks
Iα	Cellulose I allomorph with triclinic crystal lattice
Iβ	Cellulose I allomorph with monoclinic crystal lattice
L	Length
LDPE	Low density polyethylene
LLDPE	Linear low-density polyethylene

MD	Machine direction, or direction of first drawing step
MFC	Microfibrillated cellulose
MW	Molecular weight
MWCNT	Multiwalled carbon nanotube
N_A	Avogadro's number
-OH	Hydroxyl chemical group
PA11	Polyamide 11
PA12	Polyamide 12
PAN-co-MAA	Polyacrylonitrile-*co*-methacrylic acid
PBT	Polybutylene terephthalate
PE	Polyethylene
PEO	Polyethylene oxide
PET	Polyethylene terephthalate
PHB	Polyhydroxybutyrate
PHBV	Poly-3-hydroxybutyrate-*co*-3-hydroxyvalerate
PLA	Polylactic acid
PLLA	Poly-l-lactic acid
PMMA	Polymethylmethacrylate
POM	Polarized optical microscopy
PP	Polypropylene
PTFE	Polytetrafluoroethylene
PU	Polyurethane
PVA	Polyvinyl alcohol
PVAc	Polyvinyl acetate
PVA-PAA	Polyvinyl alcohol-polyacrylic acid

Q	Volumetric flowrate
Q_{11}	Element of reduced stiffness matrix describing axial stiffness
Q_{12}	Element of reduced stiffness matrix
Q_{22}	Element of reduced stiffness matrix describing transverse stiffness
Q_{66}	Element of reduced stiffness matrix describing shear stiffness
R	Width
ROMP	Ring opening metathesis polymerization
RPM	Rotations/revolutions per minute
SAXS	Small angle x-ray scattering
STM	Solution-then-melt
SWCNT	Single wall carbon nanotube
T_c	Crystallization temperature
$T_{d,1}$	Degradation temperature
TEM	Transmission electron microscopy
TEMPO	2,2,6,6-tetramethyl-piperidinyl-1-oxyl radical
TEMPO CNF	TEMPO-mediated oxidized cellulose nanofibers
T_g	Glass transition temperature
TGA	Thermogravimetric analysis
T_m	Melting temperature
TPU	Thermoplastic polyurethane
UTS	Ultimate tensile strength
V	Volume
VC, CH	Variable cooling, constant heating
VH, CC	Variable heating, constant cooling
VH, CC2	Variable heating, constant cooling with higher scanning rates

w	Mass fraction of filler
WAXS	Wide angle x-ray scattering
X_c	Crystallinity
XRD	x-ray diffraction
$\Delta E'_n$	Change in storage modulus for a specific stretching step, n
ΔH_m	Enthalpy of melt
$\Delta H_m°$	Enthalpy of melt of theoretically 100% crystalline polymer
ΔP	Pressure gradient
η	Viscosity
η_G	Shear geometric factor equation
η_L	Axial geometric factor equation
η_T	Transverse geometric factor equation
θ	Angle between long axis of CNC and direction of applied load
λ	Volume fraction of aggregated particle phase
ν	Volume fraction of individually dispersed particles
ν_{12}	Poisson's ratio of composite relating strain in transverse direction to axial direction
$\nu_{12,f}$	Poisson's ratio of CNCs
$\nu_{12,m}$	Poisson's ratio of polymer matrix
ν_{21}	Poisson's ratio of composite relating strain in axial direction to transverse direction
ν_c	Critical volume fraction for particle network formation
Σ	Summation
τ	Shear stress

SUMMARY

The objective of this research is to develop and investigate prescribed microstructures based on the idea of tensegrity in a semicrystalline thermoplastic polymer matrix with cellulose nanomaterials (CNs). Two CNs, cellulose nanocrystals (CNCs) and nanofibrillated cellulose (CNFs) were used as nanofiller in two polymer matrices, polyethylene-co-vinyl alcohol with either 44 mol.% or 48 mol.% ethylene comonomer content (44EVOH and 48EVOH). Three different processing methods were used to investigate the level of CNC dispersion in EVOH: melt mixing, solution casting, and a multi-step protocol involving first solution casting followed by melt mixing CNCs with EVOH. The level of CNC dispersion in the nanocomposites was initially characterized with polarized optical microscopy below and above the melting temperature of EVOH. The nanocomposites' thermomechanical, thermal, mechanical, and structural properties were also investigated as a function of CNC loading. The results suggested a multi-step protocol increased the level of CNC dispersion in EVOH the most compared to only melt or solution processing strategies. Next, prescribed microstructures were developed using a sequential biaxial stretching technique. The structures of the stretched samples were characterized with x-ray diffraction and thermomechanical properties were also investigated of the stretched films as a function of CNC loading. The results indicated storage modulus values increased in the direction of applied strain for a 2.5 wt.% CNC/44EVOH nanocomposite when it was uniaxially stretched versus the unstretched composite sample and these higher storage modulus values were retained and more uniform in-plane when the composite was biaxially stretched. Overall, the results indicated nanocomposites with anisotropic CNs

designed in specified spatial arrangements in a thermoplastic matrix could increase thermomechanical properties of the polymer, and these polymer-particle arrangements behaved like tensegrity-inspired microstructures. The work presented herein contributes to the overall understanding of polymer processing- structure- property relationships using processing strategies commonly employed in commercial applications to incorporate and draw polymer and composite films.

CHAPTER 1. INTRODUCTION

Cellulose is the most ubiquitous biopolymer in the world, being generated from sources such as plants, algae, bacteria, and even animals like tunicates. Crystalline cellulose has been demonstrated at the nanometer level to have mechanical properties on par with structural materials like steel while also having a much lower density [1]. The incorporation of these cellulosic nanomaterials into commercial polymers therefore offers the promise of decreasing total material weight without sacrificing desired mechanical properties.

In addition to incorporating the cellulose nanomaterials (CNs) into a mechanically isotropic polymer composite system, prescribed particle arrangements in various polymer nanocomposites have been demonstrated to increase various mechanical properties such as strength and modulus. One such particle arrangement is based on the idea of "tensegrity" or tensional integrity commonly used in macroscopic-scale projects for its inherent mechanical stability under prestresses. This concept uses the design strategy of tying a discontinuous phase of compressed members in a continuous web of tensioned material. For this work, the CNs are analogous to the compressed members in a polymer matrix that is comparable to the tensioned phase. In a previous work investigating tensegrity- inspired microstructures in a polymer nanocomposite [2], biocompatible inorganic nanoparticles decorated with block copolymers were demonstrated to increase storage modulus of a semicrystalline matrix when the nanocomposite was mechanically stretched using a sequential biaxial stretching technique. While storage modulus values below the glass transition temperature (T_g), as measured by dynamic mechanical analysis, increased in the semicrystalline polymer when the nanoparticles were incorporated and arranged into the

tensegrity-inspired microstructures, the reinforcement efficacy of these particle arrangements was not significantly different from the uniaxially stretched nanocomposites above T_g. This was attributed to the low aspect ratio of the particles used, which was approximately 6, and differences observed in storage modulus values below T_g were ascribed to constraints provided by both the amorphous polymer chains and polymer crystallites interacting with the nanoparticles. It was therefore hypothesized in this work a sequential biaxial stretching protocol could be employed to construct tensegrity- inspired microstructures by orienting polymer crystallites to facilitate the axial alignment of CNs in the specified drawing directions. Because the CNs used in this work have higher aspect ratios than the nanoparticles used in the previous study to construct tensegrity-inspired microstructures, it was anticipated the reinforcement ability of the prescribed arrangements would be higher than the nanocomposites that were unstretched or uniaxially aligned, particularly at temperatures above T_g for the polymer matrix.

The dissertation is arranged in this manner: Chapter 2 provides a background into the state-of-the-art of polymer nanocomposites employing CNs as filler, as well as processing techniques to prescribe morphology in polymer nanocomposites. The materials and methods employed in this dissertation are outlined in Chapter 3 that describe how the CNs were incorporated and dispersed in two polyethylene-co-vinyl alcohol (EVOH) matrices with different comonomer compositions as well as the characterization techniques used to elucidate the processing- structure- properties of the nanocomposites. Chapter 4 investigates three different processing strategies used to incorporate CNs into the EVOH matrices by employing a cross-polarized optical microscopy (POM) technique to study the degree of CN dispersion both at room temperature and above the melting temperature of

the matrix. Chapters 5 and 6 further explore how the processing strategy to initially incorporate and disperse the CNs impacted the composites' structure, thermal, thermomechanical, and mechanical properties using either the 48 mol.% ethylene or 44 mol.% ethylene comonomer content EVOH as the matrix, respectively. Chapter 7 then investigates the thermal properties of these polymers and their nanocomposites with 1 wt.% cellulose nanocrystal (CNC) loading using a fast scanning chip calorimetry technique. This technique utilizes heating and cooling scanning rates that are much faster than a conventional differential scanning calorimeter (DSC) can run and offers the prospect of studying polymer and composite structure and dynamics that are associated with processing methods such as injection molding or injection blow molding. Chapter 8 describes the investigation of the structure and properties of the EVOH matrix nanocomposites when they are uniaxially and biaxially stretched to determine if and when tensegrity- inspired microstructures were constructed with the CN filler. Finally, Chapter 9 outlines the conclusions of the work presented in the dissertation as well as discussion of recommendations for future work.

CHAPTER 2. BACKGROUND

2.1 Cellulose Nanomaterials

2.1.1 Structure and Production

Cellulose is the most abundant biopolymer in the world and is produced from a variety of sources including plants such as trees and cotton, animals like tunicates, algae, and even bacteria. The hierarchical structure of cellulose [3] allows it to be processed and used along several length scales such as pulp, microfibrillated cellulose (MFC), cellulose nanofibers (CNF), and cellulose nanocrystals (CNCs). Cell walls of plants such as trees are made of a composite structure of cellulose, lignin, and hemicelulloses. Within cell walls, bundles of fibrils form microfibrils that provide the mechanical reinforcement phase of the composite structure of plants. The components of these fibrils can be further broken down into nanofibrils, with cellulose chains arranged in ordered and disordered phases within the fibril. It is these ordered and disordered regions of cellulose that can be isolated and define the various cellulosic nanofillers discussed previously through various chemical and mechanical means. The two forms of cellulose that are of interest for this dissertation are CNFs and CNCs due to their having at least one dimension measurable at the nanometer length scale, dimensional anisotropy, high crystallinity, and mechanical properties comparable to structural materials such as steel and carbon fiber [1].

CNFs derived from wood-based sources are produced either by mechanical and/or chemical fibrillation of native cellulosic pulp fibers. The structure of CNFs is generally finer than MFCs but contain more disordered content and are longer in the axial direction

than CNCs. Moon *et al.*[1] described CNFs as analogous to the fibril structure of plant cell walls with similar dimensions and morphology. CNFs used in the present work were either classified as TEMPO or non-TEMPO CNFs depending on if the CNFs were produced by a 2,2,6,6-tetramethyl-piperidinyl-1-oxyl radical (TEMPO)-mediated oxidation step or not. In both cases, for wood- based sources, pulp is mechanically defibrillated using a variety of techniques including refiners and homogenizers [4, 5]. At this point, TEMPO CNFs are further processed with TEMPO which has been demonstrated to lower the overall energy needed to fibrillate pulp fibers during mechanical separation [5]. The final CNFs that can then be used in applications such as polymer nanocomposites are then separated from by-products via filtration and centrifugation. The CNFs can be packaged either as-is in a dilute aqueous suspension or dried to a powder using processes such as freeze drying. Research has also been conducted on the use of enzymes such as endoglucanase as a treatment step prior to mechanical fibrillation to produce CNFs [6, 7]**.** CNFs produced with enzymatic pre-treatment were reported to have overall smaller dimensions and degree of polymerization, but higher crystallinity, than untreated CNFs or TEMPO CNFs due to the preferential hydrolysis of disordered regions by the enzyme. CNFs are generally defined as having length dimensions of several micrometers and widths of 3 – 20 nm [5, 8]. The crystallinity of CNFs range between 25 – 87 % as measured by XRD and Raman spectroscopy [6, 9] and this range of values was attributed to the wide range of processing techniques and sources of cellulose used in the investigations. Whereas mechanically fibrillated CNFs tend to have lower values for crystallinity due to the destroying of both ordered and disordered cellulose regions during processing, chemical and enzymatic treatments provide a more directed attack and breakage of disordered cellulose regions,

leading to overall higher crystallinity values for chemically and enzymatically pretreated CNFs.

CNCs derived from wood sources, the material of choice for this work, begin as wood pulp that is then hydrolysed with a strong acid, usually sulfuric acid, or enzymes [10, 11]. As reported by Dong *et al*. [12], CNCs that are produced by sulfuric acid hydrolysis use pulp as the starting material. Pulp is mixed in a 64 wt.% sulfuric acid solution heated to 45 °C for 60 minutes. The insoluble ordered cellulose particles are then separated from the soluble by-products of acid hydrolysis with several processing steps including sonication, rinsing with water, centrifuging, and filtration. Hydrolyzing cellulose with a strong acid such as sulfuric acid exchanges some of the hydroxyl groups on the surfaces of the CNCs with sulfate ester groups [13]. These sulfate ester groups carry a negative charge in aqueous suspension and can increase the dispersion stability of CNCs in aqueous suspension. Sulfate ester groups have also been shown to negatively impact properties such as shelf life of suspensions due to aging and thermal stability of dried CNCs. Therefore, other acids such as hydrochloric, phosphoric, formic, and maleic acid have been used to hydrolyze cellulose to investigate how it impacts the morphology, stability in different solvents, and thermal stability. Espinosa *et al*. [14] observed CNCs hydrolysed with phosphoric acid and hydrochloric acid exhibited higher thermal stability and imparted different surface chemistry to the CNCs when compared to sulfuric acid-hydrolysed CNCs. The degradation temperature increased by about 50 °C when CNCs were hydrolysed with phosphoric or hydrochloric acid compared to sulfuric acid, and the aspect ratios were all approximately the same among the CNCs hydrolyzed by one of the three acids investigated [14].

After separating CNCs from the soluble by-products of acid hydrolysis, the aqueous CNC suspension can then be used as- is in the desired end application or further processed into a dry powder. The CNCs can have different morphologies in the dry state depending on the drying process. For example, freeze-dried CNCs can appear as flakes while spray dried CNC powder may appear as spherical particles, as seen in Figure 2.1 [15]. CNCs typically have dimensions of 3-5 nm and lengths between 50 nm and several hundred nanometers [1], although CNCs with longer dimensions and larger aspect ratios have been observed in particles derived from bacteria [16], and tunicates [17]. The crystallinity of CNCs has been reported to be between 54 – 88%. Tan *et al*. [18] reported CNCs with over 95% crystallinity when they were produced by solvolysis with an ionic liquid.

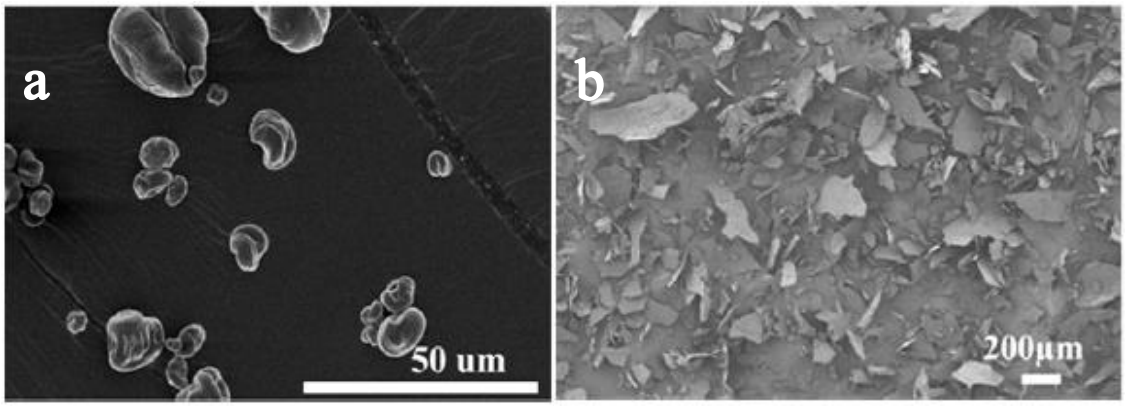

Figure 2.1 - Morphology of CNC powder that has either been (a) spray- or (b) freeze-dried [15].[1]

[1] Reprinted from Powder Technology, 261, V. Khoshkava and M. R. Kamal, "Effect of drying conditions on cellulose nanocrystal (CNC) agglormerate porosity and dispersibility in polymer nanocomposites," pp.288-298, Copyright (2014), with permission from Elsevier.

The structure of crystalline cellulose comes in several morphologies, named cellulose I, II, III, and IV. Cellulose I is the most common naturally occurring allomorph and can be categorized by two different crystal structures: triclinic cellulose Iα and monoclinic cellulose Iβ. Cellulose structures II-IV can be produced by treating or regenerating cellulose I. Cellulose II, also commonly known as regenerated cellulose or cellophane, has a monoclinic lattice and can be produced by first dissolving cellulose I and regenerating it in water or by swelling cellulose in a sodium hydroxide solution [11]. Cellulose III can be produced by treating either cellulose I or II with ammonia, and cellulose IV can be made by further heat-treating cellulose III [1, 11]. Of the two polymorphs of the cellulose I structure, cellulose Iβ is the most common form found in plant cell walls, and has a higher reported modulus than cellulose Iα [19]. The cellulose I structure has also been demonstrated to have a helical structure when observed down the long axis [1, 20].

2.1.2 Properties

Cellulose nanomaterials (CNs) have been used in many applications as neat structures [21-23], coatings [24-27], or nanocomposites [10, 28-38] in order to take advantage of their optical [39-42], mechanical [43-49], and barrier properties [19, 41, 50-52]. CNCs can be considered liquid crystals due to their rigid rod-like morphology. Several authors [40, 53-57] have demonstrated CNCs can display chiral nematic or cholesteric behavior either in a colloidal suspension or as a dried film due to the twist of crystalline cellulose down its long axis. The liquid crystalline behavior of CNCs leads to visually translucent suspensions or films. CNCs and CNFs have also been investigated for their gas barrier properties. CNC films have been reported to have oxygen permeabilities of

approximately 6 cm^3-µm/m^2-day-atm when tested at 23 °C and 0% relative humidity or 250 cm^3-µm/m^2-day-atm when tested at 23 °C and 50% relative humidity [52]. CNF films have reported permeability values of less than 1 cm^3-µm/m^2-day-atm when tested at 23 °C and 0 % relative humidity and between 3.6 and 700 cm^3-µm/m^2-day-atm at 23 °C and 50% relative humidity, depending on the surface functionality and cellulose source [51, 52]. For comparison, the oxygen permeability value for EVOH can be between 1 and 10 cm^3-µm/m^2-day-atm at 23 °C and 0% relative humidity [58], and this value depends on comonomer content of the polymer. CNF films have lower reported gas permeability compared to CNCs due to the entangled morphology of CNFs causing a more tortuous pathway for gas molecules to diffuse through in a film. However, both CNCs and CNFs are sensitive to moisture, and gas permeability rates increase when the CN films are subjected to increasing relative humidity [51, 52]. CNCs and CNFs have also been demonstrated to increase gas barrier properties of polymer films when applied as a thin coating to the polymer surface. Li *et al.* [24] investigated the effect a 1.5 µm coating of CNCs derived from cotton had on barrier properties of several polymers, including PET, PP, polyamide, and regenerated cellulose. The authors reported a decrease in oxygen permeability rate of the coated films by two or three orders of magnitude compared to uncoated films, while the water vapor permeability rate was virtually unaffected by the application of the CNC film. Fukuzumi *et al.* [41] reported the oxygen permeability of polylactic acid decreased by over 2.5 orders of magnitude when a 400 nm coating of TEMPO CNFs was applied to the surface of the PLA film.

The primary interest to use CNs in this work is for their mechanical properties and ability to increase parameters such as strength and modulus of polymer matrices in

nanocomposite systems. The theoretical modulus and strength of different CNs is reported in Table 2.1. The mechanical properties are comparable to materials such as steel but with a significantly lower density, making CNs attractive candidates for nanofiller in polymer composites. However, experimental values for modulus of crystalline cellulose have been reported to be 50 GPa [59]. The mechanical properties have been demonstrated to depend on the source material as well as processing conditions to extract the nanofibers. The modulus of TEMPO CNFs derived from tunicate cellulose was reported to be approximately 145 GPa as measured by AFM [60] while CNFs derived from bacteria and made with chemical and mechanical treatments other than TEMPO-mediated oxidation have a modulus reported between approximately 80 and 114 GPa [59, 61, 62]. These differences in the modulus of CNFs from different sources were attributed to differences in crystallinity of the parent cellulose [63]. Cheng *et al*. [64] reported a modulus of 93 GPa for cellulose fibrils derived from regenerated cellulose that were mechanically separated with sonication.

Table 2.1 - Mechanical properties of CNs.

Material	Elastic Modulus (GPa)	Tensile Strength (GPa)
CNC	50-220 [1, 59]	7.5-7.7 [1]
CNF	80-114 [59, 61, 62, 64]	1.6-3 [65]

2.2 Polyethylene-co-vinyl alcohol

2.2.1 Synthesis and Structure

Polyethylene-co-vinyl alcohol (EVOH) is a commercially available semicrystalline thermoplastic copolymer. It is commonly used in food packaging because of its high solvent barrier and gas barrier properties under dry conditions. There has also been interest in the efficacy of EVOH in medical applications such as for cell growth and tissue scaffolding [66]. The structure of EVOH is presented in Figure 2.2. EVOH is an atactic random copolymer consisting of ethylene and vinyl alcohol comonomers [67]. The copolymer is synthesized by hydrolyzing polyethylene-vinyl acetate (EVAc), although there have been investigations into other production methods. Acyclic diene [68] and ring opening metathesis polymerization [69] (ADMET and ROMP, respectively) have been employed as synthesis pathways to produce EVOH with stereoregular vinyl alcohol groups. Scherman *et al.* [69] demonstrated that EVOH with increased stereoregularity of hydroxyl side-groups led to an approximately 15 °C increase and 46 °C increase in the glass transition and melting temperatures, respectively, of the polymer as measured by DSC. EVOH is generally defined by the comonomer content of ethylene and vinyl alcohol units in mol.% rather than the molecular weight as with many commercially available thermoplastic polymers since many of the properties of interest depend on the comonomer content. The crystal structure has been demonstrated to change with comonomer content. EVOH polymers with higher vinyl alcohol comonomer content display a monoclinic crystal lattice similar to neat polyvinyl alcohol, whereas decreasing the vinyl alcohol comonomer content – or increasing the ethylene comonomer content – results in an orthorhombic crystal lattice similar to neat polyethylene [67]. However, there is no concise

opinion in literature as to the exact ranges of comonomer compositions for each crystal structure. Nakamae *et al.* [70] determined EVOH displayed an orthorhombic crystal lattice for ethylene contents exceeding 80 mol.%, a transitional pseudohexagonal structure for ethylene comonomer contents between 40 and 80 mol.%, and a monoclinic lattice for ethylene contents below 40 mol.%. Whereas Takahashi *et al*. [71] reported a monoclinic structure when ethylene content was less than 63 mol.%, a pseudohexagonal lattice for ethylene contents between 63 and 86 mol.%, and orthorhombic when ethylene content exceeded 86 mol.%. The crystal structure has been reported to be dependent on thermal history due to processing conditions. Cerrada *et al.* [72] observed in XRD patterns that EVOH of different comonomer contents would only display orthorhombic crystal lattices when they were rapidly quenched from the melt. Otherwise, when the polymers were cooled slowly from the melt, the crystal structures were reported to be similar to the trends originally observed as a function of comonomer content. The authors also showed with *in situ* WAXS testing that the structure of EVOH with 32 mol.% ethylene comonomer content (32EVOH) transitioned from monoclinic to an oriented mesomorphic phase when uniaxially stretched. Lagarón *et al.* [73] reported WAXS data that suggested the EVOH crystal structure was orthorhombic across all compositions when EVOH was blended with a polyamide and an ionomer. Martinez- Sanz *et al.* [74, 75] investigated the crystalline structure of 32EVOH matrix nanocomposites with XRD and reported a transformation in the crystal unit cell of EVOH from orthorhombic to an intermediate between orthorhombic and monoclinic when bacteria-derived CNCs were incorporated and dispersed in the EVOH polymer.

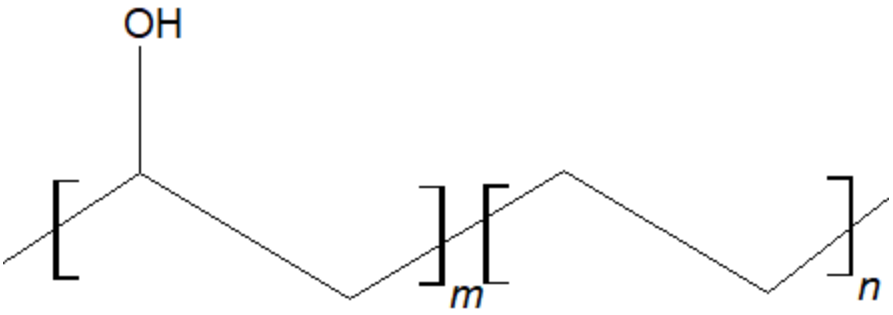

Figure 2.2 - Chemical structure of EVOH

2.2.2 Thermal, Mechanical, and Gas Barrier Properties

Properties such as mechanical, gas barrier, melting temperature, and glass transition temperature have been shown to depend on the comonomer content of EVOH. The general rule is that properties such as gas barrier and melting temperature increase with increasing vinyl alcohol comonomer content while ease of process (that is, lower melting temperature and viscosity) generally increases with increasing ethylene comonomer content. EVOH across a wide range of comonomer contents has been demonstrated to have an affinity to ambient moisture, and properties such as glass transition and gas barrier properties can be adversely affected by humid environments. As can be seen in Figure 2.3, there is an approximately linear relationship between comonomer content and T_m of EVOH [76], where T_g decreases as the amount of ethylene comonomer content increases. Aucejo *et al*. [77] reported a significant decrease in T_g of several EVOH compositions as the polymers were exposed to higher relative humidity. T_g of EVOH with 29 mol.% ethylene comonomer content decreased by as much as 40 °C from dry state to approximately 75 % relative humidity, and the authors attributed this to plasticization of EVOH by water. Zhang *et al.*

[78] observed oxygen permeability of several EVOH polymers with different comonomer compositions increased over an order of magnitude when the polymers were exposed to increasing relative humidity levels. Therefore, it is common for EVOH to be produced in a sandwich structure between polyolefins and tie layers to ensure moisture does not interfere with EVOH to better take advantage of its dry-state gas barrier properties.

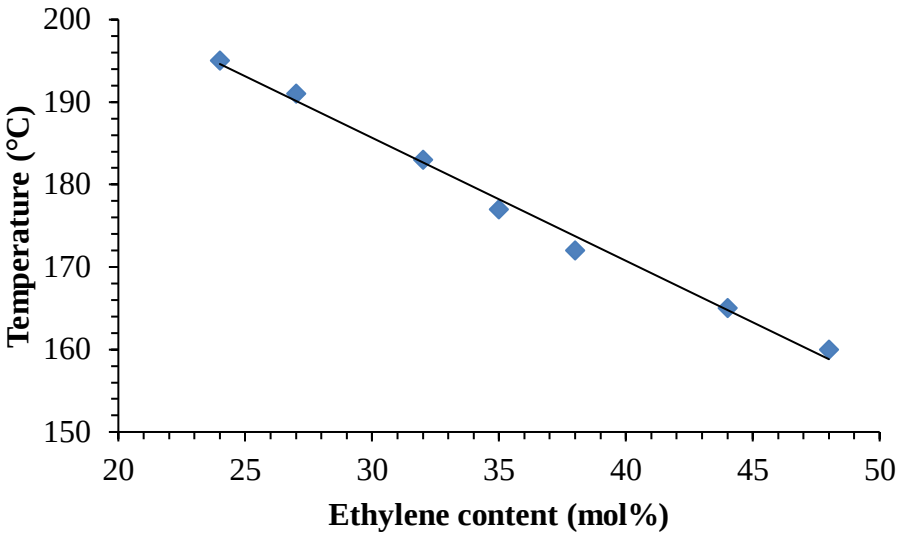

Figure 2.3 - T_m of EVOH as a function of ethylene comonomer content of the polymer plotted from technical report provided by Kuraray [76].

The type and wide array of available compositions as well as acceptance in commercial applications for food packaging make EVOH an ideal candidate of study for a polymer matrix that includes investigating polymer-particle interactions and compatibility for the dispersion of CNs. Research has been conducted to increase the mechanical and

barrier properties of EVOH for use as a standalone film rather than in a laminated structure with nanofillers including CNs [74, 75, 79], nanoclays [80-84], and graphene [85-87]. The research presented in this dissertation will also provide insight into how both incorporation of CNs and imparting microstructures affect the structure of EVOH.

2.3 Cellulose-Reinforced Polymer Nanocomposites

CNs have garnered significant interest as filler in polymer nanocomposite constructs due to their mechanical, optical, barrier, and rheological properties. Currently, CNCs and CNFs can be found in commercial use as rheological modifiers in paints, inks, coatings, and packaging [88]. CNCs and CNFs have been investigated as mechanical reinforcement in numerous polymer matrices, including PE [34, 89-91], PP [89, 92], polyvinyl acetate (PVAc) [93-96], PVA [45, 97-99], PHB[100, 101], PLA [32, 35-37, 102-104], PMMA [105], latexes [28, 29, 106, 107], polyamides [38, 43], block copolymers [108, 109], epoxies [110-112], thermoplastic and thermoset polyurethanes [113-117], and EVOH [74, 75, 118] among others.

2.3.1 Processing Strategies

Cellulose- reinforced polymer nanocomposites have been produced in a wide array of methods ranging from solution [79, 90, 105, 119, 120] to melt- based processes [43, 95-97]. Melt mixing with either extrusion or injection molding is a common method of processing thermoplastic polymers and could therefore lead to a scalable pathway to produce CNC-reinforced polymer nanocomposites. CNCs have been incorporated into thermoplastics such as PLA [32, 121, 122], PE [123, 124], polyamide [43], PVA [97], and thermoplastic polyurethane (TPU) [117] via melt mixing. Oksman *et al.* [32] incorporated

CNCs into PLA by pumping the nanocrystals into the polymer via suspension as the polymer was extruded in a twin screw extruder. They reported increases in Young's modulus and tensile strength by as much as 35 % and 90 %, respectively, when 5 wt.% CNCs were loaded in PLA. Nicharat *et al.* [43] showed Young's modulus could be doubled, tensile strength could be increased by 80 %, and storage modulus could be increased by 170 % when up to 15 wt.% CNCs were incorporated into PA12 via melt mixing. Sapkota *et al.* [95] demonstrated that solution casting followed by roller blade mixing CNCs in polyvinyl acetate (PVAc) increased the storage modulus below the glass transition temperature versus solely melt mixing. However, the nanocomposites produced by solution casting only displayed the largest increases in storage modulus. The value for storage modulus below the glass transition temperature increased by as much as 95% and several orders of magnitude in the rubbery region compared to neat PVAc. The increase in storage modulus above the glass transition temperature was attributed to the CNCs forming a percolated network in the polymer matrix. When 10 wt.% CNCs were incorporated into PVA via injection molding by Zhang *et al.* [97], the tensile strength and elastic modulus increased by 67% and an order of magnitude, respectively, even though the investigators also reported decreases in melting temperature and crystallinity of the polymer matrix. While mechanical properties were increased in the polymer matrices described previously, in many instances discoloration or decreases in degradation temperature were reported and attributed to high temperatures encountered by the CNCs during melt mixing.

Polymer nanocomposites reinforced with CNFs have also been investigated using melt mixing strategies. Jonoobi *et al.* [35, 36] reported the addition of 5 wt.% unmodified and acetylated CNFs in PLA via twin screw extrusion increased the elastic modulus and

tensile strength and shifted T_g and the highest increases in the properties came from nanocomposites with unmodified CNFs. There was also a significant increase in the storage modulus of PLA above T_g with the incorporation of CNFs from 100 MPa to 2.9 GPa regardless of surface modification of the nanofibers. Volk *et al.* [125] demonstrated pristine CNFs and CNFs with a block copolymer adsorbed to the nanoparticle surfaces could double or triple, respectively, the storage modulus of a linear low density polyethylene (LLDPE) using a melt compounding technique. Farahbakhsh *et al.* [91] also demonstrated a 10 wt.% CNF loading incorporated via twin screw extrusion could increase elastic modulus of a PE matrix by 80 %. CNFs have also been shown to increase the mechanical properties of other polymers via melt extrusion, such as PVAc [94]. Gong *et al.* reported 10 wt.% CNF loadings increased the tensile modulus of a PVAc polymer matrix by 59% and the authors suggested increases in the modulus as well as tensile strength were due to good stress transfer between the nanofibers and the polymer matrix and the CNFs restricted polymer chain segment mobility.

Solution mixing has often been implemented in lab-scale investigations of CNC- and CNF-reinforced nanocomposites in order to avoid thermal degradation of the nanomaterials. Aqueous suspensions of polymers, such as epoxy [112], PVA [126], and latex particles [28-30, 89] as well as other polymers that require organic solvents such as polyacrylonitrile copolymer (PAN-co-MAA) [46, 120], polypropylene (PP) [127], polyurethane (PU) [115] and PE [90] have been investigated to incorporate and disperse CNCs in order to avoid degrading the nanoparticles. Significant increases in the glass transition temperature and storage modulus below the glass transition temperature of PAN-co-MAA were reported by Chang *et al.* [120] and Luo *et al.* [46] when CNCs were

incorporated and dispersed via solution processing methods. Chang *et al.* reported the glass transition temperature of gel-spun nanocomposite fibers increased by 10 °C and the storage modulus increased by 50 % when up to 10 wt.% CNCs were incorporated into PAN-co-MAA while Luo et al. also reported increases in glass transition temperature and storage modulus of PAN-co-MAA films by as much as 26 °C and 170 %, respectively, with up to 40 wt.% CNC loadings. Several groups have investigated incorporating CNCs into water-based copolymer latex particles [28, 30, 89] and have demonstrated the storage modulus above the glass transition temperature of the latex increased by several orders of magnitude and it was suggested this increase was due to the formation of a percolated network of CNCs in the polymer matrix. Dong *et al.* [105] reported the glass transition temperature of electrospun polymethylmethacrylate (PMMA) fibers increased by up to 7 °C and the storage modulus measured by nanoindentation increased by 17% when up to 41 wt.% CNCs were incorporated into the polymer.

Solution- based processing strategies have also been implemented to incorporate and disperse CNFs into different polymer matrices, and changes in the mechanical behavior of the polymer was observed when CNFs were used as the filler. The mechanical properties of PLA such as flexural modulus and strength increased by 58% and 210%, respectively, when 32 wt.% CNF content was incorporated and dispersed in a PLA matrix via an aqueous suspension mixing process where polymer microparticles were mixed with a CNF suspension and subsequently dewatered and compression molded [128]. Others [129, 130] have reported increased mechanical properties of PVA when the CNFs were incorporated via solution mixing. Benhamou *et al.* [131] reported the incorporation of CNFs in a bio-based PU via solution mixing increased the tensile strength and modulus by approximately

100% each with 10 wt.% nanoparticle loadings and the mechanical properties of the CNF-reinforced PU were overall higher than CNC- reinforced PU. The authors attributed the increased mechanical properties to decreased molecular mobility of the polymer chains as well as the higher aspect ratio and residual hemicelluloses and lignin on the CNFs compared to the CNCs which allowed for increased compatibility with the PU matrix. Capadona *et al.* [132] demonstrated CNF-reinforced polyethylene oxide- *co*-epichlorohydrin could undergo significant and reversible changes in modulus when the nanocomposites were subjected to an aqueous environment. The authors attributed the reversible switching in the storage modulus to the formation and breaking of a percolated network of CNFs in the polymer matrix, where the CNFs were better dispersed when the nanocomposite was exposed to water and a rigid fiber network formed in the dry state.

2.3.2 Applications and Properties

Thermal properties of CN-reinforced nanocomposites have been studied with DSC as a means of understanding how the nanomaterials interact with the polymer matrix and affect T_g and polymer crystallinity. Thermal properties of several polymers including PLA [37, 102, 122], PVA [133], PP [127], EVOH [74, 75, 79], and others [31, 38, 43, 108] have been investigated when CNs have been incorporated. Some authors reported the melting enthalpy increased for the polymer matrix increase with the addition of either CNCs [102, 122] or CNFs [37, 131], and this increase was attributed to the nucleating effect of the nanoparticles to grow polymer crystallites. However, Martinez-Sanz *et al.* [74, 75] reported the crystallinity of 32EVOH decreased with the incorporation of CNCs originating from both bacterial and wood sources. Bahar *et al.* [127] and Turng *et al.* [133] also reported a decrease in melting temperature of polypropylene with the addition of CNCs and PVA with

CNFs, respectively and attributed these decreases to the inability of the polymer chains to form large crystallites due to the high interactions between the CNs and polymers.

Additionally, others have tried to increase CNC- and CNF-polymer compatibility by chemically modifying CNCs [34, 102, 116, 134-138]. When Girouard *et al.* [116] modified the surface of CNCs with isophrone diisocyanate, the tensile strength of 5 wt.% CNC reinforced polyurethane increased over 160% and work of fracture by over 130% compared to the same loading of unmodified CNCs in the polymer matrix. Similarly, silylated CNCs [102] increased the Young's modulus of poly L-lactide (PLLA) by 40% and doubled the polymer's crystallinity with 1 wt.% loading compared to the same loading of unmodified CNCs in the polymer. Lin *et al.* [136] modified CNCs via acetylation and reported increases of 40 % and 60 % in Young's modulus and tensile strength, respectively, of PLA when up to 10 wt.% CNCs were incorporated. de Menezes *et al.* [34] produced CNC-reinforced polyethylene nanocomposites with improved elongation at break and new phase transitions related to polymer-particle interactions as measured by DMA when fatty acids were grafted onto the CNCs via an esterification reaction. TEMPO CNFs have carboxyl groups on their surfaces as a result of the TEMPO-mediated oxidation treatment which has been demonstrated to increase dispersion in suspension as well as mechanical and thermomechanical properties of polymer nanocomposites. The tensile strength and Young's modulus of carboxylated CNFs increased by as much as 200% and 300%, respectively when 7.7 wt.% lignin was mixed with the nanofibers [49]. Lignin coated CNFs were also demonstrated to increase storage modulus and elastic modulus of PVA hydrogels by 17 and 4 times, respectively, as reported by Bian *et al.* [99]. Several authors [25, 109, 139, 140] have also shown increased dispersion of CNFs and the resulting mechanical

properties of polymer nanocomposites when the surfaces of CNFs were modified via grafting or adsorption of a polymer or other interfacial materials.

Several micromechanical models have been implemented to help explain the mechanisms behind the ability of the CNs to increase the mechanical properties of polymer matrices. Models such as Halpin- Tsai [30] and Mori- Tanaka [141] have been used to predict the mechanical behavior of polymer nanocomposites, as well as polymer nanocomposites with CNs as the reinforcement phase. Several authors have reported remarkable increases in the storage modulus of polymer nanocomposites reinforced with cellulose nanoparticles beyond what the Halpin- Tsai model can predict, particularly above T_g [28, 43, 95, 106, 142]. The additional mechanical reinforcement was therefore attributed to a networked phase of CNs, and three phase models such as percolation [142] and Takayanagi [143] have been used to develop a better understanding of this phenomenon. In addition to mechanical modelling, Lewandowska *et al.* [144] and Rusli *et al.* [93] have verified through Raman spectroscopy the efficiency of stress transfer in cellulose-reinforced polymer nanocomposites through polymer-particle and particle- particle interactions when the nanocomposites were subjected to an external mechanical load.

2.4 Prescribed Microstructures in Polymer Nanocomposites

While as-processed polymer nanocomposites can offer significant increases in several desired properties, the idea of intentionally prescribing microstructures in polymer nanocomposites offers the possibility of increasing mechanical properties, electrical properties, and a variety of other properties beyond what is capable of isotropic nanocomposite constructs. Gusev *et al.* [145] demonstrated through simulations the shear

modulus of a silica fiber-reinforced rubber matrix increased and this increase in shear modulus occurred at lower filler volume fractions when the filler was arranged in a prescribed morphology such as a web of honeycomb pattern compared to random packing. Chen *et al.* [146] also showed through computer simulations the tensile properties of a polymer matrix reinforced with spherical nanoparticles increased when the morphology of the nanocomposite was intentionally arranged into sandwich-like packing via oscillatory shear. Vaia *et al.* defined two means of prescribing microstructures in polymer matrices: an internal-out and an external-in approach. The internal- out approach relies on the development of phases or self- assembly either due to polymer- polymer, polymer-particle, or particle- particle interactions within a nanocomposite to drive the construction of prescribed morphologies. In order to promote the assembly of nanoparticles in a preferred phase of a block copolymer matrix, nanoparticles have been functionalized with one of the polymers that comprise the matrix [147-151]. Nanoparticles have also been used either in pristine form or functionalized to act as a surfactant at the interfaces of a block copolymer matrix [152] and even to provide compatibility to otherwise immiscible polymer blends [153, 154]. Lin *et al*. [155] reported that not only could a block copolymer matrix direct the assembly of inorganic nanoparticles, but the nanoparticles also directed the structure formation and phase development of the matrix.

The other method discussed by Vaia, the external-in method, employs external forces such as mechanical drawing [156, 157], magnetic and electric fields [66, 158-162], and light [163, 164]. Applications for polymer nanocomposites with prescribed morphology include enhanced mechanical reinforcement and electrical conductivity for energy storage and semiconductors. An external- in method employing mechanical stretching as the

external force was used for constructing tensegrity- inspired microstructures in this research. Mechanical properties of short fiber- and nanoparticle- reinforced polymers have been demonstrated to have a strong relationship with particle orientation, especially for anisotropic particles and fibers [165]. Therefore, orienting the filler phase with mechanical drawing could improve the mechanical properties in the direction of applied mechanical drawing above and beyond a composite material with a random distribution of particle orientations. Kojima *et al.* [166] reported different degrees of alignment of nanoclay sheets in an injection- molded polyamide nanocomposite bar. The degree of orientation was shown via x-ray characterization to depend on the distance from the cavity wall during injection molding and the orientation of the polymer was also affected by the addition and orientation of nanofiller during injection molding. Haggenmueller *et al*. [156] demonstrated the alignment of single-wall carbon nanotubes increased when the draw ratio subjected to SWCNT-reinforced PMMA fibers increased. This increase in alignment as determined by Raman spectroscopy also led to a 100% increase in tensile strength of the nanocomposite fibers with 8 wt.% nanotube loading. Sarfraz *et al.* [157] also demonstrated tensile properties of a polymer nanocomposite could be increased by uniaxial stretching. The authors reported increases in tensile modulus and strength of as much as 40% and 36%, respectively, when 2.5 wt.% nanoclay was incorporated into a polyvinyl chloride matrix and uniaxially stretched and these increases in mechanical properties were in addition to the 69% and 5% increases in the unstretched nanocomposites versus the neat polymer film. In addition to mechanical drawing, electromagnetic fields have been used to align nanoparticles [158, 159, 162, 167] and create nanocomposites with anisotropic mechanical and electrical properties, and in some cases a percolated network of

nanoparticles where they would otherwise not form at the given particle loading content [162]. Holographic patterning, or the use of light to induce polymerization of photosensitive monomers has also been employed in research to pattern nanoparticles in a polymer matrix in order to impart additional functionality or improved properties [163, 164, 168, 169]. The idea is that nanoparticles are able to diffuse more readily through and towards lower viscosity regions of a photosensitive matrix that has either not been polymerized yet or has a lower degree of polymerization compared to other regions of the matrix that have been subjected to light and undergo photopolymerization. Holographic patterning is typically done with photosensitive polymers such as acrylics and inorganic particles such as metals and ceramics since some of the current research focuses electric, sensor, or biomedical applications.

Polymer nanocomposites with CNC filler have been investigated to develop prescribed morphology by taking advantage of self- assembly of CNCs to direct the formation of polymer microstructure. External stimuli have also been implemented to direct the alignment and assembly of CNCs either as free-standing films or in polymer nanocomposite constructs. The ability of CNs to self-assemble has been used as a templating tool for making polymer nanocomposites with enhanced functionality [170, 171]. Risteen *et al.* [170] took advantage of the chiral nematic nature of CNCs to align conjugated polymer chains and enhanced π-π interactions between polymer chains. Beck *et al.* [39] was able to control the chiral nematic pitch of a CNC film plasticized with PVA by controlling the drying rate of the nanocomposite suspension in different locations of the film. Other external- in methods such as magnetic fields [172, 173] have been used to induce alignment of CNCs either in suspension or in composite. Pullawan *et al.* [173]

showed the mechanical properties of an all-cellulose composite system increased by 7-10 % when the CNC filler was aligned with a magnetic field.

2.5 Tensegrity Microstructures

2.5.1 Definition and Origin of Tensegrity in Macrostructures

The concept of tensegrity is an interesting means of prescribing morphology in polymer nanocomposites to potentially increase mechanical properties. Tensegrity is a contraction of "tension integrity." The idea of tensegrity was described by Buckminster Fuller as "islands of compression in a sea of tension." This quote describes a multiphase system in which one phase is made of isolated compressed members held together by a continuous phase that is in tension. Based on this concept, tensegrity structures offer the possibility of stable structures under mechanical loads due to self-stresses that provide mechanical equilibrium. On a macroscale, good examples of tensegrity in practice come in the form of either art and bridges [174] due to their aesthetic appeal and mechanical stability and even satellites [175] due to geometric constraints during deployment. A typical six-strut tensegrity model can be seen in Figure 2.4, where the structure is comprised of six struts held in compression by a network of 24 tensioned cables. The model is constructed such that the compression forces in the struts are balanced by the tension forces in the cables prior to any external load being subjected to the structure. Liu *et al.* [176] developed tensegrity structures out of shape memory polymer members connected with a continuous network of elastomer cables and the tensegrity structures were able to undergo changes in both shape and size when a thermal stimulus was applied to the structure. The authors postulated the lightweight structures could be used in applications

that need to be self- deployable and respond to environmental stimuli such as space or other remote locations. Paul *et al.* [177] developed robust architectures for robots based on the concept of tensegrity. The robots were able to move with the help of mechanical stimuli and continue moving even with several damaged actuators. Yan *et al.* [178] developed a novel beam-column joint with concrete and a shape memory alloy that was determined through computer simulations to have higher load bearing capacity and good self- entering ability that was attributed to the pre-stresses applied to the structure.

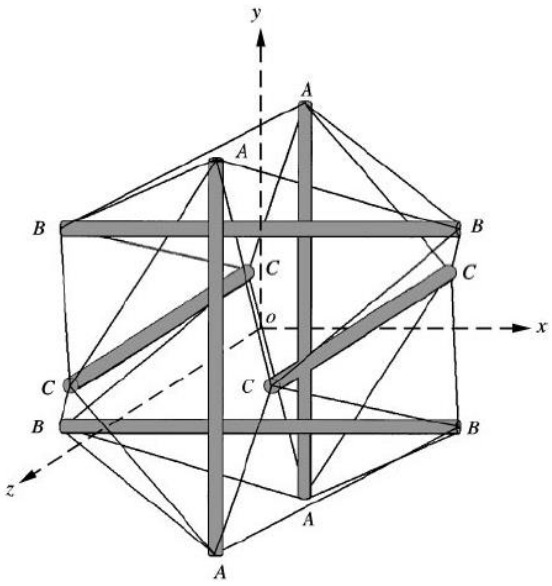

Figure 2.4 - A six-strut tensegrity model [179].[2]

[2] (Reprinted from Journal of Theoretical Biology, 201 (1), D. Stamenovic and M. F. Coughlin, "The role of prestress and architecture of the cytoskeleton and deformability of cytoskeletal filaments in mechanics of adherent cells: a quantitative analysis," pp.63-74, Copyright (1999), with permission from Elsevier.

2.5.2 Applications of Tensegrity

Biological systems have been described by the concept of tensegrity as well. One of the easiest examples is the musculoskeletal system in the human body, where bones (analogous to isolated struts as in Figure 2.4) are held in compression by continuous phase of tensioned muscles (cables). On a smaller scale, several authors [179-185] have used tensegrity to describe the mechanical stability of cells. Wang *et al.* [180, 181, 184] observed the stiffness of the cellular cytoskeleton increased with increased applied stress and suggested a tensegrity structure of microtubules [185] and filaments was formed in a cell to help respond rapidly to external mechanical stimuli on the cell. They [184] also determined stiffness increased with the level of prestress in the cell. Tensegrity structures have also been constructed out of self-assembled DNA helices [186, 187]. Liedl *et al.* [186] reported tensegrity structures made of single DNA strands in tension and compressed double helical DNA members were able to self-assemble against mechanical loads of up to 100% that which is required to prevent the function of powerful protein motors. The structure of plant cell walls has also been described using tensegrity principles [188]. Through AFM measurements of single hemicellulose molecules on a cellulose substrate, Morris *et al.* [188] determined plant cell walls undergo a self-tensioning mechanism when exposed to an external mechanical load and can adapt to changes in mechanical loading due to the tensegrity nature of the cell wall structure.

Besides examples of tensegrity being applied to biological systems, tensegrity has also been used as a guide to develop and describe behavior of polymer nanocomposites. Sidorenko *et al.* [189] developed tensegrity structures with silicon nanorods and acrylic polymer matrix in a hydrogel construct. The authors demonstrated the nanorods could be

actuated into different alignments and structures while tuning the moisture level of the hydrogel, which could be useful in sensor or stimuli-responsive applications. Wang *et al.* [190] were able to increase the impact energy absorbed by a fiber- reinforced polymer composite by as much as 79% by applying a creep load to polyamide 6,6 fibers prior to incorporating them into a thermoset polyester resin. The authors were able to determine the mechanical properties of the composite were highest at an optimum applied creep load to the fibers and this was due to the saturation of energy storage ability of the polymeric fibers when the amorphous phase was aligned under load. The mechanical behavior of liquid crystalline films has also been described with tensegrity principles. Ren *et al.* [191] attributed the strain retention and shape memory behavior of a cross-linked liquid crystalline elastomer to tensegrity where thermally trapped crosslinks create a pre-stressed structure that can only relaxed with an external stimulus such as solvent or temperature. These pinned domains led to an increase in residual stress and strain when the initial applied strain was increased as well as an increase in the Young's modulus by as much as 233% when an applied strain of 350% was used.

Previously in our group [2], tensegrity- inspired microstructures were produced in a polymer nanocomposite of hydroxyapatite (HAp) nanoparticles in a semicrystalline polyethylene oxide (PEO) matrix and an amorphous polymethylmethacrylate matrix. The HAp particles were synthesized with calcium and phosphorous precursors and either PEO-*block*-PMMA or PMMA-*block*-PMAA as a means of controlling particle morphology and increasing polymer-particle interfacial interactions. The HAp particles were produced in spherical and needle-shaped geometries. The prescribed structures were produced when nanocomposite films were mechanically stretched using a sequential biaxial drawing

method at room temperature. Storage modulus values for PEO matrix nanocomposites below the glass transition temperature from dynamic shear testing increased when the nanocomposite films were biaxially stretched as opposed to the unstretched or uniaxially stretched films. Whereas the changes in storage modulus in the PMMA matrix nanocomposites were either minimal or not statistically significant. The results from DMA characterization as well as the investigation of particle orientation with x-ray diffraction suggested tensegrity- inspired microstructures were made in the semicrystalline polymer matrix. However, increases in storage modulus above the glass transition temperature for PEO matrix nanocomposites was about the same in both uniaxially and biaxially stretched samples. The current work looks to further understand how mechanical drawing affects the construction of tensegrity- inspired microstructures and the resultant thermal and mechanical properties of a semicrystalline thermoplastic polymer with bio-derived nanoparticles that have higher aspect ratios than nanoparticles previously studied. The use of EVOH copolymer will also expand the current base of polymers used to construct prescribed microstructures as well as provide a means of understanding polymer- particle interactions through the tailoring of the comonomer composition of the matrix.

CHAPTER 3. MATERIALS AND METHODS

3.1 Materials

3.1.1 Polyethylene-co-vinyl alcohol

Two different compositions of EVOH were tested in this work with different comonomer contents of ethylene and vinyl alcohol. 44 mol.% ethylene content EVOH (Scientific Polymer Products, Ontario, NY) (44EVOH) was purchased and 48 mol.% ethylene content EVOH (Kuraray Americas, Ltd. Houston, TX) (48EVOH) was received as the matrix materials for use in this work.

3.1.2 Cellulose Nanomaterials

CNCs and CNFs were received from the USDA U.S. Forest Service Forest Products Laboratory (Madison, WI). CNCs were derived from dissolving pulp that had been hydrolyzed with 64% sulfuric acid [12, 192]. The insoluble crystalline cellulose was then separated from by-products through a series of dilutions, filtrations, centrifuging, and settling. The CNCs were then freeze-dried into a white powder. This was the form the CNCs were received for use in the dissertation. The as-received freeze-dried powder was resuspended in distilled water at a 5.5 wt.% solids content using a Talboys model 134-1 overhead mixer set at 1900 RPM for 90 minutes with a 5 cm diameter stainless steel propeller blade at room temperature in a fume hood.

CNFs were produced from bleached kraft wood pulp using a series of mechanical and chemical treatments [5]. Mechanically processed CNFs were fibrillated by running

pulp 100 passes through a refiner at 50 °C. The refined product is then screened, sonicated, and centrifuged to separate the CNFs from larger cellulosic materials. The CNFs are then concentrated in an aqueous suspension of 0.5 wt.% solids. Chemically pretreated CNFs (referred to as TEMPO CNFs) were also received from the Forest Products Laboratory. TEMPO CNFs were also derived from wood pulp that had been pre-treated with a solution of sodium hypochlorite, 2,2,6,6-tetramethyl-piperidinyl-1-oxyl radical (TEMPO) and a pH buffer heated to 60 °C and mixed for several days before being mechanically refined at 50 °C. The refined pulp was then dewatered, passed through a homogenizer, and freeze-dried into a white powder. The powder received from the Forest Products Laboratory was resuspended into distilled water at a solids content of 0.5 wt.% using a procedure similar to the aqueous CNC suspension.

3.2 Methods

3.2.1 Melt Mixing

A Haake MiniLab Rheomix (Thermo Scientific) was used to extrude and collect monofilaments of samples for melt mixing. The MiniLab is a table top mini compounder with corotating twin screws. Before compounding samples, the mini compounder was first purged with LDPE followed by either neat 44EVOH or 48EVOH depending on the samples being made. For this process, 48EVOH polymer and 1 wt.% CNC nanocomposites were used to investigate the processing method initially due to 48EVOH having a lower melting temperature between the two polymer compositions investigated. For 48EVOH polymer systems the temperature was set to 170 °C. Screw rotation speeds of 25, 50, and 100 RPM were used to investigate the melt mixing processing strategy. After the purge and neat

EVOH material, the sample of interest, either neat 48EVOH or 48EVOH with 1 wt.% CNC loading, was inserted into the feeding column of the compounder, and a time of 8 minutes (in the case of samples prepared with a screw speed of 25 RPM), 4 minutes (50 RPM), or 2 minutes (100 RPM) was allowed to pass before collecting the extruded monofilament on a take-up roll. For nanocomposite systems, the aqueous CNC suspension was first mixed with EVOH resin before being directly fed into the feeding column of the mini compounder. After each sample was fully inserted into the mini compounder, neat EVOH resin was fed through to ensure the remaining material inside was pushed through and collected. The collected monofilament was then consolidated into a film via compression moulding.

3.2.2 Solution Mixing

The solution mixing process was investigated for both 44EVOH and 48EVOH polymers and nanocomposites up to 5 wt.% CNC loadings. EVOH polymer solution was first prepared by dissolving the polymer in a cosolvent of IPA and distilled water in a closed beaker heated with a water bath on a hotplate and stirred with a magnetic stir bar. For polymer nanocomposites, an aqueous CNC suspension was added to the EVOH solution. The aqueous CNC suspension was made by mixing freeze-dried CNCs in distilled water using a Talboys overhead mixer and then sonicated for a designated amount of time with a Misonix Sonicator 3000 cup horn sonicator at 80 W power setting. After the polymer was fully dissolved, the sonicated aqueous CNC suspension was then added to the solution and stirred for an additional hour at the prescribed temperature on the hotplate. In total, the solids content of the polymer-CNC suspension was 3 wt.% in the IPA-water cosolvent. After one hour of mixing, the suspension was cast into Petri dishes and the solvent was

allowed to evaporate for at least 48 hours in a fume hood. The resultant powder was then collected and consolidated into a film with compression moulding. 48EVOH with 1 wt.% CNCs was used as a representative system to further investigate processing variables such as stir bar mixing speed, temperature, sonication time of the CNCs, and cosolvent composition and their effects on CNC dispersion in the polymer matrix.

3.2.3 Solution-then-Melt Method (STM)

After investigating both melt mixing and solution casting methods independently to determine how they affected the level of CNC dispersion in an EVOH matrix, a multi-step protocol combining these methods was investigated to determine if CNCs could be further dispersed and/ or distributed in the polymer. The first processing step used results from the solution casting method to determine the processing variables needed to produced nanocomposites with the highest levels of CNC dispersion in EVOH. An aqueous suspension of CNCs was first sonicated for 15 minutes with a cup horn sonicator at 80 W power. After sonication, the CNC suspension was then added to an EVOH solution such that the final solids content was 3 wt.% in a cosolvent of 70 vol.% IPA and 30 vol.% distilled water. The temperature of the CNC-polymer suspension was 70 °C in a water bath on a hot plate. The suspension was stirred for an hour with a stir bar mixing speed of 250 RPM in a closed beaker. After stirring, the suspension was cast into Petri dishes and the solvent was allowed to evaporate for at least 48 hours in a fume hood. The resulting powder was then collected and consolidated into a film with compression molding. The films were then pelletized to prepare for the second processing step: melt mixing. As in the melt mixing method, LDPE and neat EVOH were sequentially added to the mini compounder as purge prior to feeding the nanocomposite system of choice. For 44EVOH polymer and

nanocomposites, the barrel temperature for the mini compounder was set to 185 °C while for 48EVOH systems the temperature was 170 °C. The screw speed was set to 50 RPM, and 4 minutes were allowed to pass after the nanocomposite system was fed into the mini compounder before collecting the monofilament from the exit on a take up roll. After feeding all of the pelletized nanocomposite film into the extruder, neat EVOH was fed through the extruder to push any sample remaining in the barrel. The collected monofilament was then consolidated with compression molding.

3.2.4 Film Consolidation

For all three processing strategies described previously, films were made of the polymers and nanocomposites using compression molding to further characterize their structure and properties. The polymer or nanocomposite material was sandwiched between PTFE sheets with a PTFE spacer to control the final thickness of the pressed films. A Carver 3851-0 (Wabash, IN) hot press was used at a temperature of 170 °C for all systems. The pressure was set to 1 metric ton and held at pressure for 5 minutes before releasing it and removing the resultant film. The final thickness of the films was 0.45 +/- 0.05 mm.

3.2.5 Stretching Protocols

In order to construct the prescribed microstructures in the nanocomposite films, a sequential biaxial stretching protocol was implemented using an Instron 5566 universal testing machine with a 500-series environmental chamber. For the stretching protocols, only polymers and composites made with the STM method were used. Compression-molded films were soaked at a temperature of T_g + 40 °C for 15 minutes and then stretched

to a strain of 300 % at a crosshead extension rate of 1 or 10 mm/min. Immediately after reaching the final applied strain value, the furnace was turned off and the environmental chamber opened to allow the film to cool to below 30 °C while still clamped in the testing frame. Once the film was removed from the clamps, it was rotated 90° and stretched to an applied strain value of 150 % at a crosshead extension rate of 10 mm/min and temperature of T_g + 40 °C. Again, prior to the second drawing step, the sample was allowed to acclimate to the elevated temperature for 15 minutes prior to stretching. Other settings such as applied strains in either the first or second drawing direction were investigated for constructing the tensegrity- inspired microstructures, and these details along with property characterization are discussed further in Chapter 8.

3.2.6 Optical Microscopy

An Olympus BX51 optical microscope was used in brightfield mode to visually monitor changes in dispersion of polymer nanocomposites, as well as determine orientation, if any, was imparted by the stretching protocols to prescribe the microstructures in EVOH with CNCs. The film sample was placed between cross-polarizers with a 530 nm red waveplate. The addition of the red waveplate gave an otherwise black image a magenta color as long as the sample placed between the polarizers was optically isotropic. Images were taken with an Olympus UC30 camera and 5x and 10x objective lenses using StreamEssentials software. For those samples monitored at temperatures above ambient conditions, the normal stage was exchanged for a Linkam LTS420 hot stage. 44EVOH polymers and nanocomposites were heated to 185 °C while 48EVOH polymers and nanocomposites were heated to 170 °C at a rate of 10 °C/ minute

and held isothermal for at least 5 minutes to ensure the entire sample was melted before images were taken with a 10x objective lens using a Q-Imaging QIC-F-CLR-12 camera and LinkSys32 software. After imaging samples above their melting point, the samples were allowed to cool ambiently to below the glass transition temperature of the polymer matrix and imaged again.

3.2.7 X-ray Diffraction (XRD)

A Malvern Panalytical X'Pert PRO MRD XRD (UK) was used to collect wide angle x-ray scattering (WAXS) patterns of neat CNs as well as isotropic and stretched polymer and nanocomposite systems made with the STM method. A Cu-Kα source (λ = 0.15406 nm) was employed for XRD studies. For WAXS, a 2θ sweep from 5° to 45° was conducted with a scan step of 0.02° and time per step of 0.5 s. Peaks were indexed and the areas calculated using a Lorentzian function. Crystallinity (X_c) was calculated using Equation 3.1:

$$X_c = \frac{\sum I_c}{\sum I_{total}} \tag{3.1}$$

where I_c is the sum of all areas under the deconvoluted crystalline peaks and I_{total} is the area under all peaks including the amorphous peak. The polymer crystalline phase density was also calculated for all samples tested using Equation 3.2:

$$density = \frac{MW}{V * N_A} \tag{3.2}$$

where MW is the molecular weight of the repeating comonomer unit, approximately 72 g/mol, V is the volume of the orthorhombic crystal lattice, and N_A is Avogadro's number. To calculate the volume of the crystal lattice, the *a* lattice parameter was measured from the d-spacing of the (100) diffraction peak, the *b* lattice parameter was assumed to be 0.254 nm and related to the planar zig-zag spacing between polymer chains [71], and the *c* lattice parameter was derived from the d spacing of the (101) diffraction peak in the neat polymer XRD pattern.

In order to better understand how the polymers and nanocomposites aligned with applied uniaxial and biaxial strains, XRD patterns were also collected for stretched nanocomposites such that the MD was oriented parallel and perpendicular to the beam and collector. For these tests, a Malvern PANalaytical Empyrean was used with a Chi-Phi-Z stage. A PIXcel3D detector was used in line focus mode. 0.04 radian soller slits were used on both the source and detector sides of the sample, along with a 10 mm mask, 1/2° divergence slit, and a 2° anti-scatter slit used in the mirror directly after the source. CuKα radiation was used (λ = 0.154046 nm). A 2θ sweep procedure from 5°-45° with 0.02° step size was used as well.

3.2.8 Fourier Transformed Infrared Spectroscopy (FT-IR)

A Nicolet iS 50 FT-IR Spectrometer (ThermoFisher Scientific) with an attenuated total reflectance fixture (ATR FT-IR) was used in its attenuated total reflectance mode to characterize the chemical structure of EVOH and any changes to the structure of EVOH as a result of the incorporation and dispersion of CNs. Before scanning, a background scan was collected for each sample. 64 scans were collected for each system from 400 to 4000 cm^{-1} with a resolution of 4 cm^{-1} at room temperature and with a nitrogen atmosphere set to 15 psi.

3.2.9 Differential Scanning Calorimetry (DSC)

In order to characterize thermal properties such as percent crystallinity (X_c) and glass transition (T_g) and melting temperatures (T_m), a DSC Q200, Q100, or Discovery DSC (TA Instruments, New Castle, DE) was used under a nitrogen atmosphere flowing at 50.00 mL/ minute. Nominal sample masses of 10.00 +/- 1.00 mg were used for testing and placed in standard aluminium pans. The samples were tested with an empty aluminium pan as a reference. A heat-cool-heat procedure was implemented between 0 °C and 210 °C with heating and cooling rates of 10 °C/ minute and 3- minute isothermal steps between each heating and cooling step. T_g, T_m, and X_c were all collected from the first heating step while the crystallization temperature (T_c) was collected from the maximum value in the exothermic peak from the cooling step. T_g was defined as the onset of the change in heat capacity before the exothermic curve during the first heating step. T_m was defined as the

minimum value in the exothermic curve from the first heating step. X_c was calculated from Equation (3.3):

$$X_c = \frac{\Delta H_m}{\Delta H_m^\circ * w} * 100 \tag{3.3}$$

where ΔH_m is the melting enthalpy measured by integrating the exothermic peak observed in the first heating step, ΔH_m° is the melting enthalpy of a theoretically 100% crystalline polymer matrix, and w is the weight fraction of polymer in nanocomposite systems. ΔH_m° was taken to be 216.6 J/g based on studies Lagaron *et al.* [73] did comparing enthalpy data from DSC with XRD data for a 32 mol.% ethylene EVOH polymer. This value may or may not be accurate for the comonomer compositions of EVOH studied in this work, and therefore values calculated for X_c were not taken as absolute but rather relative to compare samples to one another.

3.2.10 Thermogravimetric Analysis (TGA)

A TGA Q50 (TA Instruments, New Castle, DE) was used to characterize the onset degradation temperature ($T_{d,1}$) for each polymer and nanocomposite system produced. A platinum pan was used to hold a nominal sample mass of 10 mg and nitrogen gas was used as an inert atmosphere in the furnace. $T_{d,1}$ was defined at the point at which 5 wt.% of the sample mass was gone from the polymer sample after accounting for any mass loss due to water around 100 °C.

3.2.11 Dynamic Mechanical Analysis (DMA)

DMA was used to characterize thermomechanical properties of the polymer and nanocomposite systems. A DMA/SDTA861[e] (Mettler Toledo, Columbus, OH) was used with a tensile clamp assembly that had an interclamp length of 9.0 mm. Samples were cut with an ASTM D638-V dogbone die from compression moulded films and conditioned in ambient lab conditions for at least one week. A strain amplitude sweep test was conducted at 30 °C to determine the linear viscoelastic region for each system. Two samples for each system were tested with a thermal sweep test from 30 °C to 120 °C at a heating rate of 2 °C/ minute. A 1 micrometer amplitude was used for each thermal sweep test as determined by strain amplitude sweep tests. Storage modulus (E') and loss modulus (E") were reported as a function of temperature. The glass transition temperature from DMA was defined as the peak in the E" curve for each system. For stretched samples, two samples were tested in the direction of the first stretching step (called the machine direction, or MD) and orthogonal to the first stretching step (cross direction, or CD).

3.2.12 Quasi-static Mechanical Testing

A universal testing frame (Instron 5566, Norwood, MA) was used to characterize tensile strength of the polymers and nanocomposites. Samples were cut with an ASTM D1708 dogbone die and conditioned in ambient lab conditions for at least 1 week. A 1 kN load cell was used and a 1 mm/ minute crosshead extension rate was implemented to test the sample until failure. For stretched samples, tensile bars of approximately 3 mm widths were cut and tested using a 100 N load cell and a 1 mm/minute crosshead extension rate. Samples were prepared in both the MD and CD. At least 4 samples were tested for each system and statistical analysis including t tests were used to analyse statistically significant

differences in mechanical properties between systems with a 95 % confidence interval. Yield strength and strength at break were reported for isotropic samples, which were defined as the stress values that occurred at the end of the elastic deformation region and the point of failure, respectively. For stretched composites, the yield stress was not as easily defined especially in samples tested in the MD. Therefore, tensile strength for these samples was determined by the maximum value in stress when plotting stress versus strain. This value occurred at failure for samples measured in the MD and the point at yield for samples measured in the CD.

3.2.13 Fast Scanning Chip Calorimetry (FSC)

A commercially available Flash DSC 1 (Mettler Toledo, Columbus, OH) was used in conjunction with MultiSTAR UFS 1 sensor chips (Xensor Integration, Netherlands). Analysis was conducted with STARe software version 10.00d. The chips are made of a silicon nitride/ oxide membrane coated with aluminum on the testing surfaces. Two areas on the membrane are connected with eight thermocouples each for homogenous thermal control. Each area has a 500 μm diameter, one is left blank as the reference and the other is where the sample was placed for testing. The chip heating was controlled with a dynamic power compensation heater. Flowing nitrogen was used as an inert atmosphere at 10 mL/min flow rate. The sensor was first placed in the instrument and conditioned three times followed by a temperature correction before adding the sample with a cat whisker attached to a manipulator. The sample was centered in the innermost diamond of the testing area. Three different nonisothermal procedures were then administered to the chip with a

sample: variable heating rates with a constant cooling rate (VH, CC) and variable cooling rates with a constant heating rate (VC, CH). Samples and sensor chips were stored in a sealed container under dry atmosphere through the use of desiccant materials to reduce moisture adsorption between tests. The VH, CC protocol ran a heat- cool- heat template with heating rates of 50, 100, 200, 300, 400, 500, 600, 700, 800, 900, 1000, 2000, 3000, and 4000 °C/s with a cooling rate of 25 °C/s between 30 °C and 210 °C. Isothermal steps of two seconds were used before and after each heating and cooling step. The first heating rate was used to ensure the chip adhered to the chip as well as a means of comparing the heat flow profile to a final heating step of 50 °C/s to detect any signs of degradation to the sample.

As with the VH, CC tests, a heat- cool- heat protocol was administered for the VC, CH tests. Instead of varying the heating rates, the cooling rate was varied using rates of 25, 30, 40, 50, 100, 200, 300, 400, 500, 600, 700, 800, 900, 1000, 2000, 3000, and 4000 °C/s and a heating rate of 700 °C/s between 30 °C and 210 °C. The heating rate was held constant at 700 °C/s and this rate was determined as the point in which the peak melting temperature stopped decreasing as a function of heating rate during VH, CC tests. An initial heating rate of 700 °C/s was used to erase prior thermal history and remove moisture from the sample.

CHAPTER 4. PRODUCING ISOTROPIC NANOCOMPOSITES OF POLYETHYLENE-CO-VINYL ALCOHOL REINFORCED WITH CELLULOSE NANOMATERIALS

Portions of the following chapter were adapted from Orr and Shofner [118] which can be found in *Polymer*.[3]

4.1 Introduction

Before constructing tensegrity- inspired microstructures in a polymer nanocomposite with CNs, isotropic nanocomposites must first be made and then stretched to prescribe the desired morphology. The degree of nanoparticle dispersion in the polymer matrix is an important determination of resultant mechanical and thermal properties of polymer nanocomposites. Therefore, it is critical to develop a processing strategy to incorporate and disperse CNs into an EVOH matrix. Challenges persist in effectively characterizing degree of particle dispersion in polymer nanocomposites for a number of reasons including cost, resolution, contrast between polymer and particle, and time for sample preparation and testing. Techniques such as electron microscopy offer the possibility of characterizing nanoparticle dispersion at the nanometer length scale. However, in cases where nanoparticles and matrix have structures with congruent atomic makeup, such as CNs and EVOH, poor contrast is achieved to discern dispersion of nanoparticles in the polymer matrix. Sample preparation can also be a tedious task and often harsh chemicals are

[3] (Reprinted from Polymer, 126, M.P. Orr and M.L. Shofner, "Processing strategies for cellulose nanocrystal/polyethylene-*co*-vinyl alcohol composites," pp.211-223, Copyright (2017), with permission from Elsevier. https://doi.org/10.1016/j.polymer.2017.08.043

employed to stain cellulose nanoparticles to improve contrast such as uranyl acetate or compounds with heavy metal ions [193, 194]. Therefore, other techniques have been developed to try and circumvent these challenges. Raman spectroscopy has been investigated to characterize both degree of dispersion and mixing of CNs in various polymer matrices [123, 124, 195].

Cross-polarized optical microscopy (POM) offers the opportunity to rapidly characterize degree of dispersion in polymer nanocomposites at micrometer length scales if the nanoparticles are optically anisotropic due to birefringence. The purpose of this chapter is to investigate three different processing methods to incorporate CNCs and CNFs and characterize degree of dispersion with POM. Various processing variables were also investigated for a solution mixing method to determine optimal processing conditions to increase CNC dispersion in EVOH. Finally, the polymers and nanocomposites were further investigated for degree of nanoparticle dispersion by observing the systems in the melt-phase of the polymer matrix to see if further information could be gleaned with the POM characterization method.

4.2 Optical Microscopy

Figure 4.1 shows images of the consolidated neat 48EVOH and nanocomposite films produced by melt processing at different screw speeds. The parallel striations in the POM images were artifacts from the PTFE mold used for compression molding. Both the neat 48EVOH films and the nanocomposite films had distinct and discrete discoloration in them. The discolored domains in the neat 48EVOH films were due to debris from extrusion and were much smaller in size compared to the domains found in the nanocomposite films.

The majority of the discolored domains in the nanocomposite films were attributed to CNC aggregates that degraded upon exposure to the processing conditions. Sulfate ester groups on the surface of sulfuric acid-hydrolyzed CNCs are known to contribute to a lower onset temperature for degradation of CNCs [3]. Additionally, Sapkota *et al.* [4] reported degradation of CNCs in a polyvinyl acetate (PVAc) matrix when the nanocomposite was formed by twin screw extrusion at 170 °C, a temperature below the reported degradation temperature of CNCs [1]. They attributed the degradation to the high shear forces encountered during extrusion, which led to a decrease in mechanical properties of the nanocomposite. In addition to shear forces, viscous heating during processing could also have contributed to the discoloration and degradation of the CNCs since the melt temperature would be higher than the extruder set temperature. POM images, shown in Figure 4.2, illustrate some aspects of structure in the neat and nanocomposite films. Neat 48EVOH displayed a magenta hue for films made at all three screw speeds tested, suggesting an isotropic optical scattering pattern. The POM images for the nanocomposite films showed a magenta background related to the polymer matrix with yellow, brown, and black aggregates believed to be the CNCs. When observed under crossed polarizers, the CNCs displayed birefringence due to their optical anisotropy [1,22,38,39]. The birefringence behavior of CNCs has been used to ascertain CNC dispersion and distribution at larger length scales since aggregates can appear as bright spots when viewed under polarizers [38,39]. Therefore, any images of nanocomposite films that displayed either yellow-brown or bright clusters suggested aggregation of the CNCs in the polymer matrix (Figure 4.2 d–f). Indeed, aggregation of CNCs has been reported in other melt mixed systems using twin screw extrusion, such as in PLA [5]. The size of the aggregates did not

appear to be significantly different among the three screw speeds used to produce the nanocomposite films, suggesting that dispersion of CNCs in 48EVOH did not change drastically across the set of parameters studied for the melt processing investigation.

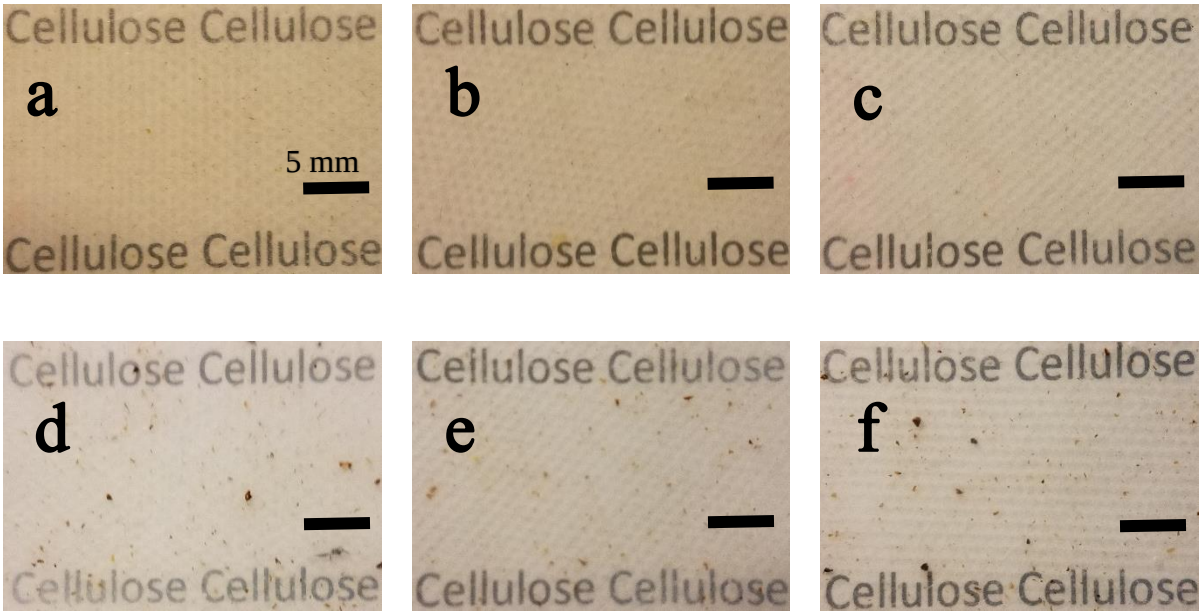

Figure 4.1 - Films produced by the melt method of 48EVOH at (a) 25 RPM, (b) 50 RPM, and (c) 100 RPM and 1 wt.% CNC/48EVOH at (d) 25 RPM, (e) 50 RPM, and (f) 100 RPM.

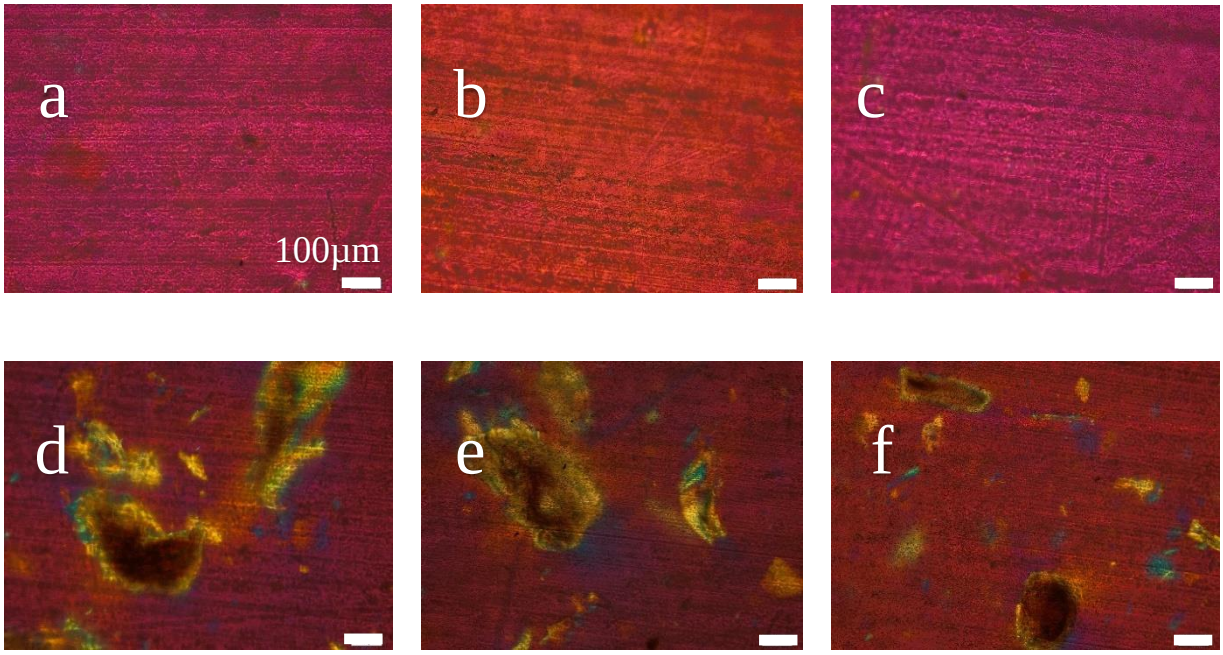

Figure 4.2 - POM images of films produced by the melt method of 48EVOH at (a) 25 RPM, (b) 50 RPM, and (c) 100 RPM and 1 wt.% CNC/48EVOH at (d) 25 RPM, (e) 50 RPM, and (f) 100 RPM.

To understand the observed microstructures better, rheological data were collected from the compounder using torque and pressure readings as the materials were mixing. The pressure drop data collected from the mini compounder were converted to relative values for viscosity and shear rate using Equations 4.1-4.3, assuming that the backchannel of the compounder was a slit capillary [40,41].

$$\tau = \frac{\Delta P h}{2L} \tag{4.1}$$

$$\dot{\gamma} = \frac{6Q}{h^2 2} \tag{4.2}$$

$$\eta = \frac{\tau}{\dot{\gamma}} \tag{4.3}$$

where h is the depth of the channel, L is the length of the channel, W is the width of the channel, Q is the volumetric flow rate of the material through the channel assumed to be constant for a given screw speed, ΔP is the pressure difference output given by the mini compounder's pressure transducers, τ is the shear stress, is the shear rate in the channel, and η is the viscosity. The depth h was measured as 1.5 mm, L was taken as 64 mm, and W was 10 mm. The value of ΔP used to calculate the shear stress was obtained while the mini compounder was operating in closed cycle mode. The mass flow rate was computed as the amount of polymer extrudate collected over a time span of 2 min for each screw speed, and thus, these data were collected when the mini compounder was not operating in closed cycle mode, rather when material was exiting the system. The volumetric flow rate was calculated from these mass flow rates by multiplying the mass flow rate by the melt density of 48EVOH. A value of 1.02 g/mL was used for the calculation based on the available data from the manufacturer for a 44EVOH polymer, which was the highest ethylene content EVOH reported [34]. Mass flow rate measurements were conducted three times, and the data were averaged for each screw speed. The data obtained are shown in

Figure 4.3. The viscosity of the melt processed nanocomposites and neat 48EVOH did not appear to change significantly in the measured range of shear rates. The relative trends between the neat polymer and nanocomposite with a 1 wt.% CNC loading as well as the change in viscosity as a function of shear rate were similar to other CNC-reinforced polymer nanocomposites for similar steady state shear rates [42–44]. The relative changes in viscosity in the polymer nanocomposites of PLA [42] and a polysaccharide [43] were reported to decrease in the shear rate range of 1–10 s^{-1}, but the magnitude of changes were within an order of magnitude, which was similar to what was observed in the viscosity as a function of shear rate in Figure 4.3. The relative consistency in viscosity within error as a function of steady state shear rate suggested the twin screw extruder would be expected to produce limited changes in CNC dispersion and distribution as a function of screw speed when incorporating the CNCs into the 48EVOH polymer with the melt method parameters used here.

The measurements presented in Figure 4.3 are limited by the collection of the mass flow rates as a function of screw rotational speed as well as screw rotational speeds available to acquire a wide range of shear rates. The feeding system for the mini compounder consists of a vertical cylinder directly connected to the extruder screws and a plunger used to develop pressure to push the material forward. As the polymer softens and melts during loading, the material is pushed into the mini compounder at a faster rate. Also, the rheological data collected in the slit capillary back flow channel may not be used to quantitatively understand the mixing conditions due to the qualitative relationship between mass flow rate and shear rate in the mini compounder [40]. A wider range of shear rates and viscosity measurements might have been able to provide a clearer picture as to how

CNCs affected the rheological properties of the EVOH when using the melt method. However, while the mini compounder can achieve higher screw rotational speeds than those used to make the nanocomposites by the melt processing method, the work reported by Sapkota *et al*. [4] suggested that CNCs degraded at even lower rotational speeds than were used for the melt processing method. Therefore, higher rotational speeds were avoided to prevent further degradation of CNCs with the melt method.

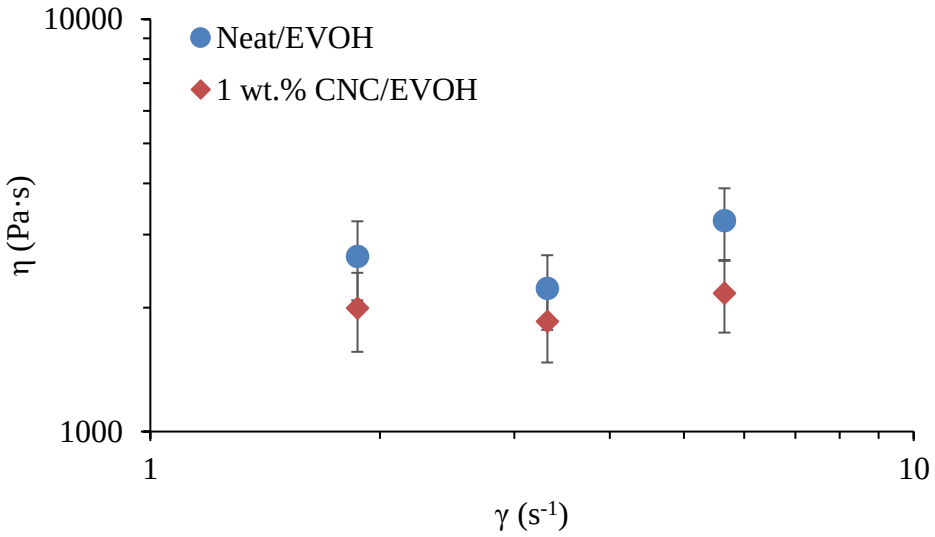

Figure 4.3 - Relative values of viscosity calculated from pressure drop readings from the mini compounder as a function of shear rate for both neat 48EVOH and 1 wt.% CNC/48EVOH produced with the melt method.

To reduce opportunities for thermal degradation of the CNCs and improve CNC dispersion and distribution, a solution casting method was also investigated. Images of the

compression molded films of 48EVOH containing 0, 1, 2.5, and 5 wt.% CNCs processed by the solution method are shown in Figure 4.4. The films were produced by sonicating an aqueous CNC suspension for 15 minutes before adding it to EVOH in a solvent mixture containing 70 vol.% IPA and 30 vol.% distilled water, stirring with a magnetic stir bar at a mixing speed of 250 RPM, and a temperature of 70 °C. Compared to the films made by the melt method in Figure 4.1, the nanocomposite films produced by the solution method appeared to have better CNC dispersion and distribution since micron-sized discolored domains were not observed. Additionally, no evidence of thermal degradation was observed, as expected.

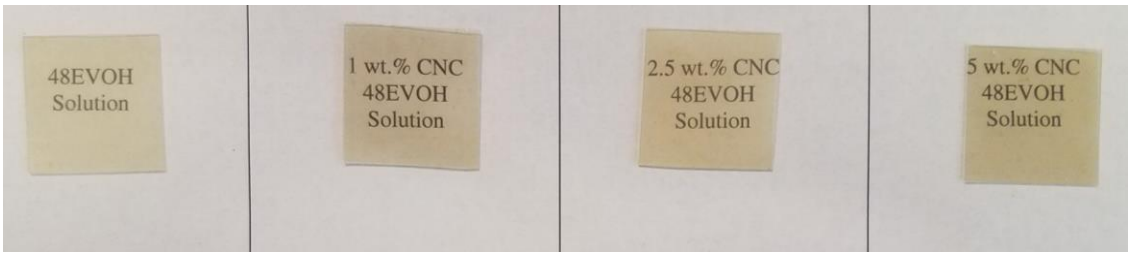

Figure 4.4 - Images of neat 48EVOH, 1 wt.% CNC/48EVOH, 2.5 wt.% CNC/48EVOH, and 5 wt.% CNC/48EVOH nanocomposites produced via solution casting.

POM images of the films from Figure 4.4 are shown in Figure 4.5. The POM images of the nanocomposite films produced by solution casting were not observed to have discrete brown/black domains like what was seen in films produced with the melt method in Figure 4.2. Additionally, the coloration of the films, with blue and orange domains, was

different from the discrete domains related to CNC aggregation and degradation observed in the films produced by the melt method. The blue and orange coloration in the films produced by the solution method suggested that the microstructure of the matrix was affected in some way by the increased dispersion of the CNCs with the solution casting method. The colors also were observed to change when the sample was rotated between the polarizers; i.e., the domains that were blue transitioned to orange and vice versa when the sample was rotated 90°. The coloration of the solid nanocomposite films in Figure 4.5 was similar to that reported by Abitbol et al. [45] in PVA/CNC hydrogels. Abitbol attributed the colors to the orientation of the CNCs in the matrix, where blue and orange are oriented in orthogonal directions to one another and 45° to the polarizers. Orientation of the CNC domains could arise from shear flow when the nanocomposites were compressed and consolidated into films. The sizes of the orange and blue domains could be attributed to the powder granules produced when the nanocomposite suspension was cast into a Petri dish and the solvent evaporated.

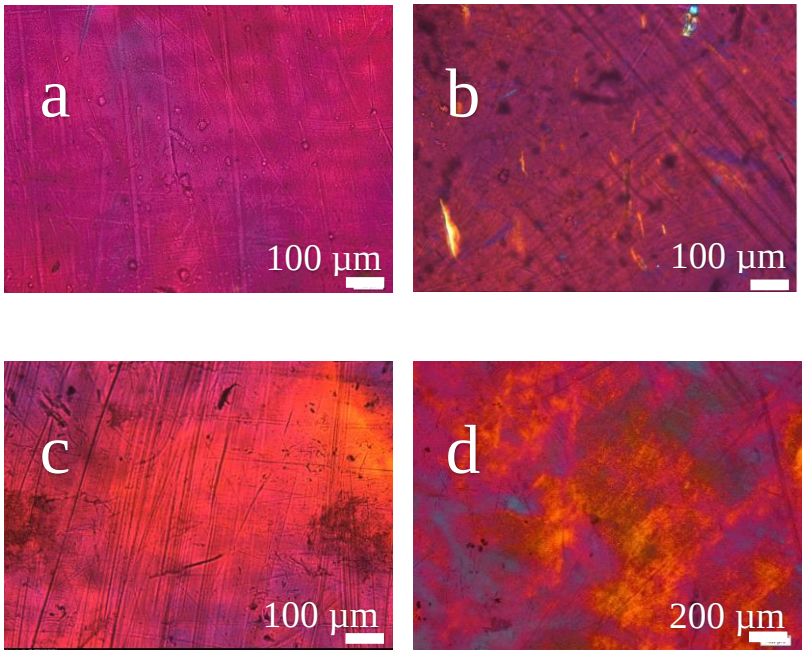

Figure 4.5 - POM Images of (a) neat 48EVOH, (b) 1 wt.% CNC/48EVOH, (c) 2.5 wt.% CNC/48EVOH, and (d) 5 wt.% CNC/48EVOH nanocomposites produced by the solution method.

To demonstrate the possibility of shear induced flow patterns in the nanocomposites during compression molding, samples of solution-casted neat 48EVOH and 48EVOH loaded with 5 wt.% CNCs were pressed without heat to the same thickness as the compression molded nanocomposite films. The images in Figure 4.6 showed the POM images of the pressed powder cakes on the hot stage covered with a glass cover slip at room temperature prior to melting the polymer. After imaging the samples at room temperature, the stage was heated to 170 °C at a heating rate of 10 °C/minute. The powder cakes appeared to be birefringent before being heated due to the forces applied during

compression molding. The black domains present in the figures of the films above the melting temperature of the polymer as well as when the film was cooled from the melt were due to bubbles of air. The bubbles of air helped as a guide to demonstrate when forces were being applied to the film and in what direction. When the final temperature was reached, the neat polymer and polymer nanocomposite films were held at the highest temperature for 5 min before the glass cover slip was pushed normal and parallel to the surface of the nanocomposite with a probe to simulate compression and shear forces, respectively, that the nanocomposites might have experienced in the hot press. As can be seen in Figure 4.6, the color of the melt-state neat 48EVOH was magenta when it was subjected to both compression and shear forces, indicating that the samples were optically isotropic and that the microstructures were not changed at the micrometer length scales observed in the microscope when force was applied. When the films were cooled to room temperature, the films appeared with many bubbles, and strain fields were observed surrounding the bubbles because the color changed from magenta to orange. However, when CNCs were dispersed in the polymer matrix, the colored domains were on the same order of magnitude as the grains of powder imaged in the original powder cakes (Figure 4.7). When a compression force was administered to the molten samples, the domains of blue and orange changed shape and size. The change in domain sizes and shapes indicated the microstructure was changing when a normal force was applied. Additionally, the color of the entire observed area shifted to orange when a shear force was applied to the cover slip in a direction perpendicular to the polarizer axis. Finally, when the outside forces were removed from the nanocomposites, the films were allowed to relax at 170 °C for 5 min before they were allowed to cool ambiently. The solid nanocomposite film imaged at a

temperature below the glass transition temperature retained orange and blue domains. These observations suggested that the CNCs aligned in the direction of applied shear and also the CNCs directed the alignment of polymer chains.

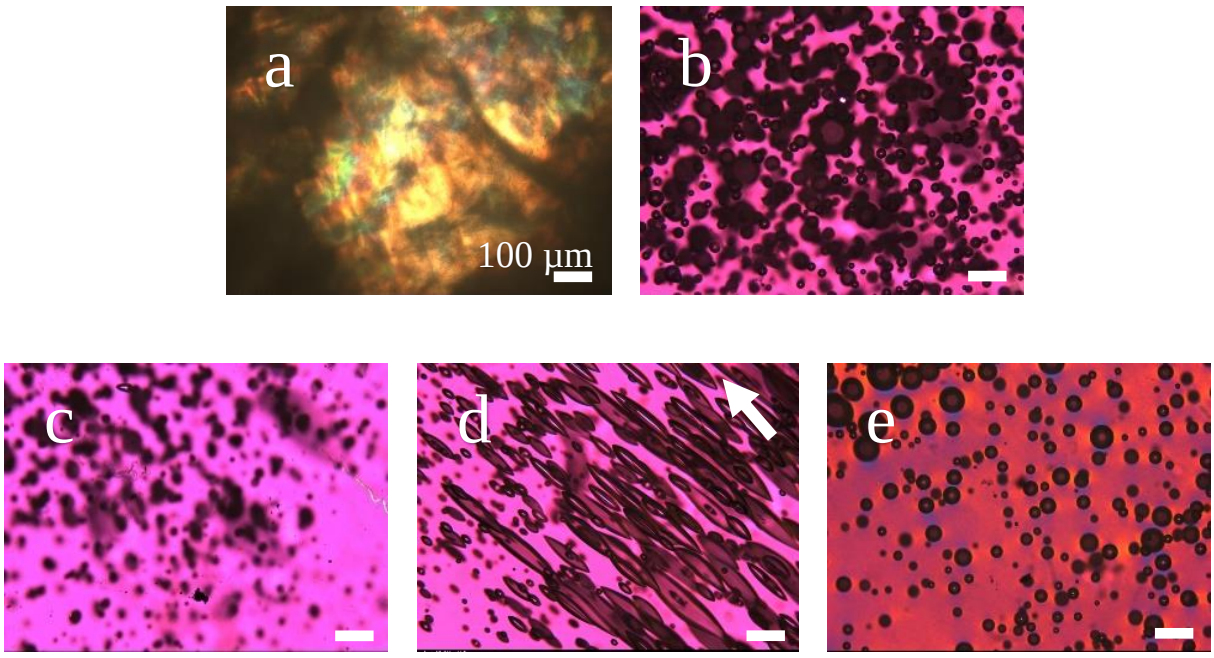

Figure 4.6 - POM images of neat 48EVOH (a) powder cake that was then subjected to (b) heating above the polymer melting temperature, (c) compressed, (d) sheared between glass surfaces, and (e) cooled from the melt. The direction of applied strain is indicated by the arrow in (d).

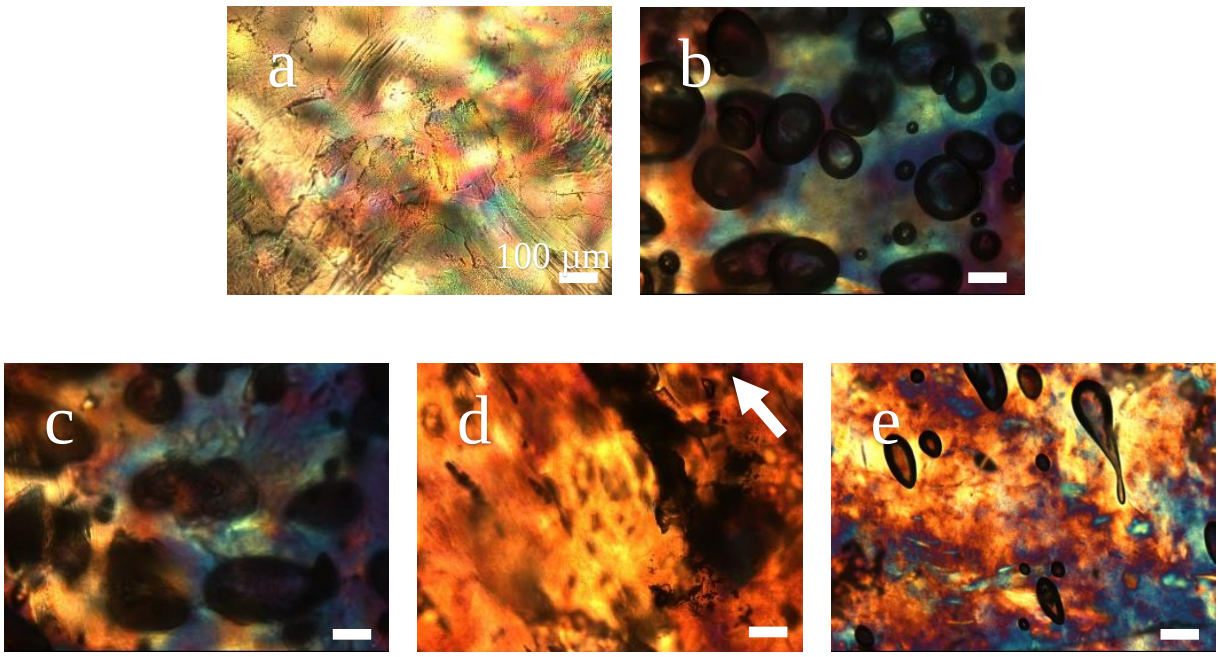

Figure 4.7 - POM images of 5 wt.% CNC/48EVOH (a) powder cake that was then subjected to (b) heating above the polymer melting temperature, (c) compressed, (d) sheared between glass surfaces, and (e) cooled from the melt. The direction of applied strain is indicated by the arrow in (d).

POM images were taken of nanocomposite films that were solution casted with one of the following variables altered: magnetic stir bar rotational speed (Figure 4.8), solvent composition (Figure 4.9), and sonication time of CNCs prior to incorporating them into the polymer solution (Figure 4.10). Bright domains were observed in the nanocomposite mixed at 125 RPM as seen in Figure 4.8a. The appearance of these domains suggested that CNCs aggregated but did not degrade since the domains were not yellow in color like those previously noted in the nanocomposites produced with the melt method. The aggregation

of the CNCs could be attributed to less mixing energy imparted on the nanocomposite suspension. Similarly, the size of the bright domains decreased as the IPA content of the solvent was increased from 40 vol.% to 70 vol.%. It was also observed that the EVOH solution became opaque when the IPA content was less than 60 vol.%. This suggested that EVOH did not readily dissolve in cosolvent compositions containing less than 60 vol.% IPA. If 48EVOH did not dissolve as readily, then the polymer-polymer interactions would be more favorable than polymer-solvent or polymer-particle interactions. This change in component compatibility could then lead to aggregation of CNCs in solution rather than dispersion amongst the EVOH chains. No distinct differences were observed in the POM images as a function of sonication time. Any birefringent spots that were observed in any of the systems where the CNCs were sonicated prior to being incorporated in the polymer solution were smaller than the aggregation observed in the melt-processed composites. However, the images appeared to have flow patterns that were different when compared to previous images. The flow patterns further validated the possibility of flow-induced ordering of CNCs in the EVOH matrix due to shear and compression forces that occurred during compression molding. The images collected for each processing variable studied suggested the highest levels of CNC dispersion in the EVOH polymer matrix came from higher mixing speed, and complete dissolution of polymer in the appropriate solvent composition. Sonicating CNCs was also demonstrated to increase CNC dispersion in the EVOH matrix at the length scales afforded by POM imaging. The POM images also suggested that solvent composition and mixing speed contributed to the most significant changes in CNC dispersion in the 48EVOH polymer.

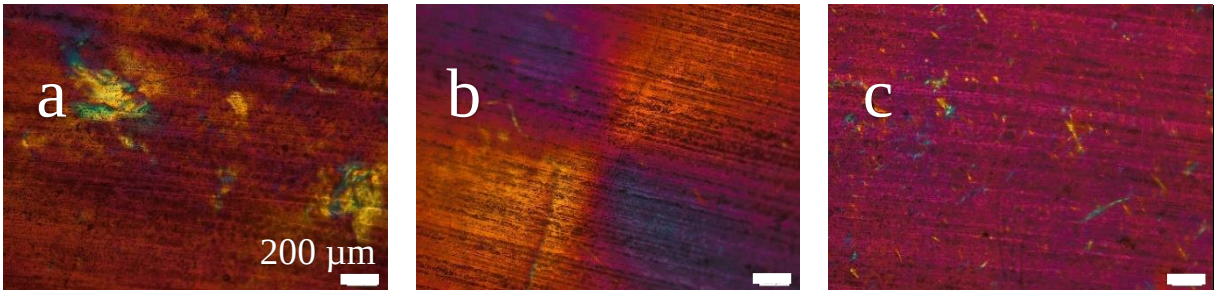

Figure 4.8 - POM images of 1 wt.% CNC/48EVOH nanocomposites produced by solution casting with a magnetic stir bar rotational speed of (a) 125, (b) 250, and (c) 500 RPM.

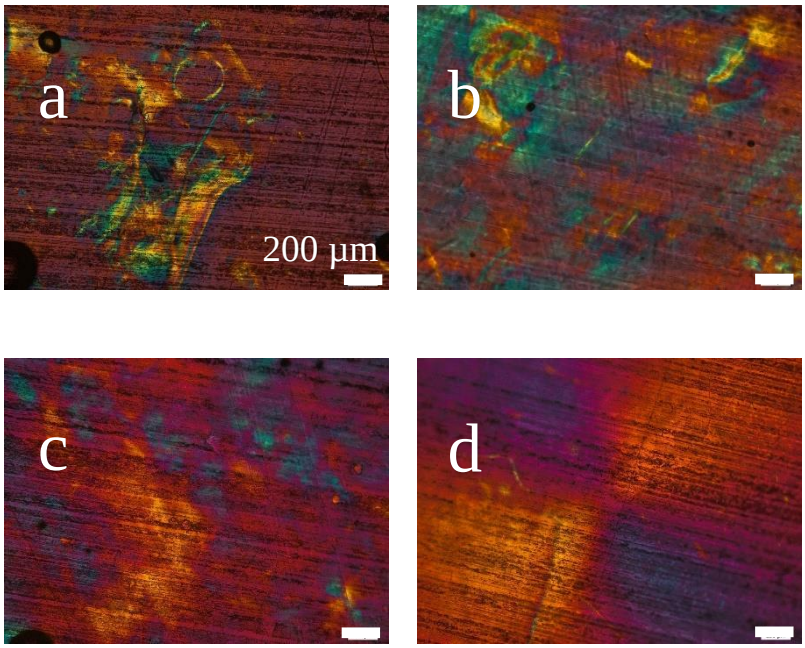

Figure 4.9 - POM images of 1 wt.% CNC/48EVOH nanocomposites produced by solution casting with a solvent composition of (a) 40, (b) 50, (c) 60, and (d) 70 vol.% IPA.

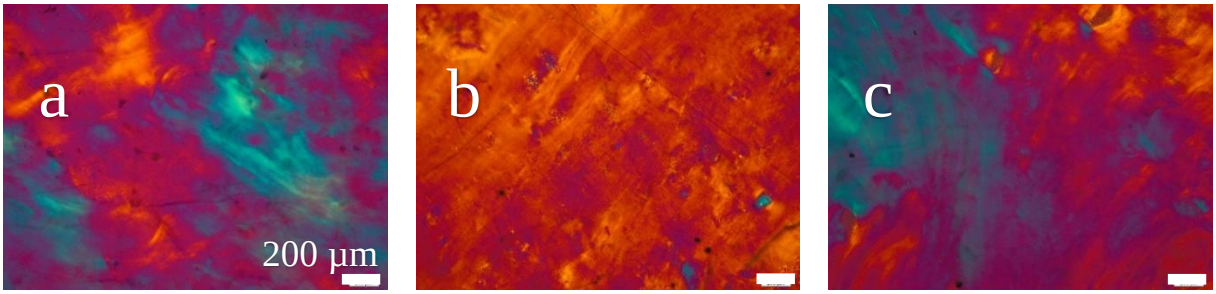

Figure 4.10 - POM images of 1 wt.% CNC/48EVOH nanocomposites produced by solution casting and sonicating the CNCs for (a) 1, (b) 5, and (c) 15 min prior to incorporating them into the polymer matrix.

POM images of nanocomposites characterized at room temperature were used to observe both CNC dispersion and the effects CNCs had on the microstructure of the EVOH polymer. The nanocomposite films were then heated above the melting temperature of the EVOH polymer to focus the investigation on CNC dispersion without any optical birefringence due to the change in polymer microstructure. Figure 4.11 shows the POM images of 48EVOH nanocomposite films in the melt with 0, 1, 2.5, and 5 wt.% CNC loadings. In the melt phase, the polymer matrix lost any orientation that was associated with crystallites. Therefore, the neat polymer matrix in the melt was optically isotropic, hence the magenta color as previously seen in the neat EVOH at room temperature. The same magenta color was observed in the nanocomposite melts as well. Additionally, bright spots were observed in the 1 wt.% nanocomposite which suggested CNC aggregation occurred to some degree during solution processing. Dark domains were observed in the 2.5 and 5 wt.% CNC nanocomposites above the melting temperature of the EVOH polymer

which suggested CNC-rich domains were present in the EVOH matrix that retain some inherent cohesion in the melt. These domains correlated to hazier regions in the nanocomposite films at room temperature that were observed by eyesight. However, it did not appear as CNCs that have aggregated or they would appear birefringent as in Figure 4.8 and Figure 4.9, nor did they appear to change the microstructure of the polymer matrix as noted in the solid-state films. Therefore, the CNCs appeared to have dispersed to a degree with the solution casting method, but the composites retained CNC-rich domains.

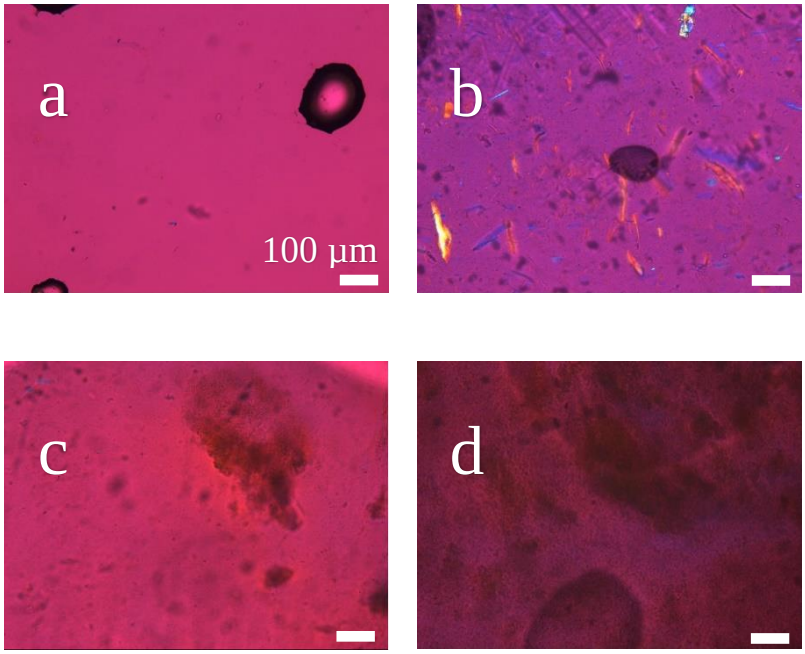

Figure 4.11 - POM images on a hot stage at 170 °C of (a) neat 48EVOH and (b) 1 wt.% CNC/48EVOH, (c) 2.5 wt.% CNC/48EVOH, and (d) 5 wt.% CNC/48EVOH nanocomposites produced by solution casting.

When the nanocomposites were produced via the STM method, there were observable changes in the microstructure when the nanocomposites were imaged in the melt. Figure 4.12 and Figure 4.13 show the solid films and melt-phase POM images of 48EVOH with 0, 1, 2.5, and 5 wt.% CNCs produced by the STM method, respectively. The films looked similar to those produced by the solution method (Figure 4.4). While the nanocomposite films produced by the solution method appeared hazy with increasing CNC loadings, the STM- produced nanocomposite films were more transparent. Additionally, the CNC-rich domains that were observed in samples produced by the solution method (Figure 4.11) did not appear in the melt-phase POM images in Figure 4.13. This observation suggested increased dispersion and distribution of CNC-rich domains

throughout the nanocomposite film as a result of the STM processing method, creating a more homogenous mixture in the nanocomposite films.

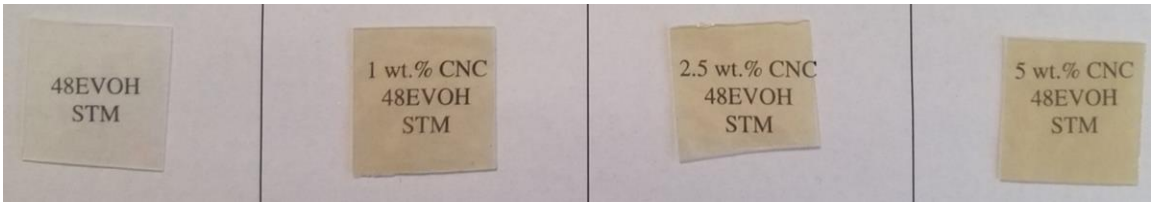

Figure 4.12 - Images of 0, 1, 2.5, and 5 wt.% CNC/48EVOH nanocomposites produced by the STM technique.

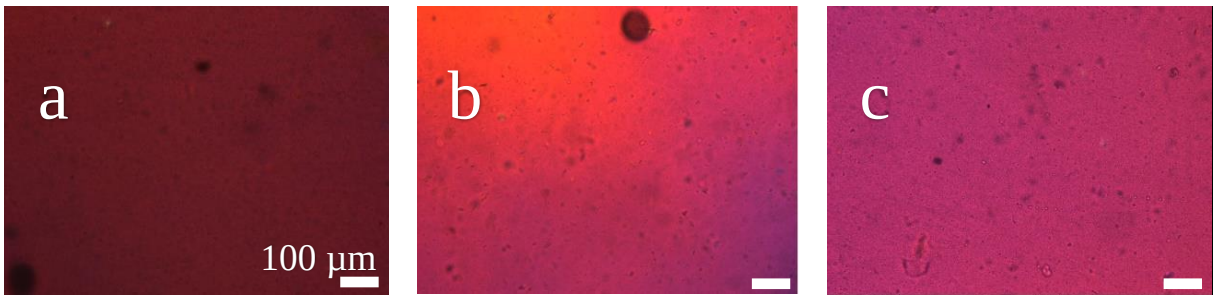

Figure 4.13 - POM images of melt-phase (a) 1 wt.% CNC/48EVOH, (b) 2.5 wt.% CNC/48EVOH, and (c) 5 wt.% CNC/EVOH nanocomposites produced by the STM technique.

Figure 4.14 shows solid films of neat 44EVOH and nanocomposites with 1, 2.5, and 5 wt.% CNCs produced by the solution and STM methods. The visual appearance of

the nanocomposites produced by the solution method and the STM method is similar. Both the color and transparency are similar in the neat and nanocomposite systems produced with either processing strategy. There were also no CNC aggregates observed at the length scales afforded by the digital camera.

Figure 4.14 - Images of neat 44EVOH, 1 wt.% CNC/44EVOH, 2.5 wt.% CNC/44EVOH, and 5 wt.% CNC/44EVOH samples produced by solution casting and STM methods.

Figure 4.15 and Figure 4.16 show POM images of the same samples produced by the solution and STM processing methods, respectively. These figures contain images of the films when they were heated to a temperature above the melting temperature of the polymer matrix and also when they were cooled to a temperature below the glass transition temperature of the polymer matrix. While the neat 44EVOH film produced by the solution method was optically isotropic when it was heated to above the melting point of the polymer, the POM images of the nanocomposite films with 1 and 5 wt.% CNC loadings became darker, and they retained optical anisotropy as noted by the orange hues in Figure

4.15 c and e. When the films were cooled to below the glass transition temperature, optical anisotropy could be observed in the films regardless of CNC loading. Optical anisotropy observed in the neat 44EVOH film could be as a result of ordering due to strains surrounding the bubbles that could be observed in the POM image in Figure 4.15b while the anisotropy observed in the 1 and 5 wt.% CNC nanocomposite films could be due to changes in the polymer microstructure imparted by the increased CNC dispersion. When the nanocomposites were produced by the STM method, there appeared to be ordering of the polymer matrix in the samples cooled from the melt phase even in the neat EVOH sample. Additionally, the 44EVOH nanocomposites displayed optical anisotropy in the melt phase. A liquid crystalline-like phase emerged in the 44EVOH nanocomposites when the STM method was employed (Figure 4.16: d and f). The liquid crystalline-like phase in the 44EVOH matrix suggested the STM strategy directed assembly of the CNCs, which then imparted a change in the microstructure of the polymer matrix. Compared to the POM images of the 48EVOH nanocomposite films, the differences in the way CNCs affected the polymer microstructure in both the melt and solid films suggested there could be differences in compatibility between the nanoparticles and polymer chains due to differences in vinyl alcohol content and therefore differences in hydrogen bonding capabilities of the polymers.

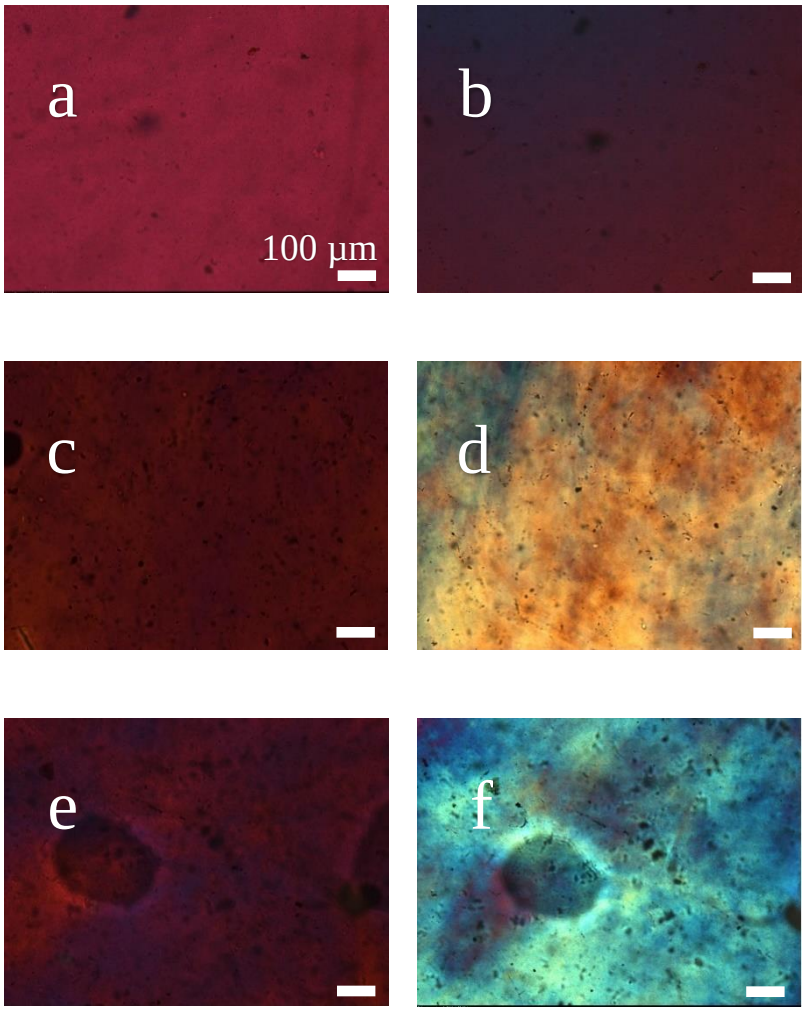

Figure 4.15 - POM images of melted (a, c, and e) and cooled from melt (b, d, and f) of (a and b) neat 44EVOH, (c and d) 1 wt.% CNC/44EVOH and (e and f) 5 wt.% CNC/44EVOH produced via solution processing.

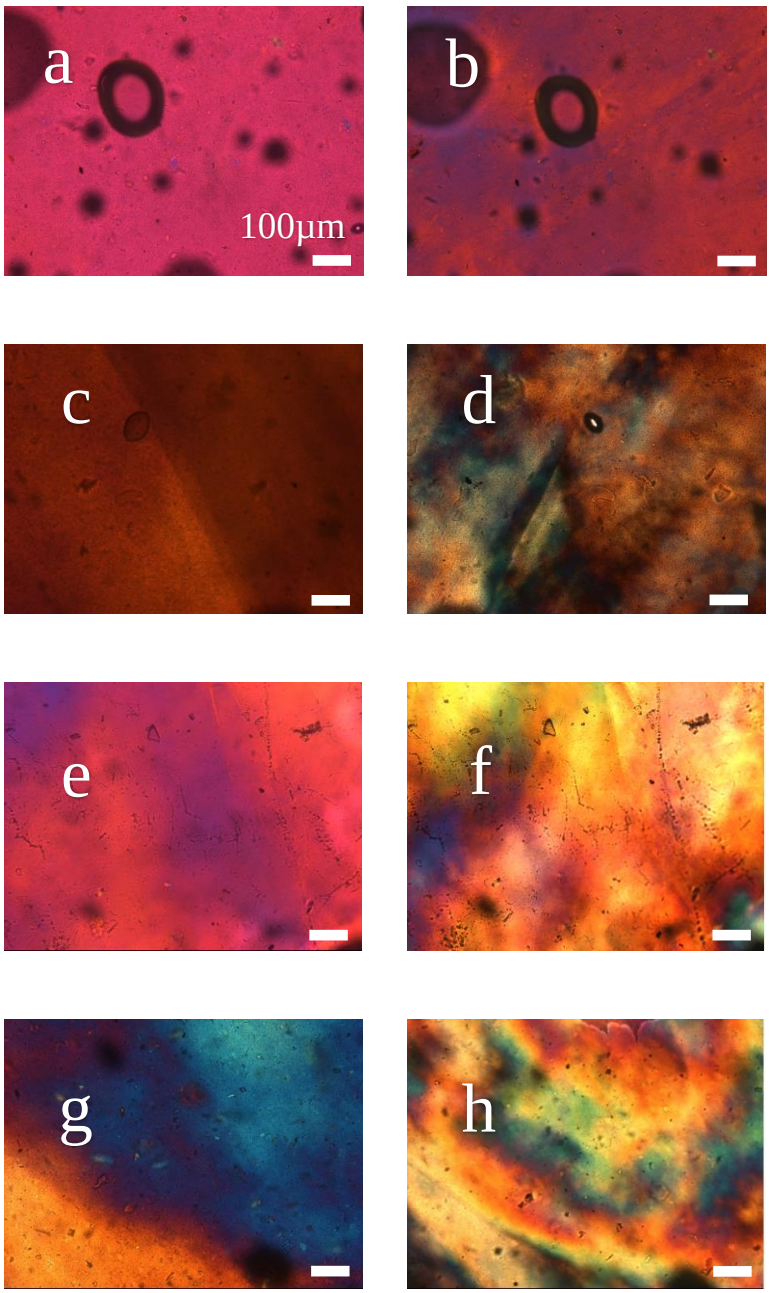

Figure 4.16 - POM images of melted (a, c, e, and g) and cooled from melt (b, d, f, and h) of (a and b) neat 44EVOH, (c and d) 1 wt.% CNC/44EVOH, (e and f) 2.5 wt.% CNC/44EVOH, and (g and h) 5 wt.% CNC/44EVOH produced via the STM method.

Figure 4.17 and Figure 4.18 display the POM images of 1 wt.% TEMPO CNF/48EVOH and 1 wt.% TEMPO CNF/44EVOH nanocomposites produced by either the solution or STM methods. Fiber-like particles were observed in the melt-phase images of both polymer nanocomposite systems that had dimensions of several microns up to several hundred microns, and these particles were assigned to the TEMPO CNFs based on the dimensions and fibrous appearance. There appear to be no discernable differences in level of TEMPO CNF dispersion in 48EVOH as a function of processing conditions chosen to make the nanocomposite, as the aggregate sizes did not change significantly in the POM images collected. However, the level of TEMPO CNF dispersion appeared to increase in the 44EVOH matrix nanocomposite produced by the STM method versus the solution method, as there were smaller aggregates and particle sizes observed. Overall in the images of the films cooled from the melt, the orange and blue domains aligned with the fiber-like morphology of the TEMPO CNFs, and these colored domains appeared similar in color and domain size as the CNC- reinforced EVOH composites of the same particle loading and processing conditions.

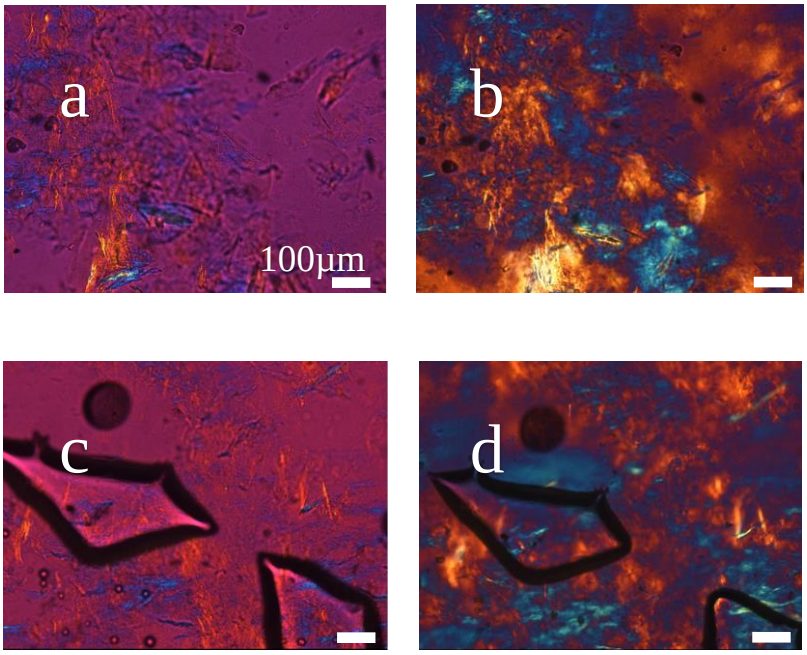

Figure 4.17 - POM images of (left column) melted and (right column) cooled from the melt 1 wt.% TEMPO CNF/48EVOH produced by either (a and b) the solution or (c and d) STM method

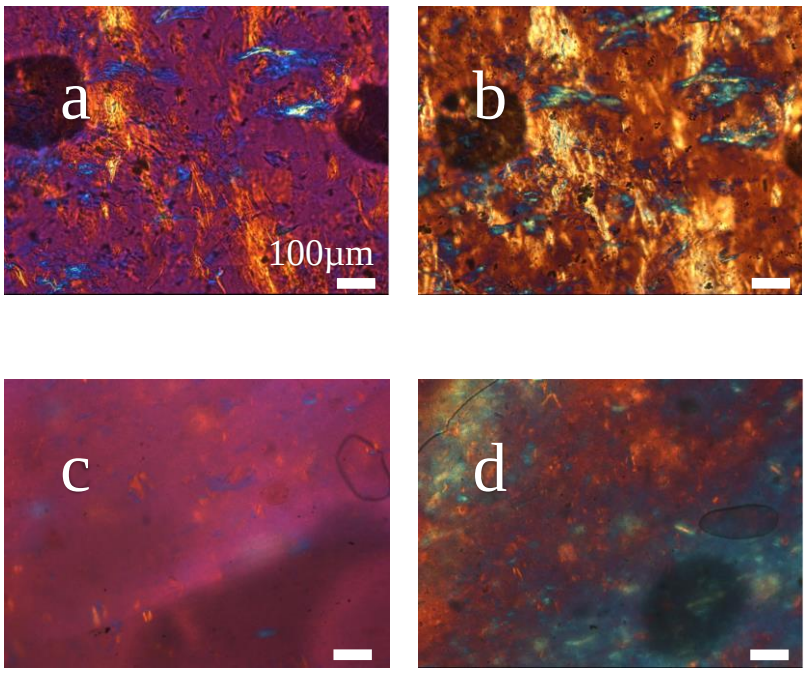

Figure 4.18 - POM images of (left column) melted and (right column) cooled from the melt 1 wt.% TEMPO CNF/44EVOH produced by either (a and b) the solution or (c and d) STM method

Due to the evidence provided by both CNC and TEMPO CNF- reinforced EVOH nanocomposites that suggested nanoparticle dispersion increased using the STM method, CNF-reinforced EVOH nanocomposites were only made and characterized using the STM method and the POM images are shown in Figure 4.19. As can be seen in the figure, the dimensions of the visible CNFs were similar if not slightly smaller in length than TEMPO CNFs observed in Figure 4.17 and Figure 4.18. While it is difficult to determine level of dispersion at the length scales provided by POM imaging, the distribution of CNF particles

in the images suggested the level of CNF dispersion was similar in the EVOH matrices when compared to composites reinforced with TEMPO CNFs.

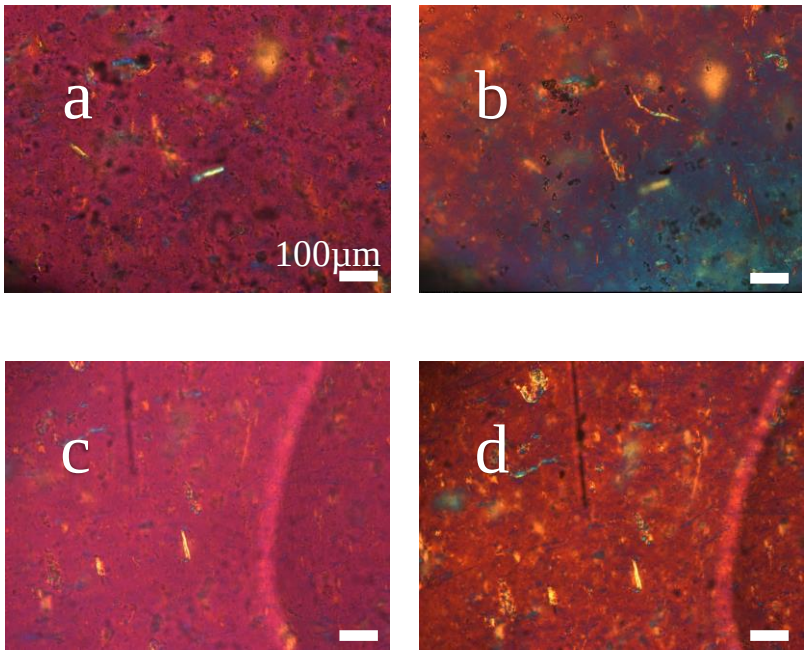

Figure 4.19 - POM images of (left column) melted and (right column) cooled from melt (a and b) 1 wt.% CNF/48EVOH and (c and d) 1 wt.% CNF/44EVOH made with the STM method.

The images from POM characterization studying the effects of incorporating CNCs, TEMPO CNFs, and CNFs into 44EVOH and 48EVOH copolymers with three different processing strategies suggested there was significant dependence of the degree of CN

dispersion and distribution at the micrometer length scale on the processing strategy used to produce the CNC-reinforced nanocomposites. Melt processing was shown to produce nanocomposites with significant CNC aggregation and degradation. POM images used to study the effects of processing variables when using the solution method suggested the strongest effects on CNC dispersion in the 48EVOH polymer matrix came from mixing speed and solvent composition for dissolving the EVOH resin. An increase in the compatibility between the polymer and solvent led to an increase in CNCs dispersing in the EVOH polymer. Also, the microstructures of the 44EVOH and 48EVOH polymers were affected differently when CNCs were incorporated and dispersed using either the solution or STM methods. This suggested that the compatibility between the CNCs and the polymer matrix was different as a function of comonomer content in the EVOH polymer. Higher vinyl alcohol comonomer content in the EVOH polymer could lead to increased compatibility between the matrix and CNCs due to increased hydrogen bonding sites. Compared to the nanocomposites produced by the melt method, the increased CNC dispersion seen when the nanocomposites were produced with the other two methods led to changes in the polymer microstructure. The changes in microstructure observed when CNCs were incorporated into either EVOH polymer were not similarly observed in nanocomposites with either TEMPO CNFs or CNFs. This was attributed to the differences in particle morphology, as the CNFs form networks at lower loadings compared to CNCs due to having a higher aspect ratio as well as the possibility of entanglements with other CNFs [196]. The network structure of CNFs meant increased particle- particle interactions would occur in the EVOH composites, leaving fewer opportunities for intermolecular interactions between CNFs and the polymer matrix. Further study using the hot stage and

a probe suggested the CNCs and surrounding polymer chains were oriented due to shear and compressive stresses during compression molding and caused the nanocomposite film to display birefringent domains. When the nanocomposites were cooled from the melt, the changes in the microstructure as a result of CNC orientation were retained in the solid nanocomposite films. Based on the results reported in this study as well as by others [11,35] comparing melt and solution processing strategies to produce CNC/EVOH composites, a solution processing step to initially incorporate CNCs resulted in the largest increase in CNC dispersion. Even though the solution method showed adequate CNC dispersion at the micrometer length scale, further investigation of the nanocomposites with POM at different temperatures revealed that a multi-step protocol could increase the homogeneity of the nanocomposites. The changes in CNC dispersion in a thermoplastic polymer matrix as a function of the process chosen follow similar trends in CNC-reinforced nanocomposites in other thermoplastic matrices reported by others [11,35]. CNF dispersion and distribution also appeared to increase in the polymer melt when the composites were made with the STM method as opposed to the solution method, although these changes were not as significant as composites made with incorporating CNCs. Similarly, Srithep *et al.* [197] observed micrometer-sized CNF aggregation in a poly (3-hydroxybutyrate-*co*-3-hydroxyvalerate) composite that was produced with a multi-step mixing protocol and was attributed to CNF network formation during the first processing step involving freeze drying of an aqueous suspension of CNFs and the polymer. The results reported herein suggested that solution processing could be used as a means of initially compounding the nanocomposite to be used as a stock feed for extrusion or other melt mixing techniques commonly used to process commercial thermoplastic polymers.

4.3 Conclusions

Three processing strategies were implemented to investigate how they affected CN dispersion in an EVOH polymer matrix: a melt processing method, a solution processing method, and a sequential processing method with solution and melt processing steps. Analysis of optical microscopy images of nanocomposite films indicated that a multi-step protocol involving solution and melt mixing steps increased the CNC dispersion and distribution more than when CNCs were incorporated with either only a solution or melt mixing procedure. The dispersion and distribution of TEMPO CNFs were also demonstrated to increase with the implementation of the multi-step protocol, particularly in the EVOH matrix with higher vinyl alcohol content. Additionally, POM imaging at different temperatures was shown to be an effective characterization tool for CNC composites. Comparing images of the composites in the solid state and at temperatures where the matrix was melted provided a better indication of component interactions and state of CNC dispersion. Specifically, these images indicated differences in matrix structuring caused by the addition of CNs for the two EVOH polymers used. Overall, the results of this work showed that effective processing strategies for CN composites could be constructed by combining conventional operations through consideration of component compatibility and stability.

CHAPTER 5. STRUCTURE AND PROPERTY INVESTIGATION OF ISOTROPIC NANOCOMPOSITES OF 48 MOL.% ETHYLENE CONTENT POLYETHYLENE-CO-VINYL ALCOHOL REINFORCED WITH CELLULOSE NANOMATERIALS

5.1 Introduction

The commercial use of EVOH as a food packaging material means thermal, thermomechanical, and mechanical properties are all vital to its efficacy as an end-use product. Nanofillers have been used as a means of trying to increase these properties in EVOH [85, 198, 199]. CNs have also been used in EVOH matrices [74, 75, 79] and many other polymer nanocomposite systems in order to increase mechanical properties such as strength and modulus [1, 10, 19, 59, 63].

Several explanations have been given as to how CNCs and CNFs have increased the mechanical properties of polymers. Because the CNs of interest in this work are dimensionally anisotropic and contain hydrophilic surface groups, the nanoparticles are able to interact with one another and form a rigid network due to hydrogen bonding above a critical threshold. Additionally, CNFs are able to form a network due to mechanical fibrillation during processing [8]. The network forming capabilities of CNs has been attributed to the increase in storage modulus as a function of temperature for various polymer matrices [28, 43, 90, 95, 96, 142, 143]. Others have demonstrated that stress transfer between both polymers and particles as well as between particles plays an

important role in mechanical reinforcement efficacy of cellulose nanoparticles in a polymer matrix [93, 200, 201]. CNs have also been demonstrated to act as nucleating agents for polymer crystal growth [37, 133, 202].

The purpose of this research is to investigate the thermal, thermomechanical, and mechanical properties as well as the structure of CNC- and CNF- reinforced 48EVOH nanocomposites as a function of processing strategy implemented. In the previous chapter, POM was utilized as an initial understanding of CN dispersion in an EVOH matrix and how the nanoparticles affected the microstructure of the nanocomposite. Based on the results of POM characterization, two processing strategies will be further investigated in this work: the solution method and STM method. The nanocomposites made with these processing strategies will be further investigated in order to determine how the incorporation and dispersion of CNCs and CNFs affected the resulting nanocomposite structure and properties. While work has been reported to increase various properties of polymer nanocomposites through alteration of the cellulose surface chemistry, the work presented in this chapter will take advantage of the ability to use EVOH with different comonomer compositions to determine how matrix selection can also impact CNC and CNF dispersion and subsequent thermal, thermomechanical, and mechanical properties of the nanocomposite construct.

5.2 Structure

5.2.1 XRD

Figure 5.1 displays the XRD patterns for neat CNCs and CNFs used to develop the isotropic nanocomposites. The CNC peaks were located at 2θ values of approximately

15.0°, 16.4°, and 22.6° which were ascribed to the $(1\bar{1}0)$, (110), and (200) planes, respectively, of the monoclinic crystal lattice for the cellulose Iβ allomorph commonly associated with wood- based CNCs [1] (Figure 5.1a). The CNF peaks were located at 2θ values of approximately 15.0°, 16.9°, 22.2°, and 23.0° (Figure 5.1b). The pattern for CNFs was also categorized as a cellulose I structure. X_c for the CNCs and CNFs were calculated to be 72% and 46%, respectively. The differences in the crystallinities are due to the increased amount of amorphous content associated with CNFs as they are primarily mechanically defibrillated as opposed to acid hydrolysis that preferentially attacks amorphous chains to produce CNCs.

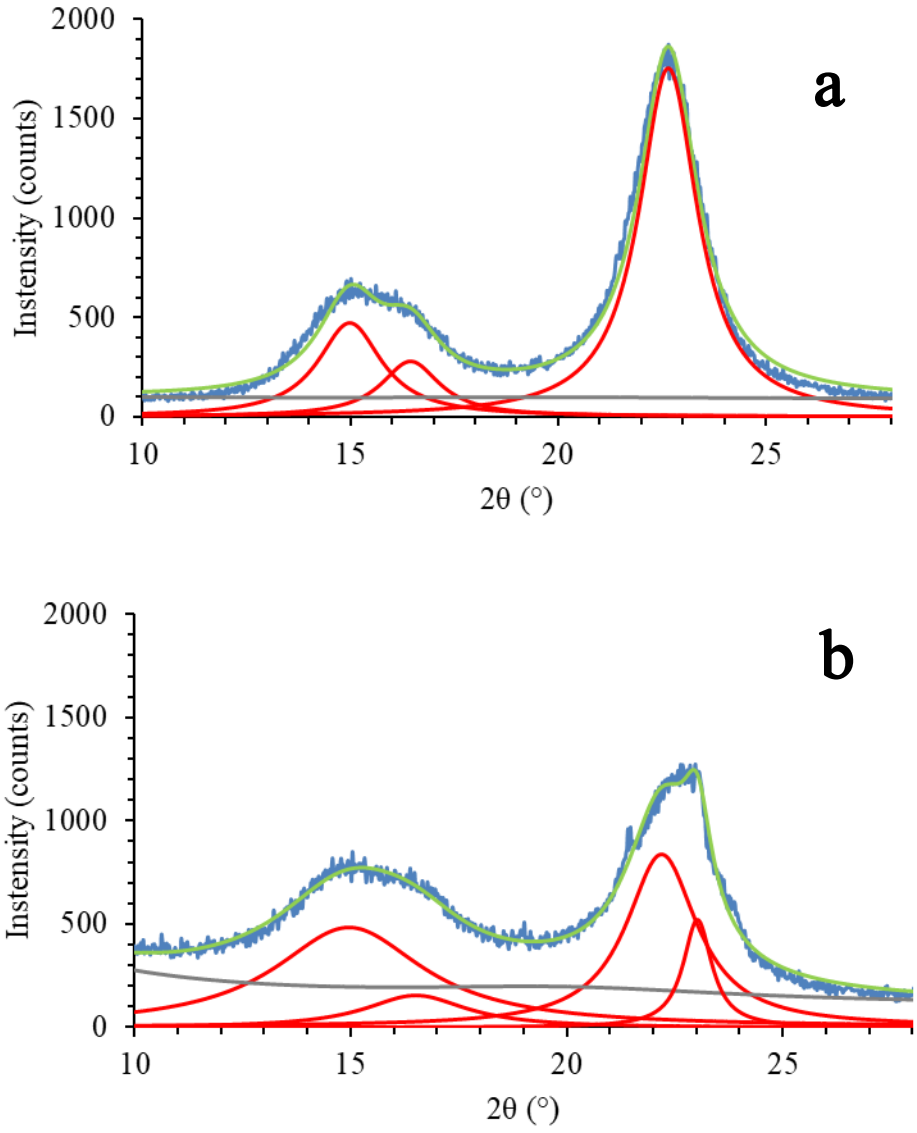

Figure 5.1 - XRD patterns for (a) CNCs and (b) CNFs.

XRD patterns for the isotropic 48EVOH nanocomposites produced with the STM method may be found in Figure 5.2. All patterns exhibited peaks at 2θ values of 10.6° and 20.5° which were attributed to the orthorhombic crystal lattice (100) and (101) planes of EVOH [72]. An additional peak was also observed at a 2θ value of 21.7° in all systems

except the neat polymer. Additionally, the intensity of the (100) and (101) peaks increased with the incorporation of nanoparticles, although there were no additional peaks observed that could be assigned to either the CNCs or CNFs. The calculated X_c and density of the matrix crystalline phase were also observed to increase with increased CN loadings (Figure 5.3). While X_c values for nanocomposites with CNFs were higher compared to nanocomposites with similar loadings of CNCs, crystal density of the polymer was only higher than both the neat polymer and nancomposites with CNCs when 2.5 wt.% CNFs were incorporated with the STM method. These increases in polymer crystallinity and crystal density with the addition of CNs suggested the nanoparticles promoted the formation of a larger and more perfect polymer crystal structure compared to the neat polymer when the nanocomposites were made with the STM method.

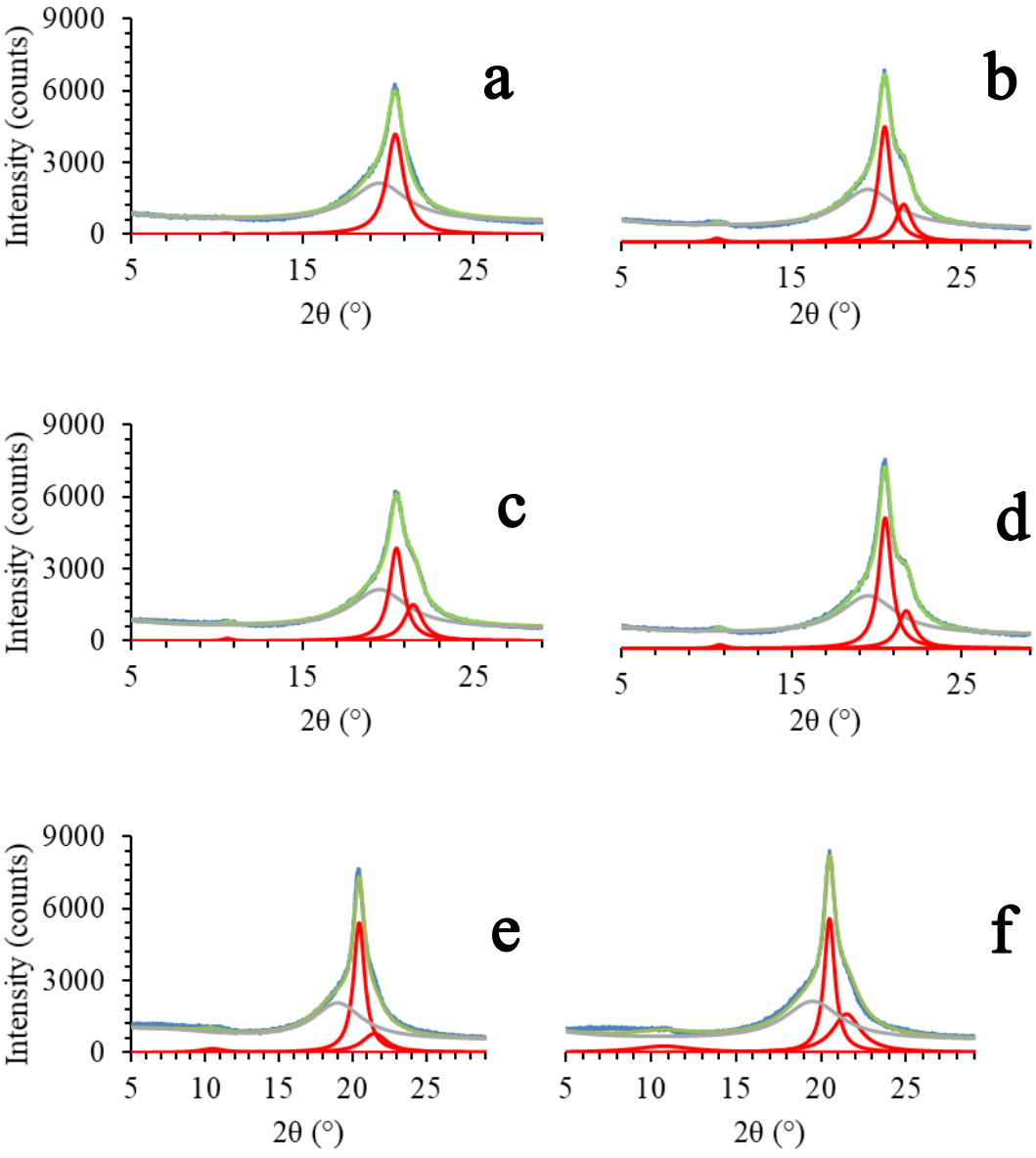

Figure 5.2 - XRD patterns for (a) 0, (b) 1, (c) 2.5, and (d) 5 wt.% CNC/48EVOH and (e) 1 and (f) 2.5 wt.% CNF/48EVOH nanocomposites produced by the STM method.

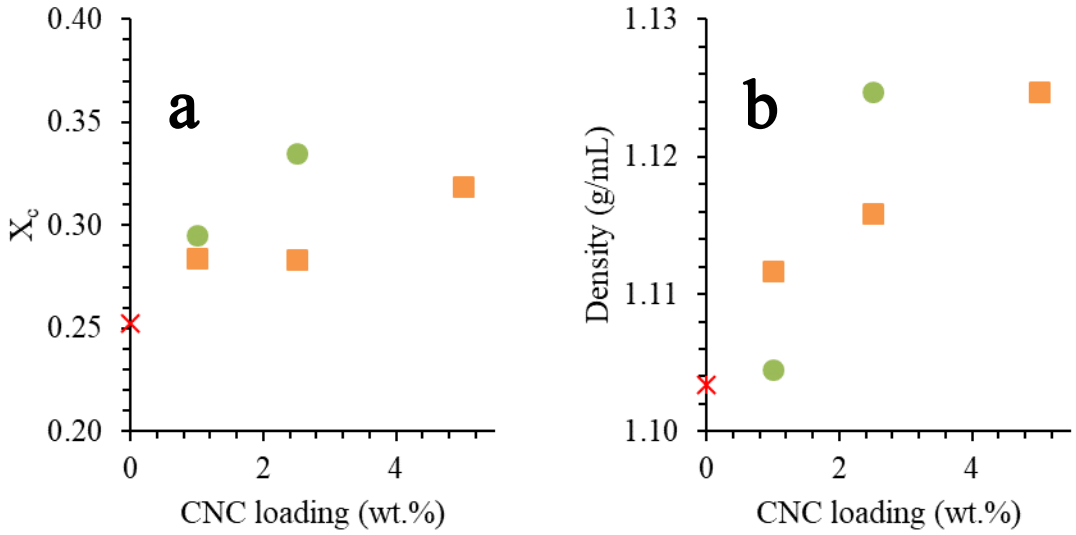

Figure 5.3 - Calculated X_c (a) and density of the crystalline phase (b) of the 48EVOH nanocomposites as a function of either CNC (squares) or CNF (circles) loading made with the STM method.

5.2.2 FT-IR

FT-IR spectra for neat CNCs, CNFs, and TEMPO CNFs may be found in Figure 5.4. The spectra for the neat cellulosic nanomaterials were normalized with the band located at ~1025 cm^{-1} which had the highest intensity for all three nanomaterials. All three CNs had bands located at ~3334, 2900, 1400-1430, and various bands between ~890-1370 cm^{-1} which were assigned to -OH bending and stretching, -CH symmetric and asymmetric stretching, $-CH_2$ scissor motion, and various deformations and vibrations of the anhydroglucose ring, respectively [203, 204]. Additionally, TEMPO CNFs had a prominent band present at ~1600 cm^{-1} which was associated with CO stretching in the

carbonyl surface groups of the nanofibrils [205]. There were also bands in all CNs at ~1640 cm^{-1} that was attributed to -OH deformations of adsorbed water [204, 206].

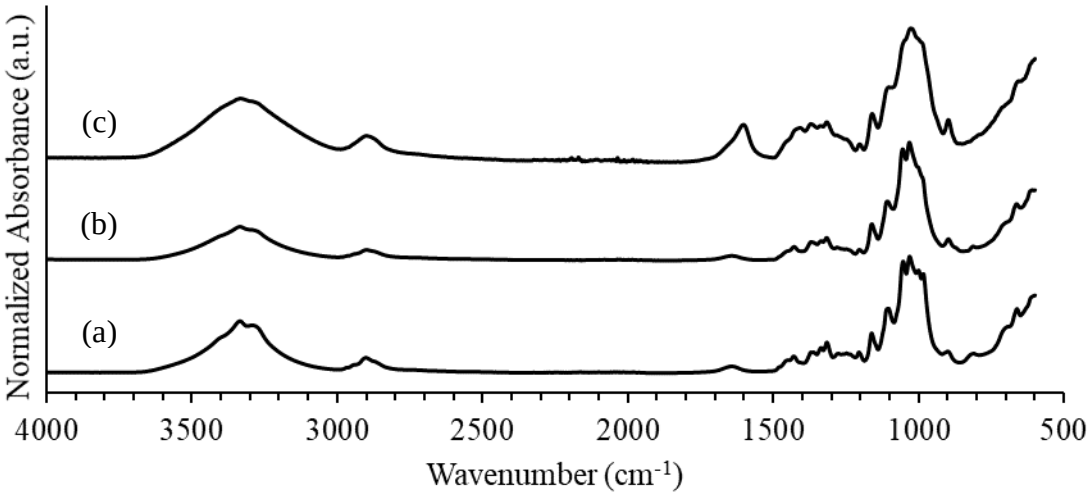

Figure 5.4 - FT-IR spectra for (a) CNCs, (b) CNFs, and (c) TEMPO CNFs.

ATR FT-IR analysis was carried out 48EVOH nanocomposites with the aim of observing changes in the chemical structure of the polymer matrix with the incorporation of CNCs and CNFs via solution and STM methods. From the spectra presented in Figure 5.5, bands were located at ~3320, 2922, 2850, 1456, 1330, 1135, 1078, and 835 cm^{-1} for each sample which were assigned to -OH bending, -CH asymmetrical and symmetrical stretching, -OH deformation, -OH deformation, EVOH crystallinity, CO stretching, and EVOH -CH_2 vibrations, respectively [207, 208]. The band at ~3320 cm^{-1} associated with -OH bending was observed to shift to lower wavenumbers by as much as 12 cm^{-1} and 6

cm^{-1} when 2.5 wt.% CNCs were incorporated into the 48EVOH matrix with the solution or the STM method, respectively. The band located at ~3320 cm^{-1} was located at either similar or higher wavenumber in the polymer and nanocomposite systems produced with the STM method versus the solution method. New bands in the range from 950-1150 cm^{-1} appeared in the nanocomposites and increased in intensity with increased loadings of CNCs regardless of processing strategy employed, and these were characteristic of CNCs [74].

Spectra of the CNF/48EVOH nanocomposite systems produced with the STM method were compared to CNC/48EVOH nanocomposites produced with the same filler loadings using the STM method. As can be seen in Figure 5.6, the locations of bands and band assignments for 48EVOH nanocomposites with CNFs were similar at 1 and 2.5 wt.% loadings to 48EVOH nanocomposites with CNCs produced with the STM method. The only exception is the C-O stretching band located at ~1240 cm^{-1} when 2.5 wt.% CNCs were incorporated into 48EVOH with the STM method that were not observed in the nanocomposites with CNFs. The band located at ~3320 cm^{-1} was at a lower wavenumber in all 48EVOH nanocomposites with CNFs compared to nanocomposites with similar loadings of CNCs and the intensity of this band for CNF- reinforced 48EVOH nanocomposites was similar to or lower than the intensity of the band when CNCs were incorporated into the 48EVOH matrix with the STM method.

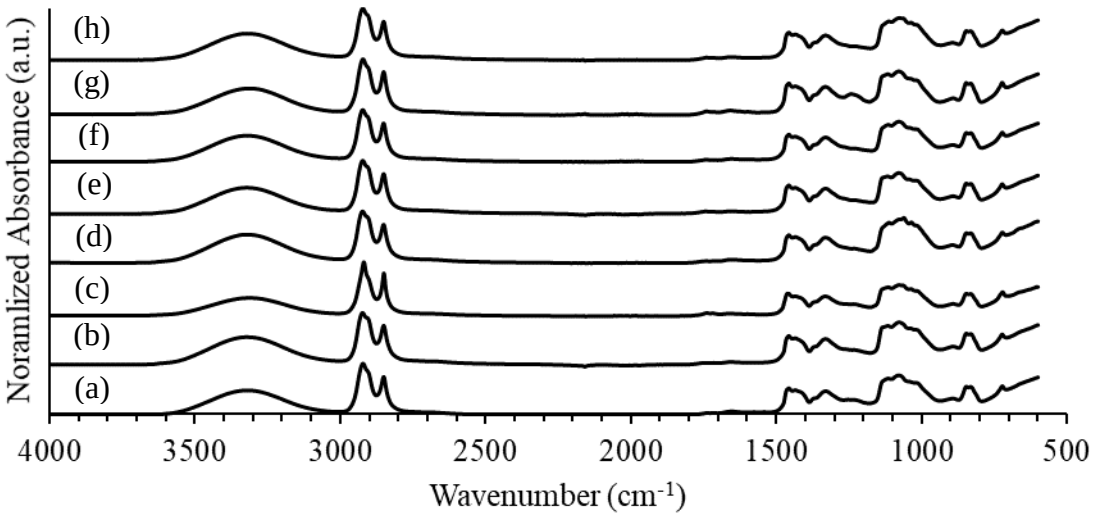

Figure 5.5 - FT-IR spectra of (a-d) solution- processed 0, 1, 2.5, and 5 wt.% CNC/48EVOH, respectively and (e-h) STM- processed 0, 1, 2.5, and 5 wt.% CNC/48EVOH, respectively.

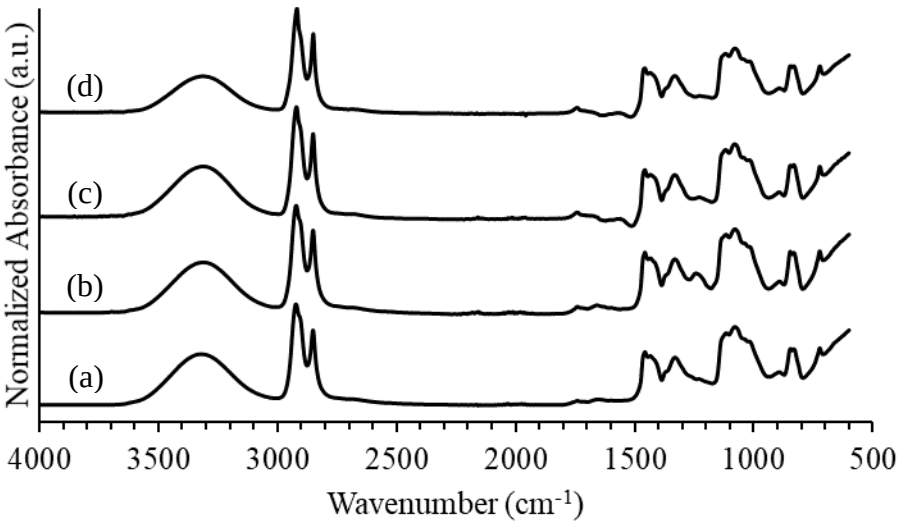

Figure 5.6 - FT-IR spectra of (a) 1 and (b) 2.5 wt.% CNC/48EVOH nanocomposites produced with the STM method and (c) 1 and (d) 2.5 wt.% CNF/48EVOH nanocomposites produced with the STM method.

5.3 Thermal properties

In order to understand how the thermal properties of 48EVOH were affected by CN addition, values of T_m, and X_c from the first heating cycle were analyzed. The first heating cycle values were used since these data would more accurately represent the properties of the samples subjected to testing with TGA, DMA, and microtensile testing. In addition,values of T_c from the first cooling cycle were examined. The average values for T_m, X_c, and T_c are given in Table 5.1. Values of T_g for the as-processed materials were measured primarily by DMA and will be discussed in that section. Considering the materials produced by solution processing, the composites had T_m values that were within

3 °C of the neat polymer. The T_m values for the composites containing lower CNC loadings (1 wt.% and 2.5 wt.%) showed the largest differences with T_m values 2 °C lower and 3 °C higher than the neat 48EVOH, respectively. X_c values for the solution processed composites were similar to the neat polymer. When considering the error in T_c values, it is possible that the CNCs in the 2.5 wt.% CNC/48EVOH and the 5 wt.% CNC/48EVOH composites assisted in nucleation of polymer crystals since their T_c values were slightly higher than the neat EVOH. Overall, these results did not suggest that dramatic changes in polymer crystalline structure occurred for composites produced by solution processing that contained 1-5 wt.% CNCs.

The composites produced by the STM method showed different trends in T_m and X_c. Overall, higher values of T_m and X_c were observed for these composites when compared to the neat 48EVOH produced by the STM method. Instead, all of the composites had slight to moderate increases in crystallinity. The neat polymer also appeared to be affected by STM processing. The value of X_c was lower than that observed for the solution processed neat 48EVOH. As with the samples produced by solution processing, a weak nucleating effect was observed through small increases in T_c. For these samples, the combination of the processing method and CNC addition appeared to affect the crystalline structure of the polymer, though the data did not definitively indicate that the neat polymer and composite samples were affected uniformly by the processing method.

When comparing 48EVOH matrix composites with 1 or 2.5 wt.% CNC or CNF loadings, the values for T_m were overall higher for the composites with CNCs while the composites with CNFs had higher X_c values. The values for T_c were within 1 °C of each

other no matter the nanofiller selected to be incorporated into 48EVOH with the STM method. These results suggested while the nanocomposites with CNFs had higher percent crystallinity, the polymer crystallites were either smaller or made less perfect compared to the nanocomposites with comparable loadings of CNCs. The effects of CNFs and CNCs on other polymer matrices such as PHBV and PEO have also been discussed. Jun *et al*. [209] reported while the T_m values increased in PHBV matrix nanotcomposites with either CNCs or CNFs as the reinforcement phase, the X_c values were overall lower than the neat polymer. These changes in the polymer crystallinity were attributed by the authors to the particle morphology, i.e. the higher aspect ratio CNFs inhibited polymer crystallization more than the shorter rod-like CNCs. Xu *et al*. [210] also suggested the CNF morphology decreased the ability of a PEO matrix composite to crystallize as much as composites with comparable loadings of CNCs as the filler due to confinement effects between CNF particles which hindered polymer crystallization.

Table 5.1 - T_m, X_c, and T_c onset of thermal degradation as a function of CNC or CNF loading in 48EVOH for systems made with the solution and STM methods. Displayed values are averages with standard deviation.

Loading (wt.%)	Method	T_m (°C)	X_c (%)	T_c (°C)
0	**Solution**	151.8 ± 0.2	35.5 ± 1.2	133.4 ± 0.5
1	**Solution**	149.8 ± 1.0	32.8 ± 0.6	135.4 ± 2.5
2.5	**Solution**	154.8 ± 0.3	32.8 ± 4.8	135.7 ± 0.3
5	**Solution**	152.3 ± 0.4	34.8 ± 1.0	135.4 ± 0.7
10	**Solution**	153.1 ± 0.4	34.5 ± 1.9	133.3 ± 4.2
0	**STM**	152.8 ± 0.5	28.8 ± 1.9	135.1 ± 0.8
1	**STM**	156.4 ± 0.9	34.7 ± 2.3	136.1 ± 0.5
2.5	**STM**	154.1 ± 0.3	36.5 ± 3.8	136.6 ± 0.1
5	**STM**	156.0 ± 1.2	32.5 ± 0.9	136.8 ± 1.4
10	**STM**	155.9 ± 0.2	36.9 ± 0.8	136.5 ± 0.2
1 CNF	**STM**	152.6 ± 0.9	40.7 ± 0.8	135.5 ± 0.2
2.5 CNF	**STM**	151.7 ± 0.5	40.0 ± 0.1	135.8 ± 0.2

To provide a comparison between the materials processed by different methods under a more precisely controlled thermal history, the second heating cycle values of T_m and X_c were examined. In this situation, polymer structure produced by the processing, such as any molecular alignment produced by STM or compression molding should be erased. The majority of the samples produced by the two methods showed values of T_m and X_c that were similar to those measured on the first heating cycle. The most striking difference between the first heating cycle data and the second heating cycle data was observed for the neat 48EVOH processed by the STM method. The values obtained during the second heating cycle for this material were similar to those of the solution processed neat 48EVOH, suggesting that structure differences caused by the processing were not permanent. These values are given in Table 5.2.

Table 5.2 - Second- heat T_m and X_c values as measured with DSC for 0, 1, 2.5, 5, and 10 wt.% CNC/48EVOH composites made with the solution and STM methods, as well as 1 and 2.5 wt.% CNF/48EVOH composites made with the STM method.

Loading (wt.%)	Method	T_m (°C)	X_c (%)
0	**Solution**	153.3 ± 0.1	35.0 ± 1.0
1	**Solution**	154.7 ± 1.8	35.6 ± 2.4
2.5	**Solution**	154.3 ± 0.2	35.5 ± 1.3
5	**Solution**	154.1 ± 1.0	35.4 ± 1.0
10	**Solution**	150.5 ± 3.7	25.7 ± 8.5
0	**STM**	154.8 ± 0.8	32.4 ± 1.2
1	**STM**	157.1 ± 0.7	35.4 ± 2.8
2.5	**STM**	155.2 ± 0.0	34.9 ± 0.5
5	**STM**	156.3 ± 1.2	32.7 ± 1.6
10	**STM**	156.3 ± 0.1	38.0 ± 0.8
1 CNF	**STM**	154.8 ± 0.6	36.1 ± 2.4
2.5 CNF	**STM**	154.9 ± 0.1	36.7 ± 0.1

With regard to the thermal degradation pattern, most of the neat polymer and nanocomposite materials exhbited a degradation curve with two mass loss events regardless of processing method implemented. The first mass loss ocurred around 100 °C resulted in a mass loss of 1 or 2 % in all systems. This mass loss was attributed to evaporation of water. The other mass loss event, and the event with the largest mass loss, ocurred between approximately 330 °C and 480 °C. This mass loss event was due to pyroloysis of the polymer and CNCs, and beyond 480 °C only char remained. Some CNC/48EVOH nanocomposites produced with the solution method exhibited a third mass loss event as shown in Figure 5.7. This event ocurred around 245-320 °C for the nanocomposite with 5 wt.% CNC loading and 240-265 °C in the nanocomposite with 10 wt.% CNC loading and was attribued to the degradation of CNCs in the polymer matrix [200, 211, 212]. The range over which this additional mass loss event ocurred was at higher temperatures than what was measured for a neat CNC or CNF film, approximately 234 °C and 287 °C, respectively, and therefore indicated the polymer matrix prevented degradation of CNCs and CNFs until higher temperatures.

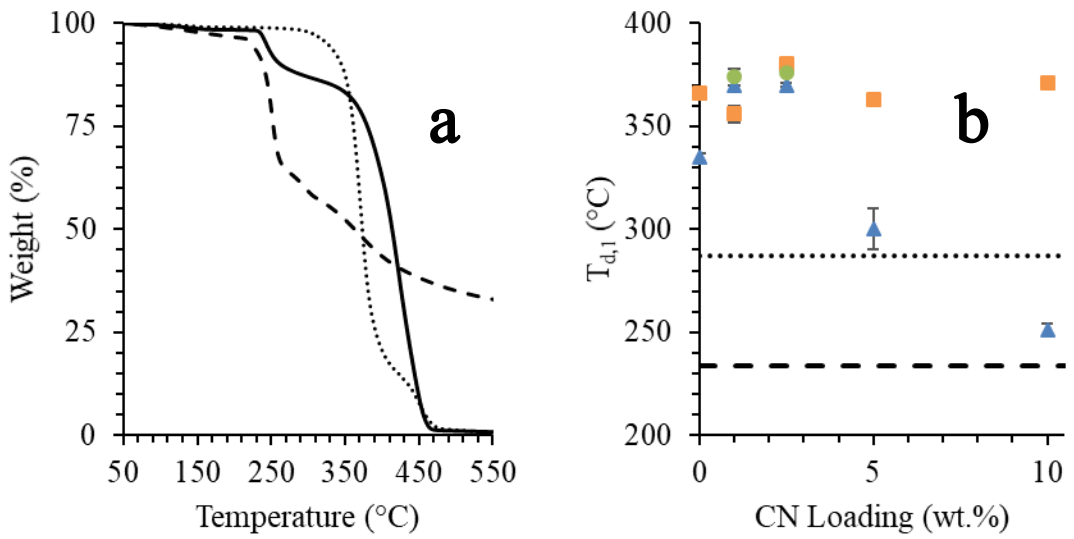

Figure 5.7 - (a) Representative TGA curves for neat CNCs (dashed curved), 48EVOH polymer (dotted curve), and 10 wt.% CNC/48EVOH nancomposite (solid curve) produced by the solution method. (b) Degradation temperature of first mass loss event after accounting for water evaporation for the 48EVOH polymer and nancomposites with CNCs made with the solution (triangles) or STM (squares) method and 48EVOH nanocomposites with CNFs made with the STM method (circles). Degradation temperatures for CNCs (dashed line) and CNFs (dotted line) also reported in (b).

5.4 Mechanical and Thermomechanical properties

DMA was used to investigate the thermomechanical properties below and above T_g of 48EVOH nanocomposites. Figure 5.8 shows E' as a function of temperature for the polymer and nanocomposite systems. Selected values for E' below, at, and above T_g may be found in Table 5.3. For most of the samples, E' values were higher than the

corresponding neat polymers across the temperature range measured. Considering the E' data obtained at 30 °C, the values did not increase monotonically with CNC loading. For samples made with either the solution or STM method, composites with CNCs had higher E' values measured at 30 °C compared to the neat polymers. When comparing the same material processed by different methods, a general trend was not observed, i.e. one processing method did not produce consistently higher values of E'. Instead differences were primarily observed for the neat polymers and the 1 wt.% CNC/48EVOH composite. For these two materials, the STM processing method produced higher values of E'. The value of E' obtained for the other composites did not vary much as a function of processing method, but they did show some changes as the CNC loading changed. In general, the value of E' increased with increasing CNC loading, though the 10 wt.% CNC/48EVOH composite produced by solution processing had a lower E' value than the 2.5 and 5 wt.% CNC/48EVOH composites. Above T_g, the values of E' were similar for materials with the same composition, except the 2.5 wt.% CNC/48EVOH composites.

These results provided more insight into the structure of the materials. For the neat 48EVOH, the degree of crystallinity was lower for the sample produced by the STM method; however, the value of E' for this same material was higher than that for the neat 48EVOH produced by solution processing. Since the values of E' were similar above T_g, structural differences in the amorphous fraction of the material were likely present for the neat 48EVOH samples. This structure would be erased above T_g, but the crystalline structure would remain in place. This result would suggest that the differences observed were also attributable to the amorphous structure, particularly for the neat polymers.

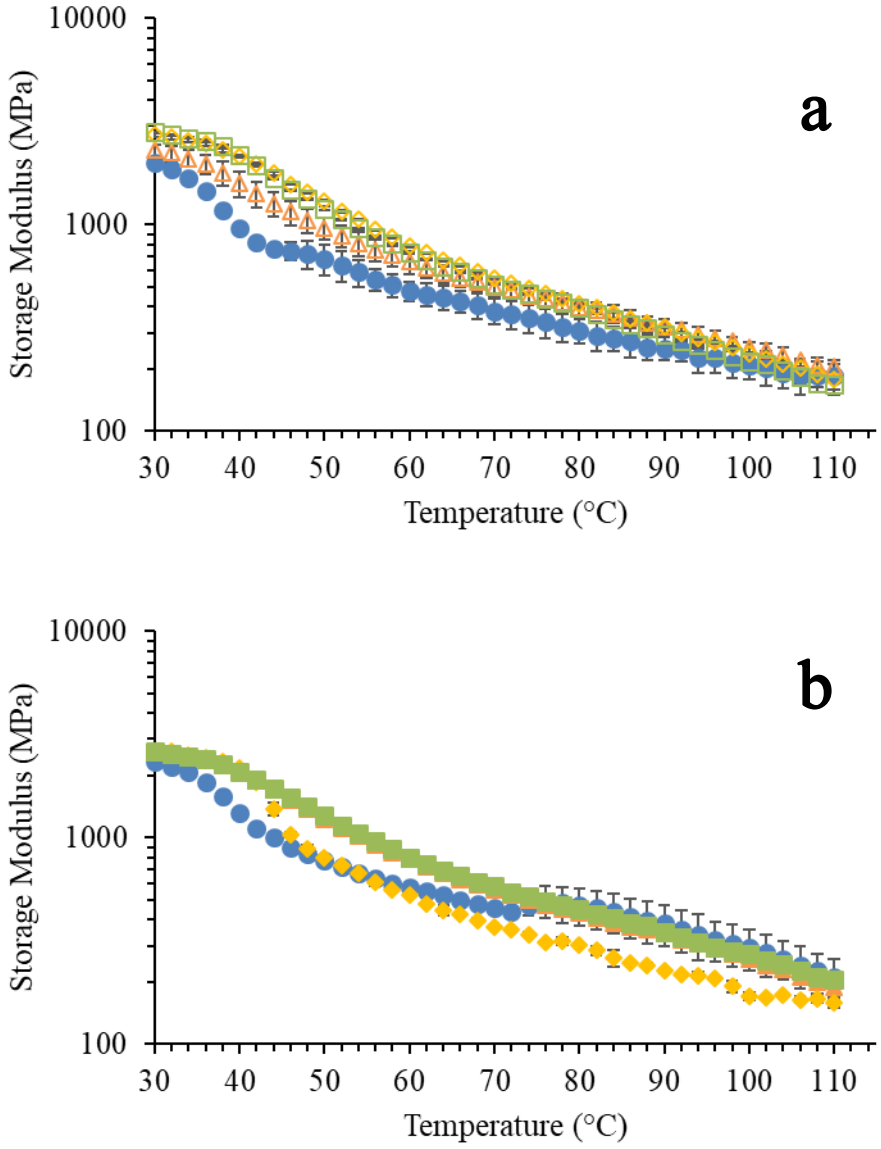

Figure 5.8 - E' as a function of temperature for neat 48EVOH (circles), 1 wt.% CNC/48EVOH (triangles), 2.5 wt.% CNC/48EVOH (diamonds), and 5 wt.% CNC/48EVOH (squares) nanocomposites produced by the solution (a) or STM method (b).

Table 5.3 - Selected storage modulus values for 48EVOH nanocomposites with CNC filler at 30 °C, T_g, and T_g + 20 °C.

Loading (wt.%)	Process	E' at 30 °C (MPa)	E' at T_g (MPa)	E' at T_g + 20 °C (MPa)
48EVOH	**Solution**	2000 ± 109	1130 ± 22	508 ± 70
1 CNC	**Solution**	2300 ± 151	1290 ± 59	587 ± 34
2.5 CNC	**Solution**	2710 ± 44	1380 ± 57	571 ± 25
5 CNC	**Solution**	2790 ± 12	1440 ± 7	585 ± 1
10 CNC	**Solution**	2590 ± 10	1750 ± 140	714 ± 15
48EVOH	**STM**	2340 ± 31	1350 ± 53	575 ± 5
1 CNC	**STM**	2590 ± 75	1420 ± 16	597 ± 11
2.5 CNC	**STM**	2600 ± 37	1310 ± 120	442 ± 11
5 CNC	**STM**	2620 ± 21	1380 ± 78	601 ± 14
10 CNC	**STM**	2680 ± 56	1560 ± 9	711 ± 6
1 CNF	**STM**	2740 ± 162	1470 ± 8	539 ± 27
2.5 CNF	**STM**	2860 ± 71	1480 ± 20	609 ± 14

To understand the component interactions more fully, the E' data at 30 °C were compared to a micromechanical model. Figure 5.9 shows E' at 30 °C of 48EVOH nanocomposites as a function of CNC loading. The particular micromechanical model used was the Takayanagi series-parallel model, also known as Model I, as modified by Loos and Manas-Zloczower [143, 213] to represent a three phase composite system as shown in Equations 5.1-5.3:

$$E_c = \frac{(1-\nu)E_m E_f^{agg} + (\nu+\lambda-1)E_f E_f^{agg}}{(1-\lambda)(1-\nu)E_m + (1-\lambda)(\lambda+\nu-1)E_f + \lambda^2 E_f^{agg}} \tag{5.1}$$

$$1-\lambda = \nu\left(\frac{\nu-\nu_c}{1-\nu_c}\right)^b \tag{5.2}$$

$$\nu_c = \frac{0.7}{\frac{L}{d}} \tag{5.3}$$

where E_c is the modulus of the nanocomposite, E_m is the modulus of the polymer matrix. E' measured at 30 °C was used for the matrix modulus in Equation 2. E_f is the modulus of CNCs that are assumed to be fully dispersed, and was assumed to be 50 GPa [59]. E_f^{agg} is the modulus of aggregated or continuous network of CNCs, 1-λ is the volume fraction of the networking phase, ν is the volume fraction of CNCs in the nanocomposite, ν_c is the critical volume fraction for percolation, and b is the percolation exponent. In this model, λ is equal to one when ν is less than ν_c, otherwise the calculation of λ follows equation 3. CNCs were previously measured with TEM to have an aspect ratio of approximately 21 [112], and therefore ν_c was calculated to be 0.033 or approximately 4.6 wt.%. In the initial

case assuming CNCs formed a three- dimensional network, the percolation exponent was taken to be 0.4. However, the slope of the E' values began to decrease as a function of CNC loading at about 1 wt.% for the systems made with the STM method and between 2.5 and 5 wt.% CNC loadings for the nanocomposites made with the solution method. Therefore, both ν_c and E_f^{agg} were used as fitting parameters (Figure 5.9a). Curves for the Takayanagi Model I were produced using the Solver add-on in Microsoft Excel. Values for fitting parameters were assigned by minimizing the sum of the differences between measured and theoretical E'. In the case of the three-dimensional network, ν_c was calculated to be 0.014 (approximately 2 wt.%) for the systems made with the solution method and 0.0035 (0.5 wt.%) when they were made with the STM method. E_f^{agg} was determined to be approximately 150 MPa for these systems (E_f^{agg} was 141 MPa for the polymer and composites made with the solution method and 151 MPa when they were made with the STM method).

However, there was still a discrepancy between predicted and measured values for E' for the systems made with the STM method, particularly for CNC loadings of 2.5 and 5 wt.%, when the CNCs were assumed to form a three-dimensional network. Therefore, Model I was also calculated assuming that CNCs formed a two-dimensional network for both systems (Figure 5.9b). For the two-dimensional Model I, the percolation exponent was taken to be 0.14 [214]. ν_c for the two- dimensional Model I was determined to be 0.033 (4.6 wt.%) for the systems made with the solution method and 0.007 (1 wt.%) for the systems made with the STM method, and E_f^{agg} was calculated to be approximately 480 MPa for both systems. The values for ν_c were higher when the two-dimensional Model I was used as opposed to the three- dimensional model, as expected [107]. Based on the

minimized error calculated between the experimental values and theoretical values for E', experimental values of the nanocomposites made with the solution method matched well with the three- dimensional Model I and the data for the systems made with the STM method aligned more closely with the two- dimensional model. This suggested CNC network formation occurred both in- plane and out of plane for the nanocomposites produced with the solution method due to hydrogen bonding among the nanoparticles and polymer chains, while network formation occurred in-plane for the nanocomposites made with the STM method and was attributed to CNC alignment during filament drawing of the melt mixing step subsequently followed by compression molding to consolidate the nanocomposite. The overall lower values for ν_c calculated for 48EVOH nanocomposites made with either the solution or STM method suggested the continuous filler phase began to possibly contribute to load bearing in the matrix at lower loadings than estimated by particle morphology alone due to long- range networking between the matrix and CNCs in addition to filler-filler interactions.

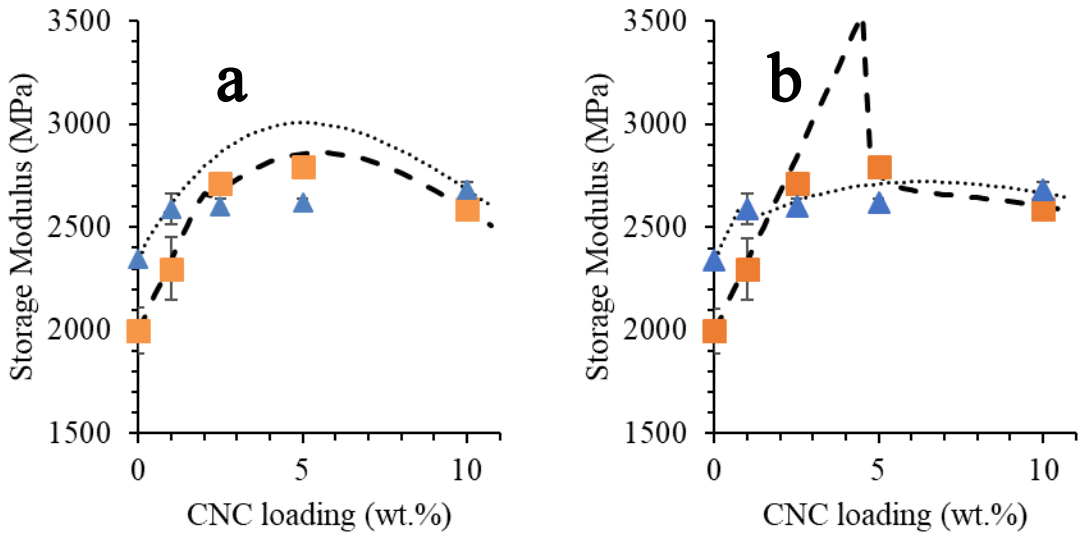

Figure 5.9 - (a) E' measured at 30 °C compared to the Takayanagi Model I assuming a three-dimensional network and (b) E' measured at 30 °C compared to the Model I assuming a two- dimensional network for 48EVOH nanocomposites made with the solution (squares) or STM method (triangles). Lines depicting Takayanagi model for E' of 48EVOH nanocomposites made with the solution (dashed line) or STM method (dotted line) displayed in (a) and (b).

T_g did show changes that were attributable to the processing and the inclusion of CNCs. The peak in E" as measured with DMA was used to monitor T_g as a function of CNC loading (Figure 5.10). Considering the peak temperature values only, an increase in T_g with respect to the corresponding neat polymer sample was observed for all of the composites except the 10 wt.% CNC/48EVOH produced by the solution method. For the solution processed samples, the largest T_g increase was observed for the 2.5 wt.% CNC/48EVOH composite. The value was increased by approximately 10 °C. As the CNC

loading increased beyond this value, T_g decreased. The composites produced by the STM method showed a different trend. A systematic increase or decrease was not observed with changing CNC loading. However, the T_g values of the composites were all higher than the neat polymer made with the STM method.

Beyond the temperature associated with the E" peak maximum, the peak shapes and positions were also examined using normalized data. While the two neat polymers were largely similar, suggesting similar dynamics for these samples, the composites showed different behavior. The E" peaks for some of the solution processed composites and all of the STM processed composites were shifted to higher temperatures while the shape of the peaks were similar to the neat samples. In some nanocomposite materials, the shape of the E" peak has been observed to change with broadening on the high temperature side, low temperature side, or both [112, 215]. A change in the peak shape suggests that interactions between the nanocomposite components are affecting different populations of polymer chains differently, i.e. for high temperature broadening, the component interactions are not affecting the polymer chains with faster dynamics but rather affecting those that are already more highly constrained. In contrast, a translation of the entire peak to higher temperatures suggested that the entire population of polymer chains was affected more uniformly and constrained by the interactions between the polymer and the nanoparticles. Such behavior has been used as an indicator of nanoparticle dispersion where peak translation was associated with more homogeneous nanoparticle dispersion [216]. If that interpretation could be applied to these data, then the STM processing method would be more effective at dispersing the CNCs for the range of nanoparticle loadings used here. Additionally, the peak position was not observed to shift greatly as the CNC loading

increased for the STM composites, and for the highest CNC loading used here, 10 wt.%, the peak was shifted to slightly lower temperatures than the other composites. This trend in T_g values indicated that the amount of interphase in the composite system became saturated at low nanoparticle loadings, suggesting more homogeneous dispersion of the nanoparticles at the lower loadings. The dispersion level could be decreasing at the highest loading since the peak was shifting to lower temperatures. The same general behavior was observed for the solution processed samples, but the peak began to shift back to lower temperatures at 5 and 10 wt.% CNC, suggesting that the dispersion level was decreased at lower loadings than the STM composites. This change could correspond to the arrangement of CNCs as well, as suggested by the results of the micromechanical modeling. These results indicated that the solution processed sample possessed a three- dimensional nanoparticle network, while the STM composites possessed a two- dimensional nanoparticle network. The two- dimensional network would have fewer nanoparticle contacts at a given loading, allowing higher levels of dispersion at loadings beyond the percolation threshold of the three- dimensional network.

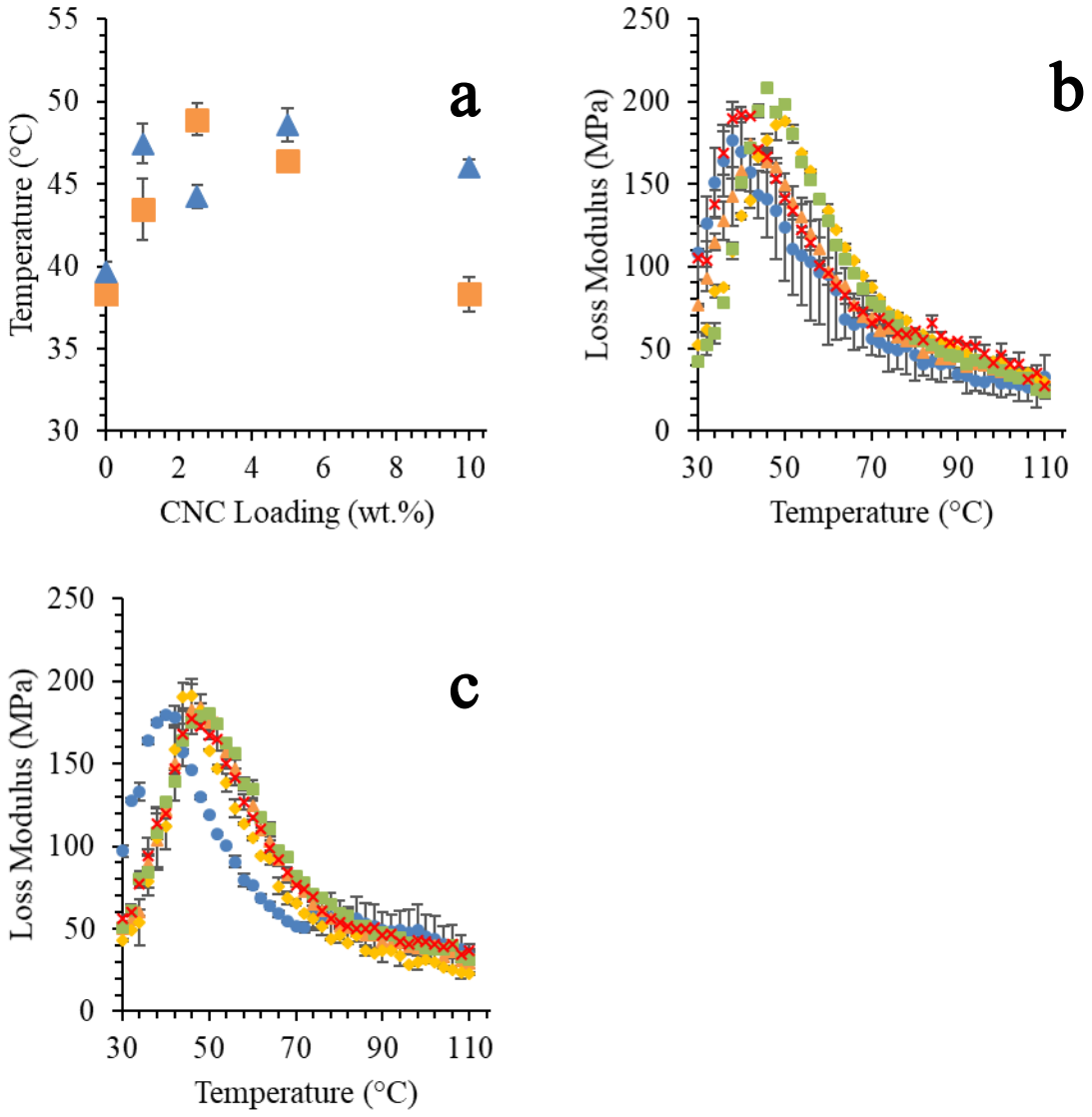

Figure 5.10 - (a) T_g measured as peak in the E" curve for 48EVOH nanocomposites made with the solution (squares) or STM method (triangles). E" as a function of temperature for 0 (circles), 1 (triangles), 2.5 (diamonds), 5 (squares), and 10 wt.% CNC/48EVOH nanocomposites (X's) made with the (b) solution or (c) STM method.

E' as a function of temperature is displayed for 48EVOH nanocomposites with CNFs produced with the STM method in Figure 5.11. The values of E' below T_g were 17 and 22% higher than neat 48EVOH when 1 and 2.5 wt.% CNFs were incorporated into the polymer matrix, respectively. While the CNC and CNF nanocomposites with 1 wt.% loadings had similar values for E' below T_g, the nanocomposite with 2.5 wt.% CNFs had a value for E' that was 10% higher than 48EVOH with 2.5 wt.% CNCs (Table 5.3). The E' values for the 2.5 wt.% CNF/48EVOH composite were also higher than the 2.5 wt.% CNC/48EVOH composite above T_g, but the 1 wt.% CNC/48EVOH composite had higher E' values than the 1 wt.% CNF/48EVOH composite in this temperature range. The higher E' values of the composite with 2.5 wt.% CNFs as opposed to CNCs both below and above T_g were attributed to a combination of higher crystallinity of the polymer matrix of the 2.5 wt.% CNF/48EVOH composite as determined by XRD measurements and increased hydrogen bonding between CNFs and the polymer matrix as observed in FT-IR spectra. However, the trends in E' values were different in the composites with lower CN loadings. The decreased E' values above T_g for the composites with 1 wt.% CNFs versus CNCs is a bit surprising, as it was expected the longer aspect ratio CNFs would be able to more readily develop a stiff network which would result in higher E' values above T_g compared to the neat polymer and the composites with CNCs in addition to contributions made by hydrogen bonding between nanoparticles and the polymer matrix. However, this was explained by the aggregation of the CNFs in the matrix that was observed in Chapter 4. The CNF aggregation observed in the previous chapter meant the apparent aspect ratio of the nanoparticles would be lower and lead to an overall lower reinforcement efficacy in the 48EVOH matrix above T_g.

T_g values as measured by DMA for 1 and 2.5 wt.% CNF-reinforced 48EVOH were approximately 5.1 and 7.1 °C higher than neat 48EVOH. When comparing differences in T_g of nanocomposites with different CN loadings, the results were not as conclusive; while T_g of 1 wt.% CNF/48EVOH was lower than the nanocomposite with similar loadings of CNCs, the 2.5 wt.% CNF nanocomposite had a T_g that was 2.6 °C higher than the nanocomposite with 2.5 wt.% CNCs. The increase in T_g of the composites with CNFs compared to the neat 48EVOH coupled with results from FT-IR suggested hydrogen bonding between the CNFs and polymer matrix hindered polymer chain mobility until higher temperatures.

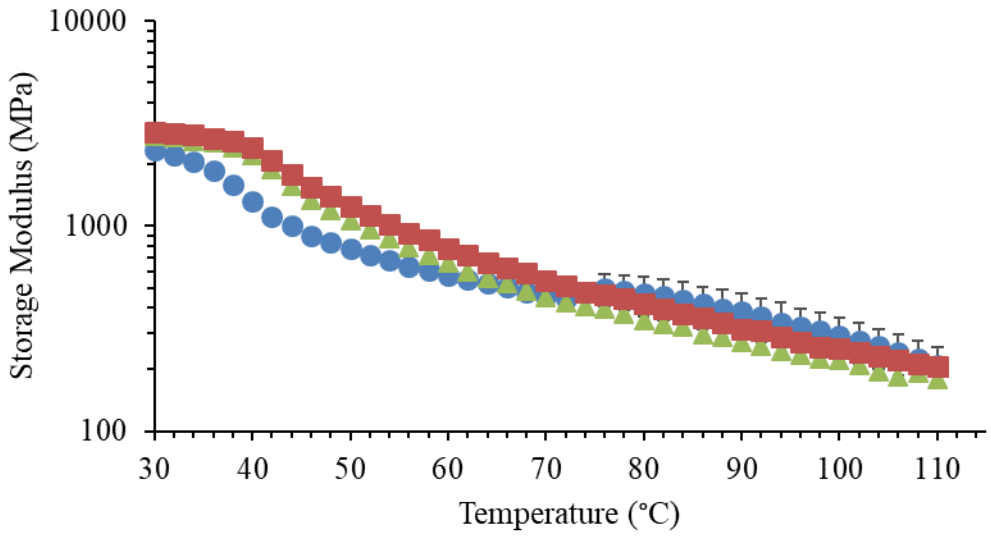

Figure 5.11 - E' as a function of temperature for neat 48EVOH (circles), 1 wt.% CNF/48EVOH (triangles), and 2.5 wt.% CNF/48EVOH (squares) produced with the STM method.

To complement the DMA data, microtensile testing was performed on the neat polymers and the nanocomposites. Figure 5.12 displays the data for yield stress, stress at break, and strain at break for the samples. The 10 wt.% CNC/48EVOH nanocomposites made with the solution method did not have a yield point, since it failed prior to yielding, so no yield stress data were reported for this nanocomposite. Considering the materials processed by the solution method, the nanocomposites had higher values of yield stress than the neat polymer with a maximum value of yield stress occurring at a CNC loading of 2.5 wt.%. Conversely, the yield stress values decreased as a function of CNC loading for nanocomposites made with the STM method. The difference in yield stress trends with processing method were attributed to the behavior of the neat polymer. Similar to the

storage modulus data, the neat polymer processed by the STM method had a higher yield stress than that processed by the solution method, affecting the trends seen for the composites. Even though the trends were different for the two processing methods, the values obtained for the composites with 1 and 5 wt.% CNC were statistically similar for both processing strategies, suggesting that the processing method did not affect the composites' resistance to elastic deformation. Similar trends were observed for the stress at break values. In all cases, the values of yield stress for the composites were statistically different than the values for the corresponding neat polymer.

Unlike the yield stress values, the strain at break values were influenced more strongly by the processing method. Notably, the strain at break values were higher in the composites produced with the STM method as compared to the solution method. These data again suggested that the processing method influenced the polymer structure. The neat polymers had very different strain at break values with the STM processed neat polymer samples showing much lower strain at break values. Additionally, the processing method seemed to have affected the distribution and possibly dispersion of the CNCs since their strain at break values were higher than the corresponding solution processed samples. These trends suggested CNC distribution and/or dispersion in the 48EVOH matrix was more homogeneous as a result of STM processing.

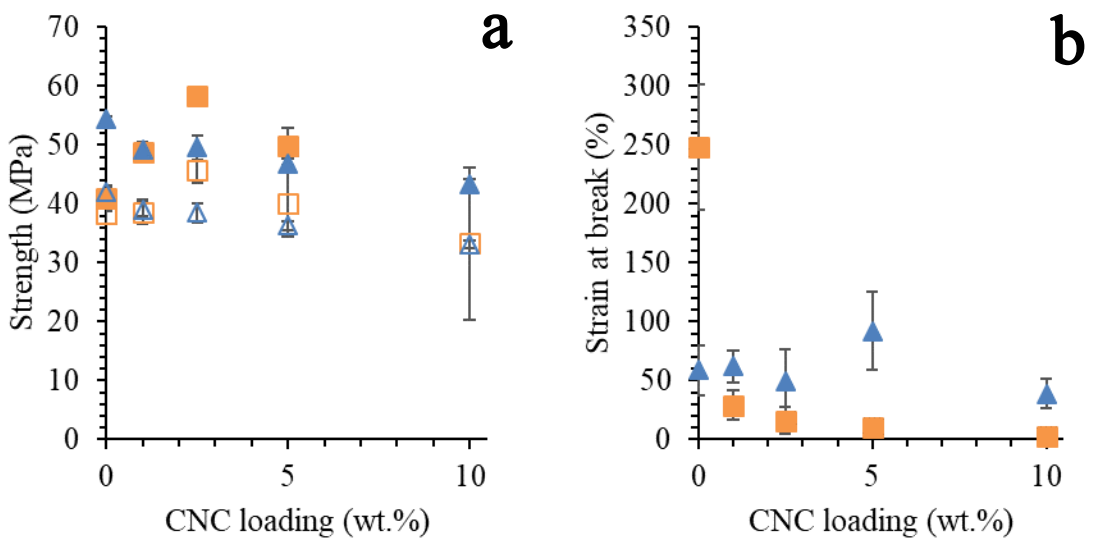

Figure 5.12 - (a) Yield strength (filled) and strength at break (open) and (b) strain at break as a function of CNC content for EVOH matrix nanocomposites made with the solution (squares) or STM (triangles) method.

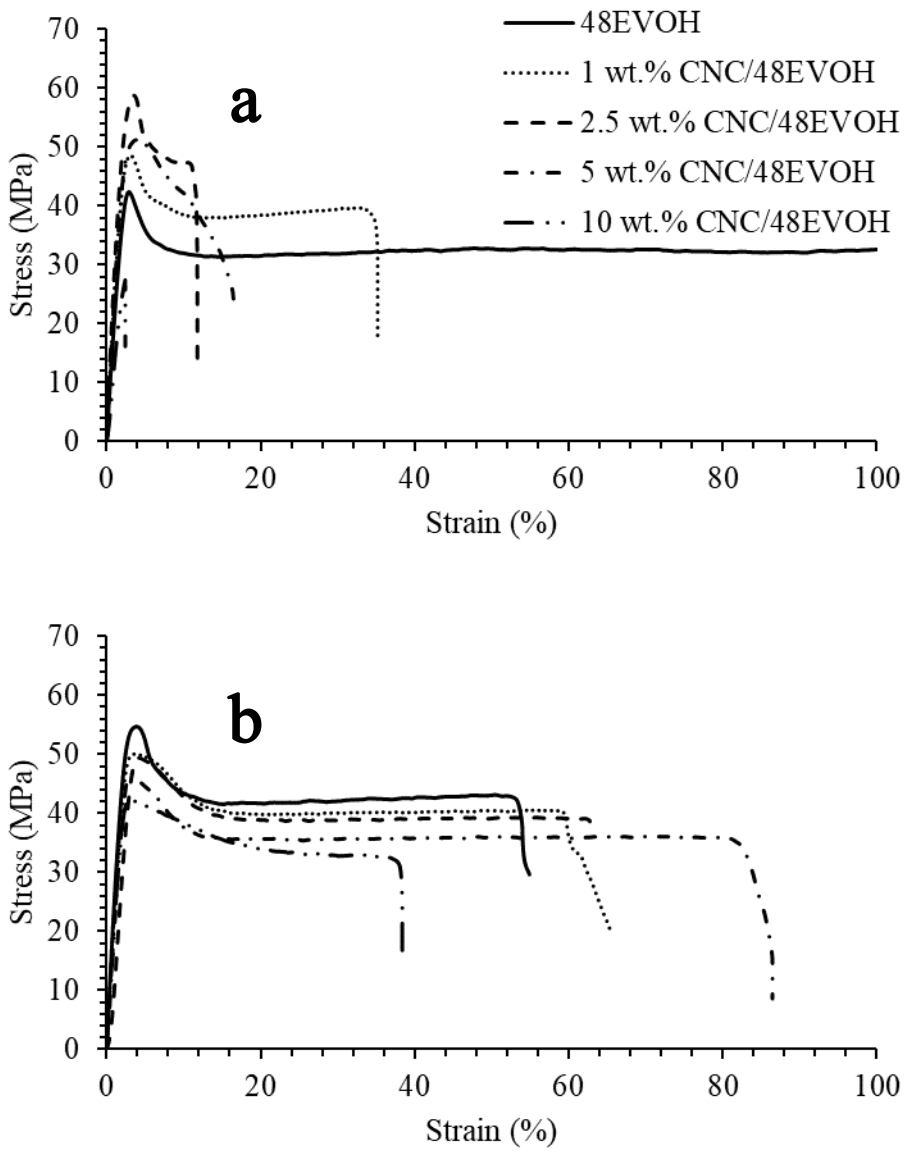

Figure 5.13 - Representative stress vs. strain curves for the 48EVOH polymers and composites made with the (a) solution or (b) STM method. Note: strain axes were formatted for easier comparison between processing methods; neat 48EVOH made with the solution method failed at a strain above 100%.

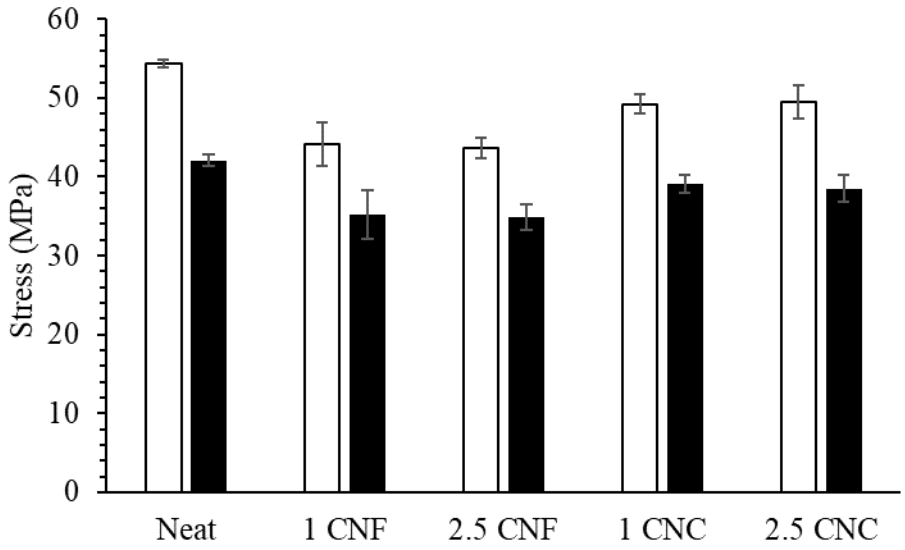

Figure 5.14 - Yield stress (white) and stress at break (black) for 48EVOH with 1 and 2.5 wt.% CNCs or CNFs.

The results of spectroscopy, thermal, and mechanical characterization experiments indicated that the multi-step STM protocol was more effective at producing CNC/EVOH composites with improved performance than the solution processing method. This result was consistent with observations discussed in previous work by the authors [118] when polarized optical microscopy (POM) was used to elucidate changes in CNC dispersion in EVOH. Shifts in the bands associated with hydrogen bonding in the EVOH matrix suggested either the bond lengths or bond stiffness of these groups changed as a result of the addition of CNCs regardless of processing strategy implemented. Higher T_g as measured by DMA when the nanocomposites were made with the STM method as opposed to the solution method suggested the STM strategy may have improved polymer-particle interactions due to increased dispersion and distribution of CNCs in the matrix. Also, the

higher values for $T_{d,1}$ of the nanocomposites compared to neat CNCs particularly at higher loadings suggested the polymer matrix protected the nanofillers from thermally degrading until higher temperatures. The increase in strain at break for nanocomposites made with the STM method versus the solution method suggested a multi-step protocol including a melt-mixing step produced nanocomposites with increased CNC dispersion.

Thermal and thermomechanical characterization provided insight into the ability of CNCs to mechanically reinforce the EVOH matrix. Below T_g, the Takayanagi Model I was used to fit the E' data. The alignment of measured E' values for the systems produced with either processing method with theoretical values along with observed changes to polymer crystallinity from first heat DSC measurements suggested increases in E' were due to the CNCs mechanically reinforcing the polymer matrix and network formation of CNCs. Additionally, the network formation occurred in three dimensions in the solution method due to hydrogen bonding among the moieties during the drying stage followed by compression molding, while the CNC network formed in the EVOH matrix with the STM method was more in-plane due to filament drawing during the melt mixing step followed by compression molding. Additionally, the values observed and calculated for critical network formation suggested the hydrogen bonding capability of the polymer matrix created a long-range network with the CNCs at lower particle loadings than was expected.

5.5 Conclusions

The results presented in this investigation looked at how processing conditions affected the thermal and thermomechanical properties of EVOH matrix nanocomposites. Thermal properties such as X_c of the neat polymer suggested the polymer structure was affected by

the selection of processing strategy, and this resulted in changes to the degradation, thermomechanical, and quasi-static mechanical properties when the polymer was processed using the solution or STM method. While there were slight differences in thermal properties like X_c as measured by DSC when CNCs were introduced to EVOH, there was a significant increase in storage modulus and T_g as a function of CNC loading as measured by DMA. These increases in mechanical properties suggested there was some compatibility between CNCs and the EVOH polymer due to hydrogen bonding between the nanoparticles and vinyl alcohol comonomers and thus increased interactions with CNCs. The increased mechanical properties below T_g as measured by DMA suggested a continuous network of CNCs formed in the EVOH matrix, and the morphology of this network was different based on the processing strategy implemented. Additionally, the value used to calculate the onset of network formation for CNCs in the Takayanagi Model I was significantly lower than the threshold calculated based on geometric considerations of the nanoparticles. This lower threshold for networking suggested CNCs and EVOH physically interacted to form a longer-range network due to hydrogen bonding between particles and polymer chains. Overall, this study provided insight into polymer-particle interactions by tuning the processing conditions and contributes to the body of work relating to processing- property relationships of polymer nanocomposites made with cellulosic nanofiller by identifying a processing pathway to increase dispersion of CNCs in a commercially available semicrystalline thermoplastic matrix.

CHAPTER 6. STRUCTURE AND PROPERTY INVESTIGATION OF ISOTROPIC NANOCOMPOSITES OF 44 MOL.% ETHYLENE CONTENT POLYETHYLENE-CO-VINYL ALCOHOL REINFORCED WITH CELLULOSE NANOMATERIALS

6.1 Introduction

In Chapters 4 and 5, 48EVOH nanocomposites were investigated both qualitatively and quantitatively to determine how processing affected CNC and CNF dispersion and structure, thermal, and mechanical properties of the resultant nanocomposites. CNs as nanofiller in 48EVOH were demonstrated to increase certain thermal, thermomechanical, and mechanical properties of the polymer matrix. The focus of this chapter is to further investigate how the incorporation of CNs can impact the structure as well as thermal, thermomechanical, and mechanical properties of an EVOH matrix with higher vinyl alcohol content. In addition of studying CNCs and CNFs, TEMPO CNFs were investigated as a nanofiller in 44EVOH due to the increased hydrophilicity of the nanoparticles from chemical pretreatment. It is hypothesized that an EVOH matrix with higher vinyl alcohol content will have increased compatibility with any of the three hydrophilic CNs of interest in this chapter. However, while EVOH with higher vinyl alcohol content has been investigated as a polymer matrix to incorporate CNCs previously [74, 75, 79], the degradation temperature of the CNs limits both processing as well as EVOH compositions that can be implemented using melt processing methods such as extrusion in the multi-step

protocol. The thermal properties of 44EVOH suggest CNs can be incorporated into the matrix using extrusion at temperatures that do not risk thermal degradation of the nanofiller [76]. The results from POM in Chapter 4 also suggested 44EVOH interacted with the nanoparticles differently from the 48EVOH matrix. Therefore, 44EVOH was chosen as the matrix of interest in this chapter to increase the breadth of commercially attractive polymer matrices that may be used to incorporate CNs as a reinforcement phase. Investigating polymer-particle compatibility based on polymer selection rather than altering the surface chemistry of the CNs also contributes to the overall understanding of the interaction of CNs with thermoplastic matrices.

6.2 Structure

6.2.1 XRD

To better understand how CNs impacted the structure of the 44EVOH matrix, XRD patterns were collected for the neat CNs, polymer, and nanocomposites made with the STM method. XRD patterns for neat CNCs and CNFs were presented in Chapter 5, and the pattern for neat TEMPO CNFs is displayed in Figure 6.1. As with the other CNs, TEMPO CNFs displayed diffraction peaks that were typical of a cellulose Iβ allomorph. The crystallinity calculated for TEMPO CNFs was approximately 61%, which is less than CNCs but higher than CNFs. The crystallinity value calculated for TEMPO CNFs suggested the chemical pretreatment prior to mechanical fibrillation assisted in the decrease of disordered cellulose regions compared to CNFs, but still had more disordered cellulose content compared to CNCs.

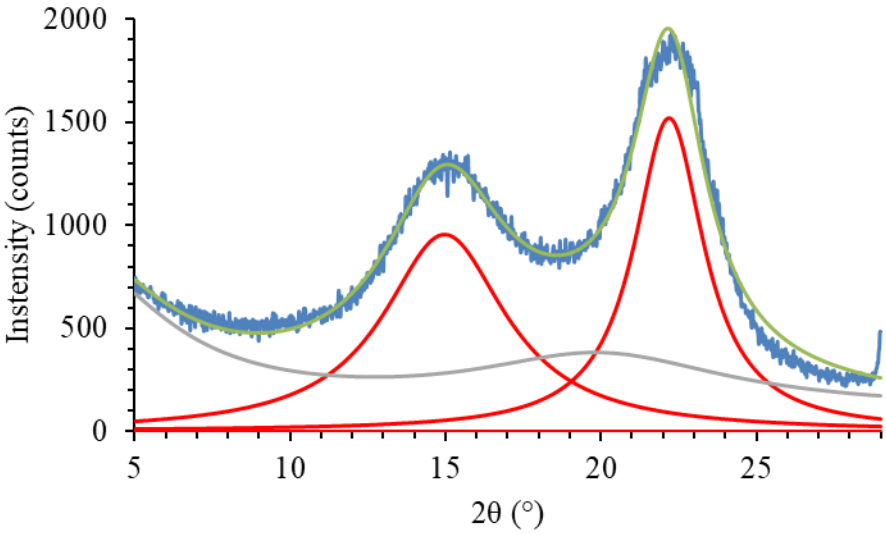

Figure 6.1 - XRD pattern for TEMPO CNFs.

XRD patterns for CNC- and CNF-reinforced 44EVOH nanocomposites are shown in Figure 6.2. Diffraction peaks were observed at approximately 10.7°, 20.4°, and 21.8° in all 44EVOH polymer and nanocomposite systems. These peaks were assigned to (100), (101), and (200) planes of the orthorhombic crystal structure of EVOH [72]. The orthorhombic crystal structure was expected for the neat polymer at this composition of ethylene and vinyl alcohol comonomer units, although there is debate as to whether this structure represents a pseudohexagonal lattice for vinyl alcohol contents between 40-80 mol.% ethylene content [70]. The intensity of the peaks, specifically of the peak at 20.4°, increased with increasing nanoparticle content which correlated to an increase in X_c. X_c and the density of the nanocomposites with CNCs were higher than neat 44EVOH, and the nanocomposites with CNFs had overall higher values for X_c compared to 44EVOH matrix composites with similar loadings of CNCs. However, the density was higher in CNC-

reinforced nanocomposites than CNF- reinforced nanocomposites, and the density of the nanocomposites with CNFs were lower than the neat polymer (Figure 6.4). This suggested while the addition of CNFs led to an overall higher crystalline phase content in the 44EVOH matrix, the crystals were made less perfect compared to the neat polymer and the nanocomposites with CNCs. The opposite was observed for 44EVOH with 1 wt.% TEMPO CNFs: X_c was higher than the neat 44EVOH although still lower than the nanocomposites with CNCs or CNFs, but the crystal density achieved the highest value in the 1 wt.% TEMPO CNF/44EVOH composite compared to the other nanocomposites and neat 44EVOH. Overall, the X_c values of the nanocomposites suggested the polymer crystal sizes increased with the addition of CNs, although the crystal perfection varied depending on which nanofiller was selected. When comparing the CNC- reinforced nanocomposites in the two different EVOH matrices, the values for X_c were higher in the 44EVOH systems, but the density of the crystalline phase was higher in the 2.5 wt.% CNC/48EVOH and 5 wt.% CNC/48EVOH composites. This suggested that although the amount of crystalline phase in the 48EVOH composite systems was smaller compared to 44EVOH, the polymer crystals were made more perfect with the addition of CNs in the EVOH polymer with lower vinyl alcohol content.

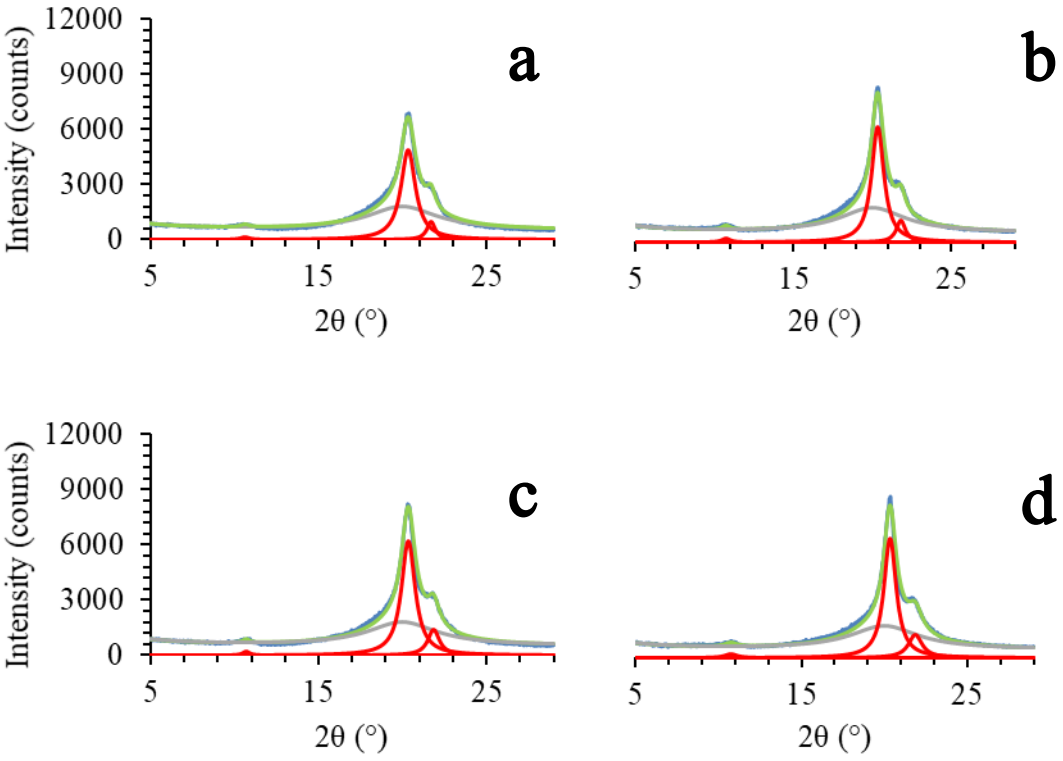

Figure 6.2 - XRD patterns for isotropic (a) 0, (b) 1, (c) 2.5, and (d) 5 wt.% CNC/ 44EVOH nanocomposites produced by the STM method.

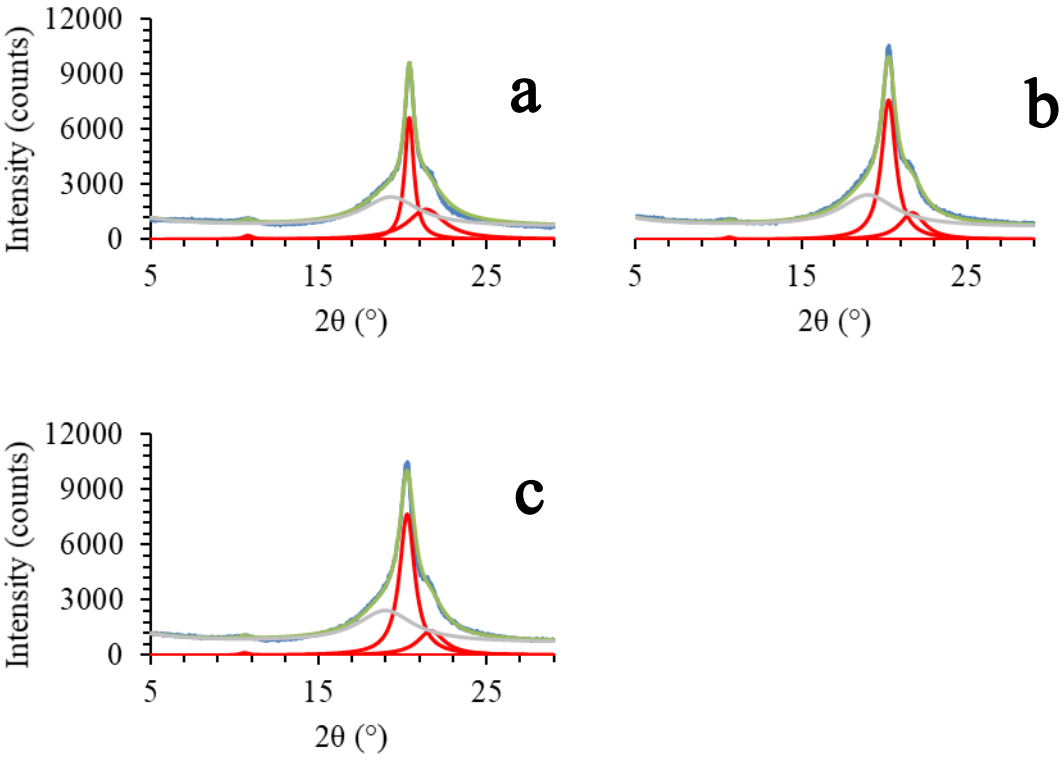

Figure 6.3 - XRD patterns for isotropic (a) 1 wt.% TEMPO CNF/44EVOH, (b) 1 and (c) 2.5 wt.% CNF/44EVOH nanocomposites produced by the STM method.

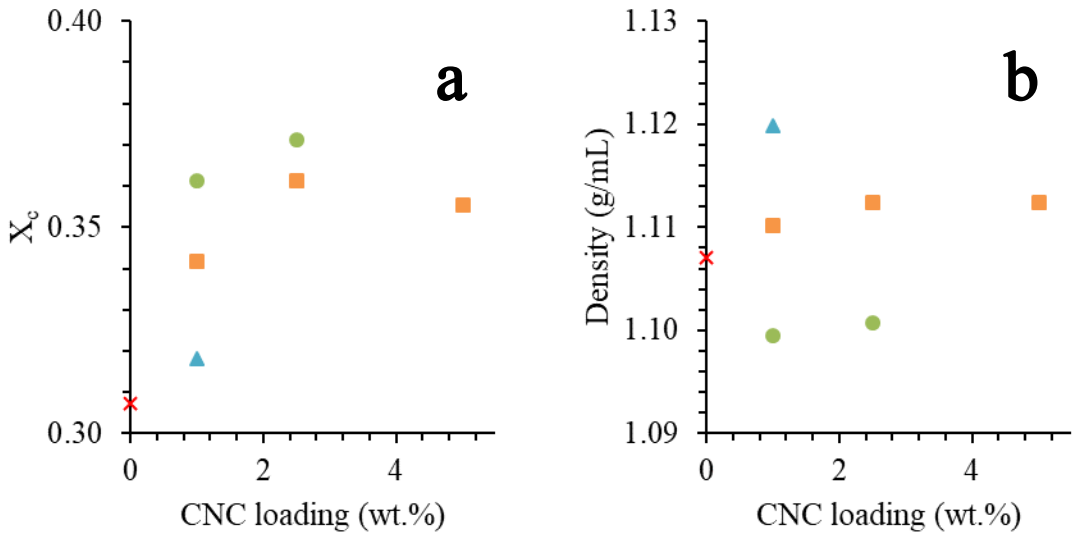

Figure 6.4 - Calculated values for (a) X_c and (b) density of the polymer crystalline phase as a function of CNC (squares), TEMPO CNF (triangle) or CNF (circles) loading produced with the STM method. Values for the neat 44EVOH are denoted with a X symbol.

6.2.2 FT-IR

Figure 6.5 displays the FT-IR spectra for 44EVOH polymers and nanocomposites made with either the solution or STM method. As with 48EVOH nanocomposites discussed in Chapter 5, bands were located at ~3320, 2922, 2850, 1456, 1330, 1135, 1078, and 835 cm^{-1} for each sample which were assigned to -OH bending, -CH asymmetrical and symmetrical stretching, -OH deformation, -OH deformation, EVOH crystallinity, C-O stretching, and EVOH $-CH_2$ vibrations, respectively [207, 208]. When comparing processing protocols to make 44EVOH nanocomposites, the -OH bending band at ~3320 cm^{-1} was observed at similar wavenumbers for a given CNC loading. When compared to

the neat polymer, this band shifted to lower wavenumbers when 2.5 wt.% CNCs were incorporated by either method and was located at higher wavenumbers when 5 wt.% CNCs were incorporated versus neat 44EVOH. The shift to lower wavelengths in the 2.5 wt.% CNC/44EVOH nanocomposite indicated an increase in hydrogen bonding character between the components [217], while the increase in wavelength of the ~3320 cm^{-1} band in the 5 wt.% CNC/44EVOH nanocomposite was due to the increasing contribution of CNCs to the spectra, as the shift was directed toward the ~3334 cm^{-1} peak found in the neat CNC film (Figure 5.4). The increased hydrogen bonding character of some of the nanocomposites compared to the neat polymers along with increased X_c values of the composites compared to the neat 44EVOH as measured with XRD suggested the intermolecular bonding between the CNCs and polymer chains promoted the close packing and/or alignment of polymer chains necessary for polymer crystallization and this crystalline phase accounted for a higher fraction in the composites than the neat polymers. The band at ~1135 cm^{-1} assigned to EVOH crystallinity generally had a higher intensity at a given CNC or CNF loading in the 44EVOH matrix nanocomposites compared to the 48EVOH matrix nanocomposites discussed in Chapter 5, which is corroborated with the X_c values determined from XRD. Also, an additional peak was observed at ~1240 cm^{-1} in the 44EVOH nanocomposite with 2.5 wt.% CNCs prepared with the solution method, and this was assigned to C-O stretching from the CNCs [203]. New bands were observed in the range from ~950-1160 cm^{-1} that were located at bands characteristic of CNCs in the polymer matrix [74].

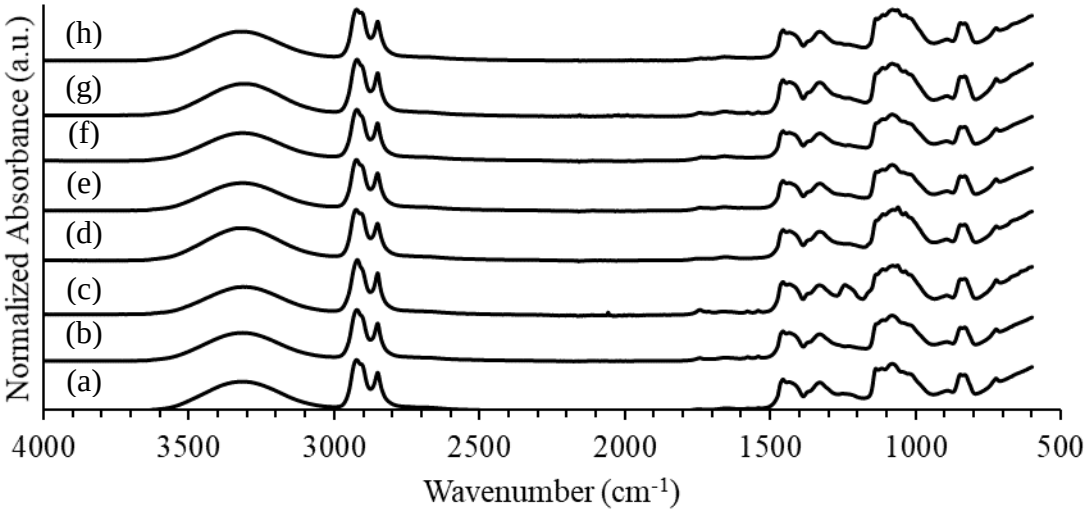

Figure 6.5 - FT-IR spectra of (a-d) solution- processed 0, 1, 2.5, and 5 wt.% CNC/44EVOH, respectively and (e-h) STM- processed 0, 1, 2.5, and 5 wt.% CNC/44EVOH, respectively.

Spectra for 44EVOH reinforced with either TEMPO CNFs or CNFs are displayed in Figure 6.6. Bands that were reported in the previous chapter and discussion of 44EVOH nanocomposites with CNCs were observed in the spectra for 44EVOH nanocomposites reinforced with CNFs or TEMPO CNFs. The band located at ~3320 cm^{-1} shifted to lower wavenumbers for all loadings of either CNFs or TEMPO CNFs regardless of processing strategy employed. The largest shift was approximately 13 cm^{-1} when 2.5 wt.% CNFs were incorporated into a 44EVOH matrix with the STM method, although the intensity of the band decreased compared to neat 44EVOH and the 44EVOH nanocomposite with 1 wt.% CNFs. The wavenumber shift in 44EVOH nanocomposites with TEMPO CNFs was similar for both processing strategies, and the intensity of the band was similar to the neat polymer

for the corresponding processing strategy. The wavenumber location of the -OH deformations for 44EVOH nanocomposites with 1 wt.% CNFs or TEMPO CNFs was lower than the 44EVOH nanocomposites with similar loadings of CNCs, and the intensity of the band was similar in both nanocomposite systems. This indicated more hydrogen bonding occurred when either TEMPO CNFs or CNFs were incorporated into 44EVOH compared to CNCs due to either different anions on the CN surfaces in the case of TEMPO CNFs [4] or the availability of more hydroxyl groups on the particle surfaces in the case of CNFs [196] compared to the acid- hydrolyzed CNCs. Increased hydrogen bonding was expected for the 44EVOH nanocomposites with TEMPO CNFs, as TEMPO pretreatment of the nanofibers has been demonstrated to introduce hydrophilic carboxylate groups on the CNF surfaces [218]. Therefore, a polymer matrix with hydrogen bonding capability, such as 44EVOH with vinyl alcohol comonomers, would be expected to have good compatibility with TEMPO CNFs and create hydrogen bonding between the components. When compared to 48EVOH matrix nanocomposites, the wavenumber values for the -OH stretching band were similar in both matrices investigated for a given particle loading except for the nanocomposites with 2.5 wt.% CNFs which was located at a lower wavenumber in the 44EVOH matrix compared to the 48EVOH matrix nanocomposite. Also, intensity of the band at ~3320 cm^{-1} was higher in 44EVOH nanocomposites at all loadings investigated with either CNFs or TEMPO CNFs which suggested more hydroxyl groups on the CN surfaces were exposed and available for bonding with the 44EVOH due to increased CN dispersion compared to 48EVOH nanocomposites with comparable loadings of CNFs. This increased CN dispersion would be expected in the 44EVOH matrix

as there were more opportunities for hydrogen bonding between the matrix and nanoparticles.

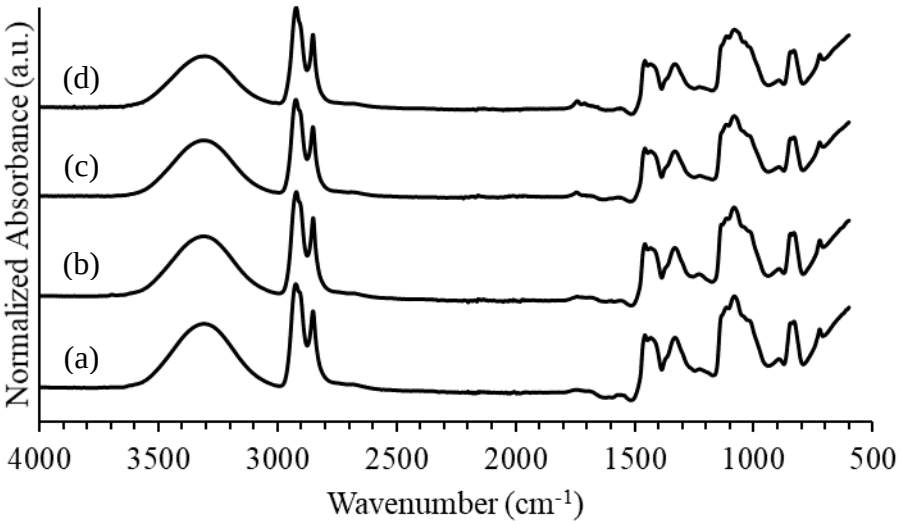

Figure 6.6 - FT-IR spectra for (a) 1 wt.% TEMPO CNFs/44EVOH produced with the solution method, (b) 1 wt.% TEMPO CNFs/44EVOH produced with the STM method and (c) 1 and (d) 2.5 wt.% CNFs/44EVOH produced with the STM method.

6.3 Thermal properties

Thermal properties of the 44EVOH polymer and nanocomposite systems produced with either the solution or STM method are presented in Table 6.1. These properties were measured by DSC and TGA. When the 44EVOH polymer and nanocomposites were produced with the solution method, the nanocomposite with 1 wt.% CNCs displayed the highest value for $T_{m,}$ but otherwise other values for T_m were similar to or lower than the

neat polymer. The higher T_m value for the 44EVOH nanocomposite with 1 wt.% CNCs suggested the nanoparticles assisted with the formation of more perfect polymer crystallites, while the similar or decreased values for T_m in 44EVOH nanocomposites with higher loadings suggested the nanoparticles either did not affect or disrupted the polymer structure when the CNCs were incorporated with the solution method, respectively. However, it was observed in some samples of neat 44EVOH, 1 wt.% CNC/44EVOH, and 5 wt.% CNC/44EVOH produced with the solution method a T_m peak that was located at a lower temperature than reported in Table 6.1. The T_m value for this lower peak was located at approximately 162 °C in the first heating scan for these samples (Figure 6.7), and was not observed in the second-heat scans. One possible explanation for this to have ocurred is that there was a population of polymer crystals with a less thermodynamically stable structure. However, no polycrystallinity was observed from the XRD patterns. Multiple melting peaks have been observed upon heating EVOH polymers with higher vinyl alcohol content than studied in the current work [219, 220], and these were attributed to populations of polymer crystals with different sizes and degrees of perfection. Therefore, the first- heat T_m values observed for neat 44EVOH, 1 wt.%, and 5 wt.% CNC/44EVOH composites suggested there was a wide distribution of crystal sizes in the polymer matrix when they were made with the solution method. Another and more likely reason for observing multiple melting peaks during heating is the melting-recrystallization-remelting of polymer crystallites formed at lower temperatures that can reorganize faster than the heating rate used in the DSC tests. This phenomenon has been reported for other semicrystalline polymers [221-223] when their thermal properties and structure were investigated at faster heating rates with FSC. Additionally, only one melting peak was observed during the

second heating scan for all samples in DSC tests and also at faster heating rates when investigated with FSC (Chapter 7).

The values for T_c were similar for the nanocomposites compared to the neat polymer except for the nanocomposite with 5 wt.% CNCs, which had a T_c value approximately 10 °C lower than the neat polymer system which further indicated the ability of CNCs to disrupt the ability for the polymer to crystallize until lower temperatures compared to the neat polymer. A decrease in T_c of a polyoxyethylene matrix was reported when CNCs derived from tunicates was incorporated at higher loadings than used in this work [224]. The authors attributed this anti-nucleating affect of the CNCs to a combination of increased viscosity of the composites compared to the neat polymer as well as hindered mobility of polymer chains at the CNC surfaces which decreased the diffusion of polymer chains to form polymer crystallites. X_c for the 44EVOH nanocomposites produced by the solution method were lower than the neat polymer, which has also been noted in other semicrystalline matrices with CNCs [196] and was attributed to hinderances in the matrix's ability to crystallize due to more favorable polymer-particle interactions or decreased interparticle distances between CNCs [225]. Based on the results from FT-IR for 1 and 2.5 wt.% CNC/44EVOH, increased hydrogen bonding between the CNCs and EVOH may have also contributed to the disruption of polymer crystallization. Increased hydrogen bonding between nanoparticles and an EVOH matrix have been observed in EVOH matrix nanocomposites with other types of nanofillers [80, 82, 85]. This polymer-particle hydrogen bonding in addition to confinement effects at higher CNC loadings disrupted the hydrogen bonding between polymer chains that contribute to the overall crystallinity in the neat polymer [67].

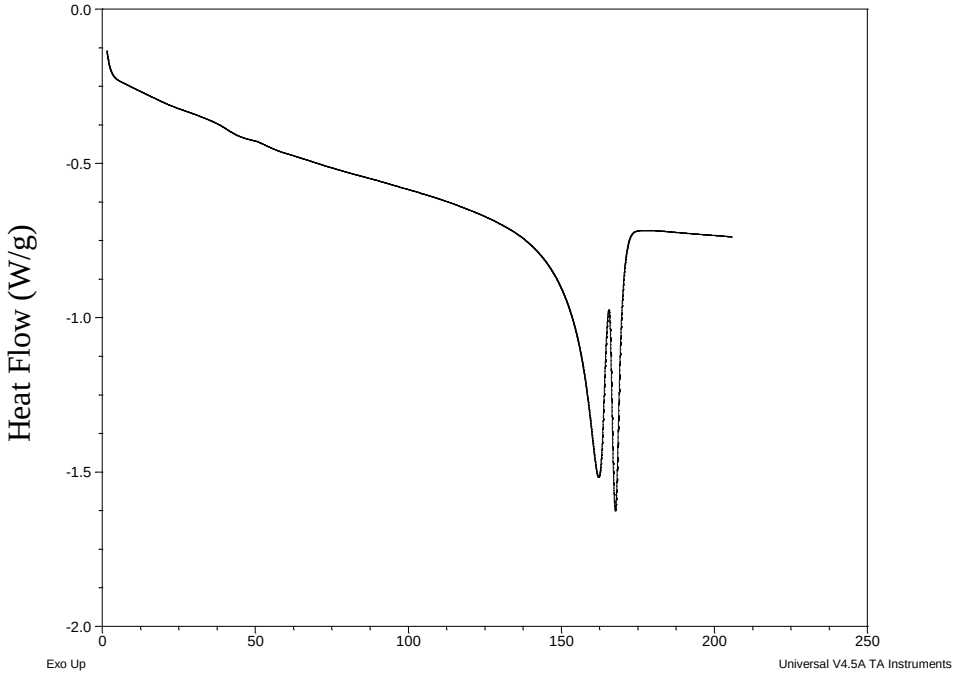

Figure 6.7 - First-heat DSC scan of 1 wt.% CNC/44EVOH composite that displayed two melting peaks.

Values for first-heat T_m and X_c were also lower when 1 wt.% TEMPO CNFs were incorporated into the 44EVOH matrix with the solution method, although T_c remained similar to the neat polymer system. These thermal properties were also lower than the same values for a 44EVOH nanocomposite with 1 wt.% CNCs. However, these changes were modest, as the difference in T_m values between the neat polymer, 1 wt.% CNC/44EVOH, and 1 wt.% TEMPO CNF composite samples were 5 °C maximum and the crystallinity was different by as much as 3.6% among these three samples. These changes in thermal

properties compared to the neat polymer as well as to the nanocomposite with similar loadings of CNCs suggested the polymer crystal structure was either moderately disrupted or unaffected with the addition of TEMPO CNFs due to increased hydrogen bonding between the nanofibers and the polymer matrix.

Values for T_m, X_c, and T_c were within error of one another in the neat polymer samples produced with either the solution or STM method. These similarities in the thermal properties suggested the polymer structure was generally unaffected by the processing conditions implemented. However, values of first-heat T_m for CNC-reinforced 44EVOH nanocomposites produced with the STM method were generally similar to or lower than the same systems produced with the solution method by as much as 3.6 °C when 1 wt.% CNCs were incorporated into the 44EVOH matrix. X_c and T_c values were similar between the two processing strategies investigated except for the value of T_c at 5 wt.% CNC loading which was over 11 °C higher in the system produced with the STM method compared to the solution method. However, this difference in T_c values for the 5 wt.% CNC/44EVOH composites is due to the anomalous decrease in T_c of the composite made with the solution method rather than a significant increase when made with the STM method. This suggestion is also punctuated by the fact the value for T_c of the 5 wt.% CNC/44EVOH nanocomposite produced with the STM method was similar to the T_c value of the neat polymer. Overall, with the exception of the 5 wt.% CNC/44EVOH composite made with the solution method, the T_c values of the composites made with either processing method were higher than the neat polymer by approximately 1 or 2 °C. This result indicated the CNCs in the specified composites had a slight nucleating affect.

When 1 wt.% TEMPO CNFs were incorporated into the 44EVOH matrix with the multi-step protocol, the values of first-heat T_m, X_c, and T_c were either similar or only increased by approximately 1 °C compared to when the TEMPO CNFs were incorporated with the solution method. These values were also either similar to or, in the case of T_c, higher than the neat polymer made with either the solution method or STM method. These similarities in first- heat data when comparing processing protocols along with the differences in X_c and density measured from XRD patterns suggested the choice in processing conditions to incorporate TEMPO CNFs into 44EVOH did not significantly impact resultant thermal properties and therefore the polymer structure. The changes observed in first- heat thermal properties made it difficult to draw any certain conclusions about how different nanoparticles affected the polymer structure when comparing nanocomposites made with CNCs, TEMPO CNFs, or CNFs using the STM method.

Table 6.1 - First- heat T_m, T_c, and X_c for 44EVOH polymer and nanocomposites produced with either the solution or STM method.

Particle Loading (wt.%)	Process	T_m (°C)	X_c (%)	T_c (°C)
0	**Solution**	165.4 ± 1.4	37.1 ± 0.9	144.3 ± 0.1
1	**Solution**	167.7 ± 0.1	34.9 ± 1.6	145.6 ± 0.1
2.5	**Solution**	162.7 ± 0.5	32.5 ± 0.5	145.9 ± 0.2
5	**Solution**	165.5 ± 1.0	35.7 ± 0.3	134.2 ± 3.0
1 TEMPO CNF	**Solution**	162.7 ± 0.2	33.5 ± 0.2	144.6 ± 0.3
0	**STM**	164.0 ± 0.8	34.6 ± 3.1	143.8 ± 0.7
1	**STM**	164.1 ± 0.2	35.6 ± 1.5	145.2 ± 0.1
2.5	**STM**	161.8 ± 0.2	32.3 ± 1.0	145.1 ± 0.3
5	**STM**	163.9 ± 0.1	37.1 ± 1.5	145.6 ± 0.3
1 TEMPO CNF	**STM**	163.7 ± 0.1	34.2 ± 1.6	145.2 ± 0.2
1 CNF	**STM**	164.2 ± 0.4	31.4 ± 1.4	144.5 ± 0.4
2.5 CNF	**STM**	163.7 ± 0.4	37.0 ± 1.8	145.2 ± 0.3

Second- heat data from DSC measurements were expected to provide insight into the polymer and composite structures when the systems were subjected to similar, more controlled thermal histories (Table 6.2). As with the thermal properties measured during the first heating scan, values for T_m and X_c were similar for neat polymers produced with either the solution method or STM method. This suggested the polymer structure of the neat polymers were similar after a precisely controlled thermal history was imparted. When comparing the second- heat data for CNC- reinforced 44EVOH systems produced with the solution method, both X_c and T_m decreased as a function of CNC loading by as much as 13 % and 11 ℃, respectively. These changes along with observations from the first heating scan further suggested the polymer- particle and particle- particle interactions in the matrix disrupted the polymer's ability to either form crystallites or the crystallites that did form were smaller and less perfect than the neat polymer. When 44EVOH nanocomposites were produced by the STM method, X_c and T_m values from the second heating cycle were not observed to decrease systematically as a function of CNC loading. While X_c values measured from both heating scans in DSC of the composites made with the solution method suggested increased polymer- particle and/or decreased interparticle distances that hindered polymer crystallization, the results from the second heating scan of the composites made with the STM method suggested the CNCs did not disrupt the polymer structure found in the neat sample. The nanocomposites with 1 wt.% TEMPO CNFs had similar thermal properties to one another when produced with either the solution or STM method which suggested the polymer structure of these composites was similar when produced with either processing method. When compared to neat 44EVOH, the second-heat thermal properties of the nanocomposites with 1 wt.% TEMPO CNFs were similar

regardless of processing strategy implemented. However, X_c decreased when nanocomposites with 1 wt.% TEMPO CNFs were compared to nanocomposites with 1 wt.% CNCs irrespective of processing strategy used. These observations in thermal properties suggested there were increased polymer-particle interactions when TEMPO CNFs were incorporated as opposed to CNCs. Results from FT-IR characterization suggested these increased interactions were due to increased hydrogen bonding between TEMPO CNFs and the polymer matrix versus CNCs which disrupted the abiltiy of the polymer to crystallize. Values for T_m and X_c were similar in value when compared to the neat polymer and other nanocomposites made with the STM method.

Table 6.2 - Second- heat T_m and X_c for 0, 1, 2.5, and 5 wt.% CNC/44EVOH composites, 1 wt.% TEMPO CNF/44EVOH composite, and 1 and 2.5 wt.% CNF/44EVOH composites.

Particle Loading (wt.%)	**Process**	**T_m (°C)**	**X_c (%)**
44EVOH	**Solution**	165.2 ± 0.1	38.5 ± 0.9
1 CNC	**Solution**	164.8 ± 0.1	38.7 ± 0.6
2.5 CNC	**Solution**	164.1 ± 0.0	36.0 ± 0.2
5 CNC	**Solution**	153.9 ± 2.6	25.7 ± 3.3
1 TEMPO CNF	**Solution**	164.8 ± 0.1	34.3 ± 1.0
44EVOH	**STM**	165.2 ± 0.3	35.9 ± 3.6
1 CNC	**STM**	164.9 ± 0.1	37.4 ± 0.7
2.5 CNC	**STM**	163.1 ± 0.2	35.4 ± 0.8
5 CNC	**STM**	164.2 ± 0.1	38.1 ± 0.1
1 TEMPO CNF	**STM**	164.9 ± 0.1	34.3 ± 0.5
1 CNF	**STM**	164.7 ± 0.4	35.6 ± 0.8
2.5 CNF	**STM**	164.6 ± 0.1	36.0 ± 1.6

As with the 48EVOH polymer and composite systems discussed in the previous chapter, 44EVOH polymer and composite systems exhibited at least two mass loss events associated with water loss and pyrolysis of the polymer and nanoparticles. Values of $T_{d,1}$ of the 1 wt.% CNC/44EVOH nanocomposites were higher than the neat polymer regardless of processing strategy implemented, with the highest value of approximately 36 °C higher than the neat polymer when 1 wt.% CNCs were incorporated via the solution method. In addition to the two mass loss events already described, the 2.5 wt.% CNC/44EVOH nanocomposite produced with the solution method and the 5 wt.% CNC/44EVOH nanocomposite produced with either the solution or STM methods exhibited another mass loss event in the range of 240-320 °C that appeared in a similar fashion to 48EVOH nanocomposites displayed in Figure 5.7. The additional mass loss event ocurred at lower temperatures than the neat polymer (Figure 6.8a) and was attributed to the main degradation of the CNCs in the polymer [79, 211]. However, the new mass loss event in these nanocomposite systems ocurred at a higher degradation temperature than neat CNs and this suggested the polymer was thermally protecting CNs from degradation until higher temperatures. Additionally, the degradation temperature for 44EVOH polymer and nanocomposites made with the STM method were overall higher than the systems made with the solution method and this suggested the polymer structure was different when made with the multi-step protocol versus the solution method which made the polymer less susceptible to thermal degradation. It has been suggested acetate residues exist in the EVOH polymer from incomplete hydrolysis of polyethylene acetate used to synthesize EVOH [66, 226], which have a lower degradation temperature than EVOH [227], although FT-IR bands for these chemical moities were not observed in the spectra collected for the

44EVOH composites. There is, however, evidence of the neat 44EVOH degrading when processed with the STM method and this was indicated by an increase in the intensity of the peak located at ~1740 cm^{-1} (Figure 6.8c). Lagaron *et al*. [228] attributed the increase in the intensity of this band to the formation of degradation products of the polymer such as double bond formation along the polymer chains. The authors along with Artzi *et al*. [84] also proposed oxidative cross-linking took place during melt mixing of their EVOH samples. Therefore, the most likely reason for higher $T_{d,1}$ values observed in the neat polymer processed with the STM method would be degradation of the polymer by way of an apparent molecular weight increase of EVOH chains due to cross-linking. The remaining polymer chains after melt mixing would then require higher temperatures to degrade versus the original structure from solution casting. An increase in the intensity band at ~1740 cm^{-1} was also observed for the 1 wt.% CNC/44EVOH composite made with the STM method compared to the composite produced with the solution method. Otherwise, the intensity of the band for the 2.5 wt.% CNC/44EVOH composites was higher when made with the solution method, and the intensity of the band for 5 wt.% CNC/44EVOH composites were similar. Therefore, the increased $T_{d,1}$ values for the CNC/44EVOH composites when they were made with the STM method versus the solution method could be due to increased CNC dispersion when the composites were made with the STM method. Increased dispersion would mean more CNCs would be surrounded by polymer matrix and thus more nanoparticles would be thermally protected from degradation until higher temperatures.

$T_{d,1}$ values for nanocomposites with 1 wt.% TEMPO CNFs were overall lower than 44EVOH nanocomposites with either 1 wt.% CNFs or 1 wt.% CNCs, although the values

for the systems with TEMPO CNFs were similar among the processing strategies investigated **(**Figure 6.8b). While nanocomposites with CNFs had higher values for $T_{d,1}$ compared to TEMPO CNFs, the values were similar for a given filler loading when compared to nanocomposites with CNCs made with the STM method. Carboxylate groups on the surfaces of TEMPO CNFs as a result of the TEMPO chemical pretreatment step have been demonstrated to decrease the onset degradation temperature compared to native cellulose [218]. While the measured $T_{d,1}$ values for a TEMPO CNF film and CNC film were similar in this work, others [229] have observed a lower degradation temperature for CNs produced with a TEMPO pretreatment compared to sulfuric acid hydrolysis. Additionally, while TEMPO CNF dispersion was reported to increase in 44EVOH when the composite was made with the STM method as opposed to the solution method from the results of POM images in Chapter 4, there were still aggregates observed in both composite films. These aggregates have less surface area for a given loading compared to CNCs with increased dispersion. This coupled with a similar or lower degradation temperature compared to untreated CNFs and acid-hydrolyzed CNCs resulted in overall lower $T_{d,1}$ values for the 1 wt.% TEMPO CNF/44EVOH composites.

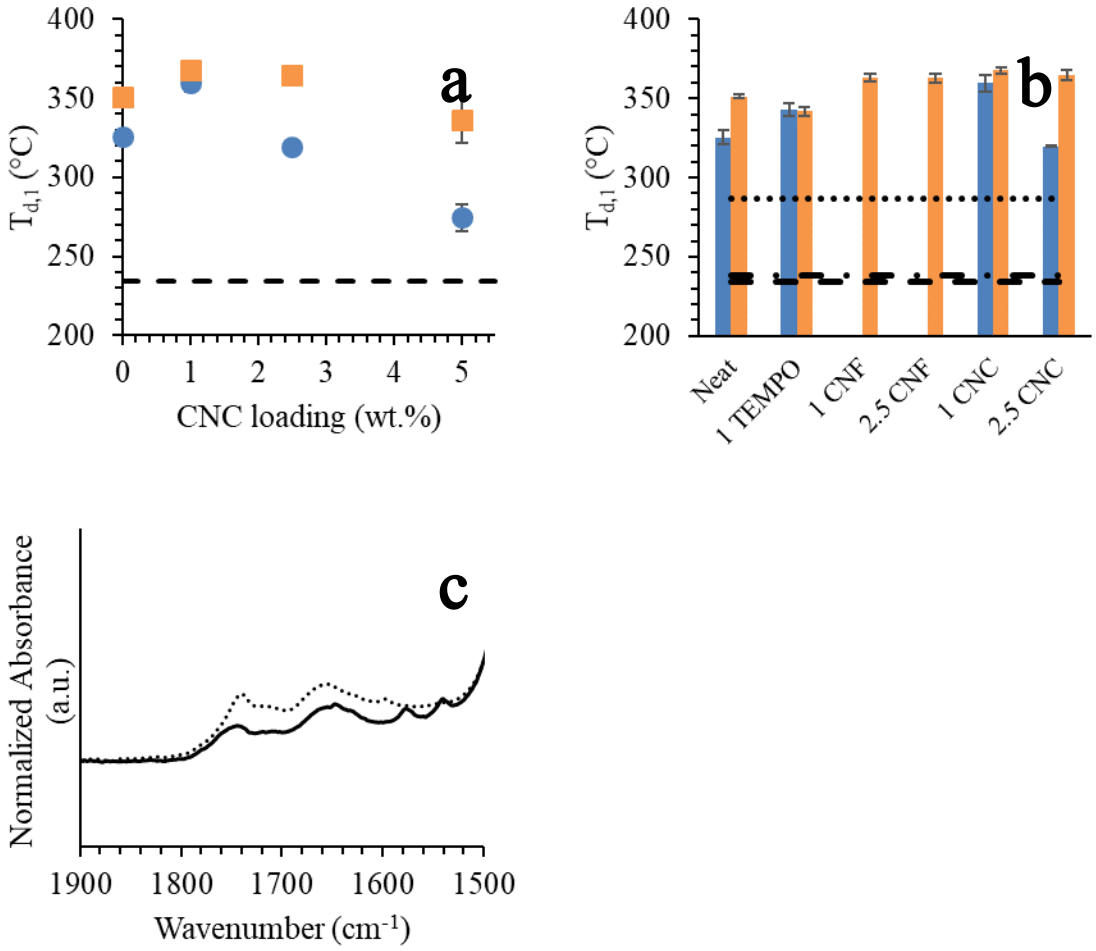

Figure 6.8 - (a) $T_{d,1}$ values of 44EVOH polymers and nanocomposites with CNCs incorporated with the solution (circles) or STM (squares) method. (b) $T_{d,1}$ values of 44EVOH nanocomposites developed with the solution (blue) or STM (orange) method. Degradation temperatures for CNCs (dashed line), TEMPO CNFs (dot-dash), and CNFs (dotted) presented as well. (c) FT-IR spectra for neat 44EVOH processed with the (solid line) solution method or (dotted line) STM method displaying the bands associated with degradation products of 44EVOH.

6.4 Mechanical properties

Figure 6.10 displays the E' below T_g as measured by DMA for 44EVOH nanocomposites as a function of CNC loading. As can be seen in Figure 6.10a and Figure 6.9, values of E' below T_g for 44EVOH matrix nanocomposites produced by the solution method were higher than the neat 44EVOH polymer across all CNC loadings with a maximum increase of 26 % when 2.5 wt.% CNCs were incorporated into 44EVOH. E' values were observed to increase with CNC loading up to 2.5 wt.% CNC loading before decreasing when 5 wt.% CNCs were incorporated with the solution method. Additionally, E' values above T_g for 44EVOH nanocomposites were higher than the neat 44EVOH polymer made by the solution method (Figure 6.9). The largest increase in E' above T_g for 44EVOH nanocomposites produced by the solution method was 38 % when 5 wt.% CNCs were incorporated into 44EVOH.

When the 44EVOH matrix nanocomposites were made with the STM method, E' values were higher for the composites compared to the neat polymer across all CNC loadings investigated. While E' values below T_g for 44EVOH matrix nanocomposites produced by the STM method were lower than values of 44EVOH nanocomposites produced by the solution method up to 2.5 wt.% CNC loading, the 5 wt.% CNC/44EVOH nanocomposite had a higher E' value below T_g when it was made with the STM method versus the solution method. This suggested at the highest CNC loadings investigated in the 44EVOH matrix, the multi-step protocol increased the ability of the CNCs to reinforce the polymer matrix compared to the solution method. Values for E' above T_g were similar or higher for 44EVOH matrix nanocomposites than neat 44EVOH when produced by the

STM method, and the largest increase was 46 % when 1 wt.% CNCs were incorporated into 44EVOH via the STM method (Table 6.3). With the exception of 1 wt.% CNC/44EVOH produced by the STM method, values for E' above T_g for composites made with the STM method were either similar to or less than E' values for 44EVOH matrix nanocomposites produced via the solution method. The E' values of 1 wt.% CNC/44EVOH nanocomposite, and to a lesser extent the 5 wt.% CNC/44EVOH nanocomposite, were observed to increase with temperature above approximately 96 °C. This behavior has been observed in other polymers [230, 231], and was attributed to cold crystallization, or crystallization of the polymer during heating rather than cooling. However, this was not observed in DSC measurements, where a cold crystallization would result in an exothermic peak during the first heating scan. This difference in behavior observed for cold crystallization between DSC and DMA studies was attributed to the faster heating rate employed during DSC testing which would make it more difficult to detect a cold crystallization peak before melting occurred. The crystallinity and crystal phase density of the polymer were observed to increase with the addition of CNCs to the matrix using the STM method, which suggested the polymer crystal structure was made more perfect or larger with the incorporation of the nanoparticles. Overall, E' values of 44EVOH nanocomposites were higher than 48EVOH nanocomposites with similar CNC loading and processing strategy implemented due to higher vinyl alcohol comonomer content and therefore more hydrogen bonding capability in the neat 44EVOH compared to neat 48EVOH.

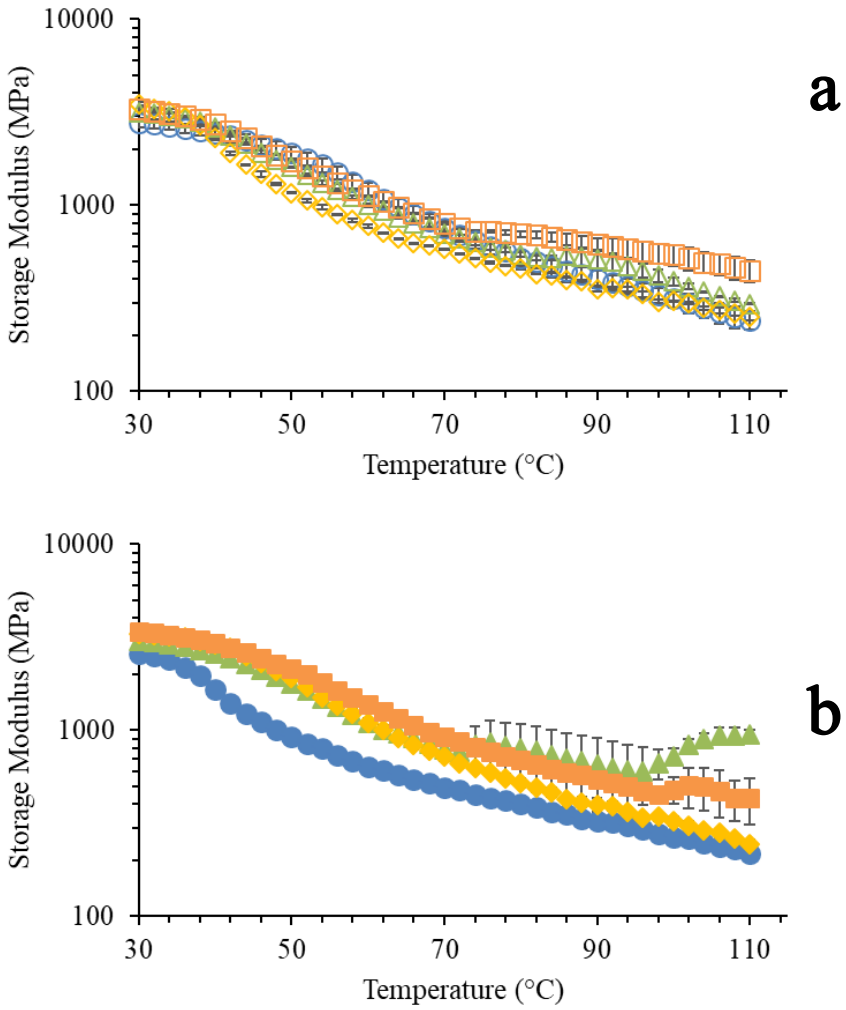

Figure 6.9 - E' as a function of temperature for neat 44EVOH (circles), 1 wt.% CNC/44EVOH (triangles), 2.5 wt.% CNC/44EVOH (diamonds), and 5 wt.% CNC/44EVOH (squares) nanocomposites produced by the solution (a) and STM (b) methods.

Table 6.3 - Selected E' values below T_g, near T_g, and above T_g for 0, 1, 2.5, and 5 wt.% CNC/44EVOH composites, 1 wt.% TEMPO CNF/44EVOH composites, and 1 and 2.5 wt.% CNF/44EVOH composites.

Loading (wt.%)	**Process**	**E' at 30 °C (MPa)**	**E' at T_g (MPa)**	**E' at T_g + 20 °C (MPa)**
44EVOH	**Solution**	2780 ± 160	1450 ± 130	595 ± 54
1 CNC	**Solution**	3160 ± 60	1810 ± 4	768 ± 8
2.5 CNC	**Solution**	3500 ± 85	2020 ± 26	736 ± 6
5 CNC	**Solution**	3300 ± 37	1760 ± 160	817 ± 50
1 TEMPO CNF	**Solution**	2690 ± 100	1300 ± 71	539 ± 18
44EVOH	**STM**	2590 ± 18	1460 ± 50	616 ± 8
1 CNC	**STM**	3020 ± 42	1480 ± 133	900 ± 211
2.5 CNC	**STM**	3290 ± 100	1660 ± 87	676 ± 54
5 CNC	**STM**	3400 ± 22	1900 ± 29	828 ± 34
1 TEMPO CNF	**STM**	3310 ± 317	1780 ± 150	912 ± 206
1 CNF	**STM**	3200 ± 26	1350 ± 5	572 ± 21
2.5 CNF	**STM**	3160 ± 45	1720 ± 81	691 ± 28

As in Chapter 5, Takayanagi Model I was used assuming both two- and three-dimensional CNC network formation to more fully understand component interactions in the 44EVOH matrix (Figure 6.10) [107, 143, 214]. For both networks, the value for ν_c using the equation derived by Favier *et al*. [142] was much higher than the apparent CNC loading when the change in the behavior in mechanical reinforcement occurred as noted by a changed in the slope of the experimental data with respect to CNC loading. The theoretical value of ν_c for CNCs with an aspect ratio of 21 [112] is approximately 4.6 wt.%. When calculated using the Solver add-on in Excel to minimize the combined overall differences between the theoretical and experimental E' values, the value of ν_c assuming a three- dimensional CNC network was 2 wt.% for 44EVOH nanocomposites produced with either processing method. While the combined sum of differences was minimized at 2 wt.% for the systems made with either the solution or STM method, the minimum difference specifically occurred at 2.5 wt.% for 44EVOH polymer and composites made with the solution method and 2 wt.% when they were made with the STM method. The values for $E_{f,}^{agg}$ were calculated as 126 MPa and 187 MPa for CNCs incorporated into the 44EVOH polymer using either the solution or STM method, respectively. For the model assuming a two- dimensional CNC network, ν_c was determined to be approximately 2.5 wt.% for both processing strategies and the values for E_f^{agg} were calculated as 818 MPa and approximately 47.2 GPa for the 44EVOH nanocomposites made with the solution or STM method, respectively. The value of E_f^{agg} for the 44EVOH nanocomposites made with the STM method did not affect the overall difference between experimental and theoretical values for modulus when the value was varied between 7 GPa and 47 GPa. These values for E_f^{agg} assuming a two- dimensional CNC network formed, specifically for the modulus

values of 818 MPa or 7 GPa, are in line or higher than the Young's modulus value reported for a neat CNC film derived from hardwood [232] which took into account hydrogen bonding between aggregated CNCs rather than individual particle stiffness. The differences between the theoretical and experimental values for E' did not definitively suggest the CNC network morphology was either two- or three-dimensional. For example, the sum of differences for a given processing strategy was the same when the network morphology was assumed to be either two- or three- dimensional and ν_c was taken to be 2.5 wt.% for 44EVOH systems. Whereas there were ν_c values for the 48EVOH composites that had distinct minimum values that were previously discussed in Chapter 5. Therefore the network morphology for 44EVOH composites made with either processing strategy was assumed to form in three dimensions based on the depiction of CNC network morphology in other polymer matrices [28, 95, 106, 142, 143]. While the modulus values for the aggregated particle phase for the three- dimensional CNC network were lower than the anticipated modulus, the results suggested the morphology of the CNC network was formed in three dimensions and was stiffer when the 44EVOH nanocomposites were produced with the STM method as opposed to the solution method. However, these values compared to a neat CNC film suggested the hydrogen bonding was weaker in the composite films. Additionally, the value for $E_{f,}^{agg}$ for a given network morphology was higher for 44EVOH nanocomposites versus 48EVOH nanocomposites produced with the STM method which suggested the additional vinyl alcohol comonomer units promoted the creation of a stiffer particle network due to stronger long range interactions, i.e. hydrogen bonding, between the matrix and CNCs.

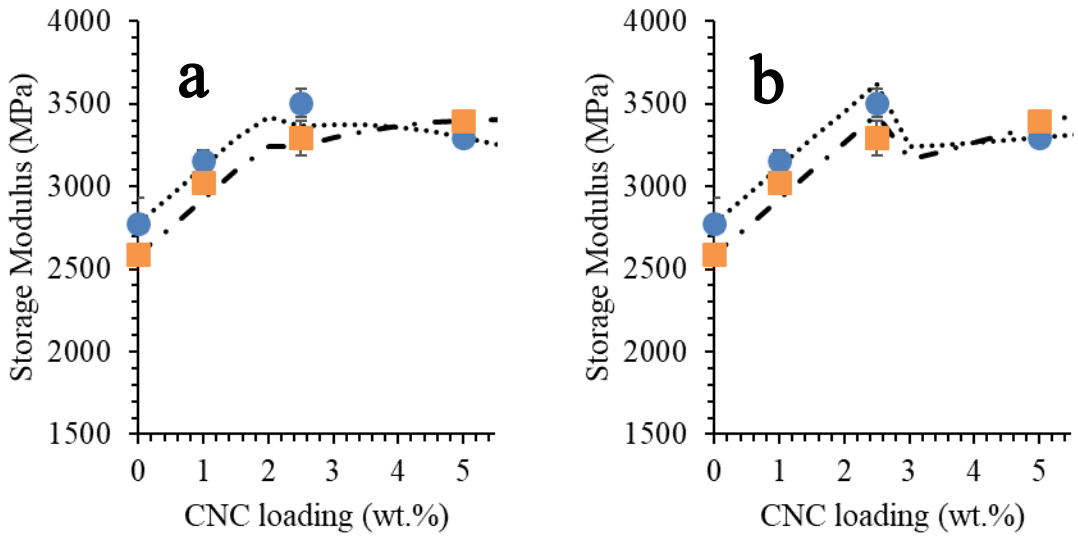

Figure 6.10 - E' at 30 °C for 44EVOH nanocomposites as a function of CNC loading when produced with the solution (circles) or STM (squares) method. The Takayanagi Model I fits were calculated for nanocomposites made with the solution (dotted line) or STM (dot and dashed line) method assuming the CNCs formed either a (a) three- dimensional or (b) two- dimensional network in the polymer matrix.

T_g was higher in the 44EVOH nanocomposites produced with the STM method compared to the neat polymer (Figure 6.11a). When compared to the neat 44EVOH polymer, the largest increase in T_g was 12.4 °C when 1 wt.% CNCs were incorporated in 44EVOH via the STM method. Increases in T_g of 44EVOH matrix nanocomposites were also higher when the nanocomposites were produced with the STM method as opposed to

the solution method, except for the neat polymer systems in which the neat polymer produced with the solution method had a higher T_g compared to the neat polymer made with the STM method. The difference in T_g of the neat polymers coupled with results measured by DSC suggested amorphous polymer phase was less mobile when it was processed with the solution method versus the STM method. However, the thermal properties such as T_m and X_c measured by DSC indicated the structures of the neat polymers made with the different processing methods were similar, and the T_g reported by others for a non-annealed 44EVOH polymer measured by DMA is similar to the neat polymer made with the STM method [219, 233]. The largest difference in T_g when comparing processing methods used to make 44EVOH matrix nanocomposites was 11.2 °C in 44EVOH with 2.5 wt.% CNCs produced with the STM method versus the solution method. The E" peaks were also observed to translate to higher temperatures when CNCs were incorporated into the 44EVOH matrix with the STM method, and the shapes of the E" curves were similar compared to the neat polymer made with the STM method. This suggested the CNCs affected the amorphous fraction of the polymer by immobilizing polymer chains until higher temperatures.

As can be seen in Figure 6.11b, while the peak in the E" curve used to define T_g was located at a higher temperature for the neat polymer than the nanocomposites when made with the solution method, the nanocomposites with 1 and 5 wt.% CNCs had overall higher E" values at temperatures above approximately 80 °C compared to the neat polymer. This indicated that the mobility of polymer chains that are already highly constrained was hindered further when CNCs were incorporated into the polymer matrix using the solution method. Whereas the entire E" peak for the nanocomposites made with the STM method

were observed to translate to higher temperatures compared to the neat polymer made with the STM method (Figure 6.11c). This suggested all polymer chains were hindered from mobilizing until higher temperatures with the incorporation of CNCs and also suggested increased particle dispersion when the nanocomposites were made with the STM method as opposed to the solution method [216].

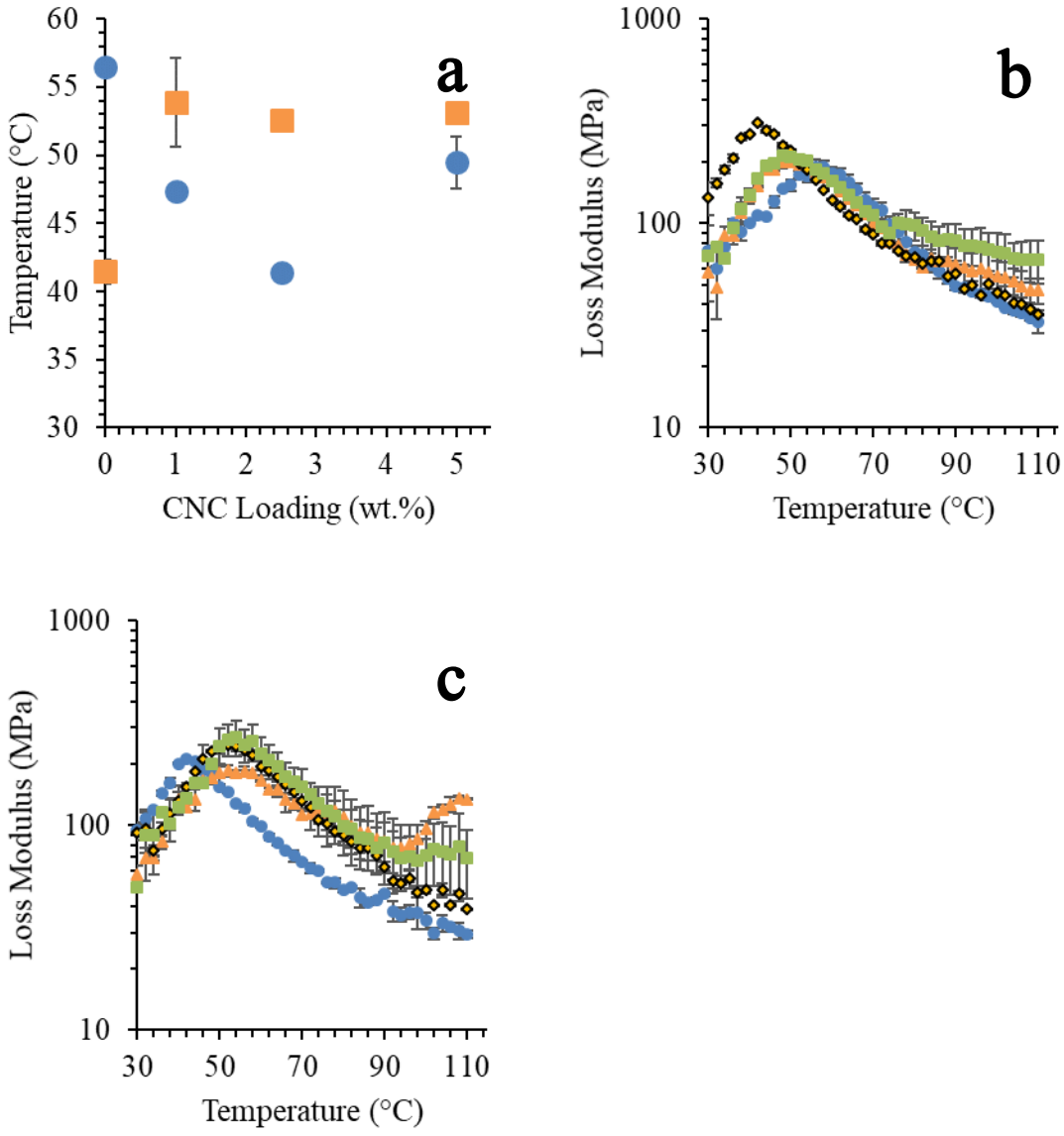

Figure 6.11 - (a) T_g of the 0, 1, 2.5, and 5 wt.% CNC/44EVOH nanocomposites made with the solution (circles) or STM method (squares). E" as a function of temperature for 0 (circles), 1 (triangles), 2.5 (diamonds), and 5 (squares) wt.% CNC/44EVOH nanocomposites made with the (b) solution or (c) STM method.

Figure 6.12 displays E' as a function of temperature when either TEMPO CNFs or CNFs were incorporated into the 44EVOH matrix. E' below T_g was lower than the neat polymer when 1 wt.% TEMPO CNFs were incorporated with the solution method, but 28% higher than the neat polymer when incorporated into the matrix with the STM method (Figure 6.13a). Additionally, the values of E' for 1 wt.% TEMPO CNF/44EVOH were more than double the values of E' for the neat polymer above T_g when the polymer and nanocomposite were made with the STM method. The increased E' values across all temperatures when 1 wt.% TEMPO CNFs were incorporated into the 44EVOH matrix with the STM method suggested the multi-step protocol promoted the mechanical reinforcement and development of a stiff network of TEMPO CNFs in the polymer matrix. The increased E' values above T_g when the TEMPO CNFs were incorporated with the STM method suggested the additional melt mixing step increased particle dispersion and distribution in the polymer matrix which would result in an increased apparent aspect ratio of the TEMPO CNFs, leading to higher E' values compared to the analogous composite made with the solution method. E' was observed to increase by 24% below T_g and 26% above T_g for 44EVOH when 1 and 2.5 wt.% CNFs were incorporated into the matrix with the STM method, but the values of E' were similar in both nanocomposites across all temperatures. The E' values below T_g were similar for nanocomposites with either TEMPO CNFs or CNFs incorporated with the STM method. The significant differences in reinforcement become clear above T_g, when E' of the nanocomposite with 1 wt.% TEMPO CNFs was 89% higher than the 44EVOH matrix with 1 wt.% CNFs. Assuming the morphology of the nanoparticles were approximately the same, the increased E' values suggested the differences in surface chemistries as a result of the chemical pretreatment step used to make

the TEMPO CNFs promoted the dispersion of the nanoparticles in the polymer matrix and formation of a stiffer network than the mechanically processed CNFs.

When comparing nanocomposites made with all three of the CNs investigated at 1 wt.% loadings (Table 6.3), E' values below T_g were similar to one another. Above T_g, the values of E' were highest in the nanocomposites with TEMPO CNFs or CNCs and lowest in the nanocomposite with CNFs. The differences in E' above T_g for the different nanomaterials suggested TEMPO CNFs, with more hydrophilic surface chemistry than CNFs, and CNCs with higher mechanical properties than CNFs were able to create a stiffer network and increase mechanical reinforcement of the amorphous polymer phase more than CNFs in the 44EVOH matrix using the STM method.

In addition to the differences in E' as a function of temperature noted when either TEMPO CNFs or CNFs were incorporated into 44EVOH, T_g was also observed to increase in the nanocomposites compared to the neat polymer made with the STM method (Figure 6.13b). The highest T_g occurred when 1 wt.% TEMPO CNFs were incorporated into 44EVOH with the STM method, which was 16 °C higher than the neat polymer. While T_g was higher in nanocomposites with CNFs compared to the neat polymer, these values were either similar or lower than nanocomposites produced with comparable loadings of CNCs with the STM method. The ability of the TEMPO CNFs and CNFs to increase T_g of 44EVOH suggested the nanofibrils hindered polymer chain mobility until higher temperatures due to increased compatibility between the moieties. The compatibility between the TEMPO CNFs or CNFs and 44EVOH matrix was substantiated by increased hydrogen bonding character observed in FT-IR spectra.

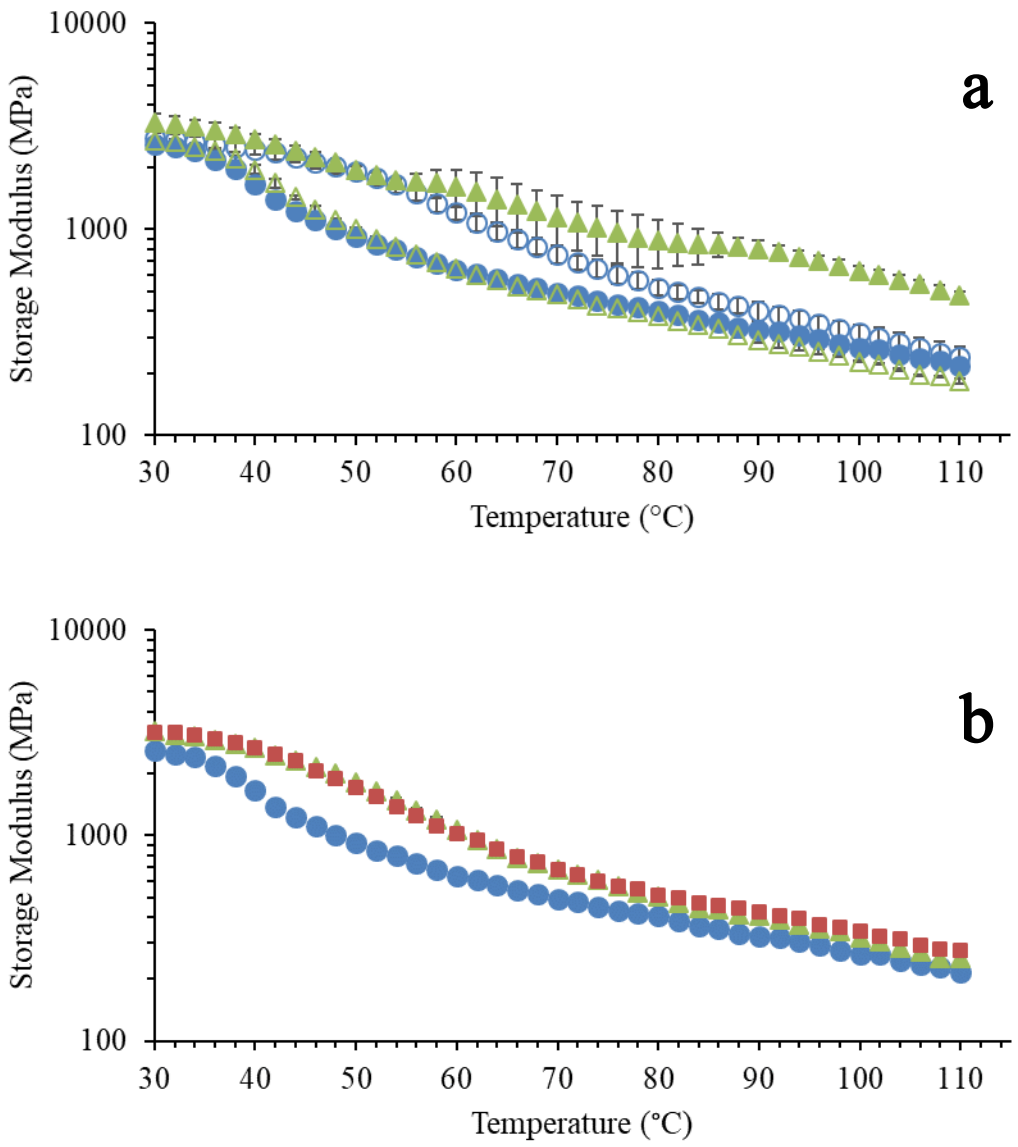

Figure 6.12 - (a) E' as a function of temperature for neat 44EVOH (circles) and 1 wt.% TEMPO CNF/44EVOH (triangles) nanocomposites produced with either the solution (open shapes) or STM (filled) method. (b) E' as a function of temperature for neat 44EVOH (circles), 1 wt.% CNF/44EVOH (triangles), and 2.5 wt.% CNF/44EVOH (squares) systems produced with the STM method.

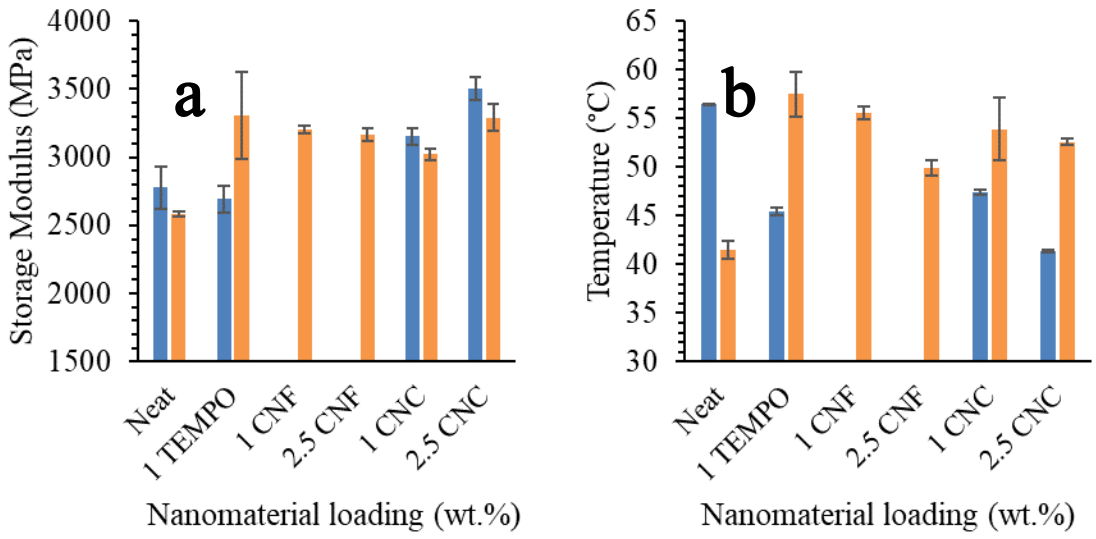

Figure 6.13 - (a) E' at 30 °C and (b) T_g for neat 44EVOH, 1 wt.% TEMPO CNF/44EVOH, 1 and 2.5 wt.% CNF/44EVOH, and 1 and 2.5 wt.% CNC/44EVOH made with either the solution (blue) or STM (orange) method.

With the exception of 2.5 wt.% CNC loadings, the 44EVOH polymer and nanocomposite systems made with the STM method had statistically significant higher yield strength compared to the corresponding systems made with the solution method, with the largest increase of approximately 21% when 5 wt.% CNCs were incorporated into the polymer matrix (Figure 6.14a). The nanocomposite with 5 wt.% CNCs was also the only system made with the STM method that had a statistically significant different yield strength than the neat polymer which was almost 6% higher than the neat polymer. This suggested the 44EVOH polymer and nanocomposite systems made with the multi-step protocol were able to resist elastic deformation more than when they were made with the solution method and the differences in yield strength values were attributed to the neat

polymer. Stress at break values were similar between the two processing strategies employed, although the nanocomposite with 2.5 wt.% CNCs made with the STM method had a 13% higher strength stress at break compared to the neat polymer. The strain at break value was also higher for the 2.5 wt.% CNC/44EVOH composite made with the STM method in addition to the 5 wt.% CNC/44EVOH composite made with the STM method (Figure 6.14b). These increases in strain at break for the composites with higher CNC loadings suggested increased CNC dispersion when the composites with higher CNC loadings were made with the multi-step protocol as opposed to the solution method. Overall, yield stress and stress at break values for 44EVOH polymer and nanocomposites were higher than 48EVOH polymer and nanocomposites for a given composition and processing method. The differences in strength values for 44EVOH systems compared to 48EVOH systems suggested the polymer with higher vinyl alcohol content was able to resist both elastic and plastic deformation more due to more and stronger hydrogen bonding capability.

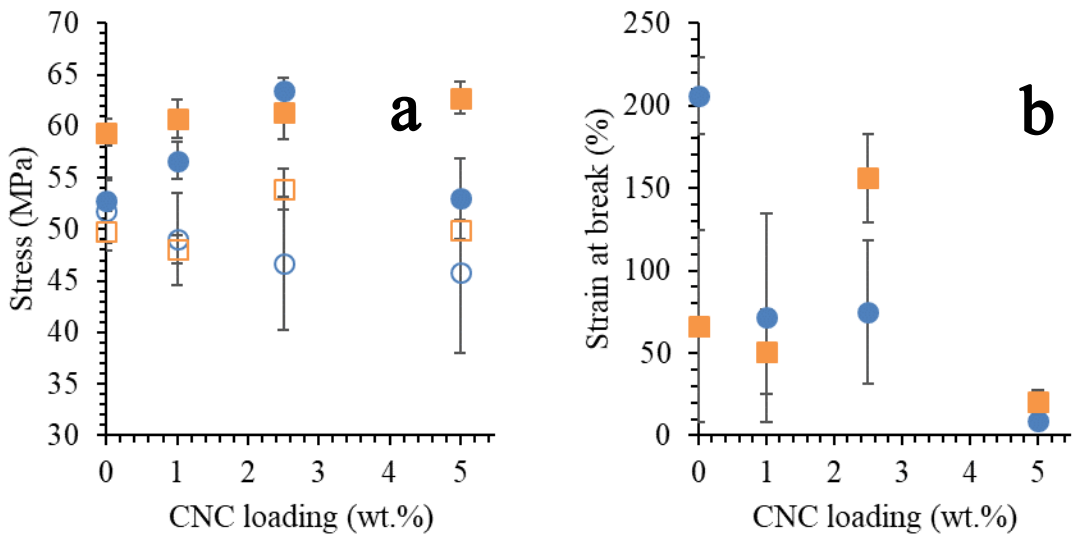

Figure 6.14 - (a) Stress values measured at the point of yield (closed symbols) and break (open) for 44EVOH polymers and nanocomposites produced with the solution (circles) or STM (squares) method. (b) Strain at break for 44EVOH polymers and composites made with the solution (circles) or STM (squares) method.

The tensile strength of 44EVOH nanocomposites reinforced with TEMPO CNFs and CNFs were analyzed and compared to nanocomposites with similar loadings of CNCs to provide a better understanding of mechanical behavior of 44EVOH with different CNs incorporated as filler (Figure 6.15). Both the yield stress and stress at break of 44EVOH with 1 wt.% TEMPO CNFs were higher when the nanocomposite was processed with the STM method versus the solution method, but these stress values were either similar or lower than the neat polymer and nanocomposite with 1 wt.% CNCs irrespective of processing strategy implemented. The yield stress and stress at break values of 44EVOH with either 1 or 2.5 wt.% CNFs incorporated with the STM method were also lower than

or similar to either the neat polymer or nanocomposites with TEMPO CNFs or CNCs incorporated into the matrix. This behavior has been reported for other nanocomposite systems with either CNCs or CNFs in a polymer matrix [209] and was generally attributed to the higher likelihood of the CNFs to agglomerate in the polymer matrix and form stress concentrations that contributed to an overall lower strength for the composite.

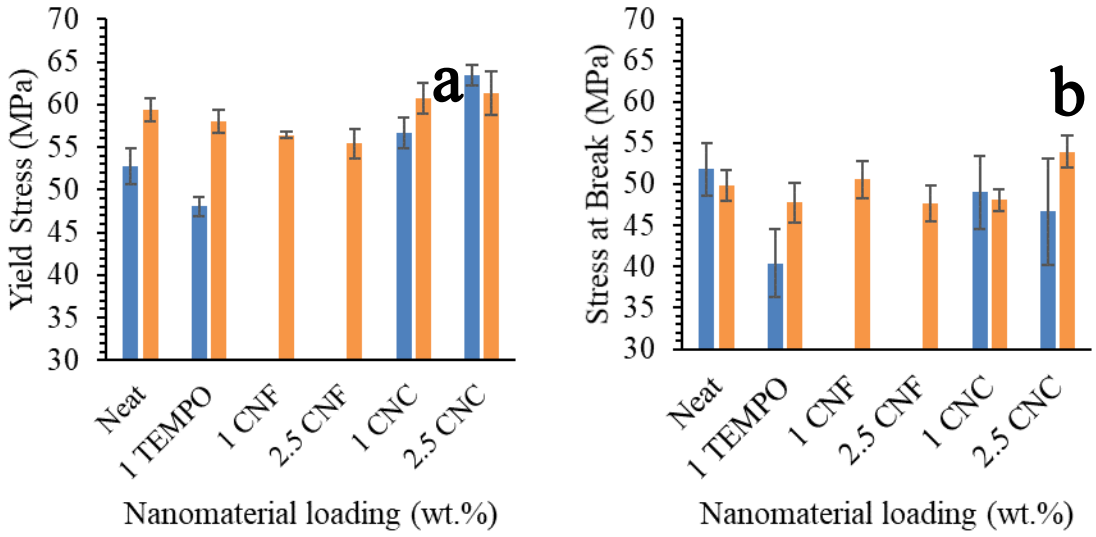

Figure 6.15 - (a) Yield stress and (b) stress at break for neat 44EVOH, 1 wt.% TEMPO CNF/44EVOH, 1 and 2.5 wt.% CNF/44EVOH, and 1 and 2.5 wt.% CNC/44EVOH made with either the solution (blue) or STM (orange) method.

As with the nanocomposites produced in the 48EVOH matrix discussed in the previous chapter, the results from spectroscopy, thermal, thermomechanical, and mechanical characterization suggested a multi-step protocol increased hydrogen bonding

between the CNs and 44EVOH matrix as well as properties of 44EVOH such as T_g, E', and yield strength. Higher T_g as measured by DMA, thermomechanical, and mechanical properties when 44EVOH nanocomposites were made with the STM method as opposed to the solution method suggested the STM strategy may have improved polymer-particle interactions due to increased dispersion and distribution of CNCs and TEMPO CNFs in the matrix. Spectroscopy indicated these interactions were through hydrogen bonding between the nanoparticles and the vinyl alcohol comonomers of the polymer matrix. Property characterization also suggested the polymer structure was more affected by the incorporation of CNs rather than processing strategy implemented, as noted by similar thermal properties of the neat polymer samples produced with the solution and STM methods and the increases in X_c and polymer density with increased CNC loading observed from XRD patterns. Therefore, the degree of CN dispersion was impacted by the processing choice implemented, and the thermomechanical and mechanical characterization results suggested the multi-step protocol increased CN dispersion in the 44EVOH matrix. However, it must be noted that some results from thermal degradation, thermomechanical, and mechanical studies suggested processing strategy did impact the polymer structure and particularly the amorphous polymer as noted by differences in $T_{d,1}$, T_g, and yield strength of the neat polymers produced with either the solution or STM method.

The role of polymer-particle compatibility was significantly tied to the changes in thermal, thermomechanical, and mechanical properties of EVOH and this was due to differences in the comonomer composition of the EVOH polymers investigated in this chapter and the previous chapter. The shifts of the -OH band in 2.5 wt.% CNC/44EVOH

nanocomposites observed in FT-IR spectroscopy suggested hydrogen bonding between the matrix and the CNs increased compared to the neat polymer. Also, second heat data from DSC measurements of solution- processed 44EVOH nanocomposites suggested the EVOH with higher vinyl alcohol content was affected more by the incorporation of CNCs as increased poylmer-particle interactions occured and led to a disruption in the crystalline structure of 44EVOH, a behavior noted in other nanocomposites with an EVOH matrix [80, 82, 85]. In addition to the spectroscopy and thermal property changes noted for the 2.5 wt.% CNC/44EVOH composite, the behavior of some of the thermomechanical and mechanical results were also observed to change around this CNC loading regardless of processing strategy employed. From micromechanical modelling, it was determined the onset of CNC network formation ocurred near this CNC loading, and therefore the interparticle spacing was determined to create confinement effects on the polymer matrix. Confinement of the polymer in composites with CNC filler has been noted for other poylmer matrices such as PHBV [209, 225] and was suggested as the reason for changes to the polymer crystallinity above and below the critical particle loading value for the onset of network formation. Polymer confinement between nanoparticles has also been attributed to increases observed in the T_g measured by DMA [234].

E' and T_g for 44EVOH nanocomposites were both higher than the 48EVOH nanocomposites independent of processing strategy chosen due to the increase in vinyl alcohol comonomer content and thus more opportunities for hydrogen bonding to occur between polymer chains as well as between polymers and CNs and reduce the mobility of the polymer chains. Modelling of thermomechanical data suggested the CNCs formed a stiff three- dimensional network in the polymer matrix due to hydrogen bonding amongst

the CNCs and between CNCs and the polymer matrix. The differences in $E_{f,}^{agg}$ values in 44EVOH and 48EVOH nanocomposite systems produced with the multi-step protocol for a given network morphology suggested CNCs were more likely to form a stiffer network in the polymer matrix with higher vinyl alcohol content in the range of particle loadings investigated. The increased hydrogen bonding capability of 44EVOH versus 48EVOH with CNs also produced nanocomposites that were more resistant to elastic deformation and failure when made with either processing strategy, and particularly at higher loadings when made with the STM method.

Differences in thermal, thermomechanical, and mechanical properties were also noted when comparing nanocomposites made with the different CNs. The thermomechanical and mechanical properties of nanocomposites with nanofibrils suggested at 1 wt.% loadings the nanofibrils were able to disperse in the polymer matrix and increase reinforcement of the polymer matrix, particularly above T_g when 1 wt.% TEMPO CNFs were incorporated with the STM method. The differences in E' above T_g when comparing nanocomposites with TEMPO CNFs as opposed to CNFs suggested the surface chemistry of the nanoparticles also played a significant role in their reinforcement capacity and networking ability in the 44EVOH matrix. The similarities or decreased storage modulus values of the 44EVOH matrix composites with CNFs compared to 44EVOH matrix composites with similar loadings of CNCs made with the STM method suggested the crystallinity and mechanical properties of the nanoparticles played an important role in determining resultant thermomechanical behavior of the composites in addition to differences in the aspect ratios of the CNCs and CNFs. While it was anticipated the higher aspect ratio CNFs would result in higher storage modulus values of EVOH

matrix composites compared to composites with similar loadings of CNCs, CNCs generally have higher crystallinity than CNFs due to the nature in which they are processed. Therefore, CNCs would generally have higher modulus values compared to the nanofibrils.

6.5 Conclusions

In this chapter, an EVOH matrix with higher vinyl alcohol content than the polymer used in Chapter 5 was used to study how polymer selection and processing strategy can affect CN reinforcement of the matrix material. CNCs, TEMPO CNFs, and CNFs were incorporated into 44EVOH via a solution or multi-step protocol including both solution and melt mixing methods. The results suggested CNs increased thermomechanical and mechanical properties of the 44EVOH matrix and these properties were higher when the nanocomposites were made with the STM method as opposed to the solution method. Thermal and x-ray analysis of the polymer and nanocomposites suggested the incorporation of CNs impacted the structure of the polymer matrix. Increased thermomechanical and thermal properties of 44EVOH polymer and nanocomposite systems compared to 48EVOH counterparts in Chapter 5 suggested the higher hydrogen bonding capacity of 44EVOH lent it to have increased compatibility with the hydrophilic CNs. Overall, the results from this chapter provide more insight into how matrix and processing selection can impact resultant properties and contributes to the knowledge base of CN- reinforced thermoplastic nanocomposites.

CHAPTER 7. INVESTIGATION OF THERMAL PROPERTIES OF ISOTROPIC NANOCOMPOSITES WITH FAST SCANNING CHIP CALORIMETRY

7.1 Introduction

DSC is an important characterization tool to determine the thermal properties and thermal transitions of material systems and specifically polymers and polymer nanocomposites. Polymers and polymer nanocomposites can undergo rapid reorganization and thermal transitions upon heating that may not be captured with conventional DSC instruments. Also, the processing methods employed for EVOH films such as injection molding and injection blow molding have rapid heating and cooling stages that may not be readily replicated with conventional DSC. Conventional DSC, with standard heating and cooling rates on the order of 10 °C/min, also may not be able to properly capture the thermal properties and morphology of polymers and polymer nanocomposite systems during processing such as rapid quenching of thin parts during injection molding or blow molding. Therefore, the desire to more fully understand polymer structure development at fast heating and cooling rates has led to the development of fast scanning chip calorimetry (FSC). FSC systems such as the commercially available Flash DSC can operate at heating rates up to 40,000 °C/second, and cooling rates up to 4,000 °C/second can be achieved [235], while custom FSC systems have been utilized at even higher scanning rates [236]. FSC has been employed to study polymers and polymer nanocomposites at fast scanning rates in order to determine crystallization kinetics [222, 237, 238] and thermal properties in systems with a degradation temperature that is near a thermal transition such as in

polyvinyl alcohol [239] or silk fibroins [240, 241]. Polymers such as PLA [242, 243], PTFE [244], copolymers [245], polymer nanocomposites [237, 246], and even metals [247] have been studied using FSC to more fully understand crystallization kinetics and reorganization at scanning rates beyond the scope of conventional DSC. Minakov *et al.* studied PET [221] and isotactic polystyrene (iPS) [222] using a custom FSC based on a thermal conductivity gauge for gas a vacuum sensors. They were able to validate reorganization of the polymers that was thought to occur during slower heating rates used in DSC. FSC therefore allowed the authors to investigate the as-cooled structure of the polymers as a function of thermal treatment rather than crystallites that may have melted, reformed, and remelted upon heating at slower rates. Wurm *et al.* [248] studied the metastable structures of two polyesters, PET and polybutylene terephthalate (PBT) reinforced with multi-walled carbon nanotubes (MWCNTs) with FSC. They observed that nucleation kinetics changed as a function of supercooling temperature using 100's and 1,000's °C/s cooling and heating rates with FSC that better mimic how the polymer crystallizes under processing conditions of injection molded parts. Others have confirmed changes in crystallization of polymer nanocomposites with commercial and custom FSC such as clay in PA11 [246] and PP [237]. Kolesov *et al.* reported while neat PA11 crystallization could be suppressed at cooling rates as high as 200 °C/s, the presence of organically-modified montmorillonite nanoclay prevented full suppression of the crystallization peak up to the maximum cooling rates capable of the Flash DSC 1. The use of FSC analysis in conjunction with DSC also allowed the authors to conclude nanoclay addition to PA11 significantly impacted its crystallization rate only at higher cooling rates that could not be seen with DSC but may exist in the as-processed structure of the composite during commercial processing

conditions that would be experienced by the polymer part. Overall, FSC has significantly contributed to the understanding of crystallization kinetics, metastability, phase formation, and reorganization in polymers and polymer nanocomposites during commercially- viable processing rates that would otherwise be impossible to probe with rates supplied by DSC.

FSC was used in this chapter to investigate the role CNCs have on thermal properties of an EVOH matrix such as melting temperature and cold crystallization at high cooling rates. Reorganization was investigated as a function of scanning rate. While nanocomposites with 5 wt.% CNCs and 1 wt.% TEMPO CNFs were investigated, they were not included in this discussion due to the significant differences observed in the sample morphology when microscope images were examined of the samples adhered to the chip. Images of these samples may be found in the appendix (Figure C.1 and Figure C.2).

7.2 FSC

7.2.1 VH, CC

In order to determine the heating rate needed to suppress reorganization of 44EVOH and 48EVOH during heating, VH, CC tests were performed. Figure 7.2 and Figure 7.2 shows the heat flow curves and T_m, respectively, obtained from the VH, CC tests as a function of heating rate applied to the sample. Two trends were studied in these tests: the value of T_m and shifts in the melting temperature as heating rates were changed. Analyzing the value of the melting temperature allowed for an understanding of how the addition of nanoparticles affected the crystallization. Since all of these samples experienced the same thermal history, this effect could be assessed for a given heating rate

and as a general behavior across heating rates. Analyzing the shift in T_m with heating rate for a given sample allowed for an understanding of reorganization processes in the material. The component interfaces in the composite samples were expected to provide areas of incomplete polymer organization, metastable structures, and/or crystal nucleation sites. The presence of the first two features could be deduced from the dependence of reorganization processes of heating rates. If the composites required higher heating rates to suppress reorganization, then such structures were likely to be present. Further investigations of polymer- particle interactions can be studied by conducting VC, CH measurements, as EVOH is reported to undergo changes to its crystal structure at sufficiently high cooling rates [72]. Cerrada *et al.* noted some EVOH polymers with a majority vinyl alcohol comonomer content had monoclinic crystal lattices. These EVOH polymers underwent restructuring to an orthorhombic lattice when they were quenched with increasing cooling rates up to 100 °C/minute. While the crystal lattice was not anticipated to change from orthorhombic to another lattice type with higher cooling rates such as what were used in this study, the polymer crystal sizes and perfection was still expected to change with higher cooling rates than what were previously reported.

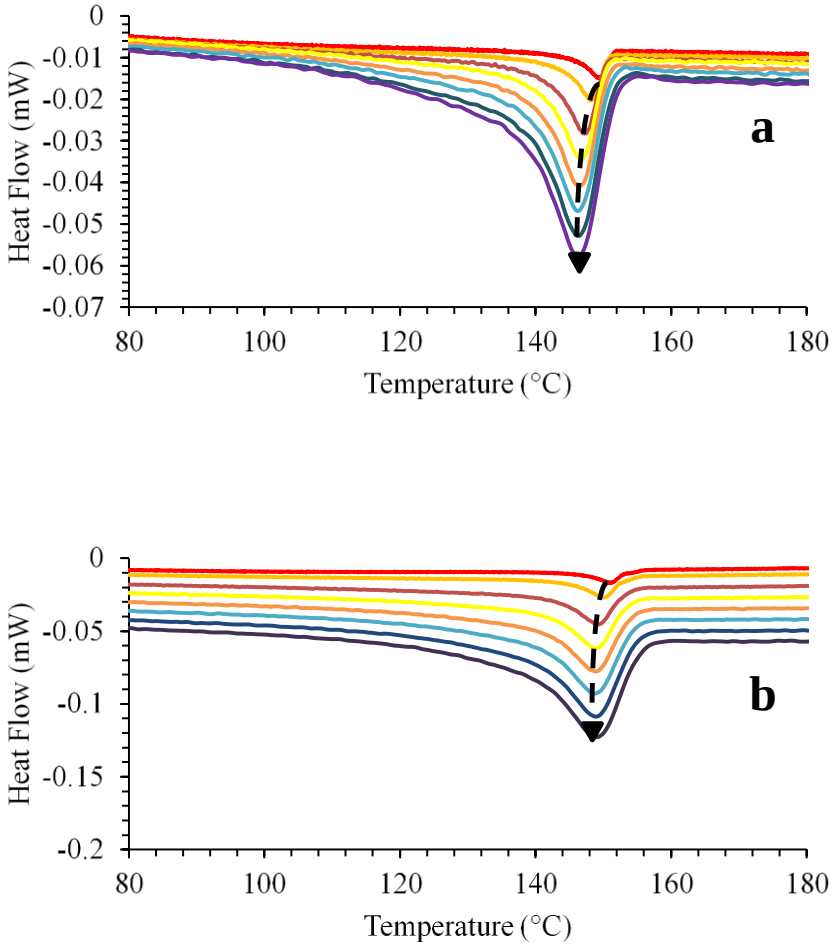

Figure 7.1 - Heat flow curves during heating in the VH, CC tests for (a) 48EVOH and (b) 1 wt.% CNC/48EVOH up to 700 and 1000 °C/s heating rates, respectively. Arrow indicates peak position as heating rate increases. Curves shifted along y-axis to better visualize shifts in T_m.

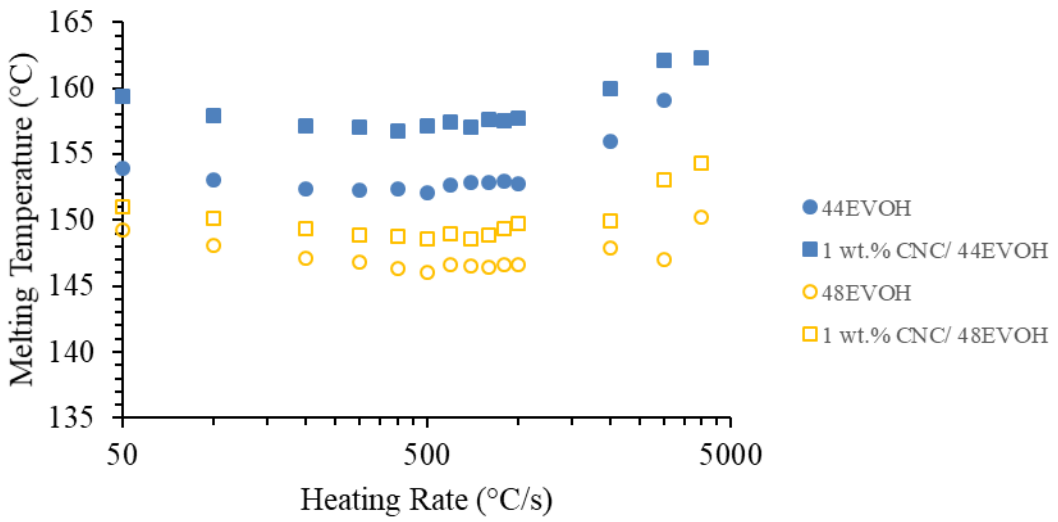

Figure 7.2 - Melting temperature as a function of heating rate for 44EVOH and 48EVOH nanocomposite samples.

Based on the melting temperature values measured at the range of heating rates, the two EVOH polymers were affected differently by the addition of CNCs. The 1 wt.% CNC/48EVOH sample showed a consistently higher T_m than the neat 48EVOH at all of the heating rates measured. The differences between T_m values of the 1 wt.% CNC/48EVOH composite and those for the neat 48EVOH were not dramatic, generally only a few degrees. These results suggested that CNCs had an ability to form more perfect polymer crystallites, but the effect was not substantial. Above 1000 °C/s, the measured values showed more variability, which was likely related to thermal lag at these rates [249]. The 44EVOH nanocomposites showed different trends in T_m with CNC addition. The differences in T_m of the neat polymer and nanocomposite system at a given heating rate were greater than those seen in the 48EVOH-based samples. When heating rates less than

or equal to 1000 °C/s were considered, the 1 wt.% CNC/44EVOH sample had T_m values that were approximately 5 °C greater than those of the neat 44EVOH. Above 1000 °C/s, the 1 wt.% CNC/44EVOH sample and the neat 44EVOH sample became more similar as heating rate was increased.

In all of the samples studied, there was a decrease in T_m as heating rate increased to a minimum point before increasing with increasing heating rate. This behavior in the T_m values with heating rate indicated the polymer underwent reorganization during slower heating rates up to a critical heating rate at which all reorganization was halted. Reorganization of the polymer meant the polymer crystallites were either made more perfect, larger, or melted-recrystallized-remelted which would result in crystallites that required higher temperature to melt than the original structure present prior to heating. The critical heating rate required to reach the minimum T_m for the neat 48EVOH and 48EVOH with 1 wt.% CNCs occurred at 500 °C/s. The critical heating rate decreased for 1 wt.% CNC/44EVOH compared to the neat 44EVOH. Neat 44EVOH had a critical heating rate of 500 °C/s while 44EVOH with 1 wt.% CNCs had a critical rate of 400 °C/s. With the exception of neat 44EVOH, there was a range of heating rates immediately after reaching the minimum T_m where the T_m would fluctuate before continuously increasing again as a function of heating rate. Therefore, the point at which T_m was considered to be increasing was defined when there was a 1 °C increase from the minimum T_m to account for these variations.

The trends in T_m with increasing heating rate suggested that the reorganization processes were the same or less prevalent in the 1 wt.% nanocomposites since the critical

heating rate did not increase. Therefore, it was unlikely that metastable structures were present at the component interfaces. Instead the CNCs were more likely serving as nucleating agents for EVOH.

The values of T_m measured with FSC were lower for all samples tested when compared to T_m values measured with conventional DSC (Table 5.1 and Table 6.1). This discrepancy was likely due to reorganization processes occurring at the heating rates used in conventional DSC as well as differences in crystal perfection and size that resulted from the different cooling rates used in DSC and FSC. It was anticipated from the results of the VH, CC tests that reorganization occurred during heating at slower rates in the polymer and nanocomposite since the critical heating rates were 400 °C/s and 500 °C/s. Reorganization processes during heating in DSC would produce a more stable crystal structure, leading to a higher measured melting temperature. Also, EVOH is known to exhibit different crystal lattice structures depending not only on comonomer composition but also on thermal history imparted during processing [72, 219, 250, 251]. The cooling rates at which Cerrada *et al.* [72] observed changes to 44EVOH and EVOH polymers with higher vinyl alcohol content than investigated in this work occurred at approximately 100 °C/min (1.67 °C/s) and this new structure was a less dense structure compared to those that were slowly cooled from the melt, and Perez *et al*. [252] determined EVOH polymer melts that were rapidly quenched exhibited less crystals and thinner crystals compared to those polymers that were annealed for a longer period of time. It was not expected for the polymer crystal lattices to be different from the orthorhombic structure reported for these EVOH compositions in literature [67, 71, 72, 251] or from XRD patterns discussed in Chapters 5 and 6. Therefore, it was anticipated the crystals of both 44EVOH and 48EVOH

would be less perfect or smaller at the cooling rates used in FSC tests compared to those tested with DSC, which would result in a lower temperature required to melt the polymer.

7.2.2 VC, CH

VC, CH tests were conducted to determine what, if any, cooling rate could make both EVOH polymers and their nanocomposites fully amorphous. Trends in T_m of the neat and composite samples were also examined in these measurements, similar to the VH, CC experiments. While tests were conducted on each sample up to a maximum cooling rate of 4000 °C/s, the maximum cooling rate that was controllable in the composite samples was 1000 °C/s. Therefore, the T_m values were only presented up to the heating step immediately following the 1000 °C/s cooling step. Figure 7.3 shows typical curves from the heating rate steps for a sample that was subjected to various cooling rates and a plot of T_m for all samples tested as a function of cooling rate used in the step prior to heating. Based on the results of the VH, CC tests, a heating rate of 700 °C/s was used to ensure that any changes in melting behavior were a result of the cooling rate used and not due to polymer reorganization during the heating scan. For the neat and composite samples, the same general trends were seen with regard to melting behavior as a function of heating rate. At sufficiently low cooling rates, the subsequent heating scan showed a step change in the heat flow in the temperature range of 30-60 °C attributed to T_g and an endothermic peak representing the melting transition. As the cooling rate was raised, the subsequent heating scans began to show an exothermic peak, indicative of cold-crystallization, before the melting peak. The cold crystallization peak increased in enthalpy as well as shifted to higher temperatures when the cooling rate increased and approached a steady value at

higher cooling rates. Cold crystallization has been noted in other semicrystalline polymers such as PET [253, 254] and PLA [255, 256] when the applied cooling rate was sufficiently fast to suppress the crystallization process in the polymer.

Nanocomposites had different critical cooling rates for the appearance of a cold-crystallization peak than the neat polymers. In both EVOH systems, the neat polymer had a critical cooling rate of 100 °C/s while the 1 wt.% CNC nanocomposites had a critical rate of 200 °C/s, indicating that higher cooling rates were needed to suppress crystallization in the nanocomposites. In addition to the appearance of a cold crystallization peak upon increased cooling rate to each sample, T_m was observed to decrease and eventually attain a constant value at higher cooling rates (Figure 7.3b). This change in T_m values was indicative of the melting of crystals formed during cold crystallization that was the dominant structure at higher cooling rates. Like the critical cooling rate for cold crystallization, the cooling rate needed for T_m to reach a constant value was also different between the samples. For neat polymers, the rate was 200 °C/s while the nanocomposites required a rate of 400 °C/s to achieve a constant value for T_m. Above the critical cooling rate, differences in values of T_m were observed between the nanocomposites and the neat polymers, although the noted changes were minimal. T_m for 1 wt.% CNC/44EVOH was approximately 1.4 °C higher than neat 44EVOH, while 1 wt.% CNC/48EVOH was only about 0.7 °C higher than neat 48EVOH. Overall, these results were consistent with the results of the VH, CC tests that indicated the CNCs were likely acting as nucleating agents for EVOH.

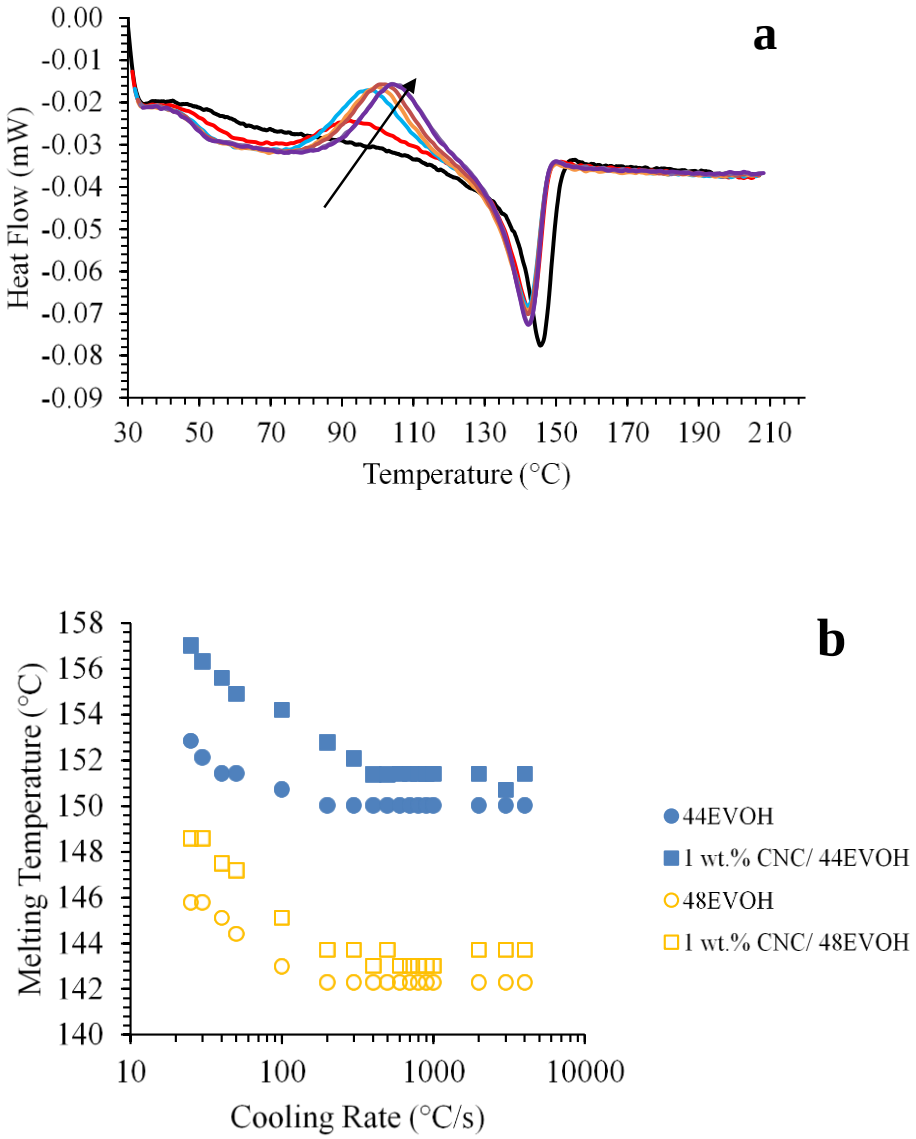

Figure 7.3 - (a) Heating scan curves of VC, CH tests for 48EVOH. Arrow indicates cold crystallization peak position as a function of increasing cooling rate. (b) Melting temperature vs. Heating rate for 44EVOH and 48EVOH nanocomposite samples.

The presence of a cold crystallization peak also coincided with a significant decrease in the peak area of the melting transition, representing a lower crystallinity at these cooling rates where cold crystallization occurred. To understand how much of the crystal structure that was melting was formed during cold crystallization, the difference in the areas of the melting peak and the cold crystallization peak were calculated. These values are shown in Figure 7.4. When the difference between these peak areas was approximately zero, it was assumed that the cooling rate used was sufficient to suppress crystallization during the cooling step. The 1 wt.% CNC/44EVOH composite showed the melting peak could be suppressed at sufficiently high cooling rates while the difference in enthalpy of melting and cold crystallization never approached zero for the neat 44EVOH. This observation in the neat 44EVOH suggested some degree of crystallinity was formed during the cooling step and the neat polymer could not be made fully amorphous at the cooling rates used in this work. The 48EVOH polymer and composite samples behaved differently. Both the neat polymer and nanocomposite could be cooled such that crystallization was suppressed during the cooling step, but the nanocomposite required higher cooling rates for this to be realized. It was expected for 44EVOH to have a more stable structure overall compared to 48EVOH due to the increased vinyl alcohol content lending to more hydrogen bonding capability and denser packing of polymer chains. Therefore, 44EVOH would require faster cooling in order to render it completely amorphous compared to 48EVOH.

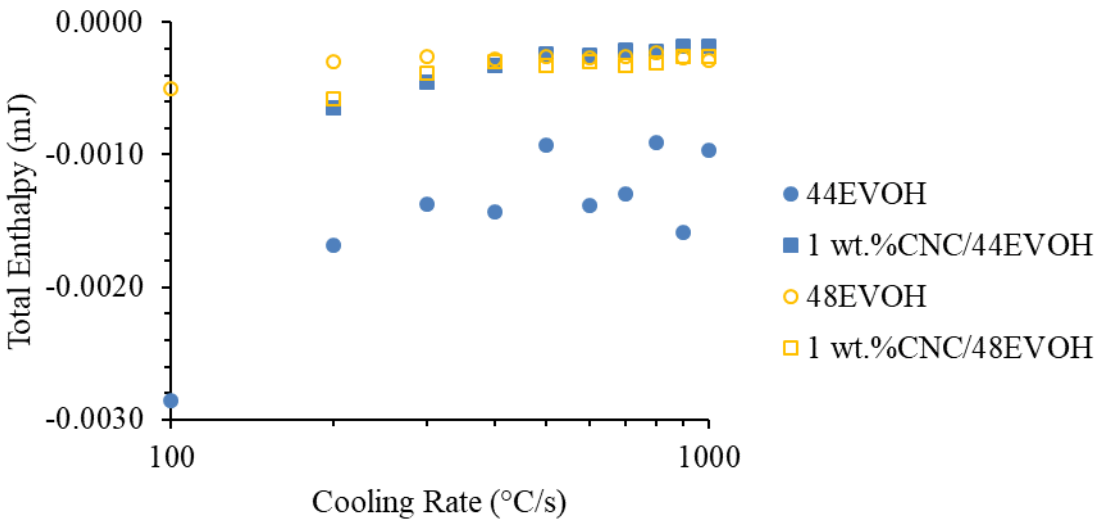

Figure 7.4 - Total enthalpy as measured upon the subsequent heating step after each cooling rate for 44EVOH and 48EVOH nanocomposites during the VC, CH tests.

7.3 Discussion

A summary of the results from FSC testing can be found in Table 7.1. For the nonisothermal tests conducted on the neat polymers and polymer nanocomposites, the heating and cooling rates required to observe changes in critical rates was beyond the capabilities of conventional DSC. A minimum melting temperature was observed as a function of heating rate for all samples tested. The minimum T_m suggested the polymer reorganized upon heating at slower rates than that used to obtain the minimum value of T_m. In VC, CH tests, a cold crystallization peak was observed above a critical cooling rate, and this observation was coupled with a decrease in the total enthalpy of melting. The results of the VC, CH tests indicated the composites and the neat 48EVOH system were able to be rendered amorphous with the cooling rates provided by FSC. The introduction of CNCs to EVOH resulted in changes to both the critical cooling and heating rates in the first set of

tests. The 44EVOH nanocomposite had notable dependences on critical heating and cooling rates. While a difference in melting temperatures was observed between the neat 48EVOH and 48EVOH composite, the difference in melting temperatures was not as significantly different as in the neat 44EVOH and 44EVOH composite. A few arguments are presented to explain the changes in both EVOH matrices when CNCs were incorporated and tested with FSC.

Table 7.1 - Summary of minimum T_m and critical heating and cooling rates for each sample.

Sample	**Minimum T_m (°C)**	**Critical Heating Rate (°C/s)**	**Critical Cooling Rate (°C/s)**
44EVOH	152	500	100
1 wt.% CNC/44EVOH	157	400	200
48EVOH	146	500	100
1 wt.% CNC/48EVOH	149	500	200

The results of the first VH, CC tests as well as trends in the melting temperature in subsequent tests provided insight into component interactions in the two composites. Increased vinyl alcohol comonomer content in 44EVOH compared to 48EVOH resulted in increased polymer- particle compatibility due to the availability of more hydroxyl groups to hydrogen bond with hydrophilic CNCs. This increased polymer-particle compatibility then led to crystal structures that required higher temperatures to completely melt

compared to neat EVOH which was also in agreement with results from XRD studies in Chapters 5 and 6. Previous work by the authors [118] using polarized optical microscopy (POM) characterization further suggest the role of comonomer content with polymer-particle compatibility as the POM images of 44EVOH nanocomposites and 48EVOH nanocomposites were different. The increased polymer crystal density and crystallinity as measured by XRD for the 44EVOH and 48EVOH along with the increased melting temperatures observed in the 1 wt.% CNC composites for both EVOH matrices suggested the incorporation of CNCs promoted the perfection and increase in crystallite size of both EVOH matrices.

The changes in critical cooling rate with the addition of CNCs in both EVOH matrices studied suggested the CNCs acted as nucleating agents in the polymer matrix, delaying the ability for EVOH to become fully amorphous and required faster cooling rates to do so. The ability of the CNCs to act as nucleating agents at similar loadings in polymer matrices as used in this work has been reported for other nanocomposites when the CNCs and polymer matrix were either unmodified or modified with different surface moieties [34, 121, 133, 202]. The decrease in melting temperature as the cooling rate increased up to the critical cooling rate suggested the crystals that were formed upon cold crystallization were either smaller or less perfect than the original structure of the nanocomposites that were quenched much slower from the melt. This would also help to explain why lower heating rates were required to fully suppress melting in the second set of VH, CC experiments, as less perfect crystal structures due to cold crystallization would not require as high of heating rates to fully suppress melting.

Polymer crystallites that are formed upon cooling are known to be thermodynamically metastable. Semicrystalline polymers and polymer nanocomposites can exhibit metastable structures due to a number of reasons ranging from defects in crystal structure, rigid amorphous regions between crystallites, and the presence of either conformationally disordered (condis) crystals or plastic crystals [257, 258]. Therefore, upon heating, semicrystalline polymers have the ability to reorganize given the heating rate is slow enough to do so. As such, the melting temperature will shift to lower temperatures when the heating rate is sufficiently fast enough to suppress reorganization as was observed in both EVOH polymers and nanocomposite samples during the first VH, CC tests. However, the decrease in critical heating rate in 44EVOH nanocomposite when CNCs were incorporated suggested that the CNCs provided the opportunity for the 44EVOH polymer to crystallize into a more stable structure that would stop reorganizing at lower heating rates. Additionally, the decrease in critical heating rate for the 44EVOH composite as well as the lack of change in critical cooling rate for the 48EVOH composite compared to their respective neat polymers during the VH, CC tests suggested no additional metastable structure was imparted on the polymer at the polymer- particle interfaces, and that the metastable structures observed at slower heating rates were located in the bulk polymer matrix.

The changes in thermal properties of both EVOH matrices with the incorporation of CNCs along with results from XRD studies in Chapters 5 and 6 also suggested EVOH underwent changes in crystallite size and perfection. While EVOH is known to undergo changes in crystal structure both as a function of thermal history and composition [72], these changes are generally observed to occur at slower cooling rates than what were used

in the VH, CC and VC, CH tests and in EVOH polymers with higher vinyl alcohol compositions than the EVOH polymers tested in this work. Additionally, the EVOH polymers that have been observed to change crystal lattice structure with cooling rate imparted were not observed to have significant changes in the melting temperature of the polymers before and after quenching, and the polymer lattice remained orthorhombic even after annealing [219]. DSC results discussed in Chapters 5 and 6 for 48EVOH and 44EVOH polymer and composite samples corroborated the findings that the crystal structure probably did not change from the first to the second heating step, and changes in the T_m values were most likely due to crystal size or thickness changes rather than lattice changes. Additionally, while the melting point of EVOH is known to depend on the comonomer content, Takahashi *et al*. [71] observed the crystal structures of 44EVOH and 48EVOH are similar as measured by wide angle x-ray diffraction. Results from XRD studies suggested there were changes in the polymer crystal density of 48EVOH when CNCs were incorporated with the multi-step protocol. Although the diffraction pattern of neat 48EVOH suggested the polymer organized into an orthorhombic lattice, the higher pronouncement of the (100) and (200) diffraction peaks when CNCs were incorporated suggested the addition of the nanoparticles increased crystallinity in the polymer matrix. While the crystallinity and crystal density increased in 44EVOH as well with the incorporation of CNCs, the crystal structure remained orthorhombic regardless of CNC loading.

7.4 Conclusions

FSC was used to elucidate structural changes in EVOH polymers of different comonomer content and loadings of CNCs. Three nonisothermal scanning tests were

performed on the polymers and polymer nanocomposites to determine what scanning rates are needed to fully suppress reorganization upon heating and crystallization during cooling. Shifts of the melting temperature as a function of heating rate in variable heating with constant cooling tests suggested the polymers and nanocomposites underwent reorganization during heating. Additionally, the polymer nanocomposites were able to be made amorphous at cooling rates of 100's to 1000's °C/s as noted by a cold crystallization peak in the variable cooling with constant heating tests. Nanocomposites with the higher vinyl alcohol content polymer matrix required higher cooling rates to make them amorphous versus the neat polymer. The critical cooling rate also was observed to increase with the addition of CNCs and this suggested the nanoparticles may have acted as nucleating agents for the growth of polymer crystallites upon cooling. Overall, FSC was demonstrated to be a useful tool for thermal characterization of thermoplastic nanocomposites by identifying structural changes that otherwise could not be detected with conventional DSC techniques. The results also provided insight into the role of component compatibility and reorganization processes for materials used in applications such as food and beverage packaging where thermal processing conditions play a key role in resultant barrier and mechanical properties.

CHAPTER 8. PRODUCING TENSEGRITY-INSPIRED MICROSTRUCTURES IN POLYETHYLENE-CO-VINYL ALCOHOL REINFORCED WITH CELLULOSE NANOMATERIALS

8.1 Introduction

Prescribing morphology in polymer nanocomposites offers the opportunity to tailor and even affect parameters of the polymer matrix such as thermomechanical [2], electrical [259], and optical properties [39, 56]. In this chapter, an external- in approach was used via a sequential biaxial mechanical stretching protocol to prescribe morphology in neat EVOH polymers as well as polymers with CN reinforcement. Uniaxial stretching and biaxial stretching of polymer nanocomposites with CNs has been demonstrated by others to increase mechanical, thermomechanical [260], and even gas barrier properties [67] of the polymer matrix. Cerrada *et al*.[261] reported the development of a mesophase structure and an increase in orientation of neat EVOH polymers due to polymer chain alignment in the direction of stretching when uniaxially stretched as measured by x-ray diffraction. The authors also determined uniaxially and biaxially orienting neat EVOH polymers increased thermomechanical properties such as E' in the directions of stretching compared to the unstretched polymers. Fiber spinning polymer nanocomposites has also been demonstrated to increase orientation of polymers and CNs due to elongational flow out of the spinnerets [120, 201, 262].

The research presented in this chapter looks to apply the concept of tensegrity as a means of prescribing morphology in EVOH with CNs through a sequential biaxial drawing method. Tensegrity structures may be found in both man-made architectures [174-176, 178] as well as biological structures [181, 183, 186] and have been demonstrated to provide increased mechanical stability when external stresses are applied. Tensegrity- inspired microstructures in a polymer nanocomposite construct were demonstrated to increase shear storage modulus values as measured with DMA and these increases were higher than either the unstretched or uniaxially stretched systems. The orientation of the needle-like nanoparticles was confirmed with XRD, and these results coupled with the results from DMA suggested the tensegrity- inspired particle arrangements contributed to the overall increases in mechanical properties. In the current work, it is anticipated that CNs, with higher aspect ratios than the HAp particles previously employed, will increase mechanical properties of EVOH when they are arranged in the nanocomposite with the biaxial stretching protocol due to increased stress transfer ability of the CNs. The tensegrity-inspired microstructures will be formed through a combination of isolated CNs in a continuous tensioned phase comprised of the polymer matrix.

In order to determine if prescribed microstructures were developed with a sequential biaxial stretching protocol, thermomechanical and mechanical properties were studied as a function of nanoparticle loading, applied uniaxial and biaxial strain, and polymer matrix. Processing conditions for creating the prescribed microstructures was also investigated by changing the extension rate during the first drawing step. The extension rates for the first drawing step were 1 mm/min or 10 mm/min, while the extension rate used for the second drawing step for all biaxially stretched samples was maintained at 10 mm/min. The

structure and thermal properties of the resulting stretched systems were also reported and used to provide further insight into how the polymer structure and orientation changed when stretched. 44EVOH and 48EVOH matrix nanocomposites were first uniaxially stretched and thermomechanical and mechanical properties of the stretched samples as well as results from the previous chapters were used as a basis for the systems selected to further investigate for the second biaxial stretching step. For the second stretching step, the uniaxially stretched films were rotated 90° and stretched. The biaxially stretched samples were characterized for thermomechanical, thermal, and mechanical properties and compared to unstretched isotropic and uniaxially stretched systems of the same composition.

8.2 Mechanical properties

8.2.1 First stretching step

Thermomechanical and mechanical properties were analyzed for uniaxially stretched neat polymers and nanocomposites with either CNCs or CNFs and compared to isotropic systems made with the STM method discussed in Chapters 5 and 6. As can be seen in Figure 8.1, the value for E' measured in the MD was highest when films such as the 44EVOH composite with 1 wt.% CNCs was uniaxially stretched to 300% applied strain for the systems stretched at a 1 mm/min extension rate. Anisotropy of in-plane storage modulus and stress at break values was also observed when the polymers and composites were uniaxially stretched (Figure 8.2 and Figure 8.4). E' values for uniaxially stretched 1 and 5 wt.% CNC/44EVOH composites were higher when measured in the MD compared to the neat polymer that was uniaxially stretched at a 1 mm/min extension rate. The increase

in E' in the MD when the neat polymer and nanocomposites were uniaxially stretched compared to the isotropic systems suggested the orientation of polymer chains and CNs increased and long axis of each was aligned in the direction of applied strain. The values of E' measured in the MD and CD for the uniaxially stretched systems were compared to upper- and lower-bound rule of mixtures micromechanical models shown in Equations 8.1 and 8.2, respectively:

$$E_c = E_f \nu + E_m(1 - \nu) \tag{8.1}$$

$$E_c = \left(\frac{\nu}{E_f} + \frac{1 - \nu}{E_m}\right)^{-1} \tag{8.2}$$

where E_c is the modulus of the nanocomposite, E_f is the modulus of the CNCs and was assumed to be 50 GPa [59], ν is the volume fraction of CNCs, and E_m is the modulus of the matrix. The storage modulus value for the composites measured at 30 °C was used as the experimental data to compare to the theoretical values calculated for E_c, and the storage modulus value for the neat polymers was used for the values of E_m. The micromechanical models were plotted in Figure 8.3. Values for ν were derived from the wt.% values assuming the density for the CNCs was approximately 1.6 g/cm^3 [1] and the polymer density was 1.14 g/cm^3 for either 44EVOH or 48EVOH [76]. Therefore, the values for ν were approximately 0.0071, 0.0179, and 0.0361 for 1, 2.5, and 5 wt.% CNC loadings, respectively. The experimental E' value for the 1 wt.% CNC/44EVOH composite exceeded the theoretical value for the uniaxially aligned system, whereas the experimental values for

the MD of 2.5 wt.% and 5 wt.% CNC/44EVOH composites were lower than the theoretical value.

When the 44EVOH polymer and nanocomposite films with CNCs were uniaxially stretched with an extension rate of 10 mm/min, there was an increase in the MD E' values in composites with 5 wt.% CNC loadings compared to the uniaxially stretched neat polymer. The E' value for the 1 wt.% CNC/44EVOH composite that was uniaxially stretched was similar to the uniaxially stretched neat polymer considering the spread in the E' values measured, and the E' value for the 2.5 wt.% CNC/44EVOH composite measured in the MD was lower than the uniaxially stretched neat polymer measured in the MD. Overall, the E' values of the uniaxially stretched polymer and composites measured in the MD were significantly higher than the E' values measured in the isotropic polymer and composite systems. There was qualitatively similar behavior of the experimental results for the uniaxially stretched composites compared to theoretical E' values calculated with the Rule of Mixtures model (Figure 8.2) with the exception of the stretched 2.5 wt.% CNC/44EVOH composite, and the experimentally measured E' for the 5 wt.% CNC/44EVOH composite exceeded the theoretical prediction when stretched at 10 mm/min extension rate. The comparison in measured and theoretical values for E' of uniaxially stretched nanocomposites and overall higher values for E' of uniaxially stretched systems measured in the MD compared to isotropic samples suggested there may have been some alignment of the nanoparticles and/or polymer chains in the direction of testing for MD samples compared to the unstretched isotropic systems. While the neat polymer and 5 wt.% CNC/44EVOH composite had higher E' values in the MD when the extension rate increased, the E' values for the composites with lower CNC loadings were similar

regardless of extension rate implemented. The reported changes in the neat polymer were attributed to increased orientation of the polymer chains in the direction of applied strain, and the increased E' value measured in the MD for the 5 wt.% CNC/44EVOH composite was due to the additional polymer orientation as well as increased X_c as measured with DSC (Figure 8.18) due to increased alignment of the polymer chains in the direction of applied strain. This increased X_c of the 5 wt.% CNC/44EVOH composite would also explain the differences in experimental value and theoretical value for E', as the model assumes the polymer structure is similar between the neat polymer and composite. The decreased value of the stretched 2.5 wt.% CNC/44EVOH composite was also attributed to differences in the polymer crystallinity compared to the other polymer and composite samples. As was noted in Figure 8.16, the X_c values for the 2.5 wt.% CNC/44EVOH composite were lower for the films stretched using the faster extension rate compared to the neat polymer, a qualitative trend also noted for the average X_c and T_m values of the unstretched composite compared to the unstretched neat 44EVOH polymer discussed in Chapter 6 (Table 6.1). This trend in decreased crystallinity of the polymer when the CNC loading is near the onset of network formation has been observed in other polymer matrices [225] and was attributed to confinement between the particles as the interparticle distances decrease near this threshold value. Ten *et al.* suggested below this threshold CNC loading, two mechanisms were competing to determine the resulting polymer crystallinity: the ability for the CNCs to nucleate polymer crystals and confinement of the polymer chains between CNCs hindering crystallization. Also, above the critical CNC loading, the authors observed the CNC network did not hinder the ability of the polymer to crystallize in a similar structure to the neat polymer. Therefore, the results suggested the ability of the

nanoparticles to confine the polymer motion around the 2.5 wt.% CNC loading reduced the ability of the polymer matrix to crystallize and resulted in a lower E' value for the stretched sample compared to the other polymer and composite samples. The difference in the polymer crystal structure, i.e. higher X_c values, for the composites with other CNC loadings was attributed to the increased E' values with respect to the neat polymer.

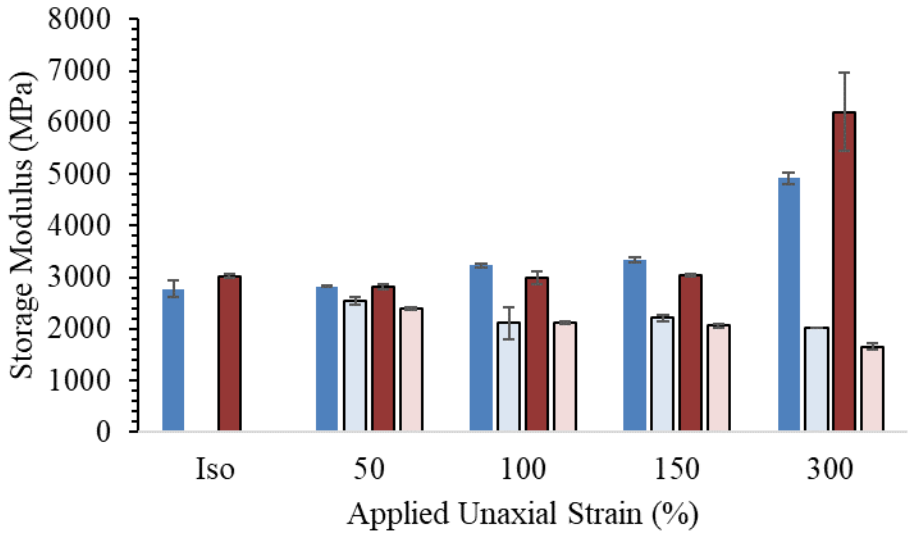

Figure 8.1 - E' at 30 °C as a function of applied strain for first stretching step of neat 44EVOH (blue) and 1 wt.% CNC/44EVOH (red) composite tested in the MD (dark) and CD (light).

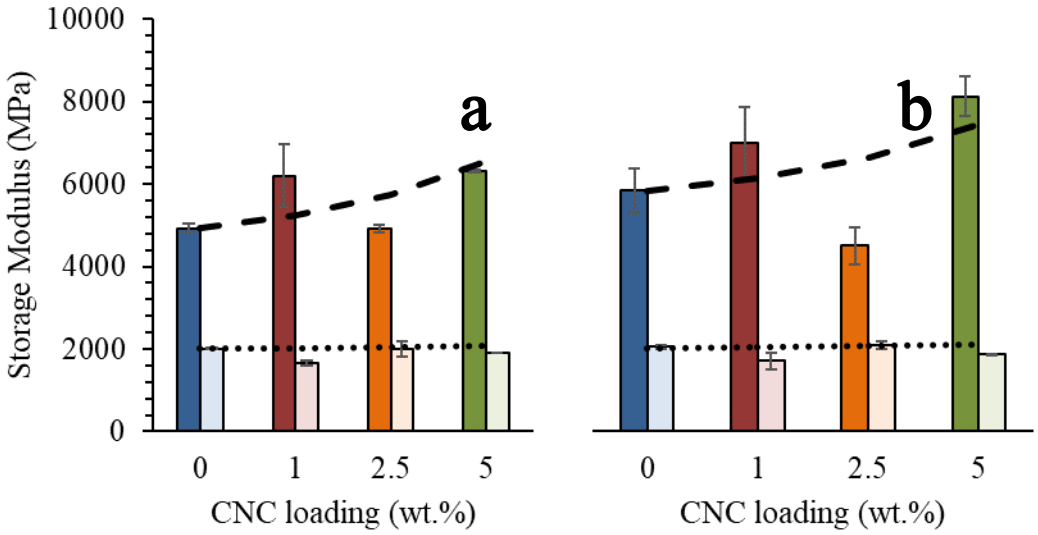

Figure 8.2 - E' at 30 °C for uniaxially stretched 44EVOH polymer and nanocomposites stretched at an applied extension rate of (a) 1 mm/min or (b) 10 mm/min. Upper- and lower-bound rule of mixtures values represented as dashed and dotted lines, respectively, for each applied extension rate.

There was also evidence of polymer and CNC orientation in the applied uniaxial strain direction for 48EVOH polymer and nanocomposite samples with a 10 mm/min extension rate. 48EVOH nanocomposite E' values were higher or similar to the neat polymer when measured in the MD. The 1 wt.% CNC/48EVOH composite had a higher value for the MD value of E' compared to the theoretical value when the Rule of Mixtures was used to predict E' values of uniaxially drawn 48EVOH matrix samples. The difference in experimental and theoretical E' values for this nanocomposite was attributed to the higher X_c value of the composite as measured by DSC (Figure 8.19) compared to the other neat 48EVOH polymer and nanocomposite samples due to increased orientation of the

polymer chains in the direction of applied strain. Otherwise the 2.5 wt.% CNC/48EVOH composite and the 5 wt.% CNC/48EVOH composite had a lower value for E' than what was predicted with the rule of mixtures. The decrease in measured E' value compared to predicted values at higher CNC loadings for uniaxially stretched 48EVOH nanocomposites suggested the CNCs did not efficiently reinforce the stretched polymer matrix. The decreases in experimental storage modulus values for the stretched 48EVOH nanocomposites with 2.5 or 5 wt.% CNCs compared to theoretical predictions qualitatively matched what was seen in the isotropic composites in Chapter 5, in which the experimental E' values of 2.5 and 5 wt.% CNC/48EVOH composites were lower than the theoretical values calculated using the Takayanagi Model I. These differences in experimental and theoretical values were attributed to CNC agglomeration. Increased anisotropy of the thermomechanical and mechanical properties with the addition of CNCs could also be explained with increased alignment of the long axis of the nanoparticles in the direction of applied strain. CD properties of both the neat polymer and nanocomposites were attributed to the behavior of the transverse thermomechanical and mechanical properties of the nanoparticles, as well as intermolecular bonding between the components.

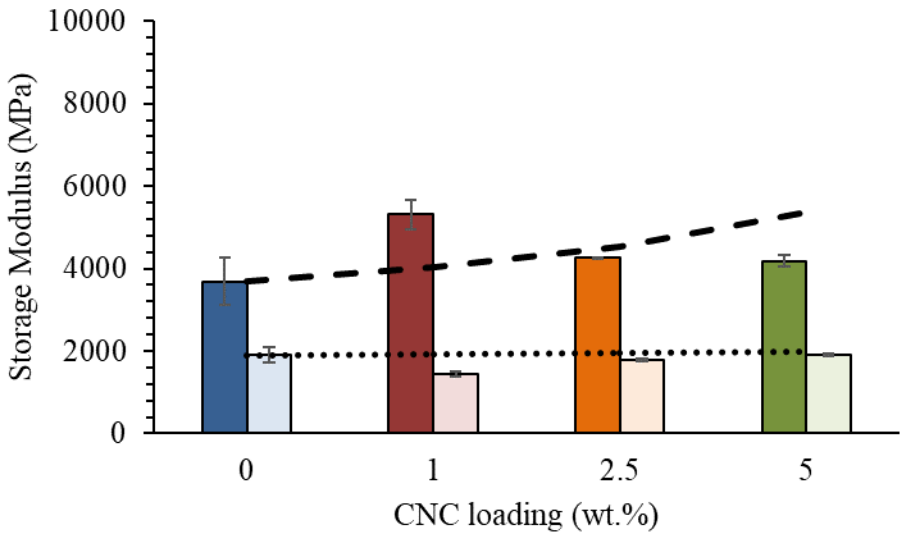

Figure 8.3 - E' at 30 °C for uniaxially stretched 48EVOH nanocomposites with CNCs tested in the MD (dark) and CD (light). Dashed and dotted lines indicate fits for the upper- and lower- bound rule of mixtures models, respectively.

The stress at break data for both 44EVOH and 48EVOH composites that were uniaxially drawn with a 10 mm/min extension rate are displayed in Figure 8.4. As can be seen in the figure, the stress at break values were statistically similar among the 44EVOH and 48EVOH composites with the exception of the 1 wt.% CNC/44EVOH composite which was significantly higher than the neat 44EVOH polymer. Overall, the strength values measured in MD were significantly higher than the unstretched samples for all polymer and composite systems, and the similarity in values of most of the composites compared to the neat stretched samples suggested the polymer matrix had a higher resistance to failure due to the increased orientation of the polymer chains and there was no additional strength benefit provided by the aligned CNCs in the matrix.

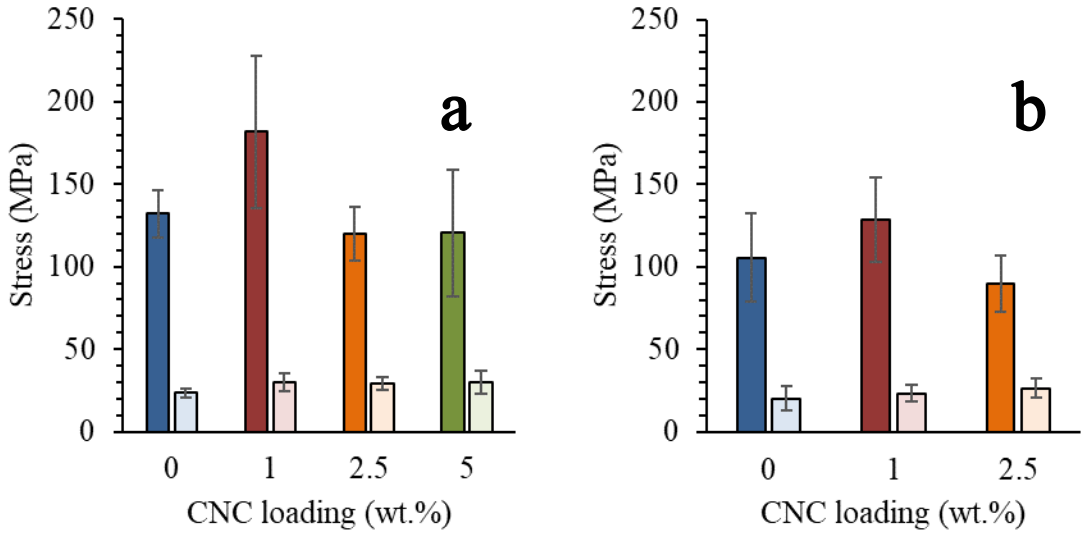

Figure 8.4 - Stress at break values for (a) 44EVOH and (b) 48EVOH composites uniaxially drawn at 10 mm/min measured in the MD (dark) and CD (light).

Figure 8.5 and Figure 8.6 show the comparisons for E' and stress at break values among the uniaxially drawn neat polymers and 1 and 2.5 wt.% CNC or CNF loadings in 44EVOH composites. As can be seen in Figure 8.5, the E' values for the 1 wt.% CN loadings were similar to one another while the composite with the 2.5 wt.% CNF/44EVOH composite had a higher E' value compared to the 2.5 wt.% CNC/44EVOH composite. However, the E' values for the nanocomposites with CNFs were within error of the stretched neat polymer. The differences in the E' values for the 2.5 wt.% CN composites was attributed to the differences in the polymer crystallinity measured with DSC due to confinement effects discussed previously for the composite with CNCs.

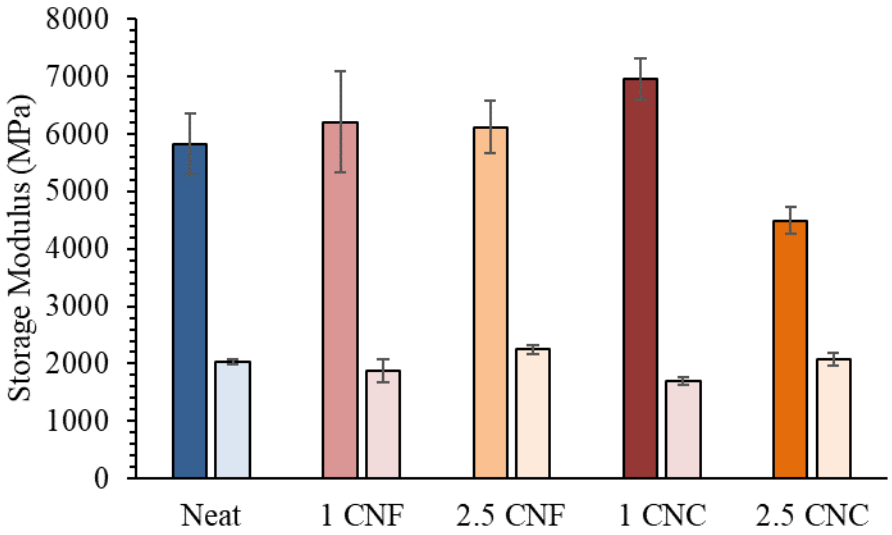

Figure 8.5 - E' values at 30 °C for 44EVOH composites with either 1 or 2.5 wt.% CNCs or CNFs uniaxially stretched.

The only composite sample that had a statistically significant different stress at break value from the other samples tested was the 2.5 wt.% CNF/44EVOH composite sample (Figure 8.6). This composite had a lower stress at break value compared to the 2.5 wt.% CNC/44EVOH composite, although it was not statistically different from the neat 44EVOH. This decrease was attributed to CNF aggregation and networking in the polymer matrix as can be seen from POM images taken above the melting temperature of the polymer matrix (Figure 8.7). The POM results suggested the polymer orientation was erased upon melting in the neat polymer sample while there was still orientation of either the polymer matrix or CNs in the composite samples. The blue domains that appear for 2.5 w.t% CNF/44EVOH suggested there were CNFs that did not align in the direction of applied uniaxial strain. The networking behavior of CNFs at lower loadings compared to

CNCs due to their morphology and higher aspect ratios impeded the alignment of CNFs in the applied strain direction, and thus some contribution to the E' value or stress at break would be from transverse properties of the nanofibrils. This behavior the decreased values in stress at break versus nanocomposites with similar loadings of CNCs.

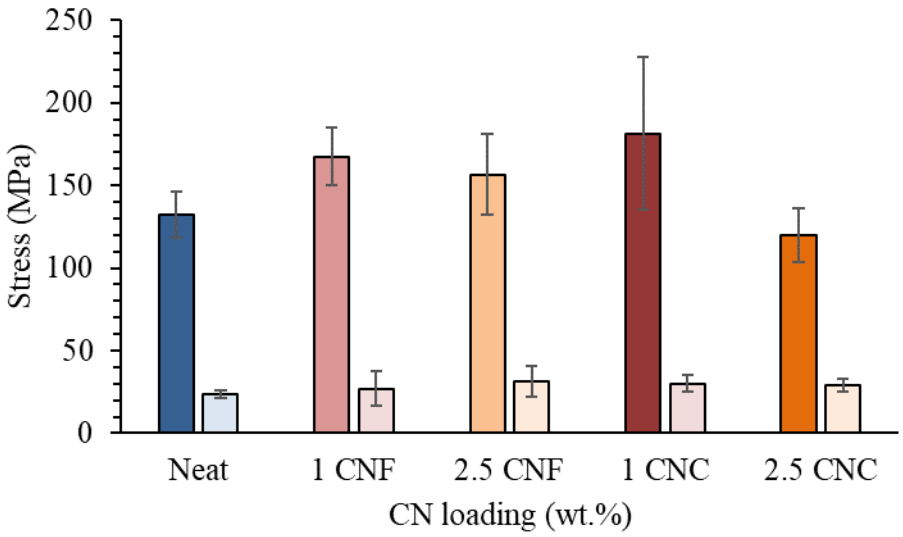

Figure 8.6 - Stress at break values for 44EVOH composites with either 1 or 2.5 wt.% CNCs or CNFs that were uniaxially stretched.

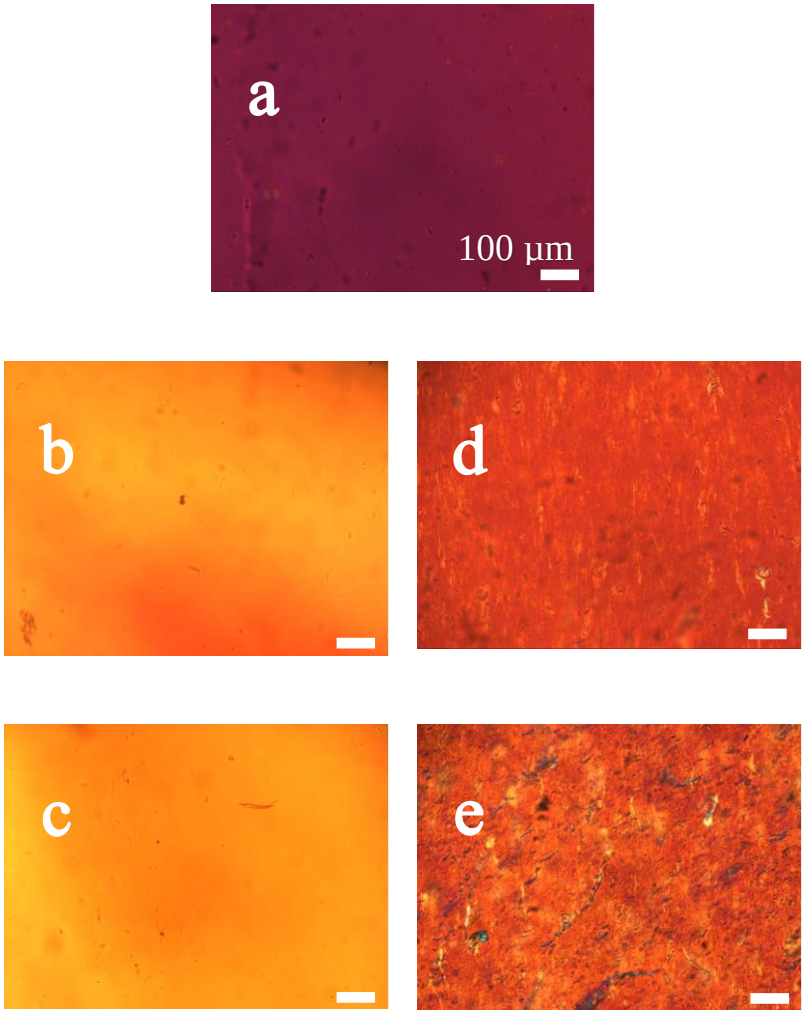

Figure 8.7 - POM of uniaxially drawn (a) neat 44EVOH, (b) 1 wt.% CNC/44EVOH, (c) 2.5 wt.% CNC/44EVOH, (d) 1 wt.% CNF/44EVOH, and (e) 2.5 wt.% CNF/44EVOH when the polymer was melted. Arrow in (a) indicated direction of applied strain for all samples.

8.2.2 Second stretching step

Because the mechanical properties were higher in both the isotropic and uniaxially drawn 44EVOH polymer and nanocomposites compared to 48EVOH samples, the second drawing step was implemented and the resultant structure, mechanical, and thermal properties were investigated only in the 44EVOH polymer and nanocomposites. Films were first drawn in one direction to 300 % applied strain with an extension rate of 1 mm/min, followed by drawing in the second direction perpendicular to the first drawing direction to an applied strain of 150 % and a 10 mm/min extension rate. It was hypothesized the arc length traveled by the long axis of the CNCs would be proportional to the draw ratio applied to the film when the sequential biaxial stretching protocol was implemented. In this context, the draw ratio is calculated by dividing the applied strain used in the first drawing direction by the strain applied in the second drawing direction. Thus, for a draw ratio of two, the nanoparticles were hypothesized to rotate approximately 45° with respect to their original orientation (Figure 8.8). The E' values from DMA were used as a means of inferring the orientation of the CNCs and polymer matrix when the films were biaxially drawn and were presented in Figure 8.9. As can be seen in the figure, E' values for the neat and 1 wt.% CNC/44EVOH samples were higher in the CD compared to MD, while both of these values were overall lower in the biaxially stretched sample compared to the MD E' values for the uniaxially stretched samples. This suggested the neat polymer and CNC loadings below the percolation threshold determined in Chapter 7 were over-rotated such that the long axis of the polymer and CNCs were oriented in the second drawing direction rather than the first drawing direction. However, the E' values in both the MD and CD for the 2.5 wt.% CNC/44EVOH 5 wt.% CNC/44EVOH samples that were biaxially stretched

were similar to one another, and the values for the biaxially stretched 2.5 wt.% CNC/44EVOH composite were similar or higher than the E' values measured for the uniaxially stretched and isotropic nanocomposites. This suggested there was a critical CNC loading for which the mobility of the nanoparticles decreased such that they were not over rotated to the second drawing direction. This loading was in the vicinity of the critical threshold for particle network formation determined in Chapter 6 for 44EVOH nanocomposites.

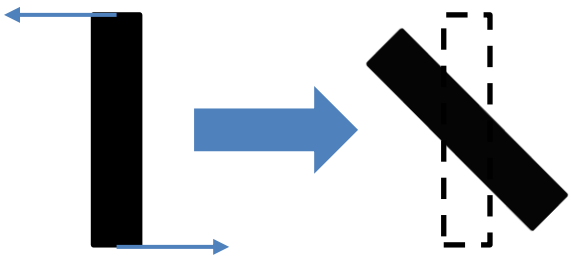

Figure 8.8 - Model depicting the rotation of a CNC during the second drawing step from its original orientation such that the long axis is parallel to the first drawing direction to its final orientation approximately 45° with respect to both drawing directions.

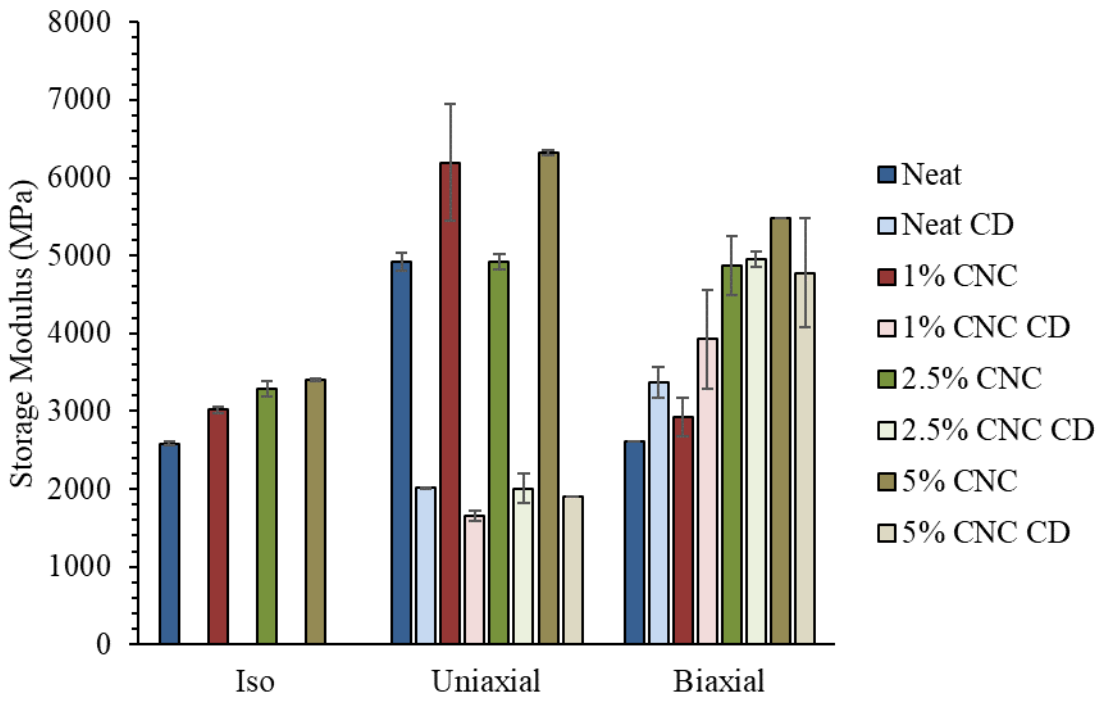

Figure 8.9 - E' values at 30 °C measured in the MD and CD for 0 (blue), 1 (red), 2.5 (green), and 5 (gold) wt.% CNC/44EVOH nanocomposites that were isotropic, uniaxially stretched with an extension rate of 1 mm/min, and biaxially stretched with a 1 mm/min extension rate in the first drawing direction and 10 mm/min extension rate in the second drawing direction with a draw ratio of two. Drawn samples were measured in MD and CD.

As can be seen in Figure 8.10, the E' values for the biaxially stretched 2.5 wt.% CNC/44EVOH sample were also similar across the range of temperatures tested compared to the uniaxially stretched sample measured in the MD, while the E' values for the neat sample that was biaxially stretched had lower values across all temperatures when compared to the uniaxially stretched sample measured in the MD. In fact, the E' values measured in the MD for the biaxially stretched neat 44EVOH decreased to values at or

below the unstretched nanocomposite above T_g and this was due to the test samples warping at higher temperatures. Likewise, for the uniaxially stretched sample measured in the CD, there was a significant decrease in E' when measured above T_g, and this was due to a rapid decrease in the sample cross section measured in the instrument attributed to relaxation of the polymer chains. Therefore, in order to ensure the modulus values reported ideally reflect the mechanical behavior of the testing sample with the original geometry, E' as a function of temperature is presented up to 60 °C in Figure 8.10 due to warping observed in the uniaxially stretched samples measured in the CD as well as in the biaxially stretched neat polymer measured in either direction. The similarity in E' values across the range of temperatures tested for the MD E' values of the uniaxially stretched 2.5 wt.% CNC/44EVOH composite and the E' values for the biaxially stretched film measured in either the MD or CD suggested there was retention of higher E' values across a wide temperature range for the composite when it was biaxially stretched compared to the isotropic composite. The isotropy of the E' values also increased when the polymer and composite were biaxially stretched as compared to the uniaxially stretched samples measured in the MD and CD. While the differences in E' values and the increased uniformity of the E' values in-plane of the biaxially stretched composite suggested the CNC arrangement imparted mechanical reinforcement benefits not observed in the uniaxially stretched samples, a biaxially stretched composite made with a faster extension rate during the first drawing step was investigated to determine how the microstructures developed under different prestressing conditions.

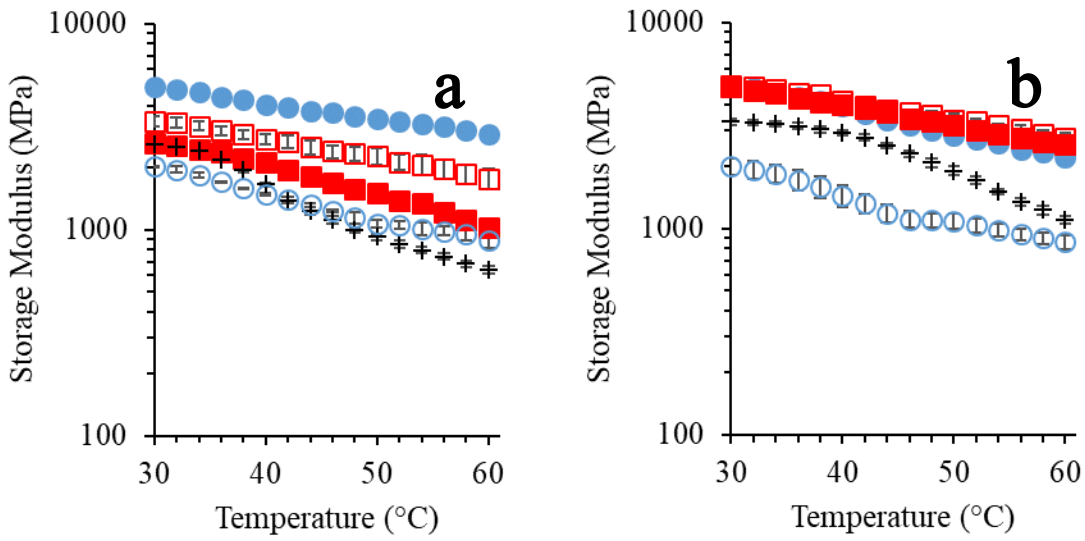

Figure 8.10 - (a) E' as a function of temperature measured in the MD (filled) and CD (open) for neat 44EVOH isotropic (+'s), uniaxially stretched (circles), and biaxially stretched (squares) stretched to final applied strain values for 300% with a 1 mm/min extension rate in the first drawing direction and 150 % with a 10 mm/min extension rate in the second drawing direction. (b) E' as a function of temperature measured in MD (filled) and CD (open) for 2.5 wt.% CNC/44EVOH composites that were isotropic (+'s), uniaxially stretched (circles) and biaxially stretched (squares) stretched to an applied strain of 300 % with a 1 mm/min extension rate in the first drawing direction and 150% with a 10 mm/min extension rate in the second drawing direction.

A faster yet still controllable extension rate for the first stretching step was implemented with the universal testing frame to determine if the anticipated prescribed microstructures could be constructed. The increased extension rate in the first drawing direction was anticipated to increase thermomechanical properties in the polymer and

nanocomposites compared to the samples first stretched with a 1 mm/min extension rate, particularly in the MD [233]. When the films were stretched with an extension rate of 10 mm/min for both drawing directions, there was a significant change in the E' values observed in the MD and CD (Figure 8.11). While MD and CD E' values for neat 44EVOH and 1 wt.% CNC/44EVOH composite samples were similar for the two extension rates, the degree of anisotropy between MD and CD for E' of 2.5 and 5 wt.% CNC/44EVOH composites increased with the increased extension rate in the first drawing direction. Additionally, the E' values measured in the MD decreased for the films stretched with a 10 mm/min rate versus 1 mm/min, while the E' values measured in the CD increased. The change in anisotropy of the measured E' values when the composites were stretched with an increased extension rate were attributed to the difference in time it took to stretch the samples during the first drawing step. The samples stretched with an extension rate of 1 mm/min were exposed to temperatures above T_g of the polymer matrix for 10 times longer than the film stretched at 10 mm/min extension rate. This would cause some annealing of the polymer structure which would be revealed as higher X_c or T_m in DSC measurements. Increased annealing of the polymer matrix would then require either faster drawing rates or higher applied strains to orient the polymer chains/ CNCs in a similar fashion to what was observed for the 10 mm/min samples that indicated anisotropy in the E' values. However, the values for X_c were similar among the biaxially stretched samples tested at two different extension rates (Figure 8.18), which suggested there was minimal annealing of the polymer structure and increased relaxation of the amorphous polymer structure due to increase dwell time when the films were stretched at the slower extension rate. Similarities in thermal properties measured by DSC were also observed by Franco-Urquiza

et al. [263] for a 44EVOH sample that was uniaxially stretched even though they also reported increased ultimate tensile stress for the EVOH sample that was stretched with a slower extension rate. The authors attributed the differences in mechanical behavior of the drawn polymers to annealing during the slower stretching rate as well as proximity to the polymer's characteristic relaxation time. The authors proposed crystal perfection was restricted at higher stretch rates due to rapid tensile drawing at a rate that was faster than polymer relaxation. Therefore, to prevent over rotation of CNCs and orientation of polymer chains in the second drawing direction, it was anticipated a lower applied strain would assist in the formation of the tensegrity- inspired microstructures of the 10 mm/min polymer and nanocomposites.

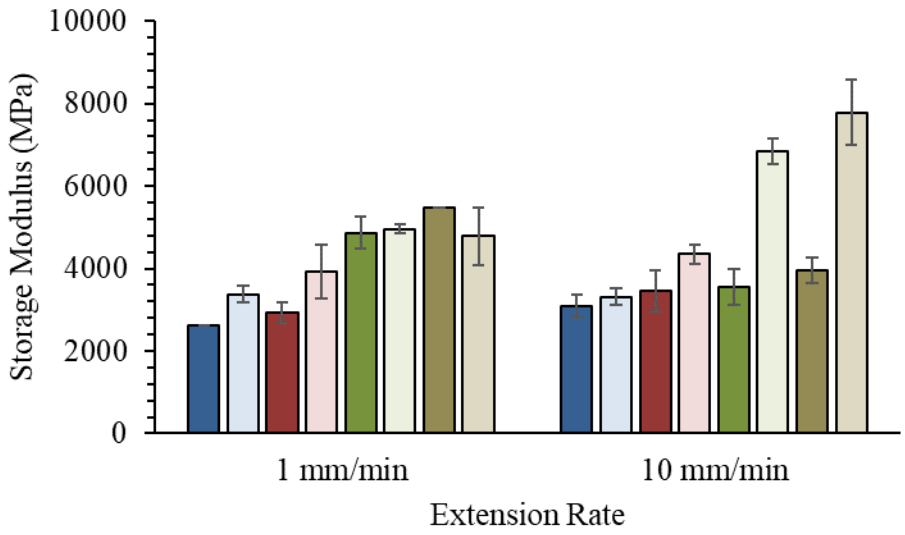

Figure 8.11 - E' values at 30 °C measured in the MD (dark) and CD (light) for 0 (blue), 1 (red), 2.5 (green), and 5 (gold) w.t% CNC/44EVOH nanocomposites biaxially stretched with a 1 mm/min extension rate or 10 mm/min extension rate implemented for the first drawing direction. Applied strains of 300 % and 150 % were used for the first and second drawing directions, respectively.

Based on the results in Figure 8.9, Figure 8.10, and Figure 8.11, the 2.5 wt.% CNC/44EVOH nanocomposite was further investigated for the implementation of the biaxial stretching protocol using the higher first drawing extension rate but to a lower applied strain (Figure 8.12). Neat 44EVOH was also studied at the lower applied strain for comparison. Uniaxially stretched samples measured in the CD as well as the biaxially stretched neat polymer measured in both the MD and CD exhibited warpage above T_g that caused the sample dimensions to be different from the initial conditions during DMA tests. This resulted in a significant decrease and/or variability in the E' values at temperatures

above approximately 60 °C. Therefore, the curves for the uniaxially stretched polymer and composite measured in the CD and the biaxially stretched neat polymer measured in either the MD or CD are only presented up to 60 °C in Figure 8.12. When the neat polymer was biaxially stretched, values for E' were similar in both the MD and CD and these values were higher than or similar to the isotropic polymer across all temperatures tested but lower than the uniaxially stretched polymer sample measured in the MD. However, when the 2.5 wt.% CNC nanocomposite was biaxially stretched, E' values below T_g were higher than the isotropic system and similar to the uniaxially stretched sample in the MD. Unlike the uniaxially stretched sample, E' values in both MD and CD were similar for the biaxially stretched nanocomposite. This suggested not only did the sequential biaxial stretching protocol increase isotropy of the thermomechanical properties of the nanocomposite, but the properties were higher than if the nanocomposite was unstretched. The increase in isotropy of the mechanical properties of the biaxially stretched nanocomposite was attributed to the decreased orientation of the polymer and CNCs in the MD and increased orientation in the CD compared to the uniaxially stretched nanocomposite.

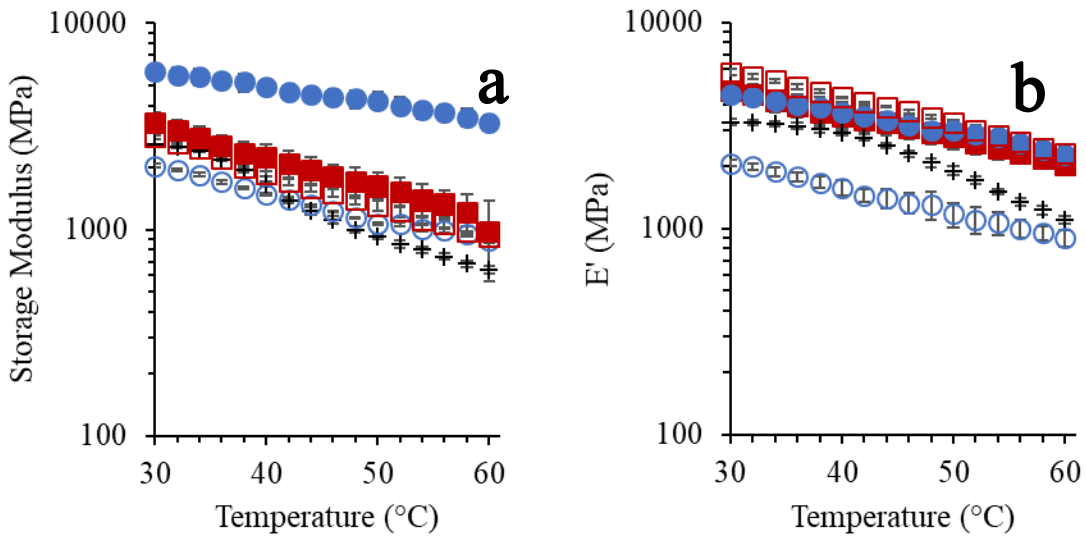

Figure 8.12 - E' as a function of temperature for (a) neat 44EVOH and (b) 2.5 wt.%/44EVOH samples that are isotropic (+ symbols), uniaxially stretched (circles) and biaxially stretched (squares). Properties of stretched samples were tested in the MD (filled symbols) and CD (open).

The stress at break values for the stretched and unstretched polymer and 2.5 wt.% CNC/44EVOH composite were compared to one another and used as a compliment to the thermomechanical data. The values for stress at break were used because the yield stress was difficult to discern for the stretched samples measured in the MD. As can be seen in Figure 8.13, the highest values for stress at break were measured in the MD of the uniaxially stretched polymer and composite. Statistical analysis via two-tailed t-tests determined the stress at break values for the uniaxially stretched polymer and composite measured in the MD were significantly different from both the isotropic and biaxially stretched samples measured in the MD. However, there were no statistically significant differences in the stress at break values for the polymer or composite samples that were

biaxially stretched measured in either the MD or CD when compared to one another as well as when these values were compared to the stress at break for the isotropic samples. The increase in mechanical isotropy of the biaxially stretched polymer and composite samples compared to the uniaxially stretched samples further suggested the polymer/ particle orientation decreased in the MD and increased in the CD when the films were biaxially stretched as opposed to just uniaxially stretched.

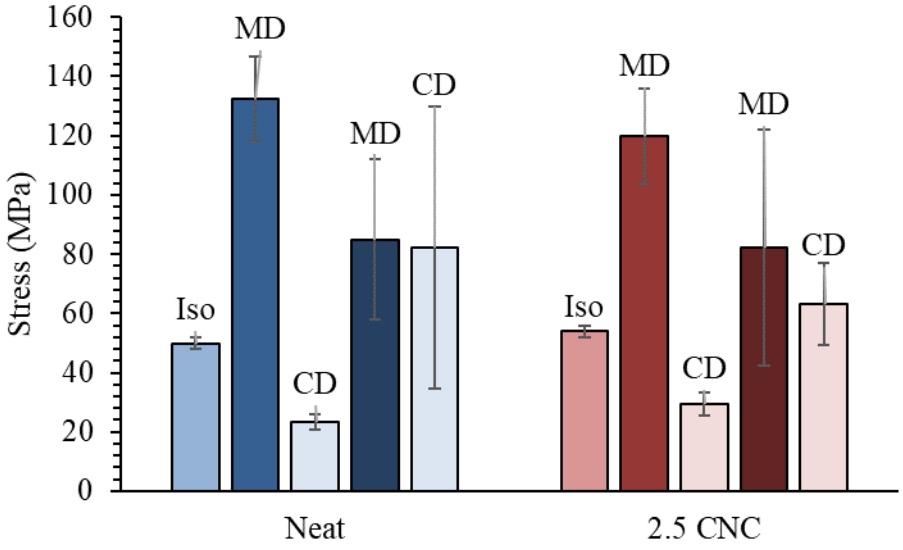

Figure 8.13 - Stress at break of 44EVOH and the 2.5 wt.% CNC/44EVOH composite that were isotropic, uniaxially stretched with an extension rate of 10 mm/min, and biaxially stretched with extension rates of 10 mm/min in both drawing directions. The biaxially stretched sample was first stretched to an applied strain of 300% followed by a second stretch to an applied strain of 100%.

8.3 Structure and morphology

8.3.1 XRD

In order to determine how the first and second stretching steps affected the polymer and nanocomposite structures of 44EVOH, WAXS patterns were captured with respect to MD and CD for the neat 44EVOH and 2.5 wt.% CNC/44EVOH nanocomposite samples that were uniaxially stretched to 300% applied strain at a 10 mm/min extension rate and biaxially stretched with the 10 mm/min extension rate in both drawing directions and an applied strain in the second drawing direction of 100%. As can be seen in Figure 8.14, the patterns of the stretched samples appeared different from the isotropic systems. When the systems were uniaxially stretched, the peak assigned to (200) was not observed in the neat polymer and the (101) peak broadened. While the (200) peak never disappeared in the nanocomposite system, the intensity of the (101) peak relative to the (200) peak increased and broadened. These changes in the XRD patterns compared to the isotropic systems have been attributed to the formation of a mesophase in the polymer matrix due to alignment of the amorphous phase in addition to the crystallites when EVOH is stretched to high applied strains [233, 261]. However, when the systems were biaxially stretched, the (200) peak/ shoulder reappeared in the neat polymer and had a relatively higher intensity with respect to the (101) peak in the nanocomposite which suggested there was some long-range ordering in direction perpendicular to that plane. When the XRD patterns that were collected such that the MD was aligned parallel with the beam and detector was compared to patterns collected in the CD (Figure D.6), there were no discernible differences in the patterns both when peak positions were compared as well as the intensity of the diffraction peaks. Also, because the diffraction peaks associated with CNs could not be deconvoluted

from the polymer diffraction peaks, it was difficult to ascertain the orientation of the CNs when the composites were uniaxially or biaxially stretched. Therefore, the only structural properties of interest that were used to glean differences in the different samples were the X_c values and polymer crystal density. Other authors have demonstrated that CNCs [120, 201] and other nanoparticles [2] in a semicrystalline polymer matrix, as well as neat EVOH [261] aligned in the direction of applied strain when the polymer or nanocomposite was subjected to uniaxial or biaxial stretching. Therefore, it is likely the CNCs and polymer chains were aligned in the direction of applied uniaxial strain in the first drawing direction and subsequently being disoriented a certain amount from the first drawing direction when the film was biaxially stretched.

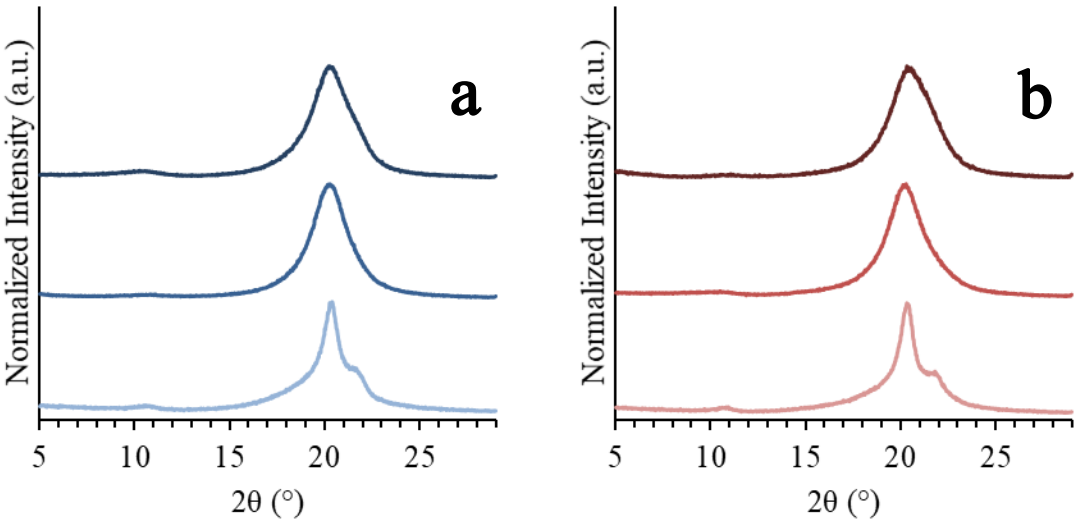

Figure 8.14 - XRD patterns for neat (a) 44EVOH (b) 2.5 wt.% CNC/44EVOH isotropic, uniaxially, and biaxially stretched samples.

In addition to the differences in the patterns for neat and 2.5 wt.% CNC/44EVOH systems when they were stretched, the values for X_c and crystal density were also observed to change when the samples were uniaxially and biaxially stretched. X_c of both uniaxially and biaxially stretched samples were higher than the respective isotropic polymer and nanocomposite, and the crystallinity of the biaxially stretched neat polymer was higher than the X_c of the biaxially stretched nanocomposite. These values were similar to those reported by others studying structural changes of neat EVOH that was uniaxially or biaxially stretched [67]. However, the crystal density was observed to decrease in the neat polymer with each stretching step implemented, whereas the density of the nanocomposite system increased from the isotropic system when it was biaxially stretched. The increase in the crystallinity coupled with a decrease in crystal density, particularly in the uniaxially

stretched samples further suggested the development of an aligned mesophase that was not necessarily attributed to a perfectly ordered polymer crystalline phase [261]. The changes in crystallinity and crystal density of the neat polymer with the sequential biaxial stretching method suggested the E' values observed in Figure 8.12 were attributed to changes in the polymer structure itself in addition to changes in the polymer chain orientation. The similarity in the values for crystallinity of the neat polymer and nanocomposite particularly when the samples were uniaxially or biaxially stretched suggested the polymer structure was similar in both samples as a result of the stretching protocol implemented.

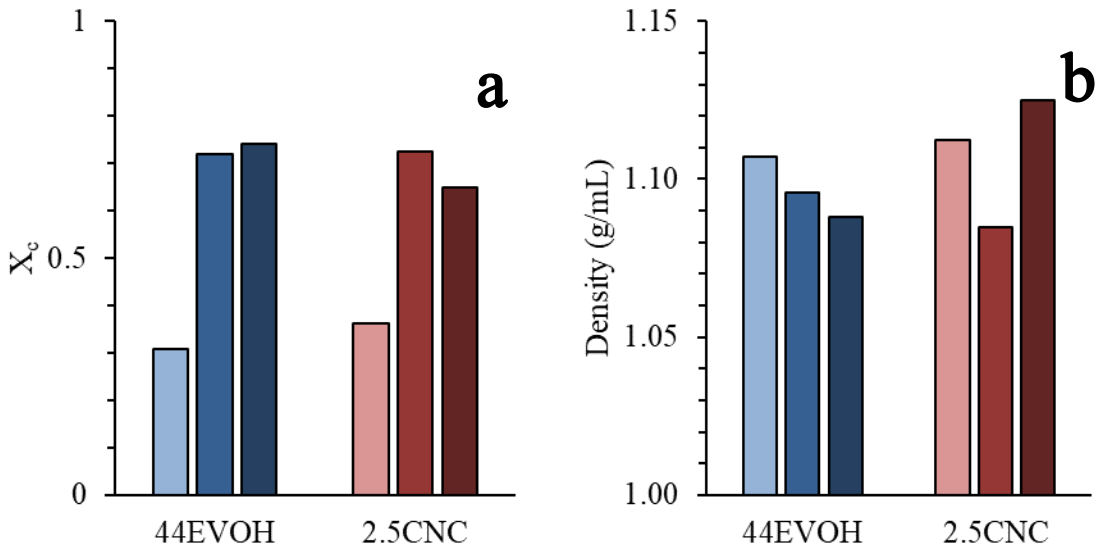

Figure 8.15 - (a) X_c and (b) density of crystalline phase of neat 44EVOH (blue) and 2.5 wt.% CNC/44EVOH (red) that were isotropic (lightest color), uniaxially stretched (medium), and biaxially stretched (darkest). Samples measured with respect to the first drawing direction.

8.3.2 Thermal Properties

X_c values calculated from the first heating cycle of DSC tests for the samples stretched in the first drawing direction at different extension rates were compared to understand their polymer structures. As can be seen in Figure 8.16, the crystallinity values of the neat 44EVOH samples that were uniaxially stretched at either a 1 or 10 mm/min extension rate were similar to one another. Additionally, the X_c values were higher in both cases when compared to the isotropic neat polymer. This suggested the polymer structure was affected by the stretching protocol, i.e. the polymer chain alignment increased when it was uniaxially stretched, but the extension rate implemented did not affect the polymer structure significantly.

The thermal properties were observed to change when the CNCs were incorporated and the nanocomposites were uniaxially stretched. While X_c values were similar for 1 wt.% CNC/44EVOH samples that were uniaxially stretched with either extension rate, the 2.5% CNC/44EVOH and 5 wt.% CNC/44EVOH composites exhibited different behavior when the extension rate was changed for the first drawing step. The 2.5 wt.% CNC/44EVOH composite had the overall lowest values for X_c when uniaxially stretched, and this change in polymer structure explained why the E' values were lower for this sample compared to the others tested. However, these results do not suggest the samples were annealed when they were stretched at the slower stretching rate as anticipated, and therefore the changes observed in the E' values were attributed to rapid orientation of the polymer chains that was maintained more in the faster stretched samples due to the slower polymer relaxation times with respect to the extension rate value applied to the film [263].

The thermal properties of the uniaxially stretched composites made in the 48EVOH matrix also suggested the polymer structure had an important role in determining the resultant E' values discussed earlier. The 1 wt.% CNC/48EVOH composite had the highest X_c value, although due to the spread in the data, the X_c value for this composite was similar to the neat polymer. The X_c values for 2.5 and 5 wt.% CNC/48EVOH composites were lower than both the neat polymer and composite with 1 wt.% CNCs. When compared to the isotropic samples, all of the polymer and composite samples exhibited higher X_c values with the exception of the 2.5 wt.% CNC/48EVOH composite, which had a similar X_c value to the isotropic counterpart. The trend in X_c values qualitatively agrees with the trend in E' values observed in Figure 8.3 and suggested the CNC agglomeration seen in the 2.5 wt.% and 5 wt.% CNC/48EVOH composites prevented the polymer from attaining the same degree of alignment in the direction of applied strain as the other samples.

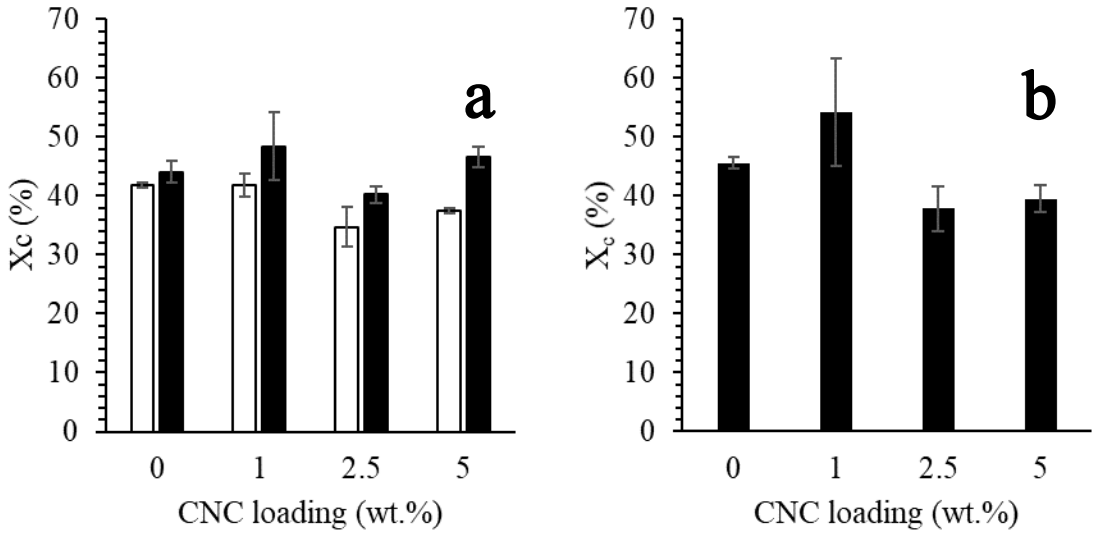

Figure 8.16 - X_c values of uniaxially stretched (a) 44EVOH samples with a 1 (white) or 10 mm/min (black) extension rate and (b) 48EVOH samples stretched with a 10 mm/min extension rate.

When comparing the composites made with CNCs to those made with CNFs, the X_c values were overall similar when comparing nanocomposites with comparable nanoparticle loadings. This suggested the changes in polymer structure were a result of the stretching imparted on the sample rather than the nanoparticle selection. Because the polymer structure was similar in the stretched samples, the increase in E' for the 2.5 wt.% CNF/44EVOH compared to the neat polymer and 2.5 wt.% CNC/44EVOH composite suggested the CNFs were able to better mechanically reinforce the polymer matrix than the CNCs when the samples were uniaxially stretched due to increased stress transfer ability of the higher aspect ratio nanofibers.

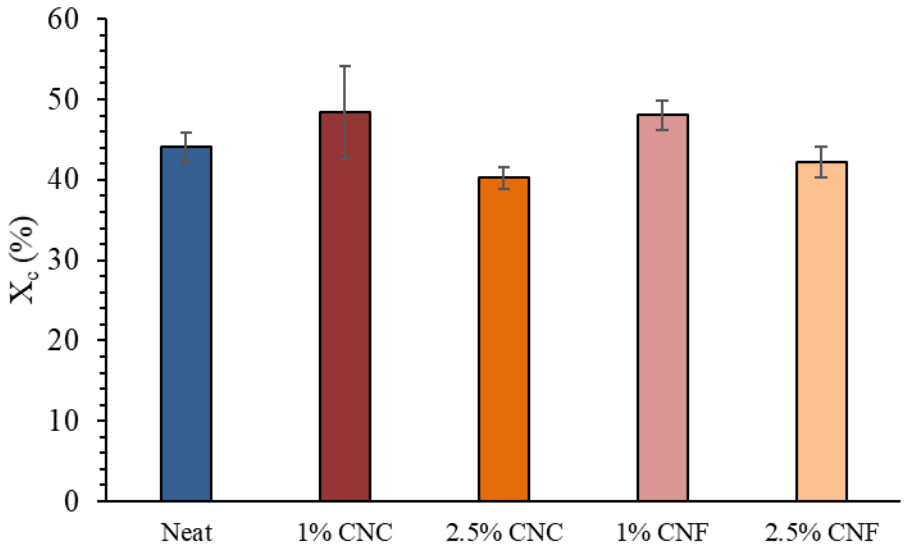

Figure 8.17 - Thermal properties for neat 44EVOH as well as 44EVOH with 1 and 2.5 wt.% CNCs or CNFs incorporated and uniaxially stretched with a 10 mm/min extension rate

When the 44EVOH samples reinforced with CNCs were biaxially stretched to an applied strain of 150%, the X_c values from the first heating scan were similar to each other when comparing the films that were first stretched at different extension rates (Figure 8.18). These values were lower than the uniaxially stretched polymer and similar to the isotropic polymer. These X_c values measured with DSC corroborate what was observed in the XRD patterns for the different stretched samples, as the structure of the biaxial samples had displayed some characteristics of the isotropic polymer structure that were not apparent in the uniaxially stretched samples. However, the 1 wt.% CNC/44EVOH composite samples that were biaxially stretched displayed higher X_c values compared to the neat polymer and other composites. The increase in X_c for 1 wt.% CNC/44EVOH did not equate to higher E'

values compared to the other composites, and therefore other factors such as CNC content and alignment affected the resultant thermomechanical properties when the samples were biaxially stretched (Figure 8.11). Otherwise, the 2.5 and 5 wt.% CNC/44EVOH composites that were biaxially stretched had similar X_c values to the neat polymer.

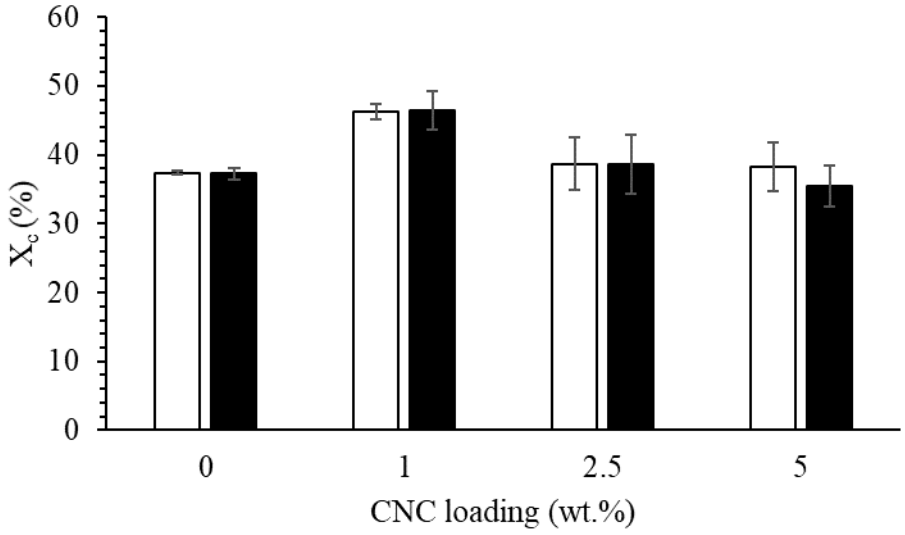

Figure 8.18 - X_c values measured from first-heat DSC scans for 0, 1, 2.5, and 5 wt.% CNC/44EVOH composites that were biaxially stretched with either a 1 mm/min (white) or 10 mm/min (black) extension rate for the first drawing direction.

Figure 8.19 displays the X_c values measured from the first heating rate of DSC tests for neat 44EVOH and 2.5 wt.% CNC/44EVOH composite samples that were isotropic, uniaxially stretched, and biaxially stretched using the 10 mm/min extension rate for both

stretching steps, as well as a 100% applied strain for the second drawing step. As can be seen in the figure, the trends and values for X_c were similar for the neat polymer and composite regardless of stretching step analyzed. The X_c values were overall higher in the stretched samples due to increased polymer alignment than the isotropic samples. These X_c values suggested while the polymer structure changed as a result of either uniaxial or biaxial stretching, the polymer structure was similar whether there were CNCs present or not. These results lend credence to CNC alignment imparting additional mechanical reinforcement abiltiy when taking into account measured E' values observed in Figure 8.12 even though neither polymer nor CNC orientation could not be explicitly elucidated from XRD results.

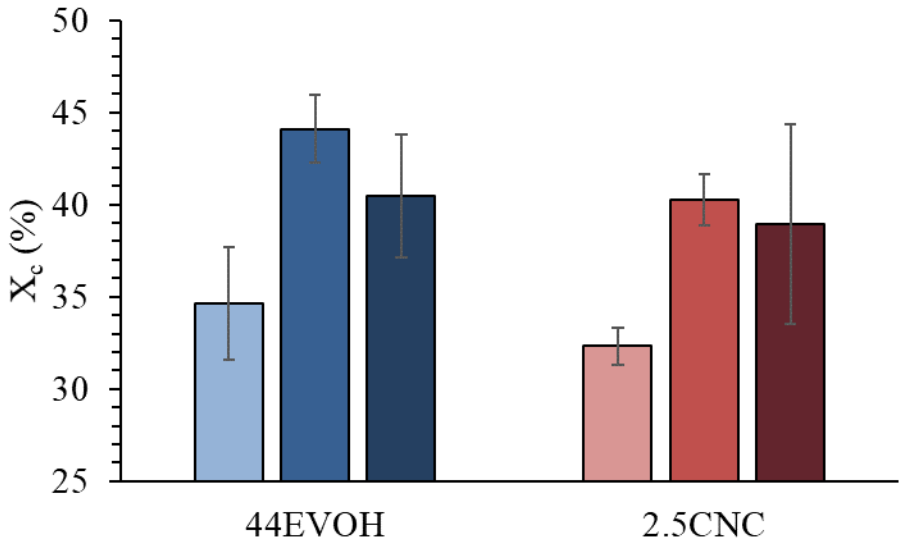

Figure 8.19 - Thermal properties of neat 44EVOH (blue) and 2.5 wt.% CNC/44EVOH (red) samples that were isotropic (light), uniaxially stretched (medium), and biaxially stretched (dark).

The results from thermomechanical, mechanical, XRD, and thermal characterization suggested additional reinforcement benefits could be attained when the CNCs were arranged in prescribed microstructures in the matrix through a biaxial mechanical drawing method. Mechanical and thermomechanical properties were used to infer CNC and polymer orientation in the nanocomposites after each drawing step, as orientation analyzed from XRD patterns was inconclusive. When the polymer and nanocomposites were uniaxially stretched, the thermomechanical and mechanical properties increased, and the anistropy of these properties increased with the exception of the 2.5 wt.% CNC/44EVOH composite. These results suggested the polymer and CNCs aligned in the direction of applied strain, and this was expected [233, 260] as the stiffness

and mechanical properties of the polymer and nanoparticles are known to be higher along certain axes of individual polymer chains, polymer crystallites and anisotropic nanoparticles [1, 264, 265]. The notable difference in the mechanical and thermomechanical properties of the uniaxially stretched 2.5 wt.% CNC/44EVOH nanocomposite were intriguing, but were attributed to the decreased crystallinity of this sample compared to stretched composites with different particle loadings due confinement of the polymer chains at a CNC loading that approached the onset of network formation.

In order to determine the role CNC incorporation and arrangement in the 44EVOH matrix had on the thermomechanical properties of the composite, a new term ΔE' was defined and calculated in Equation 8.3:

$$\Delta E'_n = E'_{n,composite} - E'_{n,polymer} \qquad 8.3$$

where $E'_{composite}$ is the storage modulus value of the composite for the given stretching step, n, and $E'_{polymer}$ is the storage modulus for the neat polymer for a given stretching step, n. The term n is used to denote the given stretching step such as isotropic, uniaxial, or biaxial. For the values calculated for stretched samples, E' values measured in the MD were used for the calculations. As can be seen when the ΔE' values are plotted as a function of temperature (Figure 8.20), the CNCs contributed differently to the overall thermomechanical behavior of the composite depending on the stertching step implemented and the temperature. Values above zero indicate increased reinforcement by the CNCs for a particular stretching step, while values below zero indicate mechanical

behavior predominately directed by the polymer. The values for the isotropic samples indicated the CNCs contributed to the overall mechanical reinforcement of the polymer matrix across all temperatures, but this contribution decreased as the temperature increased above the T_g of the neat polymer. When the samples were uniaxially stretched, the values were all below zero across the entire temperature range tested and this coincided with a decrease in X_c for the 2.5 wt.% CNC/44EVOH composite compared to the neat stretched 44EVOH sample. This suggested the mechanical behavior was primarily dictated by the changes in the polymer structure when the samples were uniaxially stretched as opposed to the particle alignment at 2.5 wt.% CNC loadings. However, when the samples were biaxially stretched the values were above zero across all temperatures and remained relatively constant through the T_g of the isotropic polymer and composite. X_c as measured by XRD and DSC indicated the polymer structure was similar in both the neat polymer and 2.5 wt.% CNC/44EVOH composite when they were biaxially stretched.

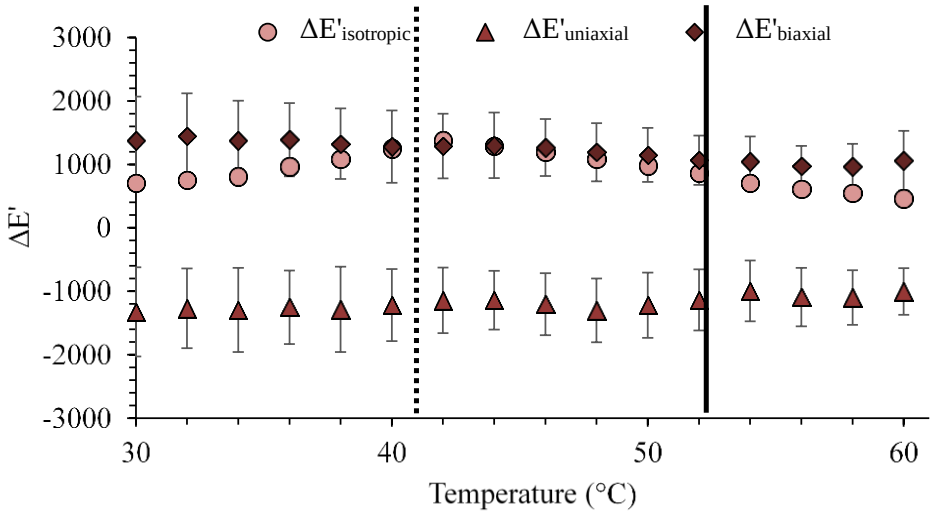

Figure 8.20 - ΔE' values calculated to compare the contribution of CNC incorporation into the 44EVOH matrix when it was isotropic (circles), uniaxially stretched (triangles), and biaxially stretched (diamonds). Vertical lines indicate the T_g of the isotropic neat polymer (dotted line) and composite (solid line).

The relative contributions of the stretching steps and the CNCs were also compared by normalizing the E' values of the stretched polymer as well as the isotropic and stretched composite with respect to the isotropic neat polymer. These values were labelled as E'_r, calculated for the MD for stretched samples in Equation 8.4 and are displayed in Figure 8.21.

$$E'_{r,i} = \frac{E'_i}{E'_{neat,isotropic}} \quad 8.4$$

where *i* denotes the sample and stretching protocol of interest to compare to the storage modulus of the isotropic neat sample. Values above 1 indicated the sample of interest had an overall beneficial contribution to the storage modulus of the polymer or composite, while values at or below 1 indicated there was no additional mechanical reinforcement imparted by that specific sample compared to an unstretched neat polymer sample. Due to warping observed specifically in the neat polymer that was biaxially stretched, the values of E'_r were only calculated and investigated up to 60 °C. As can be seen in the below figure, the highest contributions to the overall storage modulus of the polymer occurred when it was uniaxially stretched and measured in the MD. However, the lowest values calculated for E'_r were observed when the neat polymer was biaxially stretched. While the isotropic composite provided increases to the storage modulus across all temperatures of interest in Figure 8.21, these contributions began to decline above the T_g of the isotropic composite, or approximately above 52 °C. Whereas the uniaxially stretched polymer and the stretched composite samples displayed increases as a function of temperature across all temperatures of interest in the below figure. This suggested the stretched state of the polymer and aligned CNCs retained stiffness at temperatures above which the isotropic neat polymer would begin to display rubbery behavior in the amorphous phase. This indicated the amorphous polymer structure was affected by the induced polymer alignment and particle arrangements as a result of uniaxial and biaxial stretching. The changes to the amorphous structure of the polymer matrix were due to a combination of mesophase formation as seen

in XRD patterns for the stretched samples as well as interactions and immobilization until higher temperatures by the aligned polymer crystalline phase and CNC arrangements. The E'_r values for the biaxially stretched and uniaxially stretched composites were approximately similar across all temperatures, although these values were only calculated for the samples measured in the MD, and therefore the contributions of the biaxially stretched composite were overall higher in all testing directions compared to the uniaxially stretched neat polymer and composite. The overall large differences in $E'_{r,neat,uniaxial}$ and $E'_{r,neat,biaxial}$ values along with the relatively similar $E'_{r,composite,uniaxial}$ and $E'_{r,composite,biaxial}$ values indicated the prescribed particle arrangements in the biaxially stretched composite contributed to an overall beneficial reinforcement of the stretched polymer matrix.

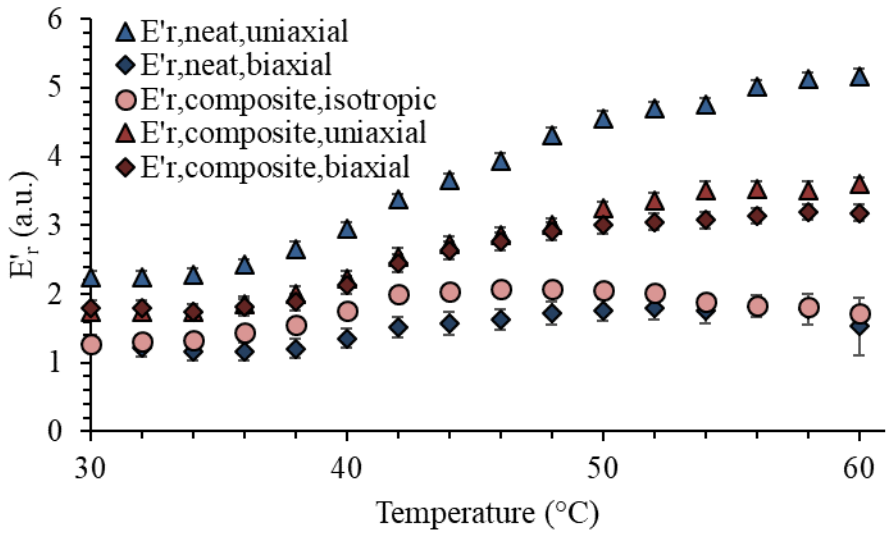

Figure 8.21 - Relative contributions to the overall storage modulus made by either the stretching step implemented or the arrangement of the CNCs. Relative contributions are presented for the uniaxially stretched neat polymer (blue triangles), biaxially stretched neat polymer (blue diamonds), isotropic 2.5 wt.% CNC/44EVOH composite (red circles), uniaxially stretched composite (red triangles), and biaxially stretched composite (red diamonds).

These trends in E' values were different from what was reported by Lee *et al*. [2] when polymer-decorated nanoparticles with a lower aspect ratio than was used in this work were arranged in a semicrystalline polymer matrix with a sequential biaxial drawing method. While the testing mode used in DMA characterization of the samples was different between the current work and Lee's work, where previously the samples were tested under shear while in the current work they were tested in tensile mode, the qualitative trends in the data calculated from $\Delta E'$ and E'_r were still used as a means of comparison between the

two systems. Lee *et al*. observed normalized contributions of shear storage modulus (G') for the composite with the arranged nanoparticles compared to the unstretched neat poylmer were higher below T_g compared to all other stretched and unstretched polymer and composite systems investigated while the normalized G' values were similar to the normalized contributions of the uniaxially stretched composite above T_g.

The qualitative differences in the storage modulus values when comparing the biaxially stretched 2.5 wt.% CNC/44EVOH composite to the uniaxially stretched polymer and composite samples were not expected based on previous work. It was anticipated that nanoparticles with higher aspect ratios such as the CNCs used in the present work compared to the HAp particles investigated previously would increase the mechanical reinforcement efficacy of the prescribed microstructures both below and above T_g. However, this was not the case for the biaxially stretched 2.5 wt.% CNC/44EVOH composite compared to the uniaxially stretched samples measured in the MD. The E' values of the biaxially stretched composite were higher than both the uniaxially stretched neat polymer and composite measured in the MD only at temperatures well above T_g.

While there was seemingly no difference in the E' values of the biaxially stretched composite versus the uniaxially stretched sample measured in the MD in samples stretched with either a 1 mm/min or 10 mm/min extension rate in the first stretching step, the properties of the biaxially stretched sample were more uniform in-plane and higher than what was anticipated for the contributions of the CNCs oriented approximately 45° with respect to each stretching direction (Figure 8.8). Anisotropic nanoparticles such as CNCs were expected to amplify differences in storage modulus in the MD and CD when the

composite was uniaxially stretched, and the overall storage modulus values for the biaxially stretched composite were anticipated to decrease compared to the MD E' value for the uniaxially stretched composite due to an increasing contribution of the transverse modulus of CNCs that coincided with a decreasing contribution of the axial modulus in the MD. In order to understand the contributions of the prescribed microstructures to the thermomechanical properties of the composite more fully, the measured values were compared to a micromechanical model derived from a classical composite laminate theory and Halpin-Tsai equations for unidirectionally aligned filler predicting composite modulus as a function of filler orientation derived from Equations 8.5-8.18 taking into account the aspect ratio and oreintation of the CNCs in the polymer matrix.

$$Q_{11}(\theta) = Q_{11}\cos^4(\theta) + 2(Q_{12} + 2Q_{66})\sin^2(\theta)\cos^2(\theta) + \sin^4(\theta) \quad 8.5$$

$$Q_{11} = \frac{E_{11}}{(1 - \nu_{12}\nu_{21})} \quad 8.6$$

$$Q_{22} = \frac{E_{22}}{(1 - \nu_{12}\nu_{21})} \quad 8.7$$

$$Q_{12} = \nu_{21}Q_{11} \quad 8.8$$

$$Q_{66} = G_{12} \quad 8.9$$

$$E_{11} = E_m \frac{1 + 2(\frac{l}{d})\eta_L \nu}{1 - \eta_L \nu} \quad 8.10$$

$$E_{22} = E_m \frac{1 + 2\eta_T \nu}{1 - \eta_T \nu} \tag{8.11}$$

$$G_{12} = G_m \frac{1 + \eta_G \nu}{1 - \eta_G \nu} \tag{8.12}$$

$$\eta_L = \frac{\frac{E_f}{E_m} - 1}{\frac{E_f}{E_m} + 2(\frac{l}{d})} \tag{8.13}$$

$$\eta_T = \frac{\frac{E_f}{E_m} - 1}{\frac{E_f}{E_m} + 2} \tag{8.14}$$

$$\eta_G = \frac{\frac{G_f}{G_m} - 1}{\frac{G_f}{G_m} + 1} \tag{8.15}$$

$$\nu_{12} = \nu_{12,f} \nu + \nu_{12,m}(1 - \nu) \tag{8.16}$$

$$\nu_{21} = \nu_{12} \frac{E_{22}}{E_{11}} \tag{8.17}$$

$$\nu_{12,m} = \frac{E_m}{2G_m} - 1 \tag{8.18}$$

where Q_{11}, Q_{22}, Q_{12}, and Q_{66} are members of a reduced stiffness matrix that relates strength to strain in mechanical testing [266], $Q_{11}(\theta)$ is the reduced stiffness contribution in the MD direction for a composite with anisotropic particles aligned in an angle θ with respect to the applied load. For the two cases of uniaxial and biaxial alignment, it was assumed θ was 0° or 45°, respectively. Equations 8.10-8.18 are Halpin-Tsai equations and their respective definitions for a composite laminate with unidirectionally aligned filler [267]. E_{11} is the axial modulus of the composite, E_{22} is the transverse modulus, G_{12} is the shear modulus, and ν_{12} and ν_{21} are Poisson's ratios for the in-plane directions. The Poisson's ratio of the polymer, $\nu_{12,m}$, was determined to be approximately 0.36 from measurements in the difference in dimensions of neat polymer samples before and after uniaxial stretching on the universal testing frame. The Poisson's ratio of crystalline cellulose, $\nu_{12,f}$, is approximately 0.3 [268]. E_m is the modulus of the 44EVOH matrix, G_m is the shear modulus of the polymer matrix, and ν is the volume fraction of the CNCs. In the case of 2.5 wt.% CNC loading, this value is 0.0179. For means of comparison with experimental values, all modulus values were taken as the storage modulus measured at 30 °C. Also, in the case of uniaxially stretched samples, E_m was defined as either the storage modulus measured in the MD or CD (approximately 5.8 GPa and 2.0 GPa, respectively) and E_f was assumed to be 50 GPa [59] for the axial modulus and 10 GPa [1] for the transverse modulus of CNCs when calculating values for η_L or η_T, respectively and E_{11} or E_{22}, respectively. The aspect ratio of the CNCs l/d was approximately 21 [112]. Based on these equations, a decrease of approximately 53% was expected in the E' for the biaxially stretched composite with CNCs oriented 45° with respect to either stretching direction compared to the uniaxially stretched composite. However, this was not what was observed in the

experimental data, where the E' values for the biaxially stretched composite remained similar to the uniaxially stretched composite measured in the MD. This difference in theoretical values and measured values of the biaxially stretched samples suggested there was additional mechanical reinforcement of the CNC arrangement in the composite due to the interactions between particles as well as the particles and polymer matrix in the prescribed microstructures. While changes in polymer structure as determined by X_c values measured with DSC and XRD explained the differences in the polymer and composite when they were uniaxially stretched, i.e. higher X_c values in the uniaxially stretched neat polymer indicated more alignment of the polymer chains compared to the composite, the similarity in polymer structure when these systems were biaxially stretched does not fully explain why there was a significant retention in the E' values when the composite was biaxially stretched compared to the biaxially stretched neat polymer and the uniaxially stretched composite. Therefore, the retention of the composite stiffness was attributed to the particle arrangement and interactions between the polymer and particles that was not observed in the biaxially stretched neat polymer, as the stiffness decreased in the neat polymer that was biaxially stretched compared to the uniaxially stretched polymer, and these E' values were similar to the unstretched isotropic neat polymer.

In order to better understand the interactions and spacial arrangement of CNCs in the polymer matrix, interparticle distances were calculated based on the elementary unit cells displayed in Figure 8.22. The CNCs were assumed to have dimensions of approximately 163 nm long (L) and 6.4 nm wide (R) [112], and the polymer was assumed to perfectly coat all CNC surfaces in a well dispersed system. Based on calculations for interparticle distances (2d) in Table 8.1 represented in Figure 8.22, the CNCs were

relatively close to one another with respect to their long axes, and therefore it is possible for the CNCs to interact with one another at this particle loading and create confined areas in the matrix that were stiffer than expected for the bulk polymer. The interphase layer connecting the nanoparticles to the bulk polymer matrix was also suggested to have played an important role in increased thermomechanical properties in the biaxially stretched nanocomposite. The interphase layer is a transition zone between the nanoparticles and the bulk polymer matrix and can consist of cross linking, immobilized polymer chains, entangled polymer chains around or adsorbed to the particle surfaces, and intermolecular bonds such as hydrogen bonding [269, 270]. Pakzad *et al*. [269] determined through changes in the modulus around CNCs in a PVA and a blended PVA-PAA matrix measured with AFM that the interphase thickness between nanoparticles and matrix could extend approximately 12 nm from the CNC surfaces for nanoparticles with similar diameters to those used in the current work. The authors attributed the thickness of the interphase to hydrogen bonding between the CNCs and polymer chains in close proximity to the nanoparticle surfaces. This interphase thickness further extends the ability of CNCs to interact with one another while not physically touching each other such as in a continuous network. T_g, a property that was anticipated to increase if there was confinement of the polymer mobility by the prescribed particle arrangement, decreased when the composite was biaxially stretched compared to the isotropic composite from approximately 52.6 °C to approximately 43.9 °C. Although this decrease in T_g was attributed to the reduction of the mesophase when the composite was biaxially stretched as noted in XRD patterns. Therefore while the changes in storage modulus values of the biaxially stretched composite suggested there were additional and/or different polymer-particle interactions that occurred

as a result of constraints to the polymer matrix afforded by the 2.5 wt.% CNC loading and arrangement in 44EVOH that contributed to increased overall stiffness, these interactions were not due to increased confinement of the polymer chains between nanoparticles when the composite was biaxially stretched.

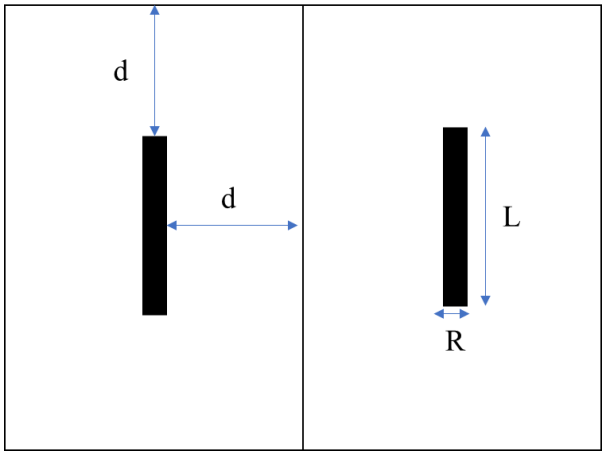

Figure 8.22 - Elementary unit cells containing one CNC (black) in each unit cell surrounded by polymer matrix (white) with thickness d.

Table 8.1 - Interparticle distances calculated from two elementary unit cells containing one CNC surrounded by polymer matrix.

CNC loading (wt.%)	CNC spacing (2d, nm)
0.25	108
0.5	79
1.0	57
2.5	36
5.0	24

The increase in thermomechanical properties when the 2.5 wt.% CNC/44EVOH composite was biaxially stretched was also attributed to the formation of tensegrity-inspired microstructures as a result of applied strains inducing CNC arrangement as well as the polymer-particle interactions in the stretched construct at particle loadings near the onset of CNC network formation in the matrix. The sequential biaxial drawing method was intended to induce prestresses into the composite structure in a similar fashion to tensioning a web of cables in the strut-and-cable model (Figure 2.4). Increased stiffness of tensegrity structures has also been related to the level of prestress imparted in biological systems and predicted in mechanical models [181, 183, 184]. This increase in stiffness was analogous

to the increase in E' values, particularly compared to the isotropic unstretched composite, when the nanocomposite film was prestressed with the sequential biaxial stretching protocol. The thermal properties and the structure observed from XRD patterns of the biaxially stretched composites also suggested while the polymer structure changed when the polymer or composite was uniaxially or biaxially stretched, there were no significant changes to the polymer structure when the biaxially stretched neat polymer and composite were compared to one another. Therefore, the results suggested the polymer crystallites oriented in the direction of applied strains and assisted in the arrangement of the CNCs in the directions of applied strain as there were additional increases to the mechanical and thermomechanical properties of the stretched samples when CNCs were incorporated. This CNC arrangement imparted additional benefits to the thermomechanical behavior of the composite. Also, the increases in the thermechanical properties with the incorporation of stretching to the composite was attributed to the construction of prestressed tensegrity-inspired structures.

8.4 Conclusions

The development of tensegrity- inspired microstructures was investigated using a sequential biaxial stretching protocol of neat 44EVOH and 2.5 wt.% CNC/44EVOH composite systems. The thermomechanical, mechanical, structure, and thermal properties were used to elucidate the structural changes of these systems as well as other 44EVOH and 48EVOH composites with different CNC and CNF loadings. While XRD patterns indicated stretching induced structural changes to the polymer and composites, the orientation could not be deduced. Also, the polymer structure was similar between the neat polymer and composite that was biaxially stretched but different when the 2.5 wt.%

CNC/44EVOH composite and neat 44EVOH were uniaxially stretched and these changes were corroborated with X_c values measured from DSC. The structure of the uniaxially stretched samples suggested the confinement effects of the CNCs at loadings near the onset of network formation in the matrix inhibited the polymer from crystallizing which contributed to lower overall thermomechanical and mechanical properties for this composite compared to the neat polymer. However, the structure and thermal properties of the biaxially stretched samples suggested that although the polymer structure was altered from the stretching process, the structure was not different when the CNCs were incorporated and the film was biaxially stretched. These results coupled with increases in the thermomechanical properties across a range of temperatures spanning below and above T_g of the 2.5 wt.% CNC/44EVOH composite compared to the neat polymer suggested the CNC arrangement imparted additional benefits to the thermomechanical behavior of the polymer. Also, the increase in thermomechanical behavior when the composite was stretched indicated this behavior was due to the construction of tensegrity- inspired microstructures.

CHAPTER 9. CONCLUSIONS AND FUTURE WORK

In this chapter, the conclusions of the work presented in this dissertation are summarized and discussed in the context of how it contributes to the overall understanding of prescribed morphology in polymer nanocomposites using CNs. Future work is also recommended based on the findings in in this work.

9.1 Conclusions

9.1.1 Chapter 4 Conclusions

- POM images of EVOH matrices with CNs collected at room temperature and above the melting temperature of the EVOH matrix composites suggested the STM method increased CN dispersion and distribution when compared to composites made with solely melt mixing or solution casting techniques.
- Color patterns of the room temperature films appeared different in both nanocomposites, particularly when they were made with the STM method. This difference suggested the CNs affected the microstructure of the polymer matrix and the way the CNs affected the microstructure of the polymer matrices was different due to differences in comonomer composition.

9.1.2 Chapter 5 Conclusions

- Increased E' values for 48EVOH matrix composites regardless of processing strategy implemented were due to a combination of changes to the polymer matrix crystallinity, the incorporation of CNCs, and the formation of a CNC network in

the matrix. The morphology of the continuous CNC network when produced with the solution method was three-dimensional while the morphology was two-dimensional when the composites were made with the STM method. Long-range interactions between the CNCs and polymer matrix contributed to a decrease in the CNC loading required for network formation compared to the theoretical value.

- Increases in T_g and certain mechanical properties particularly at higher CNCs loadings suggested the multi-step protocol increased CNC dispersion and distribution in the 48EVOH matrix versus the solution method.

9.1.3 Chapter 6 Conclusions

- Increased E' values for 44EVOH matrix composites regardless of processing strategy implemented were due to the incorporation of CNCs and the formation of a CNC network in the matrix. Increased polymer-particle compatibility between CNCs and 44EVOH also resulted in increases to thermomechanical and mechanical properties of 44EVOH matrix composites versus 48EVOH matrix composites. A continuous CNC networked phase contributed to increased thermomechanical properties, and the onset of CNC network behaviour occurred at approximately 2 wt.% CNC loadings in 44EVOH.
- Overall, results from 44EVOH polymers and composites indicated processing strategy impacted CN dispersion and distribution in a matrix with higher vinyl alcohol content than studied in the previous chapter. The results also demonstrated polymer matrix selection impacted polymer-particle interactions and the degree to which CNs reinforced the polymer.

9.1.4 Chapter 7 Conclusions

- VH, CC tests revealed reorganization of the polymer matrix during heating in all samples tested which suggested metastable structures were present in the polymer matrix at the scanning rates studied with FSC. However, these metastable structures did not change significantly with the addition of CNCs.
- Results from VC, CH tests suggested CNCs at 1 wt.% loadings in 44EVOH and 48EVOH matrices acted as nucleating agents which prevented cold crystallization from occurring until faster cooling rates.

9.1.5 Chapter 8 Conclusions

- Polymer chain and nanoparticle alignment in the direction of applied strain was inferred from changes in thermomechanical and mechanical properties measured in the MD and CD when 44EVOH and 48EVOH matrix polymers and composites were uniaxially or biaxially stretched. The 44EVOH composite with 2.5 wt.% CNCs did not increase as much as anticipated when uniaxially stretched and this was due to changes in polymer structure and/or confinement of the polymer matrix between CNCs.
- The increase in isotropy and retention of E' values when the 2.5 wt.% CNC/44EVOH composite was biaxially stretched indicated the particle arrangement imparted in the composite with the biaxial stretching protocol contributed additional mechanical reinforcement.
- Overall, prescribed microstructures inspired by the concept of tensegrity were able to be constructed using a sequential biaxial drawing method in a polymer

nanocomposite with CNCs as the isolated compressed members in a continuous phase of 44EVOH matrix. These prescribed microstructures increased the stiffness of the polymer composite beyond what was accomplished in unstretched and uniaxially drawn composites and this behavior was observed under different prestressing conditions.

The results of this dissertation work provided insight into the ability of CNs arranged in prescribed microstructures to increase thermomechanical properties of a commercially available semicrystalline thermoplastic polymer matrix. The results of POM indicated the importance of processing strategy on resultant CN dispersion in two EVOH matrices. Thermal, thermomechanical, and mechanical results displayed how both processing as well as matrix selection impacted the ability of CNs to be incorporated and dispersed in a polymer matrix and how the CNs impacted properties of the nanocomposite. These results indicated a multi-step protocol was needed to increase CN dispersion the most in an EVOH matrix. The onset of a continuous filler phase of CNCs assisted in determining a rational approach to the particle loading needed to construct tensegrity- inspired microstructures. Particles in the polymer nanocomposite needed to be close enough to interact with both the polymer matrix and other particles while still retaining enough space between particles to change arrangements upon stretching. Tensegrity- inspired microstructures were developed with this in mind using relatively simple and commercially available processing techniques such as mechanical drawing. Furthermore, this work contributes to the general body of work relating to polymer nanocomposite processing- structure- property relationships and polymer nanocomposites with prescribed morphology. This work also contributes to the body of work pertaining to CNs as mechanical reinforcement in

thermoplastic polymer matrices and provides an overall better understanding of processing- structure- property relationships of polymer nanocomposite constructs with prescribed microstructures based on the concept of tensegrity

9.2 Recommendations for Future Work

9.2.1 Additional characterization of the tensegrity-inspired microstructures

While thermomechanical property increases when EVOH was reinforced with CNs and stretched are significant findings, the barrier properties of the EVOH nanocomposites need to be probed since the main application of the polymer is in packaging applications. Therefore, oxygen permeability and water vapor transmission tests should be conducted on the isotropic and stretched neat polymers and nanocomposites. Because gas molecules are known to diffuse more easily through the polymer amorphous phase, it is anticipated the barrier properties will be improved in the stretched nanocomposites due to increased polymer crystallinity and crystal perfection compared to the isotropic composites.

In order to further investigate the role of confined polymer chains between CNCs in the tensegrity-inspired microstructures and development of a mesophase during stretching, it is recommended to conduct Modulated DSC (MDSC) tests to determine what, if any, rigid amorphous content or mesophase is present. In addition to crystalline and amorphous phases in a semicrystalline thermoplastic such as EVOH, some polymers have been observed to exhibit both mobile and rigid amorphous fractions [271]. The rigid amorphous fraction arises due to confinement between crystalline phases or nanoparticles and has been demonstrated to be present in polymer nanocomposites [272], but it can be hard to distinguish from the mobile amorphous fraction or melting of small/less perfect

polymer crystallites measured with conventional DSC. Therefore, the MDSC technique was developed to separate the reversible and irreversible heat flows at the glass transition that are attributed to mobile and rigid amorphous phases, respectively.

In addition to the characterization of gas barrier properties and probing for rigid amorphous fraction or mesophase development in the tensegrity- inspired microstructures, it is also recommended to investigate the coefficient of thermal expansion of the composites during the construction of tensegrity- inspired microstructures in the polymer nanocomposites.

9.2.2 Further investigation of CNFs, and processing strategies for tensegrity structure construction

The onset of a continuous filler phase was demonstrated in the current work to dictate the ability of nanoparticles to arrange into tensegrity- inspired microstructures with the biaxial starching protocol. It is therefore recommended to investigate incorporating TEMPO CNFs or CNFs at lower particle loadings in 44EVOH than what were used in this work. While the morphology of TEMPO CNFs and CNFs is different from CNCs and may make it more difficult to fully prevent particle-particle interactions and networking, lower particle loadings in an EVOH matrix are anticipated to promote the formation of tensegrity-inspired microstructures using the TEMPO CNFs or CNFs.

Different processing strategies are recommended to determine if prescribed microstructures can be constructed in CN-reinforced semicrystalline polymer composites. In continuous fiber- reinforced thermosetting matrices, investigators have demonstrated increased mechanical performance when the filler phase was prestressed prior to

impregnating the fiber mat with polymer resin [190]. Therefore, investigating the development and prestressing of CN nanopapers followed by imbedding the prestressed nanopaper with a thermosetting resin could develop novel microstructures with increased mechanical properties.

9.2.3 Comparing sequential to simultaneous biaxial stretching protocol

EVOH films undergo various deformations when they are processed to make packaging materials including sequential or simultaneous biaxial stretching such as what is experienced during blown film extrusion. Investigators [273-277] have shown the structure of semicrystalline polymers is different when it either undergoes simultaneous or sequential biaxial stretching due to the way the polymer chains and crystallites align during the different stretching steps. This difference in structural development is expected to be further amplified with the incorporation of anisotropic nanoparticles such as CNs. It is therefore recommended to investigate the development of prescribed microstructures in EVOH using a simultaneous biaxial stretching protocol and comparing the mechanical, thermomechanical, and gas barrier behavior to the films made with the sequential biaxial drawing method used in this work.

9.2.4 Studies of cellulosic nanomaterials with FSC

FSC was demonstrated in the current work as well as by other researchers to be a powerful tool to determine polymer and composite dynamics that occur on timescales that are too fast to be detected by conventional DSC. The scanning rates used in FSC have also been used to probe thermal properties of polymers that would otherwise degrade in conventional DSC, such as silk [240, 241] and PVA [239]. CNCs and CNFs are both

highly ordered cellulosic nanomaterials, but little is understood about the disordered content of these materials. Therefore, it is recommended to use FSC as a means of probing and better understanding the behavior of disordered cellulose in CNs and how the overall structure evolves at different length scales during processing from native cellulose down to the nanomaterial.

APPENDIX A. COMPARISON OF DIFFERENT BATCHES OF CELLULOSE NANOCRYSTALS

EVOH composites were made with CNCs from two different batches over the course of the time it took to complete the work for this dissertation. The results presented in this appendix compared properties such as hydrodynamic radius distribution, chemical structure, crystal structure, and thermomechanical behavior when the CNCs were incorporated in 44EVOH or 48EVOH at 1 wt.% loadings.

Hydrodynamic radius was measured with dynamic light scattering. The CNCs were suspended in distilled water at a concentration of 75 mg/100mL. The CNCs were sonicated for 15 minutes in a cup horn sonicator at 80 W power output. A BI-200SM light scattering system (Brookhaven Instruments Co., Holtsville, NY) was used for dynamic light scattering tests. The temperature was maintained at 25 °C, and a polarized 532 nm laser was used at a 11 mW power output. The detector was oriented perpendicular to the incident beam, and the data were collected over a two minutes timeframe. The viscosity and refractive index used for water at 25 °C were 0.890 mPa*s and 1.334, respectively.

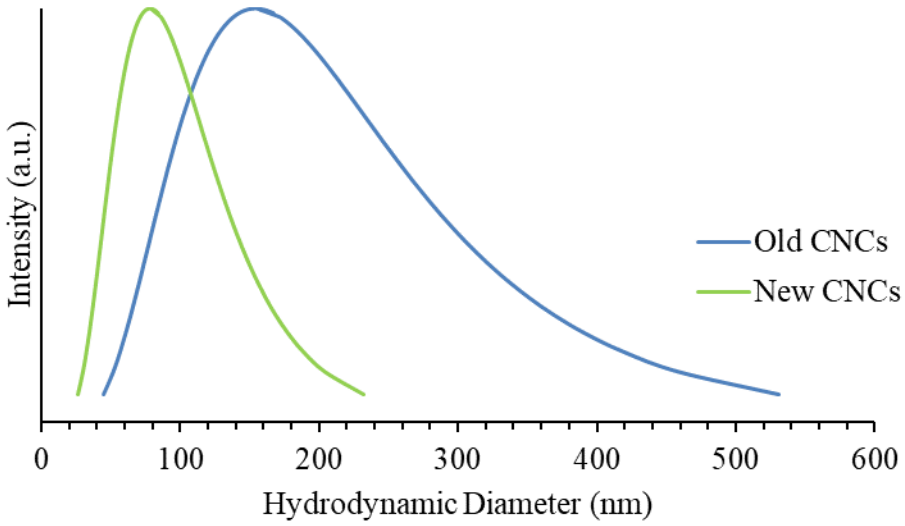

Figure A.1 - Distribution of hydrodynamic diameters for the old and new CNC suspensions as measured by dynamic light scattering.

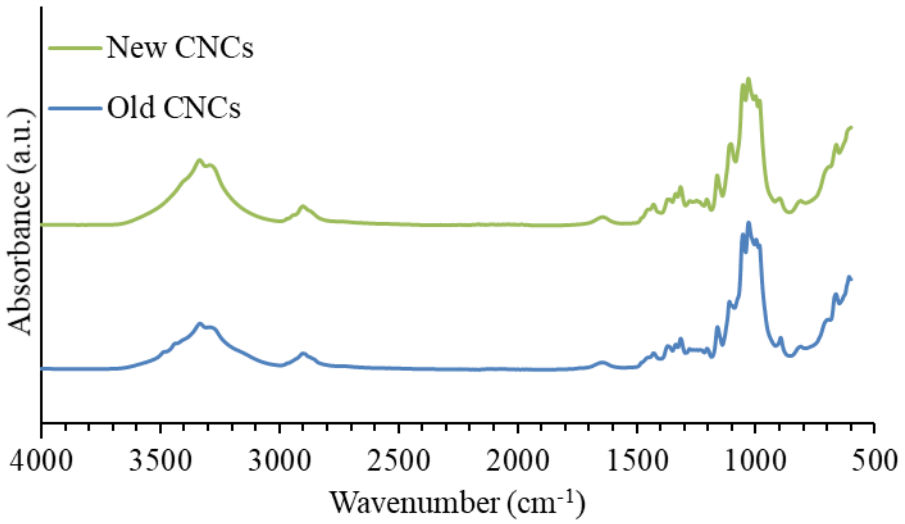

Figure A.2 - FT-IR spectra for the old and new CNCs measured from dried films of neat CNCs.

Figure A.3 displays the XRD patterns for the old and new CNCs as well as the X_c and the crystallinity index (CI) values calculated from the patterns. X_c was calculated as described in Equation 3.1 after deconvoluting the crystalline peaks and the amorphous halo. The CI was determined from Equation A.1:

$$CI = \frac{(I_{max} - I_{min})}{I_{max}} \quad \text{(A.1)}$$

Where I_{max} was assigned to the (200) diffraction peak located at approximately 22.6° for both CNCs and I_{min} was assigned to the local minimum located at approximately 19°. The local minimum was attributed to the peak in the amorphous halo.

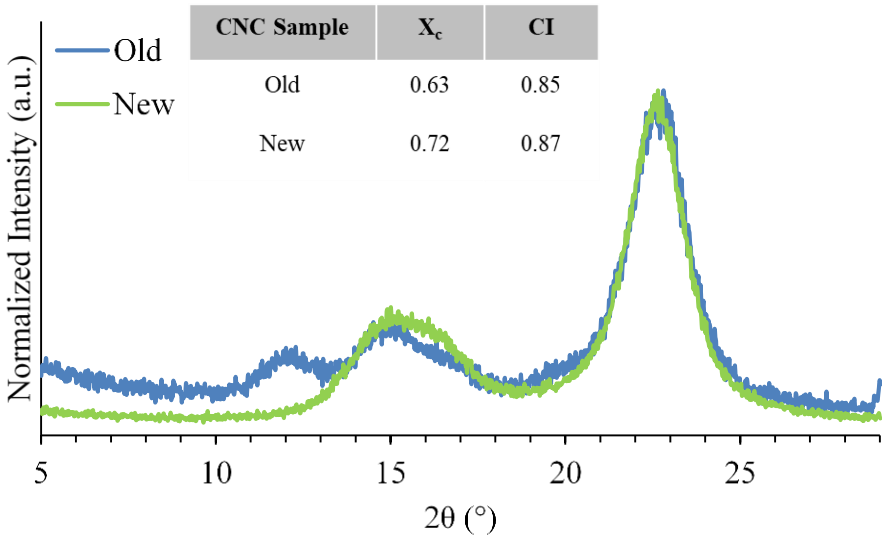

CNC Sample	X_c	CI
Old	0.63	0.85
New	0.72	0.87

Figure A.3 - XRD patterns for the old and new CNCs measured from dried films of the CNCs.

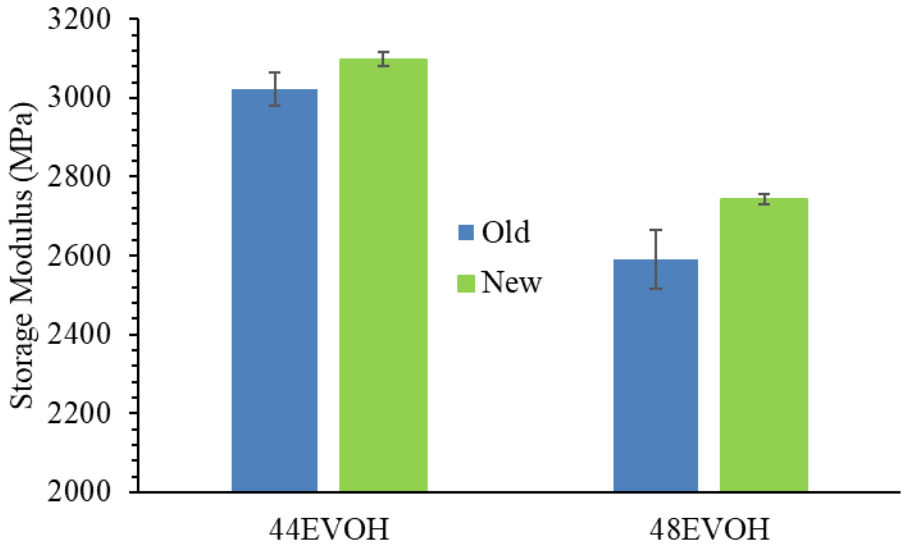

Figure A.4 - E' measured at 30 °C for 1 wt.% CNC/44EVOH and 1 wt.% CNC/48EVOH composites made with both the old and new CNCs using the STM method.

APPENDIX B. ISOTROPIC EVOH NANOCOMPOSITES

For scanning electron microscopy images, a Hitachi SU8010 SEM (Tokyo) was used to image cross-sections of isotropic polymers and nanocomposite systems. Films were cryofractured using liquid nitrogen to cool the samples. Cross sections were then applied to 90° mounts (Ted Pella, Redding, CA) with carbon tape and carbon coated with a Quorum Q-150T ES (UK) for 30 seconds. The images were taken using settings of 1 kV and 10 µA at x3,500 and x35,000 magnifications.

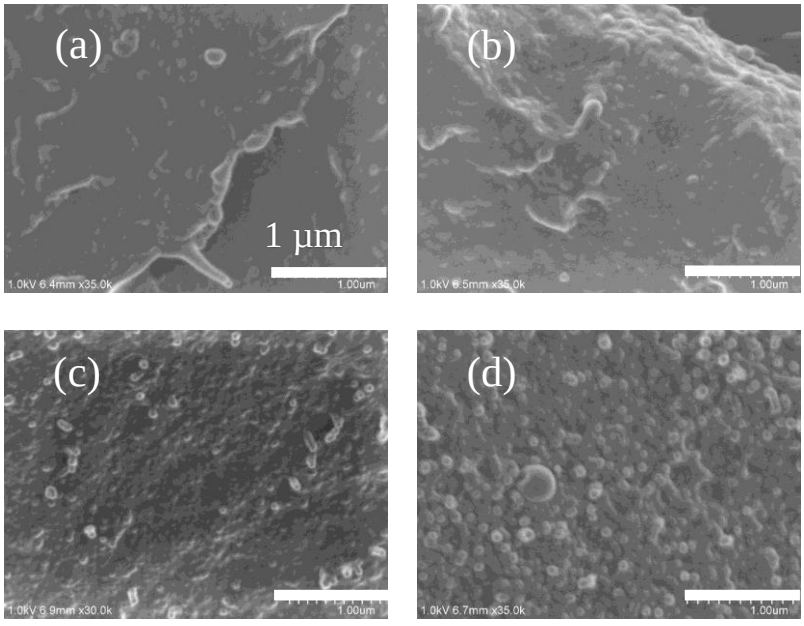

Figure B.1 - Scanning electron micrographs of (1) 0, (b) 1, (c) 2.5, and (d) 5 wt.% CNC/44EVOH composite cross-sections produced with the STM method.

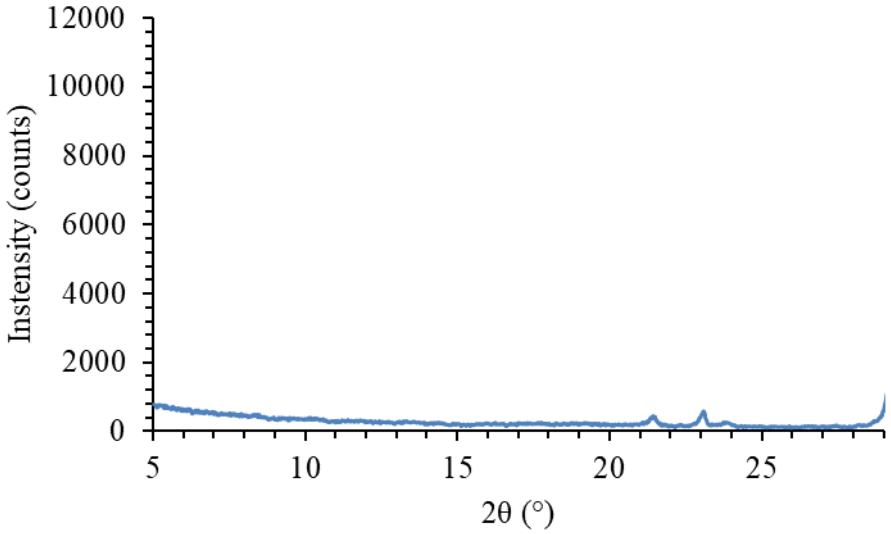

Figure B.2 - Background XRD pattern collected from the PANalytical MRD in the range of 2theta where diffraction peaks were observed for CNs, EVOH and their composites.

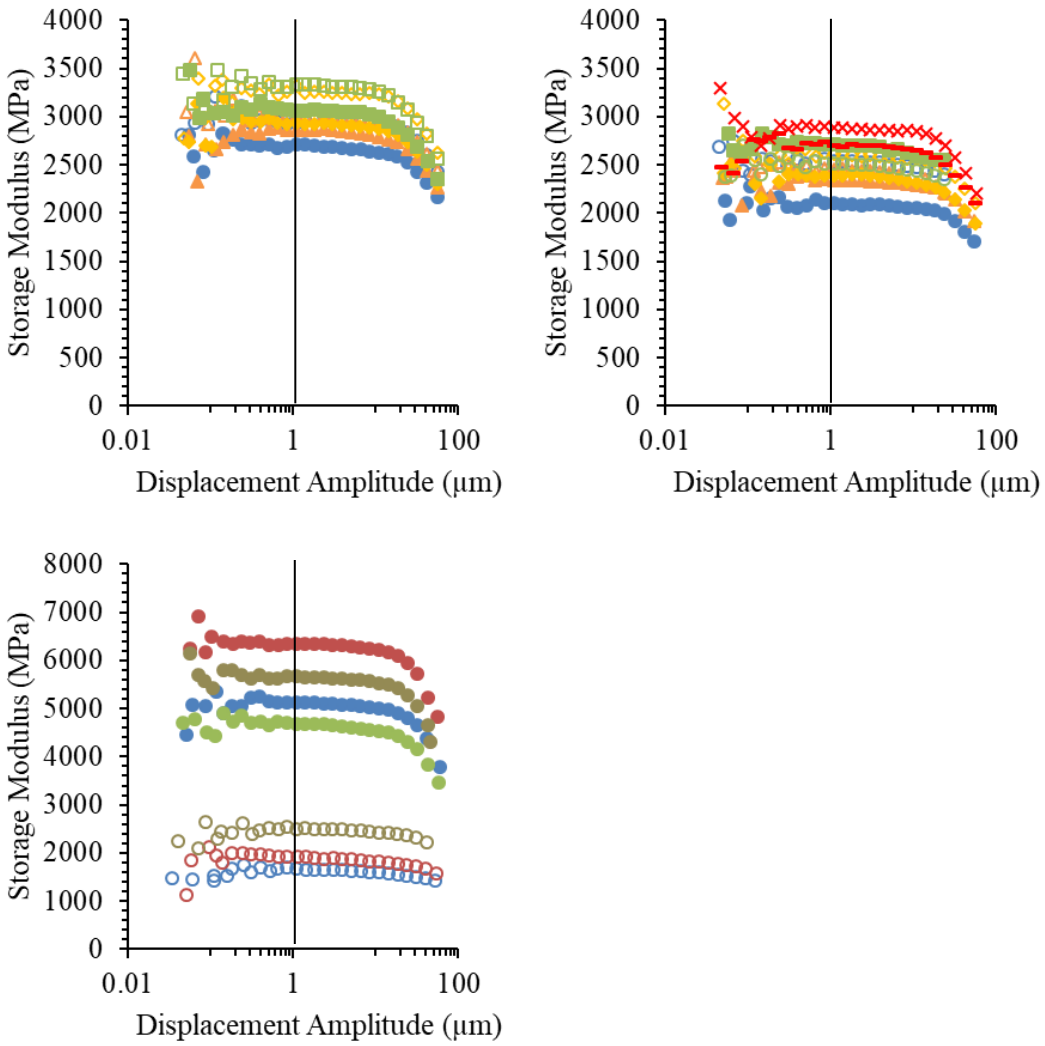

Figure B.3 - E' values as a function of displacement amplitude to determine the linear viscoelastic region. Representative curves for (a) isotropic 44EVOH composites, (b) isotropic 48EVOH composites, and (c) uniaxially stretched 44EVOH composites. For (a) and (b), composites with 0, 1, 2.5, 5, and 10 wt.% CNC loadings represented by circles, triangles, diamonds, squares, or x's/-'s, respectively. Also, filled shapes are composites made with the STM method and open shapes with the solution method, while –'s are the 10 wt.% CNC/48EVOH composite made with the STM method and x's are with the solution method. For (c), 0, 1, 2.5, and 5 wt.% CNC/44EVOH composites are represented by blue, red, green, and gold circles, respectively. The uniaxially stretched composites measured in the MD are represented by filled symbols, and the CD are represented with open symbols. Vertical lines indicate strain amplitude chosen for DMA tests discussed in Chapters 5, 6, and 8.

APPENDIX C. FAST SCANNING CHIP CALORIMETRY SAMPLE IMAGES

Images of the samples used for FSC measurements were presented in Figure C.1 and Figure C.2. Images were captured with an Olympus BX51 microscope under reflection mode and an Olympus UC30 camera with a 10x objective lens.

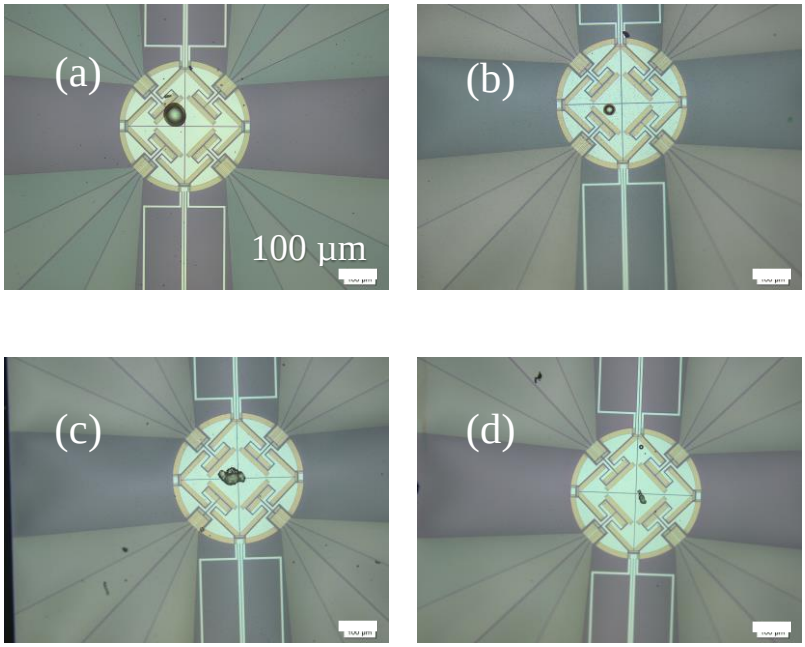

Figure C.1 - Optical microscope images of (a) 0, (b) 1, (c) 5 wt.% CNC/44EVOH composites and (d) 1 wt.% TEMPO CNF/44EVOH composite.

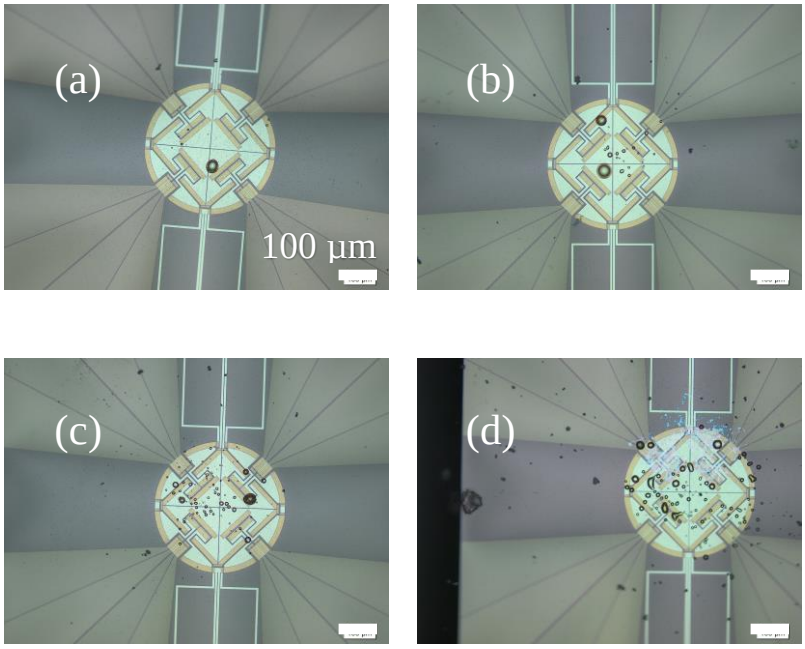

Figure C.2 - Optical microscope images of (a) 0, (b) 1, (c) 5 wt.% CNC/48EVOH composites and (d) 1 wt.% TEMPO CNF/48EVOH composite.

APPENDIX D. CHARACTERIZATION OF STRETCHED EVOH AND COMPOSITES

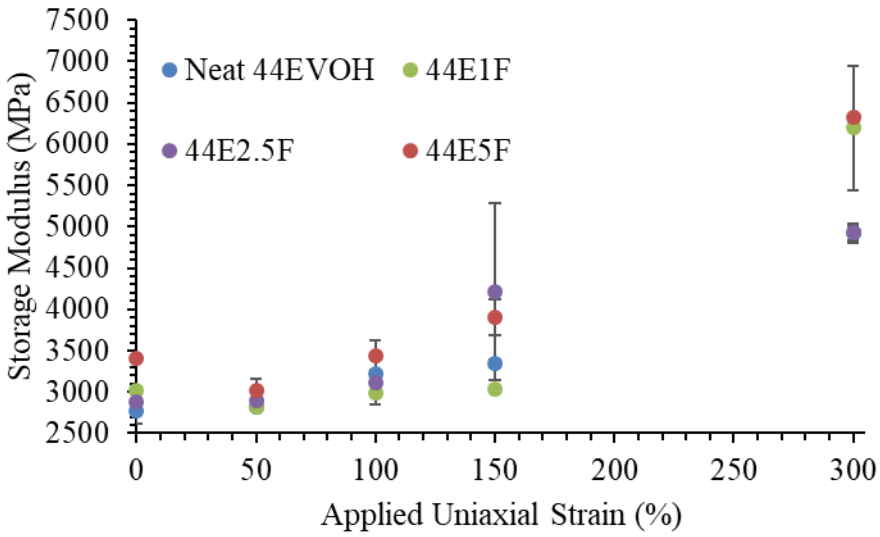

Figure D.1 - E' values measured at 30 ℃ as a function of applied uniaxial strain for 44EVOH with 0, 1, 2.5, and 5 wt.% CNCs.

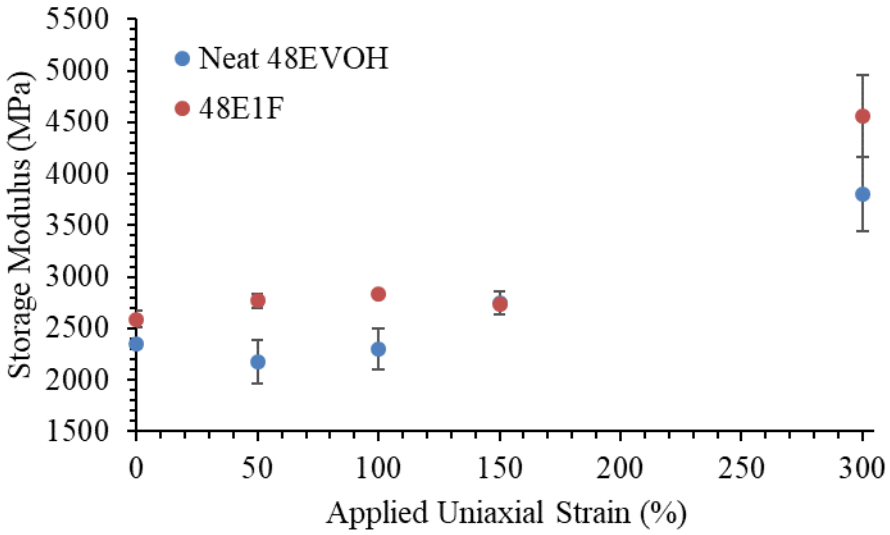

Figure D.2 - E' values measured at 30 °C as a function of applied uniaxial strain for 48EVOH with 0, and 1 wt.% CNCs.

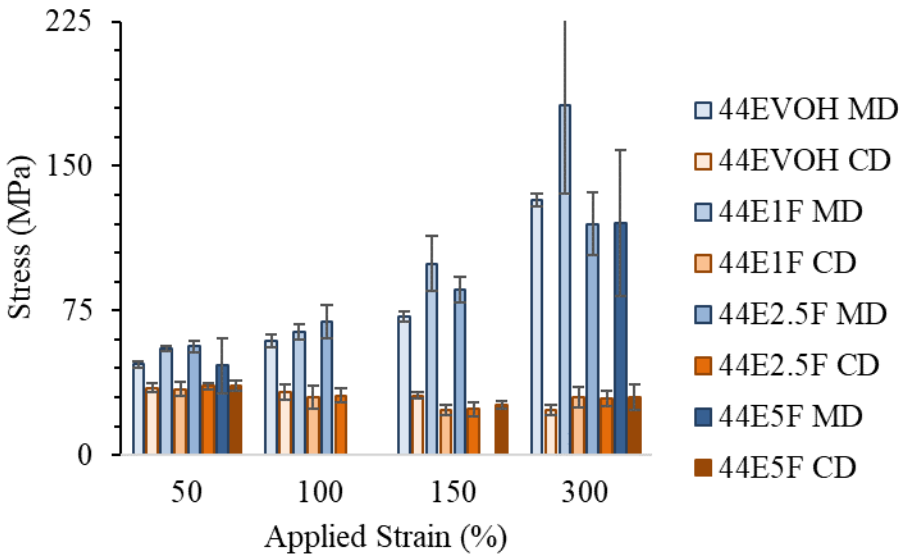

Figure D.3 - Stress at break measurements from quasi-static mechanical testing as a function of applied uniaxial strain for 44EVOH composites with 0, 1, 2.5, and 5 wt.% CNCs measured in the MD and CD.

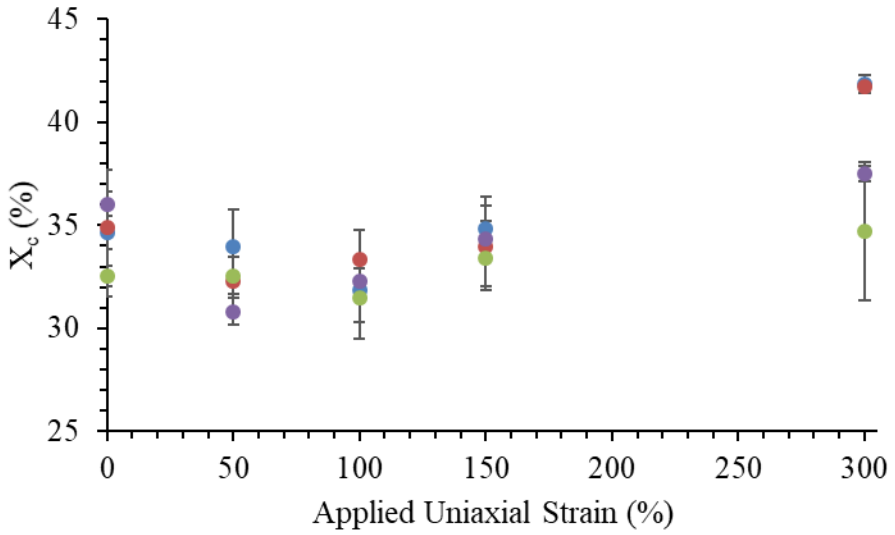

Figure D.4 - X_c values as calculated from DSC measurments as a function of applied uniaxial strain for 44EVOH composites with 0, 1, 2.5, and 5 wt.% CNCs.

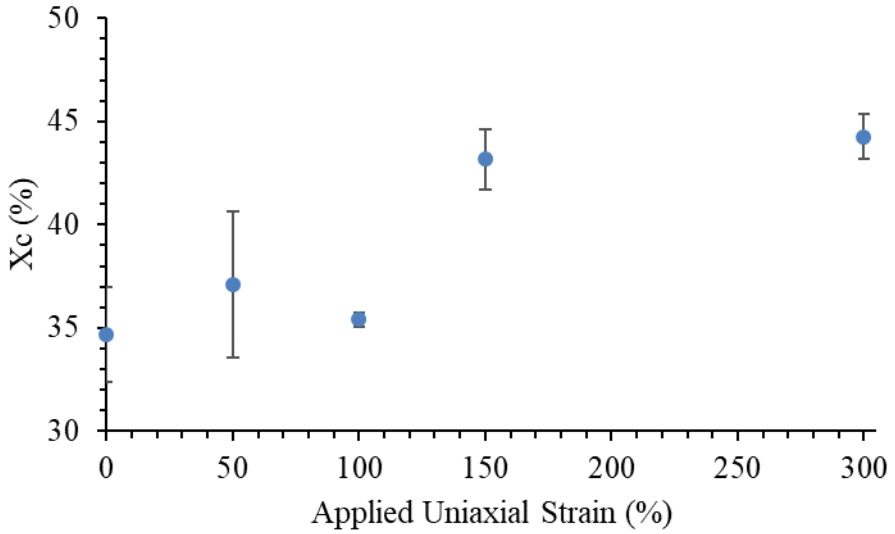

Figure D.5 - X_c values calculated from DSC measurements as a function of applied uniaxial strain for 1 wt.% CNC/48EVOH.

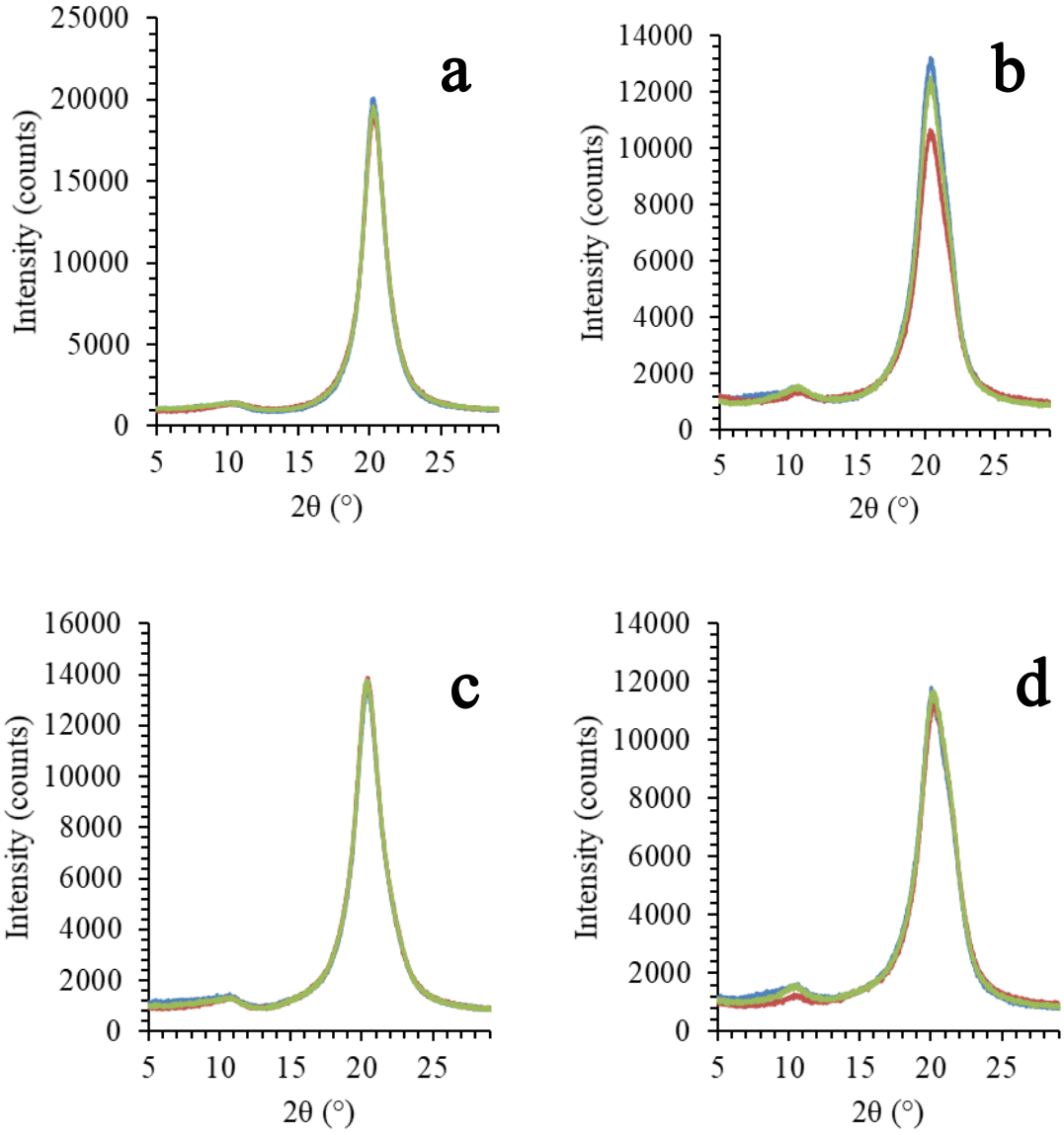

Figure D.6 - XRD patterns of (a) uniaxially stretched neat 44EVOH, (b) biaxially stretched neat 44EVOH, (c) uniaxially stretched 2.5 wt.% CNC/44EVOH, and (d) biaxially stretched 2.5 wt.% CNC/44EVOH composite. Samples were measured such that the MD was oriented (blue) parallel, (green) 45°, and (red) perpendicular with respect to the incident beam path and detector.

APPENDIX E. PERMISSIONS FOR REUSE OF COPYRIGHTED MATERIALS

ELSEVIER LICENSE
TERMS AND CONDITIONS

Oct 26, 2018

This Agreement between Georgia Institute of Technology -- Matthew Orr ("You") and Elsevier ("Elsevier") consists of your license details and the terms and conditions provided by Elsevier and Copyright Clearance Center.

License Number	4395931310168
License date	Jul 25, 2018
Licensed Content Publisher	Elsevier
Licensed Content Publication	Powder Technology
Licensed Content Title	Effect of drying conditions on cellulose nanocrystal (CNC) agglomerate porosity and dispersibility in polymer nanocomposites
Licensed Content Author	V. Khoshkava,M.R. Kamal
Licensed Content Date	Jul 1, 2014
Licensed Content Volume	261
Licensed Content Issue	n/a
Licensed Content Pages	11
Start Page	288
End Page	298
Type of Use	reuse in a thesis/dissertation
Intended publisher of new work	other
Portion	figures/tables/illustrations

Number of figures/tables/illustrations	2
Format	both print and electronic
Are you the author of this Elsevier article?	No
Will you be translating?	No
Original figure numbers	Figure 5 and Figure 6
Title of your thesis/dissertation	Constructing Tensegrity-Inspired Microstructures in a Polymer Nanocomposite with Cellulosic Nanomaterials
Publisher of new work	Georgia Institute of Technology
Author of new work	Matthew P. Orr and Meisha L. Shofner
Expected completion date	Oct 2018
Estimated size (number of pages)	1
Requestor Location	Georgia Institute of Technology 778 Atlantic Drive Atlanta, GA 30332 United States Attn: Georgia Institute of Technology
Publisher Tax ID	98-0397604
Total	0.00 USD
Terms and Conditions	

INTRODUCTION

1. The publisher for this copyrighted material is Elsevier. By clicking "accept" in connection with completing this licensing transaction, you agree that the following terms and conditions apply to this transaction (along with the Billing and Payment terms and conditions established by Copyright Clearance Center, Inc. ("CCC"), at the time that you opened your Rightslink account and that are available at any time at http://myaccount.copyright.com).

GENERAL TERMS

2. Elsevier hereby grants you permission to reproduce the aforementioned material subject to the terms and conditions indicated.

3. Acknowledgement: If any part of the material to be used (for example, figures) has appeared in our publication with credit or acknowledgement to another source, permission must also be sought from that source. If such permission is not obtained then that material may not be included in your publication/copies. Suitable acknowledgement to the source must be made, either as a footnote or in a reference list at the end of your publication, as follows:

"Reprinted from Publication title, Vol /edition number, Author(s), Title of article / title of chapter, Pages No., Copyright (Year), with permission from Elsevier [OR APPLICABLE SOCIETY COPYRIGHT OWNER]." Also Lancet special credit - "Reprinted from The Lancet, Vol. number, Author(s), Title of article, Pages No., Copyright (Year), with permission from Elsevier."

4. Reproduction of this material is confined to the purpose and/or media for which permission is hereby given.
5. Altering/Modifying Material: Not Permitted. However figures and illustrations may be altered/adapted minimally to serve your work. Any other abbreviations, additions, deletions and/or any other alterations shall be made only with prior written authorization of Elsevier Ltd. (Please contact Elsevier at permissions@elsevier.com). No modifications can be made to any Lancet figures/tables and they must be reproduced in full.
6. If the permission fee for the requested use of our material is waived in this instance, please be advised that your future requests for Elsevier materials may attract a fee.
7. Reservation of Rights: Publisher reserves all rights not specifically granted in the combination of (i) the license details provided by you and accepted in the course of this licensing transaction, (ii) these terms and conditions and (iii) CCC's Billing and Payment terms and conditions.
8. License Contingent Upon Payment: While you may exercise the rights licensed immediately upon issuance of the license at the end of the licensing process for the transaction, provided that you have disclosed complete and accurate details of your proposed use, no license is finally effective unless and until full payment is received from you (either by publisher or by CCC) as provided in CCC's Billing and Payment terms and conditions. If full payment is not received on a timely basis, then any license preliminarily granted shall be deemed automatically revoked and shall be void as if never granted. Further, in the event that you breach any of these terms and conditions or any of CCC's Billing and Payment terms and conditions, the license is automatically revoked and shall be void as if never granted. Use of materials as described in a revoked license, as well as any use of the materials beyond the scope of an unrevoked license, may constitute copyright infringement and publisher reserves the right to take any and all action to protect its copyright in the materials.
9. Warranties: Publisher makes no representations or warranties with respect to the licensed material.
10. Indemnity: You hereby indemnify and agree to hold harmless publisher and CCC, and their respective officers, directors, employees and agents, from and against any and all claims arising out of your use of the licensed material other than as specifically authorized pursuant to this license.
11. No Transfer of License: This license is personal to you and may not be sublicensed, assigned, or transferred by you to any other person without publisher's written permission.
12. No Amendment Except in Writing: This license may not be amended except in a writing signed by both parties (or, in the case of publisher, by CCC on publisher's behalf).
13. Objection to Contrary Terms: Publisher hereby objects to any terms contained in any purchase order, acknowledgment, check endorsement or other writing prepared by you, which terms are inconsistent with these terms and conditions or CCC's Billing and Payment terms and conditions. These terms and conditions, together with CCC's Billing and Payment terms and conditions (which are incorporated herein), comprise the entire agreement between you and publisher (and CCC) concerning this licensing transaction. In the event of any conflict between your obligations established by these terms and conditions and those established by CCC's Billing and Payment terms and conditions, these terms and conditions shall control.

14. Revocation: Elsevier or Copyright Clearance Center may deny the permissions described in this License at their sole discretion, for any reason or no reason, with a full refund payable to you. Notice of such denial will be made using the contact information provided by you. Failure to receive such notice will not alter or invalidate the denial. In no event will Elsevier or Copyright Clearance Center be responsible or liable for any costs, expenses or damage incurred by you as a result of a denial of your permission request, other than a refund of the amount(s) paid by you to Elsevier and/or Copyright Clearance Center for denied permissions.

LIMITED LICENSE

The following terms and conditions apply only to specific license types:

15. **Translation**: This permission is granted for non-exclusive world **English** rights only unless your license was granted for translation rights. If you licensed translation rights you may only translate this content into the languages you requested. A professional translator must perform all translations and reproduce the content word for word preserving the integrity of the article.

16. **Posting licensed content on any Website**: The following terms and conditions apply as follows: Licensing material from an Elsevier journal: All content posted to the web site must maintain the copyright information line on the bottom of each image; A hyper-text must be included to the Homepage of the journal from which you are licensing at http://www.sciencedirect.com/science/journal/xxxxx or the Elsevier homepage for books at http://www.elsevier.com; Central Storage: This license does not include permission for a scanned version of the material to be stored in a central repository such as that provided by Heron/XanEdu.

Licensing material from an Elsevier book: A hyper-text link must be included to the Elsevier homepage at http://www.elsevier.com . All content posted to the web site must maintain the copyright information line on the bottom of each image.

Posting licensed content on Electronic reserve: In addition to the above the following clauses are applicable: The web site must be password-protected and made available only to bona fide students registered on a relevant course. This permission is granted for 1 year only. You may obtain a new license for future website posting.

17. **For journal authors:** the following clauses are applicable in addition to the above:

Preprints:

A preprint is an author's own write-up of research results and analysis, it has not been peer-reviewed, nor has it had any other value added to it by a publisher (such as formatting, copyright, technical enhancement etc.).

Authors can share their preprints anywhere at any time. Preprints should not be added to or enhanced in any way in order to appear more like, or to substitute for, the final versions of articles however authors can update their preprints on arXiv or RePEc with their Accepted Author Manuscript (see below).

If accepted for publication, we encourage authors to link from the preprint to their formal publication via its DOI. Millions of researchers have access to the formal publications on ScienceDirect, and so links will help users to find, access, cite and use the best available version. Please note that Cell Press, The Lancet and some society-owned have different preprint policies. Information on these policies is available on the journal homepage.

Accepted Author Manuscripts: An accepted author manuscript is the manuscript of an article that has been accepted for publication and which typically includes author-incorporated changes suggested during submission, peer review and editor-author communications.
Authors can share their accepted author manuscript:

- immediately
    - via their non-commercial person homepage or blog
    - by updating a preprint in arXiv or RePEc with the accepted manuscript
    - via their research institute or institutional repository for internal institutional uses or as part of an invitation-only research collaboration work-group
    - directly by providing copies to their students or to research collaborators for their personal use
    - for private scholarly sharing as part of an invitation-only work group on commercial sites with which Elsevier has an agreement
- After the embargo period
    - via non-commercial hosting platforms such as their institutional repository
    - via commercial sites with which Elsevier has an agreement

In all cases accepted manuscripts should:

- link to the formal publication via its DOI
- bear a CC-BY-NC-ND license - this is easy to do
- if aggregated with other manuscripts, for example in a repository or other site, be shared in alignment with our hosting policy not be added to or enhanced in any way to appear more like, or to substitute for, the published journal article.

Published journal article (JPA): A published journal article (PJA) is the definitive final record of published research that appears or will appear in the journal and embodies all value-adding publishing activities including peer review co-ordination, copy-editing, formatting, (if relevant) pagination and online enrichment.
Policies for sharing publishing journal articles differ for subscription and gold open access articles:
Subscription Articles: If you are an author, please share a link to your article rather than the full-text. Millions of researchers have access to the formal publications on ScienceDirect, and so links will help your users to find, access, cite, and use the best available version.
Theses and dissertations which contain embedded PJAs as part of the formal submission can be posted publicly by the awarding institution with DOI links back to the formal publications on ScienceDirect.
If you are affiliated with a library that subscribes to ScienceDirect you have additional private sharing rights for others' research accessed under that agreement. This includes use for classroom teaching and internal training at the institution (including use in course packs and courseware programs), and inclusion of the article for grant funding purposes.

Gold Open Access Articles: May be shared according to the author-selected end-user license and should contain a CrossMark logo, the end user license, and a DOI link to the formal publication on ScienceDirect.
Please refer to Elsevier's posting policy for further information.
18. **For book authors** the following clauses are applicable in addition to the above: Authors are permitted to place a brief summary of their work online only. You are not allowed to download and post the published electronic version of your chapter, nor may you scan the printed edition to create an electronic version. **Posting to a repository:** Authors are permitted to post a summary of their chapter only in their institution's repository.
19. **Thesis/Dissertation**: If your license is for use in a thesis/dissertation your thesis may be submitted to your institution in either print or electronic form. Should your thesis be published commercially, please reapply for permission. These requirements include permission for the Library and Archives of Canada to supply single copies, on demand, of the complete thesis and include permission for Proquest/UMI to supply single copies, on demand, of the complete thesis. Should your thesis be published commercially, please reapply for permission. Theses and dissertations which contain embedded PJAs as part of the formal submission can be posted publicly by the awarding institution with DOI links back to the formal publications on ScienceDirect.

Elsevier Open Access Terms and Conditions
You can publish open access with Elsevier in hundreds of open access journals or in nearly 2000 established subscription journals that support open access publishing. Permitted third party re-use of these open access articles is defined by the author's choice of Creative Commons user license. See our open access license policy for more information.
Terms & Conditions applicable to all Open Access articles published with Elsevier:
Any reuse of the article must not represent the author as endorsing the adaptation of the article nor should the article be modified in such a way as to damage the author's honour or reputation. If any changes have been made, such changes must be clearly indicated. The author(s) must be appropriately credited and we ask that you include the end user license and a DOI link to the formal publication on ScienceDirect.
If any part of the material to be used (for example, figures) has appeared in our publication with credit or acknowledgement to another source it is the responsibility of the user to ensure their reuse complies with the terms and conditions determined by the rights holder.
Additional Terms & Conditions applicable to each Creative Commons user license:
CC BY: The CC-BY license allows users to copy, to create extracts, abstracts and new works from the Article, to alter and revise the Article and to make commercial use of the Article (including reuse and/or resale of the Article by commercial entities), provided the user gives appropriate credit (with a link to the formal publication through the relevant DOI), provides a link to the license, indicates if changes were made and the licensor is not represented as endorsing the use made of the work. The full details of the license are available at http://creativecommons.org/licenses/by/4.0.
CC BY NC SA: The CC BY-NC-SA license allows users to copy, to create extracts, abstracts and new works from the Article, to alter and revise the Article, provided this is

ELSEVIER LICENSE
TERMS AND CONDITIONS

Oct 26, 2018

This Agreement between Georgia Institute of Technology -- Matthew Orr ("You") and Elsevier ("Elsevier") consists of your license details and the terms and conditions provided by Elsevier and Copyright Clearance Center.

License Number	4395980676830
License date	Jul 25, 2018
Licensed Content Publisher	Elsevier
Licensed Content Publication	Journal of Theoretical Biology
Licensed Content Title	The Role of Prestress and Architecture of the Cytoskeleton and Deformability of Cytoskeletal Filaments in Mechanics of Adherent Cells: a Quantitative Analysis
Licensed Content Author	DIMITRIJE STAMENOVIĆ,MARK F COUGHLIN
Licensed Content Date	Nov 7, 1999
Licensed Content Volume	201
Licensed Content Issue	1
Licensed Content Pages	12
Start Page	63
End Page	74
Type of Use	reuse in a thesis/dissertation
Intended publisher of new work	other
Portion	figures/tables/illustrations
Number of figures/tables/illustrations	1
Format	both print and electronic
Are you the author of this Elsevier article?	No
Will you be translating?	No

Original figure numbers	Figure 3
Title of your thesis/dissertation	Constructing Tensegrity-Inspired Microstructures in a Polymer Nanocomposite with Cellulosic Nanomaterials
Publisher of new work	Georgia Institute of Technology
Author of new work	Matthew P. Orr and Meisha L. Shofner
Expected completion date	Oct 2018
Estimated size (number of pages)	1
Requestor Location	Georgia Institute of Technology 778 Atlantic Drive Atlanta, GA 30332 United States Attn: Georgia Institute of Technology
Publisher Tax ID	98-0397604
Total	0.00 USD
Terms and Conditions	

INTRODUCTION

1. The publisher for this copyrighted material is Elsevier. By clicking "accept" in connection with completing this licensing transaction, you agree that the following terms and conditions apply to this transaction (along with the Billing and Payment terms and conditions established by Copyright Clearance Center, Inc. ("CCC"), at the time that you opened your Rightslink account and that are available at any time at http://myaccount.copyright.com).

GENERAL TERMS

2. Elsevier hereby grants you permission to reproduce the aforementioned material subject to the terms and conditions indicated.
3. Acknowledgement: If any part of the material to be used (for example, figures) has appeared in our publication with credit or acknowledgement to another source, permission must also be sought from that source. If such permission is not obtained then that material may not be included in your publication/copies. Suitable acknowledgement to the source must be made, either as a footnote or in a reference list at the end of your publication, as follows:
"Reprinted from Publication title, Vol /edition number, Author(s), Title of article / title of chapter, Pages No., Copyright (Year), with permission from Elsevier [OR APPLICABLE SOCIETY COPYRIGHT OWNER]." Also Lancet special credit - "Reprinted from The Lancet, Vol. number, Author(s), Title of article, Pages No., Copyright (Year), with permission from Elsevier."
4. Reproduction of this material is confined to the purpose and/or media for which permission is hereby given.
5. Altering/Modifying Material: Not Permitted. However figures and illustrations may be altered/adapted minimally to serve your work. Any other abbreviations, additions, deletions and/or any other alterations shall be made only with prior written authorization of Elsevier Ltd. (Please contact Elsevier at permissions@elsevier.com). No modifications can be made to any Lancet figures/tables and they must be reproduced in full.

6. If the permission fee for the requested use of our material is waived in this instance, please be advised that your future requests for Elsevier materials may attract a fee.
7. Reservation of Rights: Publisher reserves all rights not specifically granted in the combination of (i) the license details provided by you and accepted in the course of this licensing transaction, (ii) these terms and conditions and (iii) CCC's Billing and Payment terms and conditions.
8. License Contingent Upon Payment: While you may exercise the rights licensed immediately upon issuance of the license at the end of the licensing process for the transaction, provided that you have disclosed complete and accurate details of your proposed use, no license is finally effective unless and until full payment is received from you (either by publisher or by CCC) as provided in CCC's Billing and Payment terms and conditions. If full payment is not received on a timely basis, then any license preliminarily granted shall be deemed automatically revoked and shall be void as if never granted. Further, in the event that you breach any of these terms and conditions or any of CCC's Billing and Payment terms and conditions, the license is automatically revoked and shall be void as if never granted. Use of materials as described in a revoked license, as well as any use of the materials beyond the scope of an unrevoked license, may constitute copyright infringement and publisher reserves the right to take any and all action to protect its copyright in the materials.
9. Warranties: Publisher makes no representations or warranties with respect to the licensed material.
10. Indemnity: You hereby indemnify and agree to hold harmless publisher and CCC, and their respective officers, directors, employees and agents, from and against any and all claims arising out of your use of the licensed material other than as specifically authorized pursuant to this license.
11. No Transfer of License: This license is personal to you and may not be sublicensed, assigned, or transferred by you to any other person without publisher's written permission.
12. No Amendment Except in Writing: This license may not be amended except in a writing signed by both parties (or, in the case of publisher, by CCC on publisher's behalf).
13. Objection to Contrary Terms: Publisher hereby objects to any terms contained in any purchase order, acknowledgment, check endorsement or other writing prepared by you, which terms are inconsistent with these terms and conditions or CCC's Billing and Payment terms and conditions. These terms and conditions, together with CCC's Billing and Payment terms and conditions (which are incorporated herein), comprise the entire agreement between you and publisher (and CCC) concerning this licensing transaction. In the event of any conflict between your obligations established by these terms and conditions and those established by CCC's Billing and Payment terms and conditions, these terms and conditions shall control.
14. Revocation: Elsevier or Copyright Clearance Center may deny the permissions described in this License at their sole discretion, for any reason or no reason, with a full refund payable to you. Notice of such denial will be made using the contact information provided by you. Failure to receive such notice will not alter or invalidate the denial. In no event will Elsevier or Copyright Clearance Center be responsible or liable for any costs, expenses or damage incurred by you as a result of a denial of your permission request, other than a refund of the amount(s) paid by you to Elsevier and/or Copyright Clearance Center for denied permissions.

LIMITED LICENSE

The following terms and conditions apply only to specific license types:

15. **Translation**: This permission is granted for non-exclusive world **English** rights only unless your license was granted for translation rights. If you licensed translation rights you may only translate this content into the languages you requested. A professional translator must perform all translations and reproduce the content word for word preserving the integrity of the article.

16. **Posting licensed content on any Website**: The following terms and conditions apply as follows: Licensing material from an Elsevier journal: All content posted to the web site must maintain the copyright information line on the bottom of each image; A hyper-text must be included to the Homepage of the journal from which you are licensing at http://www.sciencedirect.com/science/journal/xxxxx or the Elsevier homepage for books at http://www.elsevier.com; Central Storage: This license does not include permission for a scanned version of the material to be stored in a central repository such as that provided by Heron/XanEdu.

Licensing material from an Elsevier book: A hyper-text link must be included to the Elsevier homepage at http://www.elsevier.com . All content posted to the web site must maintain the copyright information line on the bottom of each image.

Posting licensed content on Electronic reserve: In addition to the above the following clauses are applicable: The web site must be password-protected and made available only to bona fide students registered on a relevant course. This permission is granted for 1 year only. You may obtain a new license for future website posting.

17. **For journal authors:** the following clauses are applicable in addition to the above:

Preprints:

A preprint is an author's own write-up of research results and analysis, it has not been peer-reviewed, nor has it had any other value added to it by a publisher (such as formatting, copyright, technical enhancement etc.).

Authors can share their preprints anywhere at any time. Preprints should not be added to or enhanced in any way in order to appear more like, or to substitute for, the final versions of articles however authors can update their preprints on arXiv or RePEc with their Accepted Author Manuscript (see below).

If accepted for publication, we encourage authors to link from the preprint to their formal publication via its DOI. Millions of researchers have access to the formal publications on ScienceDirect, and so links will help users to find, access, cite and use the best available version. Please note that Cell Press, The Lancet and some society-owned have different preprint policies. Information on these policies is available on the journal homepage.

Accepted Author Manuscripts: An accepted author manuscript is the manuscript of an article that has been accepted for publication and which typically includes author-incorporated changes suggested during submission, peer review and editor-author communications.

Authors can share their accepted author manuscript:

- immediately
    - via their non-commercial person homepage or blog
    - by updating a preprint in arXiv or RePEc with the accepted manuscript

    - via their research institute or institutional repository for internal institutional uses or as part of an invitation-only research collaboration work-group
    - directly by providing copies to their students or to research collaborators for their personal use
    - for private scholarly sharing as part of an invitation-only work group on commercial sites with which Elsevier has an agreement
- After the embargo period
    - via non-commercial hosting platforms such as their institutional repository
    - via commercial sites with which Elsevier has an agreement

In all cases accepted manuscripts should:

- link to the formal publication via its DOI
- bear a CC-BY-NC-ND license - this is easy to do
- if aggregated with other manuscripts, for example in a repository or other site, be shared in alignment with our hosting policy not be added to or enhanced in any way to appear more like, or to substitute for, the published journal article.

Published journal article (JPA): A published journal article (PJA) is the definitive final record of published research that appears or will appear in the journal and embodies all value-adding publishing activities including peer review co-ordination, copy-editing, formatting, (if relevant) pagination and online enrichment.
Policies for sharing publishing journal articles differ for subscription and gold open access articles:
Subscription Articles: If you are an author, please share a link to your article rather than the full-text. Millions of researchers have access to the formal publications on ScienceDirect, and so links will help your users to find, access, cite, and use the best available version.
Theses and dissertations which contain embedded PJAs as part of the formal submission can be posted publicly by the awarding institution with DOI links back to the formal publications on ScienceDirect.
If you are affiliated with a library that subscribes to ScienceDirect you have additional private sharing rights for others' research accessed under that agreement. This includes use for classroom teaching and internal training at the institution (including use in course packs and courseware programs), and inclusion of the article for grant funding purposes.
Gold Open Access Articles: May be shared according to the author-selected end-user license and should contain a CrossMark logo, the end user license, and a DOI link to the formal publication on ScienceDirect.
Please refer to Elsevier's posting policy for further information.
18. **For book authors** the following clauses are applicable in addition to the above: Authors are permitted to place a brief summary of their work online only. You are not allowed to download and post the published electronic version of your chapter, nor may you scan the printed edition to create an electronic version. **Posting to a repository:** Authors are permitted to post a summary of their chapter only in their institution's repository.

19. **Thesis/Dissertation**: If your license is for use in a thesis/dissertation your thesis may be submitted to your institution in either print or electronic form. Should your thesis be published commercially, please reapply for permission. These requirements include permission for the Library and Archives of Canada to supply single copies, on demand, of the complete thesis and include permission for Proquest/UMI to supply single copies, on demand, of the complete thesis. Should your thesis be published commercially, please reapply for permission. Theses and dissertations which contain embedded PJAs as part of the formal submission can be posted publicly by the awarding institution with DOI links back to the formal publications on ScienceDirect.

Elsevier Open Access Terms and Conditions

You can publish open access with Elsevier in hundreds of open access journals or in nearly 2000 established subscription journals that support open access publishing. Permitted third party re-use of these open access articles is defined by the author's choice of Creative Commons user license. See our open access license policy for more information.

Terms & Conditions applicable to all Open Access articles published with Elsevier:

Any reuse of the article must not represent the author as endorsing the adaptation of the article nor should the article be modified in such a way as to damage the author's honour or reputation. If any changes have been made, such changes must be clearly indicated. The author(s) must be appropriately credited and we ask that you include the end user license and a DOI link to the formal publication on ScienceDirect.

If any part of the material to be used (for example, figures) has appeared in our publication with credit or acknowledgement to another source it is the responsibility of the user to ensure their reuse complies with the terms and conditions determined by the rights holder.

Additional Terms & Conditions applicable to each Creative Commons user license:

CC BY: The CC-BY license allows users to copy, to create extracts, abstracts and new works from the Article, to alter and revise the Article and to make commercial use of the Article (including reuse and/or resale of the Article by commercial entities), provided the user gives appropriate credit (with a link to the formal publication through the relevant DOI), provides a link to the license, indicates if changes were made and the licensor is not represented as endorsing the use made of the work. The full details of the license are available at http://creativecommons.org/licenses/by/4.0.

CC BY NC SA: The CC BY-NC-SA license allows users to copy, to create extracts, abstracts and new works from the Article, to alter and revise the Article, provided this is not done for commercial purposes, and that the user gives appropriate credit (with a link to the formal publication through the relevant DOI), provides a link to the license, indicates if changes were made and the licensor is not represented as endorsing the use made of the work. Further, any new works must be made available on the same conditions. The full details of the license are available at http://creativecommons.org/licenses/by-nc-sa/4.0.

CC BY NC ND: The CC BY-NC-ND license allows users to copy and distribute the Article, provided this is not done for commercial purposes and further does not permit distribution of the Article if it is changed or edited in any way, and provided the user gives appropriate credit (with a link to the formal publication through the relevant DOI),

REFERENCES

REFERENCES

[1] R. J. Moon, A. Martini, J. Nairn, J. Simonsen, and J. Youngblood, "Cellulose nanomaterials review: structure, properties and nanocomposites," (in English), *Chemical Society Reviews,* vol. 40, no. 7, pp. 3941-3994, 2011.

[2] J. H. Lee and M. L. Shofner, "Tensegrity-inspired polymer nanocomposites," *Polymer,* vol. 111, pp. 9-19, 2017/02/24/ 2017.

[3] M. T. Postek *et al.*, "Development of the metrology and imaging of cellulose nanocrystals," *Measurement Science and Technology,* vol. 22, no. 2, p. 024005, 2011.

[4] T. Saito, S. Kimura, Y. Nishiyama, and A. Isogai, "Cellulose nanofibers prepared by TEMPO-mediated oxidation of native cellulose," (in English), *Biomacromolecules,* vol. 8, no. 8, pp. 2485-2491, Aug 2007.

[5] R. S. Reiner and A. W. Rudie, *Pilot plant scaleup of TEMPO-pretreated cellulose nanofibrils* (Production and Applications of Cellulose Nanomaterials). TAPPI PRESS, 2013, pp. 177-178.

[6] Y. Qing, R. Sabo, J. Y. Zhu, U. Agarwal, Z. Cai, and Y. Wu, "A comparative study of cellulose nanofibrils disintegrated via multiple processing approaches," *Carbohydrate Polymers,* vol. 97, no. 1, pp. 226-234, 2013/08/14/ 2013.

[7] W. Wang, R. C. Sabo, M. D. Mozuch, P. Kersten, J. Y. Zhu, and Y. Jin, "Physical and Mechanical Properties of Cellulose Nanofibril Films from Bleached Eucalyptus Pulp by Endoglucanase Treatment and Microfluidization," *Journal of Polymers and the Environment,* journal article vol. 23, no. 4, pp. 551-558, December 01 2015.

[8] T. Zimmermann, N. Bordeanu, and E. Strub, "Properties of nanofibrillated cellulose from different raw materials and its reinforcement potential," *Carbohydrate Polymers,* vol. 79, no. 4, pp. 1086-1093, 2010/03/17/ 2010.

[9] E. J. Foster *et al.*, "Current characterization methods for cellulose nanomaterials," *Chemical Society Reviews,* 10.1039/C6CS00895J vol. 47, no. 8, pp. 2609-2679, 2018.

[10] M. A. Hubbe, O. J. Rojas, L. A. Lucia, and M. Sain, "Cellulosic Nanocomposites: A Review," (in English), *Bioresources,* vol. 3, no. 3, pp. 929-980, 2008.

[11] Y. Habibi, L. A. Lucia, and O. J. Rojas, "Cellulose nanocrystals: chemistry, self-assembly, and applications," *Chem Rev,* vol. 110, no. 6, pp. 3479-500, Jun 09 2010.

[12] X. M. Dong, J.-F. Revol, and D. G. Gray, "Effect of microcrystallite preparation conditions on the formation of colloid crystals of cellulose," *Cellulose,* journal article vol. 5, no. 1, pp. 19-32, March 01 1998.

[13] T. Abitbol, E. Kloser, and D. G. Gray, "Estimation of the surface sulfur content of cellulose nanocrystals prepared by sulfuric acid hydrolysis," (in English), *Cellulose,* vol. 20, no. 2, pp. 785-794, Apr 2013.

[14] S. Camarero Espinosa, T. Kuhnt, E. J. Foster, and C. Weder, "Isolation of Thermally Stable Cellulose Nanocrystals by Phosphoric Acid Hydrolysis," *Biomacromolecules,* vol. 14, no. 4, pp. 1223-1230, 2013/04/08 2013.

[15] V. Khoshkava and M. R. Kamal, "Effect of drying conditions on cellulose nanocrystal (CNC) agglomerate porosity and dispersibility in polymer nanocomposites," *Powder Technology,* vol. 261, pp. 288-298, 2014/07/01/ 2014.

[16] A. Hirai, O. Inui, F. Horii, and M. Tsuji, "Phase Separation Behavior in Aqueous Suspensions of Bacterial Cellulose Nanocrystals Prepared by Sulfuric Acid Treatment," *Langmuir,* vol. 25, no. 1, pp. 497-502, 2009/01/06 2009.

[17] I. A. Sacui *et al.*, "Comparison of the Properties of Cellulose Nanocrystals and Cellulose Nanofibrils Isolated from Bacteria, Tunicate, and Wood Processed Using Acid, Enzymatic, Mechanical, and Oxidative Methods," *ACS Applied Materials & Interfaces,* vol. 6, no. 9, pp. 6127-6138, 2014/05/14 2014.

[18] X. Y. Tan, S. B. Abd Hamid, and C. W. Lai, "Preparation of high crystallinity cellulose nanocrystals (CNCs) by ionic liquid solvolysis," *Biomass and Bioenergy,* vol. 81, pp. 584-591, 2015/10/01/ 2015.

[19] M. Marcos, E. K. Nadia, and D. Alain, "Cellulose nanocrystals and related nanocomposites: Review of some properties and challenges," *Journal of Polymer Science Part B: Polymer Physics,* vol. 52, no. 12, pp. 791-806, 2014.

[20] A. Viswanathan and S. G. Shenouda, "The helical structure of cellulose I," *Journal of Applied Polymer Science,* vol. 15, no. 3, pp. 519-535, 1971.

[21] S. Iwamoto, A. Isogai, and T. Iwata, "Structure and Mechanical Properties of Wet-Spun Fibers Made from Natural Cellulose Nanofibers," *Biomacromolecules,* vol. 12, no. 3, pp. 831-836, 2011/03/14 2011.

[22] H. Sehaqui, N. Ezekiel Mushi, S. Morimune, M. Salajkova, T. Nishino, and L. A. Berglund, "Cellulose Nanofiber Orientation in Nanopaper and Nanocomposites by

Cold Drawing," *ACS Applied Materials & Interfaces,* vol. 4, no. 2, pp. 1043-1049, 2012/02/22 2012.

[23] Q. Wu *et al.*, "Influence of temperature and humidity on nano-mechanical properties of cellulose nanocrystal films made from switchgrass and cotton," *Industrial Crops and Products,* vol. 48, pp. 28-35, 2013/07/01/ 2013.

[24] F. Li, P. Biagioni, M. Bollani, A. Maccagnan, and L. Piergiovanni, "Multi-functional coating of cellulose nanocrystals for flexible packaging applications," *Cellulose,* journal article vol. 20, no. 5, pp. 2491-2504, October 01 2013.

[25] Y. Tan *et al.*, "Homogeneous Dispersion of Cellulose Nanofibers in Waterborne Acrylic Coatings with Improved Properties and Unreduced Transparency," (in English), *Acs Sustainable Chemistry & Engineering,* vol. 4, no. 7, pp. 3766-3772, Jul 2016.

[26] N. Lavoine, V. Guillard, I. Desloges, N. Gontard, and J. Bras, "Active bio-based food-packaging: Diffusion and release of active substances through and from cellulose nanofiber coating toward food-packaging design," *Carbohydrate Polymers,* vol. 149, pp. 40-50, 2016/09/20/ 2016.

[27] V. Kumar, A. Elfving, H. Koivula, D. Bousfield, and M. Toivakka, "Roll-to-Roll Processed Cellulose Nanofiber Coatings," *Industrial & Engineering Chemistry Research,* vol. 55, no. 12, pp. 3603-3613, 2016/03/30 2016.

[28] V. Favier, G. R. Canova, J. Y. Cavaille, H. Chanzy, A. Dufresne, and C. Gauthier, "Nanocomposite Materials from Latex and Cellulose Whiskers," (in English), *Polymers for Advanced Technologies,* vol. 6, no. 5, pp. 351-355, May 1995.

[29] P. Hajji, J. Y. Cavaille, V. Favier, C. Gauthier, and G. Vigier, "Tensile behavior of nanocomposites from latex and cellulose whiskers," (in English), *Polymer Composites,* vol. 17, no. 4, pp. 612-619, Aug 1996.

[30] W. Helbert, J. Y. Cavaille, and A. Dufresne, "Thermoplastic nanocomposites filled with wheat straw cellulose whiskers .1. Processing and mechanical behavior," (in English), *Polymer Composites,* vol. 17, no. 4, pp. 604-611, Aug 1996.

[31] M. Grunert and W. T. Winter, "Nanocomposites of cellulose acetate butyrate reinforced with cellulose nanocrystals," (in English), *Journal of Polymers and the Environment,* vol. 10, no. 1-2, pp. 27-30, Apr 2002.

[32] K. Oksman, A. P. Mathew, D. Bondeson, and I. Kvien, "Manufacturing process of cellulose whiskers/polylactic acid nanocomposites," (in English), *Composites Science and Technology,* vol. 66, no. 15, pp. 2776-2784, Dec 2006.

[33] M. Roohani, Y. Habibi, N. M. Belgacem, G. Ebrahim, A. N. Karimi, and A. Dufresne, "Cellulose whiskers reinforced polyvinyl alcohol copolymers

nanocomposites," (in English), *European Polymer Journal,* vol. 44, no. 8, pp. 2489-2498, Aug 2008.

[34] A. J. de Menezes, G. Siqueira, A. A. S. Curvelo, and A. Dufresne, "Extrusion and characterization of functionalized cellulose whiskers reinforced polyethylene nanocomposites," (in English), *Polymer,* vol. 50, no. 19, pp. 4552-4563, Sep 10 2009.

[35] M. Jonoobi, J. Harun, A. P. Mathew, and K. Oksman, "Mechanical properties of cellulose nanofiber (CNF) reinforced polylactic acid (PLA) prepared by twin screw extrusion," (in English), *Composites Science and Technology,* vol. 70, no. 12, pp. 1742-1747, Oct 31 2010.

[36] M. Jonoobi, A. P. Mathew, M. M. Abdi, M. D. Makinejad, and K. Oksman, "A Comparison of Modified and Unmodified Cellulose Nanofiber Reinforced Polylactic Acid (PLA) Prepared by Twin Screw Extrusion," (in English), *Journal of Polymers and the Environment,* vol. 20, no. 4, pp. 991-997, Dec 2012.

[37] A. N. Frone, S. Berlioz, J. F. Chailan, and D. M. Panaitescu, "Morphology and thermal properties of PLA-cellulose nanofibers composites," (in English), *Carbohydrate Polymers,* vol. 91, no. 1, pp. 377-384, Jan 2 2013.

[38] D. M. Panaitescu, A. N. Frone, and C. Nicolae, "Micro- and nano-mechanical characterization of polyamide 11 and its composites containing cellulose nanofibers," (in English), *European Polymer Journal,* vol. 49, no. 12, pp. 3857-3866, Dec 2013.

[39] S. Beck, J. Bouchard, G. Chauve, and R. Berry, "Controlled production of patterns in iridescent solid films of cellulose nanocrystals," *Cellulose,* journal article vol. 20, no. 3, pp. 1401-1411, June 01 2013.

[40] A. D. Haywood and V. A. Davis, "Effects of liquid crystalline and shear alignment on the optical properties of cellulose nanocrystal films," (in English), *Cellulose*, vol. 24, no. 2, pp. 705-716, Feb 2017.

[41] H. Fukuzumi, T. Saito, T. Iwata, Y. Kumamoto, and A. Isogai, "Transparent and High Gas Barrier Films of Cellulose Nanofibers Prepared by TEMPO-Mediated Oxidation," *Biomacromolecules,* vol. 10, no. 1, pp. 162-165, 2009/01/12 2009.

[42] Y. Zhou *et al.*, "Recyclable organic solar cells on cellulose nanocrystal substrates," *Scientific Reports,* Article vol. 3, p. 1536, 03/25/online 2013.

[43] A. Nicharat, J. Sapkota, C. Weder, and E. J. Foster, "Melt processing of polyamide 12 and cellulose nanocrystals nanocomposites," (in English), *Journal of Applied Polymer Science,* vol. 132, no. 45, Dec 5 2015.

[44] E. M. Sullivan, R. J. Moon, and K. Kalaitzidou, "Processing and Characterization of Cellulose Nanocrystals/Polylactic Acid Nanocomposite Films," (in English), *Materials,* vol. 8, no. 12, pp. 8106-8116, Dec 2015.

[45] A. N. Frone, C. A. Nicolae, R. A. Gabor, and D. M. Panaitescu, "Thermal properties of water-resistant starch - polyvinyl alcohol films modified with cellulose nanofibers," (in English), *Polymer Degradation and Stability,* vol. 121, pp. 385-397, Nov 2015.

[46] J. Luo *et al.*, "Influence of high loading of cellulose nanocrystals in polyacrylonitrile composite films," (in English), *Cellulose,* vol. 24, no. 4, pp. 1745-1758, Apr 2017.

[47] J. Sapkota, J. C. Natterodt, A. Shirole, E. J. Foster, and C. Weder, "Fabrication and Properties of Polyethylene/Cellulose Nanocrystal Composites," (in English), *Macromolecular Materials and Engineering,* vol. 302, no. 1, Jan 2017.

[48] L. Wang *et al.*, "Effects of hydrophobic-modified cellulose nanofibers (CNFs) on cell morphology and mechanical properties of high void fraction polypropylene nanocomposite foams," (in English), *Composites Part a-Applied Science and Manufacturing,* vol. 98, pp. 166-173, Jul 2017.

[49] Y. X. Liu, "Strong and Flexible Nanocomposites of Carboxylated Cellulose Nanofibril Dispersed by Industrial Lignin," (in English), *Acs Sustainable Chemistry & Engineering,* vol. 6, no. 4, pp. 5524-5532, Apr 2018.

[50] G. Siqueira, J. Bras, and A. Dufresne, "Cellulosic Bionanocomposites: A Review of Preparation, Properties and Applications," (in English), *Polymers,* vol. 2, no. 4, pp. 728-765, Dec 2010.

[51] S. S. Nair, J. Zhu, Y. Deng, and A. J. Ragauskas, "High performance green barriers based on nanocellulose," *Sustainable Chemical Processes,* journal article vol. 2, no. 1, p. 23, November 07 2014.

[52] J. W. Wang, D. J. Gardner, N. M. Stark, D. W. Bousfield, M. Tajvidi, and Z. Y. Cai, "Moisture and Oxygen Barrier Properties of Cellulose Nanomaterial-Based Films," (in English), *Acs Sustainable Chemistry & Engineering,* vol. 6, no. 1, pp. 49-70, Jan 2018.

[53] S. Beck-Candanedo, M. Roman, and D. G. Gray, "Effect of reaction conditions on the properties and behavior of wood cellulose nanocrystal suspensions," (in English), *Biomacromolecules,* vol. 6, no. 2, pp. 1048-1054, Mar-Apr 2005.

[54] J. Majoinen, E. Kontturi, O. Ikkala, and D. G. Gray, "SEM imaging of chiral nematic films cast from cellulose nanocrystal suspensions," (in English), *Cellulose,* vol. 19, no. 5, pp. 1599-1605, Oct 2012.

[55] D. G. Gray, "Order and gelation of cellulose nanocrystal suspensions: an overview of some issues," (in English), *Philosophical Transactions of the Royal Society a-Mathematical Physical and Engineering Sciences,* vol. 376, no. 2112, Feb 13 2018.

[56] S. Beck, J. Bouchard, and R. Berry, "Controlling the Reflection Wavelength of Iridescent Solid Films of Nanocrystalline Cellulose," (in English), *Biomacromolecules,* vol. 12, no. 1, pp. 167-172, Jan 2011.

[57] A. Dufresne, "Nanocellulose: a new ageless bionanomaterial," (in English), *Materials Today,* vol. 16, no. 6, pp. 220-227, Jun 2013.

[58] L. J. and W. Yves, "Recent innovations in barrier technologies for plastic packaging—a review," *Packaging Technology and Science,* vol. 16, no. 4, pp. 149-158, 2003.

[59] S. J. Eichhorn, "Cellulose nanowhiskers: promising materials for advanced applications," (in English), *Soft Matter,* vol. 7, no. 2, pp. 303-315, 2011.

[60] S. Iwamoto, W. Kai, A. Isogai, and T. Iwata, "Elastic Modulus of Single Cellulose Microfibrils from Tunicate Measured by Atomic Force Microscopy," *Biomacromolecules,* vol. 10, no. 9, pp. 2571-2576, 2009/09/14 2009.

[61] G. Guhados, W. Wan, and J. L. Hutter, "Measurement of the Elastic Modulus of Single Bacterial Cellulose Fibers Using Atomic Force Microscopy," *Langmuir,* vol. 21, no. 14, pp. 6642-6646, 2005/07/01 2005.

[62] Y.-C. Hsieh, H. Yano, M. Nogi, and S. J. Eichhorn, "An estimation of the Young's modulus of bacterial cellulose filaments," *Cellulose,* journal article vol. 15, no. 4, pp. 507-513, August 01 2008.

[63] S. J. Eichhorn *et al.*, "Review: current international research into cellulose nanofibres and nanocomposites," *Journal of Materials Science,* journal article vol. 45, no. 1, p. 1, September 24 2009.

[64] Q. Z. Cheng and S. Q. Wang, "A method for testing the elastic modulus of single cellulose fibrils via atomic force microscopy," (in English), *Composites Part a-Applied Science and Manufacturing,* vol. 39, no. 12, pp. 1838-1843, Dec 2008.

[65] T. Saito, R. Kuramae, J. Wohlert, L. A. Berglund, and A. Isogai, "An Ultrastrong Nanofibrillar Biomaterial: The Strength of Single Cellulose Nanofibrils Revealed via Sonication-Induced Fragmentation," *Biomacromolecules,* vol. 14, no. 1, pp. 248-253, 2013/01/14 2013.

[66] E. R. Kenawy *et al.*, "Electrospinning of poly(ethylene-co-vinyl alcohol) fibers," (in English), *Biomaterials,* vol. 24, no. 6, pp. 907-913, Mar 2003.

[67] K. K. Mokwena and J. Tang, "Ethylene Vinyl Alcohol: A Review of Barrier Properties for Packaging Shelf Stable Foods," (in English), *Critical Reviews in Food Science and Nutrition,* vol. 52, no. 7, pp. 640-650, 2012.

[68] D. J. Valenti and K. B. Wagener, "Direct Synthesis of Well-Defined Alcohol-Functionalized Polymers via Acyclic Diene Metathesis (ADMET) Polymerization," *Macromolecules,* vol. 31, no. 9, pp. 2764-2773, 1998/05/01 1998.

[69] O. A. Scherman, R. Walker, and R. H. Grubbs, "Synthesis and Characterization of Stereoregular Ethylene-Vinyl Alcohol Copolymers Made by Ring-Opening Metathesis Polymerization," *Macromolecules,* vol. 38, no. 22, pp. 9009-9014, 2005/11/01 2005.

[70] K. Nakamae, M. Kameyama, and T. Matsumoto, "Elastic moduli of the crystalline regions in the direction perpendicula to the chain axis of ethylene-vinyl alcohol copolymers," *Polymer Engineering and Science,* vol. 19, no. 8, pp. 572-578, June 1979 1979.

[71] M. Takahashi, K. Tashiro, and S. Amiya, "Crystal structure of ethylene- vinyl alcohol copolymers," *Macromolecules,* vol. 32, pp. 5860-5871, 1999.

[72] M. L. Cerrada, E. Perez, J. M. Perena, and R. Benavente, "Wide-angle X-ray diffraction study of the phase behavior of vinyl alcohol ethylene copolymers," (in English), *Macromolecules,* vol. 31, no. 8, pp. 2559-2564, Apr 21 1998.

[73] J. M. Lagaron, E. Gimenez, J. J. Saura, and R. Gavara, "Phase morphology, crystallinity and mechanical properties of binary blends of high barrier ethylene-vinyl alcohol copolymer and amorphous polyamide and a polyamide-containing ionomer," (in English), *Polymer,* vol. 42, no. 17, pp. 7381-7394, Aug 2001.

[74] M. Martinez-Sanz, A. Lopez-Rubio, and J. M. Lagaron, "Nanocomposites of ethylene vinyl alcohol copolymer with thermally resistant cellulose nanowhiskers by melt compounding (I): Morphology and thermal properties," (in English), *Journal of Applied Polymer Science,* vol. 128, no. 5, pp. 2666-2678, Jun 5 2013.

[75] M. Martinez-Sanz, A. Lopez-Rubio, and J. M. Lagaron, "Nanocomposites of ethylene vinyl alcohol copolymer with thermally resistant cellulose nanowhiskers by melt compounding (II): Water barrier and mechanical properties," (in English), *Journal of Applied Polymer Science,* vol. 128, no. 3, pp. 2197-2207, May 5 2013.

[76] "EVAL, a unique Kuraray technology," 2011.

[77] A. Susana, M. Carlos, and G. Rafael, "Water effect on the morphology of EVOH copolymers," *Journal of Applied Polymer Science,* vol. 74, no. 5, pp. 1201-1206, 1999.

[78] Z. Zhongbin, B. I. J., and T. M. A., "Permeation of oxygen and water vapor through EVOH films as influenced by relative humidity," *Journal of Applied Polymer Science,* vol. 82, no. 8, pp. 1866-1872, 2001.

[79] M. Martinez-Sanz, R. T. Olsson, A. Lopez-Rubio, and J. M. Lagaron, "Development of electrospun EVOH fibres reinforced with bacterial cellulose nanowhiskers. Part I: Characterization and method optimization," (in English), *Cellulose,* vol. 18, no. 2, pp. 335-347, Apr 2011.

[80] N. Artzi, Y. Nir, D. Wang, M. Narkis, and A. Siegmann, "EVOH/clay nanocomposites produced by melt processing," (in English), *Polymer Composites,* vol. 22, no. 5, pp. 710-720, Oct 2001.

[81] N. Artzi, Y. Nir, M. Narkis, and A. Siegmann, "Melt blending of ethylene-vinyl alcohol copolymer/clay nanocomposites: Effect of the clay type and processing conditions," (in English), *Journal of Polymer Science Part B-Polymer Physics,* vol. 40, no. 16, pp. 1741-1753, Aug 15 2002.

[82] N. Artzi, Y. Nir, M. Narkis, and A. Siegmann, "The effect of maleated compatibilizers on the structure and properties of EVOH/clay nanocomposites," (in English), *Polymer Composites,* vol. 24, no. 5, pp. 627-639, Oct 2003.

[83] N. Artzi, M. Narkis, and A. Siegmann, "Review of melt-processed nanocomposites based on EVOH/organoclay," (in English), *Journal of Polymer Science Part B-Polymer Physics,* vol. 43, no. 15, pp. 1931-1943, Aug 1 2005.

[84] N. Artzi, A. Tzur, M. Narkis, and A. Siegmann, "The effect of extrusion processing conditions on EVOH/clay nanocomposites at low organo-clay contents," (in English), *Polymer Composites,* vol. 26, no. 3, pp. 343-351, Jun 2005.

[85] J. Yang *et al.,* "Thermal Reduced Graphene Based Poly(ethylene vinyl alcohol) Nanocomposites: Enhanced Mechanical Properties, Gas Barrier, Water Resistance, and Thermal Stability," (in English), *Industrial & Engineering Chemistry Research,* vol. 52, no. 47, pp. 16745-16754, Nov 27 2013.

[86] S. W. Kim and H. M. Choi, "Enhancement of thermal, mechanical, and barrier properties of ethylene vinyl alcohol copolymer by incorporation of graphene nanosheets: effect of functionalization of graphene oxide," (in English), *High Performance Polymers,* vol. 27, no. 6, pp. 694-704, Sep 2015.

[87] H. Kwon, D. Kim, and J. Seo, "Thermal and Barrier Properties of EVOH/EFG Nanocomposite Films for Packaging Applications: Effect of the Mixing Method," (in English), *Polymer Composites,* vol. 37, no. 6, pp. 1744-1753, Jun 2016.

[88] R. J. Moon, G. T. Schueneman, and J. Simonsen, "Overview of Cellulose Nanomaterials, Their Capabilities and Applications," *JOM,* journal article vol. 68, no. 9, pp. 2383-2394, September 01 2016.

[89] A. Dufresne, J. Y. Cavaille, and W. Helbert, "Thermoplastic nanocomposites filled with wheat straw cellulose whiskers .2. Effect of processing and modeling," (in English), *Polymer Composites,* vol. 18, no. 2, pp. 198-210, Apr 1997.

[90] J. Sapkota, M. Jorfi, C. Weder, and E. J. Foster, "Reinforcing Poly(ethylene) with Cellulose Nanocrystals," (in English), *Macromolecular Rapid Communications,* vol. 35, no. 20, pp. 1747-1753, Oct 2014.

[91] N. Farahbakhsh, P. S. Roodposhti, A. Ayoub, R. A. Venditti, and J. S. Jur, "Melt extrusion of polyethylene nanocomposites reinforced with nanofibrillated cellulose from cotton and wood sources," (in English), *Journal of Applied Polymer Science,* vol. 132, no. 17, May 5 2015.

[92] V. Khoshkava and M. R. Kamal, "Effect of Cellulose Nanocrystals (CNC) Particle Morphology on Dispersion and Rheological and Mechanical Properties of Polypropylene/CNC Nanocomposites," *ACS Applied Materials & Interfaces,* vol. 6, no. 11, pp. 8146-8157, 2014/06/11 2014.

[93] R. Rusli, K. Shanmuganathan, S. J. Rowan, C. Weder, and S. J. Eichhorn, "Stress-Transfer in Anisotropic and Environmentally Adaptive Cellulose Whisker Nanocomposites," (in English), *Biomacromolecules,* vol. 11, no. 3, pp. 762-768, Mar 2010.

[94] G. Gong, J. Pyo, A. P. Mathew, and K. Oksman, "Tensile behavior, morphology and viscoelastic analysis of cellulose nanofiber-reinforced (CNF) polyvinyl acetate (PVAc)," (in English), *Composites Part a-Applied Science and Manufacturing,* vol. 42, no. 9, pp. 1275-1282, Sep 2011.

[95] J. Sapkota, S. Kumar, C. Weder, and E. J. Foster, "Influence of Processing Conditions on Properties of Poly (Vinyl acetate)/Cellulose Nanocrystal Nanocomposites," (in English), *Macromolecular Materials and Engineering,* vol. 300, no. 5, pp. 562-571, May 2015.

[96] A. Nicharat, J. Sapkota, and E. J. Foster, "Pre-mixing and masterbatch approaches for reinforcing poly(vinyl acetate) with cellulose based fillers," (in English), *Industrial Crops and Products,* vol. 93, pp. 244-250, Dec 25 2016.

[97] W. Zhang *et al.*, "High performance poly (vinyl alcohol)/cellulose nanocrystals nanocomposites manufactured by injection molding," (in English), *Cellulose,* vol. 21, no. 1, pp. 485-494, Feb 2014.

[98] C. E. Meree, G. T. Schueneman, J. C. Meredith, and M. L. Shofner, "Rheological behavior of highly loaded cellulose nanocrystal/poly(vinyl alcohol) composite suspensions," (in English), *Cellulose,* vol. 23, no. 5, pp. 3001-3012, Oct 2016.

[99] H. Y. Bian, L. Q. Wei, C. X. Lin, Q. L. Ma, H. Q. Dai, and J. Y. Zhu, "Lignin-Containing Cellulose Nanofibril-Reinforced Polyvinyl Alcohol Hydrogels," (in

English), *Acs Sustainable Chemistry & Engineering*, vol. 6, no. 4, pp. 4821-4828, Apr 2018.

[100] J. Chen, D. Wu, K. C. Tam, K. Pan, and Z. Zheng, "Effect of surface modification of cellulose nanocrystal on nonisothermal crystallization of poly(β-hydroxybutyrate) composites," *Carbohydrate Polymers*, vol. 157, pp. 1821-1829, 2017/02/10/ 2017.

[101] C. Zhijiang and Y. Guang, "Optical nanocomposites prepared by incorporating bacterial cellulose nanofibrils into poly(3-hydroxybutyrate)," *Materials Letters*, vol. 65, no. 2, pp. 182-184, 2011/01/31/ 2011.

[102] A. H. Pei, Q. Zhou, and L. A. Berglund, "Functionalized cellulose nanocrystals as biobased nucleation agents in poly(L-lactide) (PLLA) - Crystallization and mechanical property effects," (in English), *Composites Science and Technology*, vol. 70, no. 5, pp. 815-821, May 2010.

[103] R. Scaffaro, L. Botta, F. Lopresti, A. Maio, and F. Sutera, "Polysaccharide nanocrystals as fillers for PLA based nanocomposites," (in English), *Cellulose*, vol. 24, no. 2, pp. 447-478, Feb 2017.

[104] D. M. Panaitescu, A. N. Frone, I. Chiulan, R. A. Gabor, I. C. Spataru, and A. Casarica, "Biocomposites from Polylactic Acid and Bacterial Cellulose Nanofibers Obtained by Mechanical Treatment," (in English), *Bioresources*, vol. 12, no. 1, pp. 662-672, 2017.

[105] H. Dong, K. E. Strawhecker, J. F. Snyder, J. A. Orlicki, R. S. Reiner, and A. W. Rudie, "Cellulose nanocrystals as a reinforcing material for electrospun poly(methyl methacrylate) fibers: Formation, properties and nanomechanical characterization," (in English), *Carbohydrate Polymers*, vol. 87, no. 4, pp. 2488-2495, Mar 1 2012.

[106] V. Favier, G. R. Canova, S. C. Shrivastava, and J. Y. Cavaille, "Mechanical percolation in cellulose whisker nanocomposites," (in English), *Polymer Engineering and Science*, vol. 37, no. 10, pp. 1732-1739, Oct 1997.

[107] V. Favier, R. Dendievel, G. Canova, J. Y. Cavaille, and P. Gilormini, "Simulation and modeling of three-dimensional percolating structures: Case of a latex matrix reinforced by a network of cellulose fibers," (in English), *Acta Materialia*, vol. 45, no. 4, pp. 1557-1565, Apr 1997.

[108] M. Mariano, C. Chirat, N. El Kissi, and A. Dufresne, "Impact of Cellulose Nanocrystal Aspect Ratio on Crystallization and Reinforcement of Poly(butylene adipate-co-terephthalate)," (in English), *Journal of Polymer Science Part B-Polymer Physics*, vol. 54, no. 22, pp. 2284-2297, Nov 2016.

[109] K. Sakakibara, H. Yano, and Y. Tsujii, "Surface Engineering of Cellulose Nanofiber by Adsorption of Diblock Copolymer Dispersant for Green

Nanocomposite Materials," (in English), *Acs Applied Materials & Interfaces,* vol. 8, no. 37, pp. 24893-24900, Sep 21 2016.

[110] Y. Shimazaki *et al.*, "Excellent thermal conductivity of transparent cellulose nanofiber/epoxy resin nanocomposites," (in English), *Biomacromolecules,* vol. 8, no. 9, pp. 2976-2978, Sep 2007.

[111] R. Rusli, K. Shanmuganathan, S. J. Rowan, C. Weder, and S. J. Eichhorn, "Stress Transfer in Cellulose Nanowhisker Composites-Influence of Whisker Aspect Ratio and Surface Charge," (in English), *Biomacromolecules,* vol. 12, no. 4, pp. 1363-1369, Apr 2011.

[112] S. H. Xu, N. Girouard, G. Schueneman, M. L. Shofner, and J. C. Meredith, "Mechanical and thermal properties of waterborne epoxy composites containing cellulose nanocrystals," (in English), *Polymer,* vol. 54, no. 24, pp. 6589-6598, Nov 14 2013.

[113] A. H. Pei, J. M. Malho, J. Ruokolainen, Q. Zhou, and L. A. Berglund, "Strong Nanocomposite Reinforcement Effects in Polyurethane Elastomer with Low Volume Fraction of Cellulose Nanocrystals," (in English), *Macromolecules,* vol. 44, no. 11, pp. 4422-4427, Jun 14 2011.

[114] N. Ucar *et al.*, "Thermal and mechanical properties of composite nanofiber webs and films containing cellulose nanowhiskers," (in English), *Textile Research Journal,* vol. 83, no. 13, pp. 1335-1344, Aug 2013.

[115] J. C. Liu, D. J. Martin, R. J. Moon, and J. P. Youngblood, "Enhanced thermal stability of biomedical thermoplastic polyurethane with the addition of cellulose nanocrystals," (in English), *Journal of Applied Polymer Science,* vol. 132, no. 22, Jun 10 2015.

[116] N. M. Girouard, S. H. Xu, G. T. Schueneman, M. L. Shofner, and J. C. Meredith, "Site-Selective Modification of Cellulose Nanocrystals with Isophorone Diisocyanate and Formation of Polyurethane-CNC Composites," (in English), *Acs Applied Materials & Interfaces,* vol. 8, no. 2, pp. 1458-1467, Jan 20 2016.

[117] A. Nicharat, A. Shirole, E. J. Foster, and C. Weder, "Thermally activated shape memory behavior of melt-mixed polyurethane/cellulose nanocrystal composites," (in English), *Journal of Applied Polymer Science,* vol. 134, no. 27, Jul 15 2017.

[118] M. P. Orr and M. L. Shofner, "Processing strategies for cellulose nanocrystal/polyethylene-co-vinyl alcohol composites," (in English), *Polymer,* vol. 126, pp. 211-223, Sep 22 2017.

[119] M. S. Peresin, Y. Habibi, A. H. Vesterinen, O. J. Rojas, J. J. Pawlak, and J. V. Seppala, "Effect of Moisture on Electrospun Nanofiber Composites of Poly(vinyl alcohol) and Cellulose Nanocrystals," (in English), *Biomacromolecules,* vol. 11, no. 9, pp. 2471-2477, Sep 2010.

[120] H. B. Chang, A. T. Chien, H. C. Liu, P. H. Wang, B. A. Newcomb, and S. Kumar, "Gel Spinning of Polyacrylonitrile/Cellulose Nanocrystal Composite Fibers," (in English), *Acs Biomaterials Science & Engineering,* vol. 1, no. 7, pp. 610-616, Jul 2015.

[121] N. Herrera, A. M. Salaberria, A. P. Mathew, and K. Oksman, "Plasticized polylactic acid nanocomposite films with cellulose and chitin nanocrystals prepared using extrusion and compression molding with two cooling rates: Effects on mechanical, thermal and optical properties," (in English), *Composites Part a-Applied Science and Manufacturing,* vol. 83, pp. 89-97, Apr 2016.

[122] A. Arias, M. C. Heuzey, M. A. Huneault, G. Ausias, and A. Bendahou, "Enhanced dispersion of cellulose nanocrystals in melt-processed polylactide-based nanocomposites," (in English), *Cellulose,* vol. 22, no. 1, pp. 483-498, Feb 2015.

[123] A. E. Lewandowska and S. J. Eichhorn, "Quantification of the degree of mixing of cellulose nanocrystals in thermoplastics using Raman spectroscopy," (in English), *Journal of Raman Spectroscopy,* vol. 47, no. 11, pp. 1337-1342, Nov 2016.

[124] A. E. Lewandowska and S. J. Eichhorn, "Raman imaging as a tool for assessing the degree of mixing and the interface between polyethylene and cellulose nanocrystals," (in English), *37th Riso International Symposium on Materials Science,* vol. 139, 2016.

[125] N. Volk, R. L. He, and K. Magniez, "Enhanced homogeneity and interfacial compatibility in melt-extruded cellulose nano-fibers reinforced polyethylene via surface adsorption of poly(ethylene glycol)-block-poly (ethylene) amphiphiles," (in English), *European Polymer Journal,* vol. 72, pp. 270-281, Nov 2015.

[126] T. Abitbol, T. Johnstone, T. M. Quinn, and D. G. Gray, "Reinforcement with cellulose nanocrystals of poly(vinyl alcohol) hydrogels prepared by cyclic freezing and thawing," (in English), *Soft Matter,* vol. 7, no. 6, pp. 2373-2379, 2011.

[127] E. Bahar *et al.*, "Thermal and mechanical properties of polypropylene nanocomposite materials reinforced with cellulose nano whiskers," (in English), *Journal of Applied Polymer Science,* vol. 125, no. 4, pp. 2882-2889, Aug 15 2012.

[128] T. Wang and L. T. Drzal, "Cellulose-Nanofiber-Reinforced Poly(lactic acid) Composites Prepared by a Water-Based Approach," (in English), *Acs Applied Materials & Interfaces,* vol. 4, no. 10, pp. 5079-5085, Oct 2012.

[129] D. G. Liu, X. Sun, H. F. Tian, S. Maiti, and Z. S. Ma, "Effects of cellulose nanofibrils on the structure and properties on PVA nanocomposites," (in English), *Cellulose,* vol. 20, no. 6, pp. 2981-2989, Dec 2013.

[130] E. H. Qua, P. R. Hornsby, H. S. S. Sharma, G. Lyons, and R. D. McCall, "Preparation and Characterization of Poly(vinyl alcohol) Nanocomposites Made

from Cellulose Nanofibers," (in English), *Journal of Applied Polymer Science,* vol. 113, no. 4, pp. 2238-2247, Aug 15 2009.

[131] K. Benhamou, H. Kaddami, A. Magnin, A. Dufresne, and A. Ahmad, "Bio-based polyurethane reinforced with cellulose nanofibers: A comprehensive investigation on the effect of interface," (in English), *Carbohydrate Polymers,* vol. 122, pp. 202-211, May 20 2015.

[132] J. R. Capadona, K. Shanmuganathan, D. J. Tyler, S. J. Rowan, and C. Weder, "Stimuli-responsive polymer nanocomposites inspired by the sea cucumber dermis," (in English), *Science,* vol. 319, no. 5868, pp. 1370-1374, Mar 7 2008.

[133] Y. Srithep, L. S. Turng, R. Sabo, and C. Clemons, "Nanofibrillated cellulose (NFC) reinforced polyvinyl alcohol (PVOH) nanocomposites: properties, solubility of carbon dioxide, and foaming," (in English), *Cellulose,* vol. 19, no. 4, pp. 1209-1223, Aug 2012.

[134] J. C. Natterodt, J. Sapkota, E. J. Foster, and C. Weder, "Polymer Nanocomposites with Cellulose Nanocrystals Featuring Adaptive Surface Groups," (in English), *Biomacromolecules,* vol. 18, no. 2, pp. 517-525, Feb 2017.

[135] J. C. Natterodt, A. Petri-Fink, C. Weder, and J. O. Zoppe, "Cellulose Nanocrystals: Surface Modification, Applications and Opportunities at Interfaces," (in English), *Chimia,* vol. 71, no. 6, pp. 376-383, 2017.

[136] N. Lin, J. Huang, P. R. Chang, J. W. Feng, and J. H. Yu, "Surface acetylation of cellulose nanocrystal and its reinforcing function in poly(lactic acid)," (in English), *Carbohydrate Polymers,* vol. 83, no. 4, pp. 1834-1842, Feb 1 2011.

[137] M. Peltzer, A. H. Pei, Q. Zhou, L. Berglund, and A. Jimenez, "Surface modification of cellulose nanocrystals by grafting with poly(lactic acid)," (in English), *Polymer International,* vol. 63, no. 6, pp. 1056-1062, Jun 2014.

[138] M. Pereda, N. El Kissi, and A. Dufresne, "Extrusion of Polysaccharide Nanocrystal Reinforced Polymer Nanocomposites through Compatibilization with Poly(ethylene oxide)," (in English), *Acs Applied Materials & Interfaces,* vol. 6, no. 12, pp. 9365-9375, Jun 25 2014.

[139] S. Fujisawa, T. Saito, S. Kimura, T. Iwata, and A. Isogai, "Surface Engineering of Ultrafine Cellulose Nanofibrils toward Polymer Nanocomposite Materials," (in English), *Biomacromolecules,* vol. 14, no. 5, pp. 1541-1546, May 2013.

[140] G. Lo Re *et al.*, "Improved Cellulose Nanofibril Dispersion in Melt-Processed Polycaprolactone Nanocomposites by a Latex-Mediated Interphase and Wet Feeding as LDPE Alternative," *ACS Applied Nano Materials,* vol. 1, no. 6, pp. 2669-2677, 2018/06/22 2018.

[141] G. Josefsson, F. Berthold, and E. K. Gamstedt, "Stiffness contribution of cellulose nanofibrils to composite materials," (in English), *International Journal of Solids and Structures,* vol. 51, no. 5, pp. 945-953, Mar 1 2014.

[142] V. Favier, H. Chanzy, and J. Y. Cavaille, "Polymer Nanocomposites Reinforced by Cellulose Whiskers," (in English), *Macromolecules,* vol. 28, no. 18, pp. 6365-6367, Aug 28 1995.

[143] M. R. Loos and I. Manas-Zloczower, "Micromechanical models for carbon nanotube and cellulose nanowhisker reinforced composites," (in English), *Polymer Engineering and Science,* vol. 53, no. 4, pp. 882-887, Apr 2013.

[144] N. H. Inai, A. E. Lewandowska, O. R. Ghita, and S. J. Eichhorn, "Interfaces in polyethylene oxide modified cellulose nanocrystal - polyethylene matrix composites," *Composites Science and Technology,* vol. 154, pp. 128-135, 2018.

[145] A. A. Gusev and M. G. Rozman, "Numerical search for morphologies providing ultra high elastic stiffness in filled rubbers," *Computational and Theoretical Polymer Science,* vol. 9, no. 3, pp. 335-337, 1999/12/01/ 1999.

[146] Y. Chen, L. Liu, Q. Yang, S. Wen, L. Zhang, and C. Zhong, "Computational Study of Nanoparticle Dispersion and Spatial Distribution in Polymer Matrix under Oscillatory Shear Flow," *Langmuir,* vol. 29, no. 45, pp. 13932-13942, 2013/11/12 2013.

[147] M. K. Mayeda, W.-F. Kuan, W.-S. Young, J. A. Lauterbach, and T. H. Epps, "Controlling Particle Location with Mixed Surface Functionalities in Block Copolymer Thin Films," *Chemistry of Materials,* vol. 24, no. 14, pp. 2627-2634, 2012/07/24 2012.

[148] S. W. Sides, B. J. Kim, E. J. Kramer, and G. H. Fredrickson, "Hybrid Particle-Field Simulations of Polymer Nanocomposites," *Physical Review Letters,* vol. 96, no. 25, p. 250601, 06/27/ 2006.

[149] J. J. Chiu, B. J. Kim, E. J. Kramer, and D. J. Pine, "Control of Nanoparticle Location in Block Copolymers," *Journal of the American Chemical Society,* vol. 127, no. 14, pp. 5036-5037, 2005/04/01 2005.

[150] R. Shenhar, T. B. Norsten, and V. M. Rotello, "Polymer-Mediated Nanoparticle Assembly: Structural Control and Applications," *Advanced Materials,* vol. 17, no. 6, pp. 657-669, 2005.

[151] C. György, J. R. Lovett, N. J. W. Penfold, and S. P. Armes, "Epoxy-Functional Sterically Stabilized Diblock Copolymer Nanoparticles via RAFT Aqueous Emulsion Polymerization: Comparison of Two Synthetic Strategies," *Macromolecular Rapid Communications,* vol. 0, no. 0, p. 1800289.

[152] B. J. Kim, G. H. Fredrickson, C. J. Hawker, and E. J. Kramer, "Nanoparticle Surfactants as a Route to Bicontinuous Block Copolymer Morphologies," *Langmuir,* vol. 23, no. 14, pp. 7804-7809, 2007/07/01 2007.

[153] J. S. Hong, H. Namkung, K. H. Ahn, S. J. Lee, and C. Kim, "The role of organically modified layered silicate in the breakup and coalescence of droplets in PBT/PE blends," *Polymer,* vol. 47, no. 11, pp. 3967-3975, 2006/05/17/ 2006.

[154] S. Sinha Ray, S. Pouliot, M. Bousmina, and L. A. Utracki, "Role of organically modified layered silicate as an active interfacial modifier in immiscible polystyrene/polypropylene blends," *Polymer,* vol. 45, no. 25, pp. 8403-8413, 2004/11/01/ 2004.

[155] Y. Lin *et al.*, "Self-directed self-assembly of nanoparticle/copolymer mixtures," *Nature,* vol. 434, p. 55, 03/03/online 2005.

[156] R. Haggenmueller, H. H. Gommans, A. G. Rinzler, J. E. Fischer, and K. I. Winey, "Aligned single-wall carbon nanotubes in composites by melt processing methods," *Chemical Physics Letters,* vol. 330, no. 3, pp. 219-225, 2000/11/10/ 2000.

[157] A. Sarfraz, M. F. Warsi, M. I. Sarwar, and M. Ishaq, "Improvement in tensile properties of PVC–montmorillonite nanocomposites through controlled uniaxial stretching," *Bulletin of Materials Science,* journal article vol. 35, no. 4, pp. 539-544, August 01 2012.

[158] A. M. Abdalla, R. P. Sahu, and I. K. Puri, "Tailoring the properties of a polymer nanocomposite with a magnetic field," *Polymer Composites,* vol. 0, no. 0.

[159] T. Kimura, H. Ago, M. Tobita, S. Ohshima, M. Kyotani, and M. Yumura, "Polymer composites of carbon nanotubes aligned by a magnetic field," (in English), *Advanced Materials,* vol. 14, no. 19, pp. 1380-1383, Oct 2 2002.

[160] P. W. Majewski, M. Gopinadhan, and C. O. Osuji, "Magnetic field alignment of block copolymers and polymer nanocomposites: Scalable microstructure control in functional soft materials," *Journal of Polymer Science Part B: Polymer Physics,* vol. 50, no. 1, pp. 2-8, 2012.

[161] C. A. Martin *et al.*, "Electric field-induced aligned multi-wall carbon nanotube networks in epoxy composites," *Polymer,* vol. 46, no. 3, pp. 877-886, 2005/01/26/ 2005.

[162] P. Cheol *et al.*, "Aligned single-wall carbon nanotube polymer composites using an electric field," *Journal of Polymer Science Part B: Polymer Physics,* vol. 44, no. 12, pp. 1751-1762, 2006.

[163] O. V. Sakhno, L. M. Goldenberg, T. N. Smirnova, and J. Stumpe, "Holographic patterning of organic-inorganic photopolymerizable nanocomposites," in *SPIE Security + Defence*, 2009, vol. 7487, p. 14: SPIE.

[164] S. Zeng-Bin, D. Xian-Zi, C. Wei-Qiang, S. Satoru, D. Xuan-Ming, and K. Satoshi, "Two- and three-dimensional micro/nanostructure patterning of CdS–polymer nanocomposites with a laser interference technique and in situ synthesis," *Nanotechnology,* vol. 19, no. 3, p. 035611, 2008.

[165] R. Jay, "A model for determining fiber reinforcement efficiencies and fiber orientation in polymer composites," *Polymer Composites,* vol. 13, no. 6, pp. 462-466, 1992.

[166] K. Yoshitsugu *et al.*, "Novel preferred orientation in injection-molded nylon 6-clay hybrid," *Journal of Polymer Science Part B: Polymer Physics,* vol. 33, no. 7, pp. 1039-1045, 1995.

[167] A. Theron, E. Zussman, and A. L. Yarin, "Electrostatic field-assisted alignment of electrospun nanofibres," *Nanotechnology,* vol. 12, no. 3, p. 384, 2001.

[168] K. Hyejeong and L. S. Joon, "Stomata-Inspired Membrane Produced Through Photopolymerization Patterning," *Advanced Functional Materials,* vol. 25, no. 28, pp. 4496-4505, 2015.

[169] R. A. Vaia, C. L. Dennis, L. V. Natarajan, V. P. Tondiglia, D. W. Tomlin, and T. J. Bunning, "One-Step, Micrometer-Scale Organization of Nano- and Mesoparticles Using Holographic Photopolymerization: A Generic Technique," *Advanced Materials,* vol. 13, no. 20, pp. 1570-1574, 2001.

[170] B. E. Risteen *et al.*, "Enhanced Alignment of Water-Soluble Polythiophene Using Cellulose Nanocrystals as a Liquid Crystal Template," *Biomacromolecules,* vol. 18, no. 5, pp. 1556-1562, 2017/05/08 2017.

[171] J. R. Capadona *et al.*, "A versatile approach for the processing of polymer nanocomposites with self-assembled nanofibre templates," *Nature Nanotechnology,* vol. 2, p. 765, 11/25/online 2007.

[172] K. J. De France, K. G. Yager, T. Hoare, and E. D. Cranston, "Cooperative Ordering and Kinetics of Cellulose Nanocrystal Alignment in a Magnetic Field," *Langmuir,* vol. 32, no. 30, pp. 7564-7571, 2016/08/02 2016.

[173] T. Pullawan, A. N. Wilkinson, and S. J. Eichhorn, "Influence of Magnetic Field Alignment of Cellulose Whiskers on the Mechanics of All-Cellulose Nanocomposites," *Biomacromolecules,* vol. 13, no. 8, pp. 2528-2536, 2012/08/13 2012.

[174] L. Rhode-Barbarigos, N. B. Hadj Ali, R. Motro, and I. F. C. Smith, "Designing tensegrity modules for pedestrian bridges," *Engineering Structures,* vol. 32, no. 4, pp. 1158-1167, 2010/04/01/ 2010.

[175] A. G. Tibert and S. Pellegrino, "Deployable Tensegrity Reflectors for Small Satellites," *Journal of Spacecraft and Rockets,* vol. 39, no. 5, pp. 701-709, 2002/09/01 2002.

[176] K. Liu, J. Wu, G. H. Paulino, and H. J. Qi, "Programmable Deployment of Tensegrity Structures by Stimulus-Responsive Polymers," *Scientific Reports,* vol. 7, no. 1, p. 3511, 2017/06/14 2017.

[177] C. Paul, F. J. Valero-Cuevas, and H. Lipson, "Design and control of tensegrity robots for locomotion," *IEEE Transactions on Robotics,* vol. 22, no. 5, pp. 944-957, 2006.

[178] S. Yan, Z. F. Xiao, M. Y. Lin, and J. Niu, "Numerical analysis of dynamic behavior of pre-stressed shape memory alloy concrete beam-column joints," *IOP Conference Series: Materials Science and Engineering,* vol. 348, no. 1, p. 012013, 2018.

[179] D. StamenoviĆ and M. F. Coughlin, "The Role of Prestress and Architecture of the Cytoskeleton and Deformability of Cytoskeletal Filaments in Mechanics of Adherent Cells: a Quantitative Analysis," *Journal of Theoretical Biology*, vol. 201, no. 1, pp. 63-74, 1999/11/07/ 1999.

[180] N. Wang, J. Butler, and D. Ingber, "Mechanotransduction across the cell surface and through the cytoskeleton," *Science,* vol. 260, no. 5111, pp. 1124-1127, 1993.

[181] N. Wang *et al.*, "Mechanical behavior in living cells consistent with the tensegrity model," *Proceedings of the National Academy of Sciences,* vol. 98, no. 14, pp. 7765-7770, 2001.

[182] C. Sultan, D. Stamenović, and D. E. Ingber, "A Computational Tensegrity Model Predicts Dynamic Rheological Behaviors in Living Cells," *Annals of Biomedical Engineering,* journal article vol. 32, no. 4, pp. 520-530, April 01 2004.

[183] D. StamenoviĆ, N. Wang, and D. E. Ingber, "4 - Cellular Tensegrity Models And Cell-Substrate Interactions," in *Principles of Cellular Engineering*, M. R. King, Ed. Burlington: Academic Press, 2006, pp. 81-101.

[184] N. Wang *et al.*, "Cell prestress. I. Stiffness and prestress are closely associated in adherent contractile cells," *American Journal of Physiology-Cell Physiology,* vol. 282, no. 3, pp. C606-C616, 2002.

[185] D. Stamenović, "Microtubules may harden or soften cells, depending of the extent of cell distension," *Journal of Biomechanics,* vol. 38, no. 8, pp. 1728-1732, 2005/08/01/ 2005.

[186] T. Liedl, B. Högberg, J. Tytell, D. E. Ingber, and W. M. Shih, "Self-assembly of three-dimensional prestressed tensegrity structures from DNA," (in eng), *Nature nanotechnology,* vol. 5, no. 7, pp. 520-524, 2010/07// 2010.

[187] J. Zheng *et al.*, "From molecular to macroscopic via the rational design of a self-assembled 3D DNA crystal," *Nature,* vol. 461, p. 74, 09/03/online 2009.

[188] S. Morris, S. Hanna, and M. J. Miles, "The self-assembly of plant cell wall components by single-molecule force spectroscopy and Monte Carlo modelling," *Nanotechnology,* vol. 15, no. 9, p. 1296, 2004.

[189] A. Sidorenko, T. Krupenkin, A. Taylor, P. Fratzl, and J. Aizenberg, "Reversible Switching of Hydrogel-Actuated Nanostructures into Complex Micropatterns," *Science,* vol. 315, no. 5811, pp. 487-490, 2007.

[190] B. Wang and K. S. Fancey, "Viscoelastically prestressed polymeric matrix composites: An investigation into fibre deformation and prestress mechanisms," *Composites Part A: Applied Science and Manufacturing,* vol. 111, pp. 106-114, 2018/08/01/ 2018.

[191] R. Wanting and G. A. C., "Mechanism of strain retention and shape memory in main chain liquid crystalline networks," *physica status solidi (b),* vol. 249, no. 7, pp. 1379-1385, 2012.

[192] R. S. Reiner and A. W. Rudie, *Process scale-up of cellulose nanocrystal production to 25 kg per batch at the Forest Products Laboratory*. TAPPI PRESS, 2013.

[193] M. Kaushik, C. Fraschini, G. Chauve, J.-L. Putaux, and A. Moores, "Transmission electron microscopy for the characterization of cellulose nanocrystals," in *The transmission electron microscope-theory and applications*: Intech, 2015, pp. 129-163.

[194] K. L. Stinson-Bagby, R. Roberts, and E. J. Foster, "Effective cellulose nanocrystal imaging using transmission electron microscopy," *Carbohydrate Polymers,* vol. 186, pp. 429-438, 2018/04/15/ 2018.

[195] S. J. Eichhorn, R. Rusli, K. Shanmuganathan, S. Rowan, and C. Weder, "Physical and mechanical properties of cellulose nanowhisker interfaces using Raman spectroscopy," (in English), *Abstracts of Papers of the American Chemical Society,* vol. 241, Mar 27 2011.

[196] X. Xu, F. Liu, L. Jiang, J. Y. Zhu, D. Haagenson, and D. P. Wiesenborn, "Cellulose Nanocrystals vs. Cellulose Nanofibrils: A Comparative Study on Their Microstructures and Effects as Polymer Reinforcing Agents," *ACS Applied Materials & Interfaces,* vol. 5, no. 8, pp. 2999-3009, 2013/04/24 2013.

[197] Y. Srithep *et al.*, "Melt compounding of poly (3-hydroxybutyrate-co-3-hydroxyvalerate)/nanofibrillated cellulose nanocomposites," *Polymer Degradation and Stability,* vol. 98, no. 8, pp. 1439-1449, 2013/08/01/ 2013.

[198] L. Cabeda, E. Gimenez, J. M. Lagaron, R. Gavara, and J. J. Saura, "Development of EVOH-kaolinite nanocomposites," (in English), *Polymer,* vol. 45, no. 15, pp. 5233-5238, Jul 12 2004.

[199] S. Lee, R. Tyler, J. Maia, and D. A. Schiraldi, "Structural interaction and gas barrier properties of ethylene-vinyl alcohol/tin phosphate glass composites," (in English), *Journal of Polymer Science Part B-Polymer Physics,* vol. 56, no. 13, pp. 989-998, Jul 1 2018.

[200] M. S. Peresin, Y. Habibi, J. O. Zoppe, J. J. Pawlak, and O. J. Rojas, "Nanofiber Composites of Polyvinyl Alcohol and Cellulose Nanocrystals: Manufacture and Characterization," (in English), *Biomacromolecules,* vol. 11, no. 3, pp. 674-681, Mar 2010.

[201] H. Chang, J. Luo, H. C. Liu, A. A. Bakhtiary Davijani, P.-H. Wang, and S. Kumar, "Orientation and interfacial stress transfer of cellulose nanocrystal nanocomposite fibers," *Polymer,* vol. 110, pp. 228-234, 2017/02/10/ 2017.

[202] E. Fortunati, D. Puglia, M. Monti, C. Santulli, M. Maniruzzaman, and J. M. Kenny, "Cellulose nanocrystals extracted from okra fibers in PVA nanocomposites," (in English), *Journal of Applied Polymer Science,* vol. 128, no. 5, pp. 3220-3230, Jun 5 2013.

[203] G. Socrates, *Infrared and Raman Characteristic Group Frequencies: Tables and Charts,* Third ed. Chichester, England: John Wiley & Sons, Ltd., 2001, p. 347.

[204] B. Soni, E. B. Hassan, and B. Mahmoud, "Chemical isolation and characterization of different cellulose nanofibers from cotton stalks," *Carbohydrate Polymers,* vol. 134, pp. 581-589, 2015/12/10/ 2015.

[205] S. Wang, C. Wei, Y. Gong, J. Lv, C. Yu, and J. Yu, "Cellulose nanofiber-assisted dispersion of cellulose nanocrystals@polyaniline in water and its conductive films," *RSC Advances,* 10.1039/C5RA19346J vol. 6, no. 12, pp. 10168-10174, 2016.

[206] J. Luo, N. Semenikhin, H. B. Chang, R. J. Moon, and S. Kumar, "Post-sulfonation of cellulose nanofibrils with a one-step reaction to improve dispersibility," (in English), *Carbohydrate Polymers,* vol. 181, pp. 247-255, Feb 1 2018.

[207] Y. Nir, M. Narkis, and A. Siegmann, "Morphology and infrared spectroscopy of strongly interacting polymer blends: EVOH/copolyamide-6/6.9," (in English), *Journal of Macromolecular Science-Physics,* vol. B37, no. 6, pp. 863-882, 1998.

[208] A. Lopez-Rubio *et al.*, "Effect of high pressure treatments on the properties of EVOH-based food packaging materials," (in English), *Innovative Food Science & Emerging Technologies,* vol. 6, no. 1, pp. 51-58, Mar 2005.

[209] D. Jun, Z. Guomin, P. Mingzhu, Z. Leilei, L. Dagang, and Z. Rui, "Crystallization and mechanical properties of reinforced PHBV composites using melt compounding: Effect of CNCs and CNFs," *Carbohydrate Polymers,* vol. 168, pp. 255-262, 2017/07/15/ 2017.

[210] X. Xu *et al.*, "Comparison between Cellulose Nanocrystal and Cellulose Nanofibril Reinforced Poly(ethylene oxide) Nanofibers and Their Novel Shish-Kebab-Like Crystalline Structures," *Macromolecules,* vol. 47, no. 10, pp. 3409-3416, 2014/05/27 2014.

[211] S. Noorani, J. Simonsen, and S. Atre, "Nano-enabled microtechnology: polysulfone nanocomposites incorporating cellulose nanocrystals," (in English), *Cellulose,* vol. 14, no. 6, pp. 577-584, Dec 2007.

[212] M. Martinez-Sanz, A. Lopez-Rubio, and J. M. Lagaron, "Optimization of the Dispersion of Unmodified Bacterial Cellulose Nanowhiskers into Polylactide via Melt Compounding to Significantly Enhance Barrier and Mechanical Properties," (in English), *Biomacromolecules,* vol. 13, no. 11, pp. 3887-3899, Nov 2012.

[213] M. R. Loos and I. Manas-Zloczower, "Reinforcement Efficiency of Carbon Nanotubes - Myth and Reality," (in English), *Macromolecular Theory and Simulations,* vol. 21, no. 2, pp. 130-137, Feb 2012.

[214] D. Stauffer, "Gelation in concentrated critically branched polymer solutions. Percolation scaling theory of intramolecular bond cycles," *Journal of the Chemical Society, Faraday Transactions 2: Molecular and Chemical Physics,* 10.1039/F29767201354 vol. 72, no. 0, pp. 1354-1364, 1976.

[215] X. Cao, Y. Habibi, and L. A. Lucia, "One-pot polymerization, surface grafting, and processing of waterborne polyurethane-cellulose nanocrystal nanocomposites," *Journal of Materials Chemistry,* 10.1039/B910517D vol. 19, no. 38, pp. 7137-7145, 2009.

[216] O. J. Yoon *et al.*, "Nanocomposite nanofibers of poly(d, l-lactic-co-glycolic acid) and graphene oxide nanosheets," *Composites Part A: Applied Science and Manufacturing,* vol. 42, no. 12, pp. 1978-1984, 2011/12/01/ 2011.

[217] J. Joseph and E. D. Jemmis, "Red-, Blue-, or No-Shift in Hydrogen Bonds: A Unified Explanation," *Journal of the American Chemical Society,* vol. 129, no. 15, pp. 4620-4632, 2007/04/01 2007.

[218] A. Isogai, T. Saito, and H. Fukuzumi, "TEMPO-oxidized cellulose nanofibers," *Nanoscale,* 10.1039/C0NR00583E vol. 3, no. 1, pp. 71-85, 2011.

[219] M. L. Cerrada, R. Benavente, E. Perez, and J. M. Perena, "The effect of annealing on the structure and relaxation processes of vinyl alcohol-ethylene copolymers," (in English), *Journal of Polymer Science Part B-Polymer Physics,* vol. 39, no. 1, pp. 1-12, Jan 1 2001.

[220] C. Fonseca, J. M. Perena, R. Benavente, M. L. Cerrada, A. Bello, and E. Perez, "Microhardness and Thermal Study of the Annealing Effects in Vinyl Alcohol-Ethylene Copolymers," (in English), *Polymer,* vol. 36, no. 9, pp. 1887-1892, Apr 1995.

[221] A. A. Minakov, D. A. Mordvintsev, and C. Schick, "Melting and reorganization of poly(ethylene terephthalate) on fast heating (1000 K/s)," (in English), *Polymer,* vol. 45, no. 11, pp. 3755-3763, May 13 2004.

[222] A. A. Minakov, D. A. Mordvintsev, R. Tol, and C. Schick, "Melting and reorganization of the crystalline fraction and relaxation of the rigid amorphous fraction of isotactic polystyrene on fast heating (30,000 K/min)," (in English), *Thermochimica Acta,* vol. 442, no. 1-2, pp. 25-30, Mar 15 2006.

[223] K. Jariyavidyanont, R. Androsch, and C. Schick, "Crystal reorganization of poly (butylene terephthalate)," (in English), *Polymer,* vol. 124, pp. 274-283, Aug 25 2017.

[224] M. A. S. Azizi Samir, F. Alloin, J.-Y. Sanchez, and A. Dufresne, "Cellulose nanocrystals reinforced poly(oxyethylene)," *Polymer,* vol. 45, no. 12, pp. 4149-4157, 2004/05/01/ 2004.

[225] E. Ten, L. Jiang, and M. P. Wolcott, "Crystallization kinetics of poly(3-hydroxybutyrate-co-3-hydroxyvalerate)/cellulose nanowhiskers composites," *Carbohydrate Polymers,* vol. 90, no. 1, pp. 541-550, 2012/09/01/ 2012.

[226] D. L. VanderHart, S. Simmons, and J. W. Gilman, "Solid-state 13C nuclear magnetic resonance spectroscopy of ethylene/vinyl alcohol copolymers: morphological partitioning of hydroxyls," *Polymer,* vol. 36, no. 22, pp. 4223-4232, 1995/01/01/ 1995.

[227] M. L. Marín, A. Jiménez, J. López, and J. Vilaplana, "Thermal degradation of ethylene (vinyl acetate)," *Journal of thermal analysis,* journal article vol. 47, no. 1, pp. 247-258, July 01 1996.

[228] J. M. Lagaron, E. Giménez, and J. J. Saura, "Degradation of high barrier ethylene–vinyl alcohol copolymer under mild thermal-oxidative conditions studied by thermal analysis and infrared spectroscopy," *Polymer International,* vol. 50, no. 6, pp. 635-642, 2001.

[229] X. Sun, Q. Wu, S. Ren, and T. Lei, "Comparison of highly transparent all-cellulose nanopaper prepared using sulfuric acid and TEMPO-mediated oxidation methods," *Cellulose,* journal article vol. 22, no. 2, pp. 1123-1133, April 01 2015.

[230] N. Ljungberg and B. Wesslén, "The effects of plasticizers on the dynamic mechanical and thermal properties of poly(lactic acid)," *Journal of Applied Polymer Science,* vol. 86, no. 5, pp. 1227-1234, 2002.

[231] Y.-T. Shieh, Y.-S. Lin, Y.-K. Twu, H.-B. Tsai, and R.-H. Lin, "Effect of crystallinity on enthalpy recovery peaks and cold-crystallization peaks in PET via TMDSC and DMA studies," *Journal of Applied Polymer Science,* vol. 116, no. 3, pp. 1334-1341, 2010.

[232] J. Bras, D. Viet, C. Bruzzese, and A. Dufresne, "Correlation between stiffness of sheets prepared from cellulose whiskers and nanoparticles dimensions," *Carbohydrate Polymers,* vol. 84, no. 1, pp. 211-215, 2011/02/11/ 2011.

[233] M. L. Cerrada, R. Benavente, E. Perez, and J. M. Perena, "The effect of tensile drawing on the structure and relaxation processes in vinyl alcohol-ethylene copolymers," (in English), *Polymer,* vol. 42, no. 7, pp. 3127-3138, Mar 2001.

[234] X. Qin, W. J. Xia, R. Sinko, and S. Keten, "Tuning Glass Transition in Polymer Nanocomposites with Functionalized Cellulose Nanocrystals through Nanoconfinement," (in English), *Nano Letters,* vol. 15, no. 10, pp. 6738-6744, Oct 2015.

[235] J. Schawe, "Practical Aspects of the Flash DSC 1: Sample Preparation for Measurements of Polymers," Mettler Toledo, Accessed on: July 14, 2017.

[236] E. Zhuravlev and C. Schick, "Fast scanning power compensated differential scanning nano-calorimeter: 2. Heat capacity analysis," (in English), *Thermochimica Acta,* vol. 505, no. 1-2, pp. 14-21, Jun 10 2010.

[237] V. V. Ray, A. K. Banthia, and C. Schick, "Fast isothermal calorimetry of modified polypropylene clay nanocomposites," (in English), *Polymer,* vol. 48, no. 8, pp. 2404-2414, Apr 5 2007.

[238] D. Mileva, R. Androsch, E. Zhuravlev, and C. Schick, "Morphology of mesophase and crystals of polyamide 6 prepared in a fast scanning chip calorimeter," (in English), *Polymer,* vol. 53, no. 18, pp. 3994-4001, Aug 17 2012.

[239] D. Thomas, E. Zhuravlev, A. Wurm, C. Schick, and P. Cebe, "Fundamental thermal properties of polyvinyl alcohol by fast scanning calorimetry," *Polymer,* vol. 137, pp. 145-155, 2018/02/14/ 2018.

[240] P. Cebe, B. P. Partlow, D. L. Kaplan, A. Wurm, E. Zhuravlev, and C. Schick, "Using flash DSC for determining the liquid state heat capacity of silk fibroin," (in English), *Thermochimica Acta,* vol. 615, pp. 8-14, Sep 10 2015.

[241] P. Cebe, B. P. Partlow, D. L. Kaplan, A. Wurm, E. Zhuravlev, and C. Schick, "Silk I and Silk II studied by fast scanning calorimetry," (in English), *Acta Biomaterialia,* vol. 55, pp. 323-332, Jun 2017.

[242] X. Monnier, L. Chevalier, A. Esposito, L. Fernandez-Ballester, A. Saiter, and E. Dargent, "Local and segmental motions of the mobile amorphous fraction in semi-

crystalline polylactide crystallized under quiescent and flow-induced conditions," (in English), *Polymer,* vol. 126, pp. 141-151, Sep 22 2017.

[243] X. Monnier, A. Saiter, and E. Dargent, "Physical aging in PLA through standard DSC and fast scanning calorimetry investigations," (in English), *Thermochimica Acta,* vol. 648, pp. 13-22, Feb 10 2017.

[244] N. Bosq, N. Guigo, E. Zhuravlev, and N. Sbirrazzuoli, "Nonisothermal Crystallization of Polytetrafluoroethylene in a Wide Range of Cooling Rates," (in English), *Journal of Physical Chemistry B,* vol. 117, no. 12, pp. 3407-3415, Mar 28 2013.

[245] Y. X. Chen, X. Chen, D. S. Zhou, Q. D. Shen, and W. B. Hu, "Low-temperature crystallization of P(VDF-TrFE-CFE) studied by Flash DSC," (in English), *Polymer,* vol. 84, pp. 319-327, Feb 10 2016.

[246] I. Kolesov *et al.*, "Crystallization of a polyamide 11/organo-modified montmorillonite nanocomposite at rapid cooling," (in English), *Colloid and Polymer Science,* vol. 291, no. 11, pp. 2541-2549, Nov 2013.

[247] Y. Gao, B. Zhao, B. Yang, and C. Schick, C. Schick and V. Mathot, Eds. *Fast Scanning Calorimetry*. Switzerland: Springer International Publishing AG Switzerland, 2016, p. 791.

[248] A. Wurm *et al.*, "Temperature Dependency of Nucleation Efficiency of Carbon Nanotubes in PET and PBT," (in English), *Macromolecular Materials and Engineering,* vol. 300, no. 6, pp. 637-649, Jun 2015.

[249] S. van Herwaarden, E. Iervolino, F. van Herwaarden, T. Wijffels, A. Leenaers, and V. Mathot, "Design, performance and analysis of thermal lag of the UFS1 twin-calorimeter chip for fast scanning calorimetry using the Mettler-Toledo Flash DSC 1," (in English), *Thermochimica Acta,* vol. 522, no. 1-2, pp. 46-52, Aug 10 2011.

[250] H. H. Chang, K. Beltsios, Y. H. Chen, D. J. Lin, and L. P. Cheng, "Effects of Cooling Temperature and Aging Treatment on the Morphology of Nano- and Micro-Porous Poly(ethylene-co-vinyl alcohol) Membranes by Thermal Induced Phase Separation Method," (in English), *Journal of Applied Polymer Science,* vol. 131, no. 12, Jun 15 2014.

[251] M. L. Cerrada, R. Benavente, E. Perez, and J. M. Perena, "Crystal structures and viscoelastic behavior in different morphologies of a vinyl alcohol-ethylene copolymer," (in English), *Polymer Journal,* vol. 32, no. 12, pp. 999-1006, 2000.

[252] E. Perez, M. L. Cerrada, and D. L. Vanderhart, "Rapid determination of comonomer content, crystallinity and long spacing by multiple-pulse proton NMR in ethylene-vinyl alcohol copolymers," (in English), *Journal of Polymer Science Part B-Polymer Physics,* vol. 36, no. 12, pp. 2103-2109, Sep 15 1998.

[253] I. Y. Phang, K. P. Pramoda, T. X. Liu, and C. B. He, "Crystallization and melting behavior of polyester/clay nanocomposites," (in English), *Polymer International,* vol. 53, no. 9, pp. 1282-1289, Sep 2004.

[254] P. G. Karagiannidis, A. C. Stergiou, and G. P. Karayannidis, "Study of crystallinity and thermomechanical analysis of annealed poly(ethylene terephthalate) films," (in English), *European Polymer Journal,* vol. 44, no. 5, pp. 1475-1486, May 2008.

[255] D. Lewitus, S. McCarthy, A. Ophir, and S. Kenig, "The effect of nanoclays on the properties of PLLA-modified polymers part 1: Mechanical and thermal properties," (in English), *Journal of Polymers and the Environment,* vol. 14, no. 2, pp. 171-177, Apr 2006.

[256] N. Ljungberg and B. Wesslen, "Preparation and properties of plasticized poly(lactic acid) films," (in English), *Biomacromolecules,* vol. 6, no. 3, pp. 1789-1796, May-Jun 2005.

[257] B. Wunderlich, "The Detection of Conformational Disorder by Thermal-Analysis," (in English), *Thermochimica Acta,* vol. 135, pp. 8-8, Oct 1988.

[258] B. Wunderlich, "Thermodynamic description of condensed phases," (in English), *Journal of Thermal Analysis and Calorimetry,* vol. 102, no. 2, pp. 413-424, Nov 2010.

[259] A. R. Hopkins and J. R. Reynolds, "Crystallization Driven Formation of Conducting Polymer Networks in Polymer Blends," *Macromolecules,* vol. 33, no. 14, pp. 5221-5226, 2000/07/01 2000.

[260] M. L. Cerrada, R. Benavente, E. Perez, and J. M. Perena, "The effect of orientation on the morphology and viscoelastic response of vinyl alcohol-ethylene copolymers," (in English), *Macromolecular Chemistry and Physics,* vol. 201, no. 14, pp. 1858-1868, Sep 28 2000.

[261] M. L. Cerrada, F. Fauth, J. P. Fernandez-Blazquez, and E. Perez, "Structural changes induced by deformation in an ethylene-(vinyl alcohol) copolymer: simultaneous measurements of uniaxial stretching and in situ wide-angle X-ray scattering," (in English), *Polymer International,* vol. 59, no. 8, pp. 1141-1147, Aug 2010.

[262] S. Chen, G. Schueneman, R. B. Pipes, J. Youngblood, and R. J. Moon, "Effects of Crystal Orientation on Cellulose Nanocrystals-Cellulose Acetate Nanocomposite Fibers Prepared by Dry Spinning," (in English), *Biomacromolecules,* vol. 15, no. 10, pp. 3827-3835, Oct 2014.

[263] E. A. Franco-Urquiza, J. Gamez-Perez, J. C. Velazquez-Infante, O. Santana, A. M. Benasat, and M. L. Maspoch, "Effect of the Strain Rate and Drawing Temperature on the Mechanical Behavior of EVOH and EVOH Composites," (in English), *Advances in Polymer Technology,* vol. 32, pp. E287-E296, Mar 2013.

[264] G. Raumann and D. W. Saunders, "The Anisotropy of Young's Modulus in Drawn Polyethylene," *Proceedings of the Physical Society,* vol. 77, no. 5, p. 1028, 1961.

[265] I. M. Ward, "Optical and Mechanical Anisotropy in Crystalline Polymers," *Proceedings of the Physical Society,* vol. 80, no. 5, p. 1176, 1962.

[266] Z. Yu, J. Brisson, and A. Ait-Kadi, "Prediction of mechanical properties of short kevlar fiber-nylon-6,6 composites," *Polymer Composites,* vol. 15, no. 1, pp. 64-73, 1994.

[267] J. C. Halpin and J. L. Kardos, "Halpin-Tsai Equations - Review," (in English), *Polymer Engineering and Science,* vol. 16, no. 5, pp. 344-352, 1976.

[268] K. I. Nakamura, M. Wada, S. Kuga, and T. Okano, "Poisson's ratio of cellulose Iβ and cellulose II," *Journal of Polymer Science Part B: Polymer Physics,* vol. 42, no. 7, pp. 1206-1211, 2004.

[269] A. Pakzad, J. Simonsen, and R. S. Yassar, "Gradient of nanomechanical properties in the interphase of cellulose nanocrystal composites," (in English), *Composites Science and Technology,* vol. 72, no. 2, pp. 314-319, Jan 18 2012.

[270] D. Ciprari, K. Jacob, and R. Tannenbaum, "Characterization of Polymer Nanocomposite Interphase and Its Impact on Mechanical Properties," *Macromolecules,* vol. 39, no. 19, pp. 6565-6573, 2006/09/01 2006.

[271] B. Wunderlich, "Reversible crystallization and the rigid–amorphous phase in semicrystalline macromolecules," *Progress in Polymer Science,* vol. 28, no. 3, pp. 383-450, 2003/03/01/ 2003.

[272] A. Sargsyan, A. Tonoyan, S. Davtyan, and C. Schick, "The amount of immobilized polymer in PMMA SiO2 nanocomposites determined from calorimetric data," *European Polymer Journal,* vol. 43, no. 8, pp. 3113-3127, 2007/08/01/ 2007.

[273] Y. Shen, E. Harkin-Jones, P. Hornsby, T. McNally, and R. Abu-Zurayk, "The effect of temperature and strain rate on the deformation behaviour, structure development and properties of biaxially stretched PET–clay nanocomposites," *Composites Science and Technology,* vol. 71, no. 5, pp. 758-764, 2011/03/22/ 2011.

[274] J. Shen, M. F. Champagne, Z. Yang, Q. Yu, R. Gendron, and S. Guo, "The development of a conductive carbon nanotube (CNT) network in CNT/polypropylene composite films during biaxial stretching," *Composites Part A: Applied Science and Manufacturing,* vol. 43, no. 9, pp. 1448-1453, 2012/09/01/ 2012.

[275] S. Ouchiar, G. Stoclet, C. Cabaret, A. Addad, and V. Gloaguen, "Effect of biaxial stretching on thermomechanical properties of polylactide based nanocomposites," *Polymer,* vol. 99, pp. 358-367, 2016/09/02/ 2016.

[276] P. Chandran and S. Jabarin, "Biaxial orientation of poly(ethylene terephthalate). Part III: Comparative structure and property changes resulting from simultaneous and sequential orientation," *Advances in Polymer Technology*, vol. 12, no. 2, pp. 153-165, 1993.

[277] X. Ou and M. Cakmak, "Comparative study on development of structural hierarchy in constrained annealed simultaneous and sequential biaxially stretched polylactic acid films," *Polymer*, vol. 51, no. 3, pp. 783-792, 2010/02/05/ 2010.